

DEVELOPING THERMAL INFRARED IMAGING SYSTEMS FOR MONITORING
SPATIAL CROP TEMPERATURES FOR PRECISION AGRICULTURE APPLICATIONS

by

DEVIN LYNN MANGUS

B.S., Kansas State University, 2015

A THESIS

submitted in partial fulfillment of the requirements for the degree

MASTER OF SCIENCE

Department of Biological and Agricultural Engineering
College of Engineering

KANSAS STATE UNIVERSITY
Manhattan, Kansas

2015

Approved by:

Major Professor
Ajay Sharda

Copyright

DEVIN LYNN MANGUS

2015

Abstract

Precise water application conserves resources, reduces costs, and optimizes plant performance and quality. Existing irrigation scheduling utilizes single, localized measurements that do not account for spatial crop water need; but, quick, single-point sensors are impractical for measuring discrete variations across large coverage areas. Thermography is an alternate approach for measuring spatial temperatures to quantify crop health. However, agricultural studies using thermography are limited due to previous camera expense, unfamiliar use and calibration, software for image acquisition and high-throughput processing specifically designed for thermal imagery mapping and monitoring spatial crop water need. Recent advancements in thermal detectors and sensing platforms have allowed uncooled thermal infrared (TIR) cameras to become suited for crop sensing.

Therefore, a small, lightweight thermal infrared imaging system (TIRIS) was developed capable of radiometric temperature measurements. One-time (OT) and real-time (RT) radiometric calibrations methods were developed and validated for repeatable, temperature measurements while compensating for strict environmental conditions within a climate chamber. The Tamarisk® 320 and 640 analog output yielded a measurement accuracy of $\pm 0.82^{\circ}\text{C}$ or 0.62°C with OT and RT radiometric calibration, respectively. The Tamarisk® 320 digital output yielded a measurement accuracy of ± 0.43 or 0.29°C with OT and RT radiometric calibration, respectively. Similarly, the FLIR® Tau 2 analog output yielded a measurement accuracy of ± 0.87 or 0.63°C with OT and RT radiometric calibration, respectively.

A TIRIS was then built for high-throughput image capture, correction, and processing and RT environmental compensation for monitoring crop water stress within a greenhouse and temperature mapping aboard a small unmanned aerial systems (sUAS). The greenhouse TIRIS was evaluated by extracting plant temperatures for monitoring full-season crop water stress index (CWSI) measurements. Canopy temperatures demonstrated that CWSI explained 82% of the soil moisture variation. Similarly, validation aboard a sUAS provided radiometric thermal maps with a $\pm 1.38^{\circ}\text{C}$ ($\alpha=0.05$) measurement accuracy. Due to the TIR cameras' performance aboard sUAS and greenhouse platforms, a TIRIS provides unparalleled spatial coverage and measurement accuracy capable of monitoring subtle crop stress indicators. Further studies need to be conducted to produce spatial crop water stress maps at scales necessary for variable rate irrigation systems.

Table of Contents

List of Figures	vii
List of Tables	xiv
List of Equations	xv
Acknowledgements	xvii
Preface.....	xviii
Chapter 1 - Use of Thermography for Crop Stress Assessment: A Review.....	1
1.1 Introduction.....	1
1.2 Fundamentals of Thermal Sensing	3
1.2.1 Basics of Thermal Radiation.....	3
1.2.2 Emissivity (ϵ).....	6
1.2.3 Natural Physics in Crop Sensing.....	8
1.2.4 Thermal Inertia.....	9
1.2.5 Wind Artifacts.....	11
1.2.6 Atmospheric Correction.....	12
1.3 Thermography.....	13
1.3.1 Intrinsic Properties of Thermal Cameras	13
1.3.2 Thermal Image Sensor and Sensitivity	13
1.3.3 Microbolometer Temperature Drift and Warm-Up Time	14
1.3.4 Lens Distortion.....	15
1.3.5 Image Processing	16
1.3.5.1 Radiometric Conversion	18
1.3.5.2 Atmospheric Correction.....	18
1.3.5.3 Image Management.....	19
1.3.5.4 Image Fusion.....	20
1.3.5.5 Ground Truthing	24
1.3.5.6 Whole-field Coverage and Image Mapping.....	24
1.3.6 Development Opportunities	25
1.4 Thermal Sensing Platforms.....	27
1.5 Thermal Sensing for Crop Stress	33
1.5.1 Early Crop Sensing	33
1.5.2 Alternatives to Thermal Crop Sensing.....	37
1.5.3 Crop Stress Characteristics	37
1.5.4 Thermal Indices and Techniques	38
1.5.4.1 Crop Water Stress Index	39
1.5.4.2 Stress Degree Day.....	42
1.5.4.3 Temperature-Time Threshold.....	43
1.5.4.4 Canopy Stress Index	43
1.5.5 Precision Agriculture Cost/Benefit	44

1.6 Conclusion	45
Chapter 2 - Selection and Utility of Uncooled Thermal Cameras for Spatial Crop Temperature Measurement within Precision Agriculture	46
2.1 Abstract.....	46
2.2 Introduction.....	46
2.3 Methods and Materials.....	50
2.3.1 Determining Physical Properties of TIR Camera	50
2.3.1.1 Lens Selection and Distortion.....	51
2.3.1.2 Image Resolution and Measurement.....	52
2.3.1.3 Radiometric Characterization and Measurement Accuracy	53
2.3.1.4 Warm-up Time and Automatic Recalibration	57
2.3.1.5 Connection Ease, Software, and Controllability.....	58
2.3.2 Environmental Influence on Measurement Accuracy and Repeatability.....	61
2.4 Results and Discussion	62
2.4.1 Lens Selection and Distortion.....	62
2.4.2 Image Resolution and Measurement.....	63
2.4.3 Warm-up Time.....	64
2.4.4 Radiometric Characterization and Measurement Accuracy.....	65
2.4.5 Automatic Recalibration	67
2.4.6 Connection Ease, Software, and Controllability.....	67
2.4.7 Environment Influence.....	69
2.5 Conclusion	72
Chapter 3 - Deploying a Thermal Infrared Imaging System for High Spatial and Temporal Resolution Crop Water Stress Monitoring of Corn within a Greenhouse	74
3.1 Abstract.....	74
3.2 Introduction.....	74
3.3 Methods and Materials.....	80
3.3.1 Irrigation Setup	81
3.3.2 Thermal Imaging and Environmental Monitoring.....	82
3.3.3 Radiometric Calibration.....	85
3.3.4 Automated Thermal Imaging and Processing.....	87
3.3.5 Crop Water Stress Monitoring.....	89
3.4 Results and Discussion	90
3.5 Conclusion	95
Chapter 4 - Developing a Thermal Infrared Imaging System for High Spatial Temperature Mapping aboard a Multirotor sUAS.....	96
4.1 Abstract.....	96
4.2 Introduction.....	96
4.3 Methods and Materials.....	102
4.3.1 Intrinsic Camera Properties.....	102
4.3.1.1 Image resolution and measurement	103

4.3.1.2 Lens Distortion	104
4.3.1.3 Warm-up Time and Camera Recalibration	105
4.3.1.4 Radiometric Calibration.....	106
4.3.1.5 Connection Ease, Software, and Controllability.....	108
4.3.2 Hardware and Software Development	110
4.3.3 Radiometric Calibration and Ground Reference Data	114
4.3.4 Camera Housing Design	115
4.3.5 Flight Campaigns	116
4.3.6 Image Processing	117
4.3.6.1 Ground Truthing	119
4.3.6.2 Spatial Resolution	119
4.3.6.3 Thermal Mapping	120
4.4 Results and Discussion	120
4.4.1 Lens Distortion.....	121
4.4.2 Radiometric characterization and measurement accuracy	122
4.4.3 Ground Reference Data.....	123
4.4.4 Spatial Resolution and Measurement.....	124
4.4.5 Image Filtering.....	125
4.4.6 Thermal Mapping.....	127
4.5 Conclusion	131
References	132
Appendix A - Supplemental Materials for Chapter 2	138
Appendix B - Supplemental Materials for Chapter 4	147
Appendix C - Software CD.....	149

List of Figures

Figure 1.1. Electromagnetic Spectrum. Reproduced from Schepers (2012).	4
Figure 1.2. Absolute kinetic temperature of a blackbody’s emitted radiation.....	4
Figure 1.3. Measured temperature from a blackbody object’s emitted radiant energy	5
Figure 1.4. Simulated temperature from emitted radiant energy based on varying surface emissivity.....	6
Figure 1.5. Diurnal temperature variation of desert sand depending on aspect ratio to the sun. Adapted from Kuenzer (2014).....	8
Figure 1.6. Diurnal temperatures of natural objects determined by thermal inertia. Adapted from Kuenzer (2014)	9
Figure 1.7. Graphical representation of baselines accounting for wind and solar intensity with fixed temperature depression ($T_s - T_w$). Adapted from Alves and Pereira (2000).	10
Figure 1.8. Temperature scaling algorithm’s prediction of canopy temperature at remote locations with one daily measurement. Reproduced from Peters and Evett (2004).....	11
Figure 1.9. Wind artifacts within a thermal image. Reproduced from Schepers (2012).	11
Figure 1.10. Diagram for atmospheric correction for sensing platforms. Recreated from Berk et al. (1998).....	12
Figure 1.11. Comparison between medium and large pixel arrays for a microbolometer. Reproduced from Schepers (2012)	13
Figure 1.12. Radiometric temperature changes measured by a TIR camera during warm-up period. Adapted from Berni et al. (2009).	15
Figure 1.13. Lens distortion prior to correction (left) with correction (right). Adapted from Lagueta et al. (2013).	16
Figure 1.14. Simulated atmospheric conditions and flight altitude. Reproduced from Berni et al. (2009).....	19
Figure 1.15. Visible color and thermal image comparison. Adapted from Taghvaeian et al. (2013).....	21
Figure 1.16. Typical plant canopy temperature extraction (b) demonstrating color from the (a) visible color image and the resulting temperature association (c). Reproduced from Wang et al. (2010).	21
Figure 1.17. Difference between the characterized vegetation temperature of the actual crop canopy temperature (T_c) and the averaged FOV temperature (T_i) versus crop canopy coverage (a), and measured vegetation temperature of the actual crop canopy temperature (T_c) and the averaged FOV temperature (T_i) versus crop canopy coverage (b). Reproduced from Rodriguez et al. (2005).	22
Figure 1.18. Macro image of visible color and thermal image comparing leaf temperatures under sunlit and shaded regions. Adapted from Taghvaeian et al. 2013.....	23
Figure 1.19. Thermal orthomosaic image (left) from a sUAS over a peach orchard where vegetation is extracted from soil (lower right). Reproduced from Berni et al. (2009). ...	23
Figure 1.20. Thermal satellite imagery with overlay of sUAS imagery demonstrating the spatial resolution of satellite (90 m) to sUAS (<2m) aerial imagery. Adapted from Kuenzer (2014).....	30

Figure 1.21. Infected tobacco interaction Chaerle et al. (1999).....	35
Figure 1.22. Canopy temperature differences between canopy (T_c) and ambient air (T_{air}) of 61 maize genotypes in water stress and well-watered plants. Romano et al. (2011).	36
Figure 1.23. Generalized energy balance of vegetation. Adapted from Blonquist and Bugbee (n.d.).....	38
Figure 1.24. ($T_c - T_a$) versus Vapor Pressure Deficit comparison. Reproduced from Blonquist and Bugbee (n.d.).....	39
Figure 1.25. Simulated relationships of non-water stress baselines from varied environmental conditions compared to theoretical baselines. Reproduced from Berni et al. (2009).....	40
Figure 2.1 Changes of radiometric temperature measured by TIR camera during warm-up period. Adapted from Berni et al. (2009).	49
Figure 2.2. Grid pattern tool (left) and thermal image (right) used for lens distortion.....	52
Figure 2.3. Investigation of necessary spatial resolution for temperature accuracy.....	52
Figure 2.4. (a) BB enclosure constructed to limit outside influence. (b) Surface mount thermistors measured actual target surface temperatures within an ROI (shown in red) to characterize pixel intensities. (c) Heating element, box reference equal to air temperature and a cool, wet reference.	54
Figure 2.5. BB enclosure heating element and air exchange vent controller user interface.....	54
Figure 2.6. Thermistor mounted to camera housing temperature for subsequent testing.....	54
Figure 2.7. (a) Voltage divider wiring diagram used to measure changing voltage from the corresponding change in the thermistor resistance. (b) Thermistor calibration curve used to quantify temperature with a change in voltage. (See Appendix A, Figure A.4 for more details).....	55
Figure 2.8. (b) Data acquisition (DAQ) system used to monitor BB enclosure sensors with (a) stereo plug connectors.	55
Figure 2.9. TIR Camera Evaluation system diagram used to control cameras, monitor BB enclosure conditions, and output test data.	56
Figure 2.10. TIR Camera Evaluation Software VI used to conduct radiometric calibrations while recording raw data. (See Appendix A, Figure A.7 for more details).....	56
Figure 2.11. Camera settings from level and gain control for a thermal detector. The gain control adjusts the thermal detector sensitivity to LWIR energy thereby adjusting the temperature span. Level control adjusts the center offset temperature to adjust the offset of the temperature span. Adapted from DRS Tamarisk® 320 Camera Control Software User Guide (2013).....	59
Figure 2.12. Hardware used to control, capture, and process thermal images from the TIR camera cores	60
Figure 2.13. Hardware to capture digital and analog video outputs	60
Figure 2.14. (a) BB enclosure installed in the (b) environmental chamber for strictly controlled environmental conditions. (c) Air exchange through the BB enclosure controls internal air parameters.....	61
Figure 2.15. (a) CAM1 with 11 mm and (b) CAM2 with 7.5 mm lens distortion results from the point distortion (grid) model with grid pattern with known point distances (left) point vector map (middle), and visual distortion map (right).....	63

Figure 2.16. (a) Spatial resolution versus the digital value accuracy. (b) Generalized pixel orientations and spatial resolutions of 1 pixel, 2 pixel, and 4 pixels incident on a target. Black boxes represent the individual pixel's FOV. Green objects represent an object that can be accurately measured with the pixel orientation and spatial resolution. Pink objects represent an object that is measured with error.	64
Figure 2.17. Raw image intensity and housing temperature versus camera 'on-time' of (a) CAM1 and (b) CAM2. The dotted vertical line indicates the time when measured pixel intensity was within 5% of the stable pixel intensity.	65
Figure 2.18. Radiometric calibration performed on the CAM1 (a) and CAM2 (b) at 25°C air temperature and 35% relative humidity after reaching a steady operating temperature.	66
Figure 2.19. CAM1 measurement accuracy ($\pm^{\circ}\text{C}$) of OT and RT radiometric calibration process over 1 h. The absolute difference between the actual and measured temperature is shown. CAM1 operated at a stable temperature prior to comparison.	66
Figure 2.20. CAM1 camera (a) gain for temperature span and (b) level setting characteristics for offset temperature bias.	68
Figure 2.21. CAM2 camera (a) gain for temperature span and (b) level setting characteristics for offset temperature bias.	68
Figure 2.22. Accuracy comparison of analog and digital video output over a 1 h sensing time of CAM1. The absolute difference between actual and measured temperature is shown with a 1 min NUC. Results demonstrate the digital and analog measurement accuracy to be 0.43°C or 0.82°C ($\alpha=0.05$), respectively. The TIR camera core operated at a stable temperature prior to the comparison.	69
Figure 2.23. Measurement inaccuracy due to a change in camera housing temperature over a 10 min time span. OT radiometric calibration was performed when the TIR camera housing was at 20°C. CAM1 was configured for 1 min NUC, analog video output and a temperature span of 20°C. Ambient air temperature was 10°C and relative humidity was 25%. CAM1 operated at a stable temperature prior to inducing a change in ambient air temperature.	70
Figure 2.24. Influence of relative humidity changes to measurement accuracy between the TIR camera and the stable target whose temperature is (a) above ($>5^{\circ}\text{C}$) ambient air temperature, (b) equal to air temperature, and (c) below ($>5^{\circ}\text{C}$) air temperature. CAM1 was configured for 1 min NUC, analog video output, and a temperature span of 20°C. CAM1 operated at a stable temperature prior to the inducing a change in relative humidity.	71
Figure 2.25. RT versus OT radiometric calibration under changing relative humidity. OT radiometric calibration was conducted when chamber was at a relative humidity of 25%. CAM1 was configured for 1 min NUC, analog video output, and a temperature span of 20°C. CAM1 operated at a stable temperature prior to the inducing a change in relative humidity.	71
Figure 3.1. Water stressed plant orientation (left) and well-watered plants (right).....	80
Figure 3.2. Characteristic water use of corn. Reproduced from Rogers and Alam (1998).	81
Figure 3.3. (a) Automated irrigation system and (b) corn during growth period 1.	82
Figure 3.4. Component diagram for TIRIS.....	82

Figure 3.5 Greenhouse TIRIS VI front panel for controlling loop time and camera control while monitoring and saving soil moisture of irrigation regimes, air temperature, relative humidity, solar radiance, reference panels, camera temperature, sample number, and time stamp.....	84
Figure 3.6. (a) Voltage divider wiring diagram used to measure changing voltage from the corresponding change in the thermistor resistance. (b) Thermistor calibration curve used to quantify temperature with a change in voltage. (See Appendix A, Figure A.4 for more details).....	85
Figure 3.7. Real-time radiometric calibration performed on the DRS Tamarisk® 320 at a 25°C air temperature, 45% relative humidity, and steady-state operating temperature.	86
Figure 3.8. Absolute difference between actual minus measured temperature.	87
Figure 3.9. RT radiometric calibration under changing vapor pressure deficit (VPD)	87
Figure 3.10. Image Processing VI for analyzing greenhouse data controlling input data, output metadata filename, the number of processed images and monitoring output image RT radiometric calibration, image number, and timestamp.	88
Figure 3.11. Flow chart of batch processing for image and environmental data flow	88
Figure 3.12. Automated TIRIS segmented individual corn foliage, shown in green, from background soil, cement, and pot containers. Black pixels indicate a cold surface while white pixels indicate hot surface. ROIs, shown in green, captured the individual crop intensity and reference panel temperatures.....	89
Figure 3.13. Comparison between the measured and actual temperature of the in-between reference panel temperature in the greenhouse from 6:00 to 19:00 h.	91
Figure 3.14. Real-time confidence interval of a well-watered corn plant from 12:00 to 18:00 h	91
Figure 3.15. Empirical leaf canopy-to-air temperature deficit versus VPD during (a) germination and seedling stage, (b) rapid growth stage, (c) reproductive stage, and (d) maturity stage.....	92
Figure 3.16. Predicted canopy-to-air temperature deficit versus VPD through four growth stages.....	92
Figure 3.17. Comparison of (a) non-water stressed stem-to-air temperature deficit to VPD and (b) non-water stressed canopy-to-air temperature deficit versus VPD.....	93
Figure 3.18. (a) Daily soil moisture content and peak daily CWSI throughout the experiment; (b) daily soil moisture content versus peak daily CWSI. A split plot shows the negative correction of the soil moisture versus CWSI from a CWSI value of 0.6 to 1.0 and no significant correlation from a CWSI value of 0 to 0.6.	94
Figure 4.1. Grid pattern tool (left) and thermal image (right) used for lens distortion.....	105
Figure 4.2. Image Intensity and housing temperature versus thermal camera on-time of (a) DRS Tamarisk® 320 and (b) DRS Tamarisk® 640. Indicated warm-up time was determined when the TIR camera measured with 5% of the stable pixel intensity. See Section 2.3.1.4 for more details.	106
Figure 4.3. Radiometric calibration performed on (a) DRS Tamarisk® 320 and (b) DRS Tamarisk® 640 at 25°C air temperature and 35% relative humidity when each uncooled thermal camera reached a steady operating temperature.	107

Figure 4.4. Measurement accuracy ($\pm^{\circ}\text{C}$) of the Tamarisk® 320 over 60 min. The absolute difference between the actual and measured temperature is shown.	107
Figure 4.5. The gain control adjusts the thermal detector sensitivity to LWIR energy thereby adjusting the temperature span. Level control adjusts the center offset temperature to adjust the bias of the temperature span. Adapted from DRS Tamarisk® 320 Camera Control Software User Guide (2013).....	108
Figure 4.6. DRS Tamarisk® 320 Camera (a) camera (a) gain for temperature span and (b) level setting characteristics for offset temperature bias.	108
Figure 4.7. DRS Tamarisk® 640 camera (a) gain for temperature span and (b) level setting characteristics for offset temperature bias.	109
Figure 4.8. Relationship between level control range (Δ level) and temperature span ($^{\circ}\text{C}$).....	110
Figure 4.9. TIRIS component system diagram for camera calibration and ground reference data	110
Figure 4.10. (a) Voltage divider wiring diagram used to measure voltage due to thermistor resistance change. (b) Thermistor calibration curve to quantify temperature with change in resistance. (See Appendix B, Figure A.4 for more details).....	111
Figure 4.11. (a) Ground reference panels for temperature reference and cross-calibration from sensing distance and environmental influence in radiant heat transmission with (b) the virtual interface for control and visual awareness.	112
Figure 4.12. (b) Data acquisition system used to interface ground reference sensors with (a) plug-n-play sensor inputs.....	113
Figure 4.13. OT radiometric calibration use the cold and warm temperature differential created by (a) the wet reference panel and (b) the black aluminum panel measured with surface mount thermistors in the designated ROI shown in blue and red. (c) The corresponding TIR camera FOV is shown to demonstrate the temperature differential of the cold and warm reference.	114
Figure 4.14. TIR Field Calibration (TCP) VI to create OT radiometric calibrations while recording ground reference data. The visual indicator shows the VI monitored RT ground reference data, raw video feed, and file storage specifications while providing controls to conduct a OT Calibration.....	115
Figure 4.15. TIR camera case to hold sUAS TIRIS components in (a) the exploded view and (b) the collapsed view.....	116
Figure 4.16. (a) DJI s800 Evo used for flight campaigns with sUAS TIRIS shown on (b) gimbal mount.....	116
Figure 4.17. Image process flow as the analog video file is converted to the final stitched thermal map.	117
Figure 4.18. The TVP VI converts the thermal video file to filtered images featuring selective controls of file path, camera selection for specific lens distortion, image output quality, capture frame rate, cropping dimensions, and progress indicators.....	118
Figure 4.19. ROI analysis with increasing spatial resolution. The green boxes indicate the ROIs of increasing size.	119
Figure 4.20. Resulting sUAS TIRIS featuring accessible control inputs and image acquisition ports.	121

Figure 4.21 (a) Tamarisk® 640 with 25 mm and (b) Tamarisk® 320 with 11 mm lens distortion results from the point distortion grid model with the original image (left) point vector map (middle), and visual distortion map (right).....	122
Figure 4.22. (a) Ground reference panel temperatures throughout flight campaign as recorded by the ground measurement station and (b) the ground reference panels viewable from the sUAS multirotor at an altitude of 40 m and a spatial resolution of 27 mm/pixel....	123
Figure 4.23. Measurement accuracy found from a flight campaign comparing the actual temperature versus the measured temperature as shown with a 95% confidence interval. Results reveal a TIRIS measurement accuracy of $\pm 1.38^{\circ}\text{C}$	124
Figure 4.24. ROI analysis with measured temperature (a) with respective spatial resolution centered on a corn plant target with a spatial resolution of 0.5 cm/pixel (b).	125
Figure 4.25. (a) Comparison of thermal map of raw images and (b) filtered images prior to image stitching. In the resulting raw image mosaic, the outer edge and inner portion (black boxes) of the image lacks detail represented in the resulting mosaic image captured by the filtered images.....	126
Figure 4.26. Mosaicked image resulting from capture frame rates illustrated in Table 4.7 at (a) 3 frames s^{-1} , (b) 2 frames s^{-1} , (c) 1 frame s^{-1} , (d) 1 frame 2 s^{-1} , and (e) 1 frame 3 s^{-1}	127
Figure 4.27. Camera orientation (black line normal to image) and respective image altitude. Parameters were deduced from image overlap and common pixel intensities between neighboring images.....	128
Figure 4.28. Forward and lateral overlap of stitched images. The red and blue lines indicate the invalid and valid, respectively, common points between the images.....	128
Figure 4.29. Thermal map of a golf course green at an altitude of 40 meters. This orthomosaic image is the result of 220 individual images taken at 1 FPS. After post-processing, measurement accuracy was $\pm 1.38^{\circ}\text{C}$ from an in-flight OT radiometric calibration with theoretical spatial resolution of 27 mm/pixel. A temperature legend is generated from the upper and lower temperatures found with the TIR Field Calibration software.	129
Figure 4.30 Forward and lateral overlap of stitched images. The red and blue lines indicate the invalid and valid, respectively, common points between the images.....	130
Figure 4.31. Thermal map of corn at an altitude of 80 meters. After post-processing, measurement accuracy was $\pm 1.60^{\circ}\text{C}$ from an on-ground OT radiometric calibration with theoretical spatial resolution of 54.4 mm/pixel. This orthomosaic image is the result of 180 individual images taken at 1 frame rate per second. A colorized mask is used to provide visual isotherms.....	130
Figure A.1 Tamarisk® 320 Data Specifications.....	139
Figure A.2 FLIR® Tau 2 Data Specifications	141
Figure A.3 IPORT CL-U3 External Frame Grabber	142
Figure A.4 Surface mount thermistors produced by Omega Engineering. ON-930-44005-40 and ON-930-44033 were used for research covered in Chapter 2, 3, and 4.....	143
Figure A.5 Near-Perfect Black-Body Enclosure Monitoring VI front panel (a) and back panel (b).....	144
Figure A.6 The wiring of the Thermistor sub-VI (a), front panel (b), and block diagram (c) show the input from the logarithmic calibration curve in order to convert input voltage into temperature $^{\circ}\text{C}$	145

Figure A.7 TIR Camera Evaluation VI front panel	145
Figure A.8 Tamarisk® 320 lens distortion calibration results.....	146
Figure A.9 FLIR® Tau 2 (324) lens distortion calibration results	146
Figure B.10 Tamarisk® 640 Data Specifications	147
Figure B.11 Tamarisk® 640 lens calibration results	148
Figure B.12 OT Calibration VI front panel	148

List of Tables

Table 1.1. Emissivity ($\epsilon \pm$ standard deviation) of determined crops leaves. Adapted from Idso, Jackson, Ehler, and Mitchell (1969).....	7
Table 1.2. Atmospheric conditions that influence thermographic systems. Adapted from Kuenzer (2014).	12
Table 1.3. Platform comparison between satellite, piloted aircraft, sUAS, and ground thermography.....	31
Table 1.4. Summary of thermography use, thermal camera, sensing platform, imagery software, temperature sensitivity, and source.....	31
Table 1.5. Applied nitrogen rate versus crop stress index of wheat samples. Adapted from Rodriguez et al. (2005).	36
Table 1.6. Recommended sensor accuracies to limit CWSI measurement error (Blonquist & Bugbee, n.d.).....	41
Table 2.1. Non-uniformity correction influence on measurement accuracy ($\pm^\circ\text{C}$) with OT and RT radiometric correction.....	58
Table 2.2 Lens distortion results including radial and tangential correction coefficients. (See Appendix A, Figure A.8 and A.9 for more details).....	63
Table 2.3. Measurement accuracy ($\pm^\circ\text{C}$) with OT and RT radiometric correction. (Accuracies shown represent an 95% confidence interval).....	67
Table 2.4. Temperature resolution ($^\circ\text{C}$) of specific temperature span.....	69
Table 3.1. Average recommended water-use rate for irrigated corn	81
Table 3.2. Predicted canopy-to-air temperature deficit-to-VPD.....	92
Table 4.1. Spatial resolution with selected lens at various distances. Adapted from DRS Technologies A Finmeccanica Company, (2013).	103
Table 4.2. 60 min measurement accuracy ($\pm^\circ\text{C}$) with OT calibration. ($\alpha=0.05$).....	107
Table 4.3.TIRIS Capabilities and Features	121
Table 4.4 Lens distortion analysis including radial and tangential correction coefficients.....	122
Table 4.5. Sample TIRIS camera calibration file for a flight campaign.....	123
Table 4.6. Comparison of results from raw and filtered image stitching regarding aligned images, processing time, and developed point clouds.....	125
Table 4.7. Results from various frame capture rates and image stitching results related to processing time, developed point cloud, and common point matches between consecutive images	127
Table 4.8 Image overlap percentage	128
Table 4.9. Image overlap percentage	130

List of Equations

Equation 1.1	5
Equation 1.2	5
Equation 1.3	5
Equation 1.4	6
Equation 1.5	7
Equation 1.6	9
Equation 1.7	10
Equation 1.8	16
Equation 1.9	16
Equation 1.10	18
Equation 1.11	22
Equation 1.12	38
Equation 1.13	39
Equation 1.14	40
Equation 1.15	43
Equation 1.16	43
Equation 2.1	51
Equation 2.2	51
Equation 2.3	57
Equation 2.4	57
Equation 2.5	57
Equation 2.6	59
Equation 3.1	86
Equation 3.2	86
Equation 3.3	86
Equation 3.4	86
Equation 3.5	89
Equation 3.6	89
Equation 3.7	90
Equation 4.1	105
Equation 4.2	105
Equation 4.3	109
Equation 4.4	112
Equation 4.5	112
Equation 4.6	115
Equation 4.7	115
Equation 4.8	115
Equation 4.9	115

Equation 4.10	115
Equation 4.11	115
Equation 4.12	115
Equation 4.13	129
Equation 4.14	130

Acknowledgements

This research would not be possible without the support of numerous people. First, I would like to thank my advisor, Ajay Sharda, who provided invaluable wisdom and guidance. His dedication to provide ongoing support through time, resources, and learning provided opportunities to gain insight, understand hardware and software, and grow personally and professionally. I also thank my committee members: Naiqian Zhang, Deon van der Merwe, and Vara Prasad. I have enjoyed the opportunity to experience the backgrounds, interests, expertise, and passion of these dedicated individuals.

This thesis work and all associated reports and support materials were supported by the Sustainable Agriculture Research and Education (SARE) program, funded by the U.S. Department of Agriculture - National Institute of Food and Agriculture (USDA-NIFA). Any opinions, findings, conclusions, or recommendations expressed within do not necessarily reflect the view of the SARE program or the U.S. Department of Agriculture. USDA is an equal opportunity provider and employer. A special acknowledgement and great appreciation is extended to DRS Technologies, Inc. for their assistance in providing thermal camera cores and ongoing support throughout the research. Special thanks are extended to the Kansas State University Biological and Agricultural Engineering Department for building materials, hardware, and support throughout my college career.



I want to thank my family for providing me with an agricultural background and everlasting support that led me to where I am today. I also want to thank my wife Shelby for her patience and encouragement through stressful times.

Finally, I thank God for the abilities, skills, and opportunities he has given me.

Preface

All the work presented henceforth was conducted in the Biological and Agricultural Engineering and Agronomy Department at Kansas State University in Manhattan, Kansas. The following thesis chapters were written for direct submission for individual publication. As such, each chapter is written in the corresponding journal format. Therefore, similar objectives, reference material, figures, equations, and previous chapter findings are found in subsequent introductory and methodology sections, providing support for subsequent chapter research.

As the lead investigator, I was responsible for conceptual design, data collection, and analysis, as well as manuscript composition with support from committee members, fellow researchers, and previous referenced academic work.

I began this design project on August 20th, 2013. The following chapters are an attempt to capture the long process of learning, small breakthroughs, milestones, lessons learned, and opportunities for future development. However, these chapters cannot express the long days and nights battling hardware, software, and deadlines, the eager anticipation for significant results, and the disappointment of having to go back to the drawing board.

Chapter 1 - Use of Thermography for Crop Stress Assessment: A Review

1.1 INTRODUCTION

Tactical agriculture management that uses on-demand remote sensing relies on accurate measurements, rapid response times, inexpensive sensor platforms, and user-intuitive techniques to achieve well-informed decisions. By spatially monitoring crop stress, producers use thermal remote sensing for crop canopy temperature mapping (Alves & Pereira, 2000; Ayeneh, et al., 2002; Berni, et al., 2009; Taghvaeian, et al., 2013; Wang, et al., 2010), measuring individual crop profile temperatures (Leinonen & Jones, 2004), scheduling variable rate irrigation (Cohen, et al., 2005; Colaizzi, et al., 2012; Fitzgerald, et al., 2007), crop breeding (Grant, et al., 2006; Liu, et al., 2011; Zia, et al., 2013), assessing fruit detection and quality (Bulanon, et al., 2009; Sepulcre-Canto, et al., 2007;; Zhao, et al., 2005), estimating biomass (Wooster, et al., 2013), forecasting yield (Hackl, et al., 2012), detecting disease, and determining nutrient deficiency (Hashimoto, et al., 1984; Tilling, et al., 2007; Chaerle, et al., 1999). Crop stress broadly describes a factor that limits crop yield potential (Jackson, et al., 1981) in which severity depends on stress types, timing, and duration. As producers strive for increased output from available land, economic and environmental considerations will become more critical for knowledge-based management techniques intended to increase farming efficiency, enhance profitability, lessen environmental impact, and promote precision technology advancement (Herwitz, et al., 2004; Taghvaeian, et al., 2013).

Of the many stress types placed on an agricultural production crop, water stress is the most common and limiting factor impacting potential yield (Zia, et al., 2013; Luvall & Holbo, 1991; Scherrer, et al., 2011). In the United States, agriculture annually uses approximately 80% of the consumptive ground and surface water use (USDA, 2014). Consequently, water conservation potential relies heavily on precision technologies for water decision support (Rodriguez, et al., 2005) in order to increase water use efficiency (Cohen, et al., 2005; Ballester, et al., 2013; Gontia & Tiwari, 2008). In addition, future municipal demand for clean water will restrict agricultural water usage and create more governmental regulations, potentially leading to water shortages and strict water allocations. Therefore, deficit irrigation is a scheduling technique to reduce irrigation application and improve water use efficiency (Ballester, et al., 2013; Evett, et al., 2014; Scherrer,

et al., 2011) while tolerating an acceptable reduction in yield (Moller, et al., 2007; Sepulcre-Canto, et al., 2007). The decision to irrigate is critical, but accurate determination of irrigation amount and location is as equally important for site-specific irrigation (Alves & Pereira, 2000; Cohen, et al., 2005; Wanjura, et al., 1992) that matches the precise crop water need at manageable increments to achieve desired crop performance (Cohen, et al., 2005; Taghvaeian, et al., 2013). However, extensive variability exists within commercial agricultural fields, including soil type and depth, topography, climate, crop growth stage, and variance in producer operation (Cohen, et al., 2005; Evett, et al., 2014).

The aim of this review is to demonstrate the utility of thermography in agriculture. Because crop canopy temperature can indicate crop stress, thermography is essential in agricultural studies in order to acquire qualitative and quantitative crop characteristics for supporting management decisions (Colaizzi, et al., 2012; Evans, et al., 2000). In addition, the spatial resolution (ground sample distance (e.g., 1cm/pixel)) and image processing functionality of low-resolution thermography help increase the use of crop canopy temperature characteristics in agriculture (Luquet, et al., 2003). Because arable land is currently unable to meet the increased demand for food, fuel, and fiber for future generations, available land and resources must be managed more efficiently in order to increase productivity. These management practices will be enabled with the use of precision agriculture technology such as thermography. In addition, crops sensing capabilities can increase land productivity, efficiently apply inputs (Brown, et al., 1994; Goel, et al., 2000), and sustain production growth.

Thermal infrared (TIR) sensors are categorized as thermometry and thermography. Thermometrics utilize infrared thermometers (IRT) to provide a single-point measurement of the average temperature of all objects within the field of view (FOV) (Hackl, et al., 2012), with practical use limited to ground and laboratory applications. In thermography, a TIR camera uses a thermal image sensor to generate a thermal image in which each pixel represents the average temperature of all objects in the specific pixel's area of interest (AOI) (Grant, et al., 2006).

The use of thermography in agriculture is attributed to the fundamentals of thermal sensing and the recent advancements in thermal sensor technology and sensing platforms that will be reviewed in four sections. First, the thermal domain of the electromagnetic spectrum; laws of Stefan-Boltzmann, Wien, Kirchhoff, and Planck; kinetic and radiance temperatures; emissivity and atmospheric correction; and thermal inertia are discussed. Physical limitations and constraints

impacting thermal sensing accuracy are also discussed. Thermometry is briefly discussed because basic physical fundamentals of surface temperature measurements are identical for both types of thermal sensors. Second, techniques to increase thermal sensitivity are briefly discussed in relation to intrinsic properties of thermal cameras and image analysis, as well as future needs regarding thermographic development. Third, thermal sensing platforms for production crops are summarized with an emphasis on low-altitude imagery achieved with small Unmanned Aerial Systems (sUAS) because of the ground coverage and level of sensing detail not previously possible. Lastly, thermal sensing for crop stress is discussed with regards to early crop sensing, alternative crop sensing methods, crop stress indicators, thermal indices, and cost versus benefit.

1.2 FUNDAMENTALS OF THERMAL SENSING

Thermal domain of the electromagnetic spectrum, laws of Stefan-Boltzmann, Wien, Kirchhoff, and Planck; kinetic and radiance temperatures; emissivity and correction; thermal inertia; and physical limitations and constraints that impact thermal camera measure accuracy (closeness to the true value) are discussed in the following sections.

1.2.1 Basics of Thermal Radiation

Temperature plays a fundamental and often limiting role in many biological processes that control the rate of chemical reactions between plants and surrounding microclimates (Luvall & Holbo, 1991). Physical plant mechanisms assessed with crop sensing are often regarded as cause and effect in order to simplify and describe a system (Monteith & Unsworth, 2013). In natural sciences, such as agriculture, long-wave infrared (LWIR) of the electromagnetic spectrum (7 to 14 μm) ranges in surface temperature from -66.2°C to 140.0°C (Kuenzer, 2014), as shown in Figure 1.1. The LWIR region of the electromagnetic spectrum demonstrates a longer wavelength compared to the visible (VIS) and near infrared (NIR) regions. Compared to VIS and NIR detectors, TIR detectors measure emitted radiation instead of reflected radiation (Kuenzer, 2014).

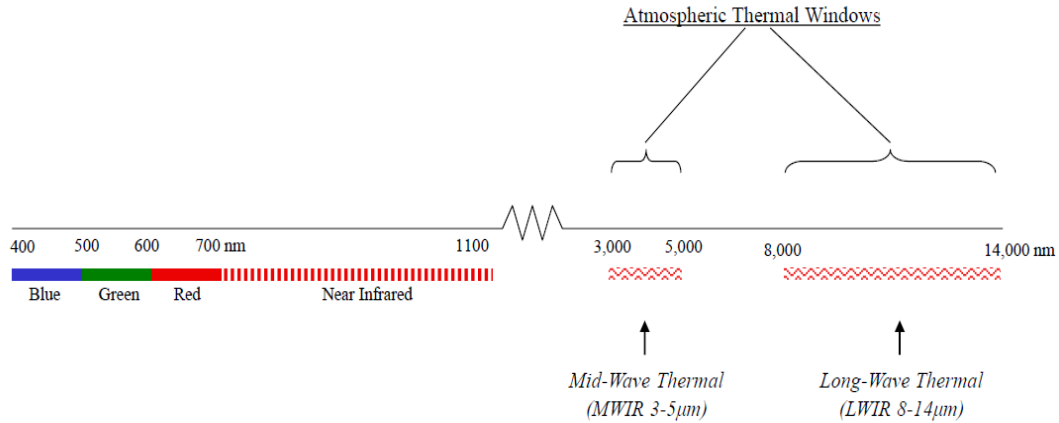


Figure 1.1. Electromagnetic Spectrum. Reproduced from Schepers (2012).

All objects with internal temperature greater than 0 K emit radiant electromagnetic energy with respective wavelengths (Maes & Steppe, 2012; Vasterling & Meyer, 2013). As suggested by the Wien Displacement Theory, the emitted energy’s wavelength from an object is a reciprocal of the object’s temperature, as shown in Figure 1.2. A shorter electromagnetic energy wavelength yields a higher absolute kinetic temperature. Molecules within an object vibrate, creating a vibrating motion that emit energy at a specific wavelength directly related to internal kinetic temperature (Hecker, et al., 2013). Because this vibration is related to physical and chemical material compositions, distinctive features in the TIR electromagnetic spectrum can be undetectable in the VIS and NIR electromagnetic range (Hecker, et al., 2013).

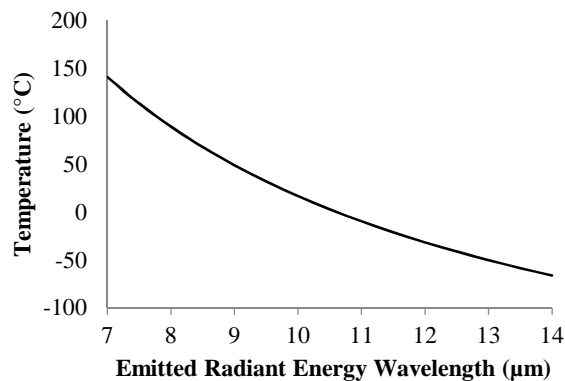


Figure 1.2. Absolute kinetic temperature of a blackbody’s emitted radiation

According to Planck’s Fundamental Blackbody Radiation Law, a blackbody emits radiant energy at a given wavelength dependent on the absolute temperature (Kuenzer, 2014). At a given wavelength, shown in Figure 1.3, the radiated energy’s wavelength can be calculated from surface temperature in Equation 1.1 which is rearranged to form Equation 1.2 in order to directly measure surface temperature.

$$R = \epsilon \sigma T^4 \quad (1.1)$$

$$T = \left(\frac{R}{\epsilon \sigma} \right)^{1/4} \quad (1.2)$$

Where:

R=Radiant energy flux of blackbody [W m⁻²]

ϵ =emissivity (i.e., $\epsilon=1$ for blackbody object)

σ =Stefan-Boltzmann constant [5.6697 x 10⁻⁸ W m⁻² K⁻⁴]

T=Kinetic Temperature [K].

The radiant energy-to-internal temperature relationship shown in Figure 1.3 can be used to measure the temperature of a blackbody surface with a TIR sensor (Kuenzer, 2014). A blackbody object is idealized as a perfect absorber and emitter, with a blackbody temperature corresponding to the object's radiant energy (Maes & Steppe, 2012), as defined by Stefan-Boltzmann's Law of radiant energy, Equation 1.2.

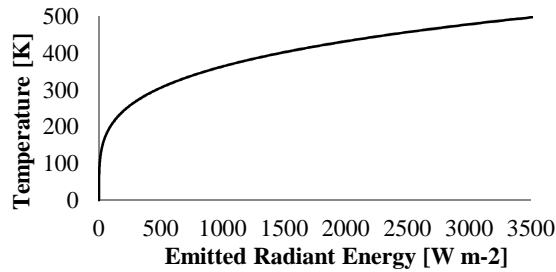


Figure 1.3. Measured temperature from a blackbody object's emitted radiant energy

However, natural objects are not perfect emitters or absorbers because they reflect an amount of background temperature, resulting in temperature estimation errors. Maes et al. (2012) asserted that the Stefan-Boltzmann Law defines total long-wave radiation (L_{out}) from a system, as shown in Equation 1.3.

$$L_{out} = L_{emitted} + L_{reflected} \quad (1.3)$$

Where:

L_{out} = Outgoing radiant energy

$L_{emitted}$ = Emitted radiant energy

$L_{reflected}$ = Reflected radiant energy.

In Equation 1.3, outgoing radiant energy (L_{out}) corresponds to the apparent temperature (T_{ap}) comprised of emitted radiant energy ($L_{emitted}$) and reflected radiant energy ($L_{reflected}$) from the object's surface. According to Maes et al. (2012), apparent temperature is influenced by background temperature (T_{bg}), surface temperature (T_s), and surface emissivity (ϵ), defined by Equation 1.4:

$$T_s = \sqrt[4]{\frac{T_{ap}^4 - (1 - \epsilon)T_{bg}^4}{\epsilon}} \quad (1.4)$$

Where:

T_s = Surface temperature

T_{ap} = Apparent temperature

ϵ = Emissivity

T_{bg} = Background temperature

For the two types of thermal sensors, IRTs measure average apparent temperature (T_{ap}) within the FOV, resulting in temperature estimation errors. However, after accounting for background temperatures (T_{bg}) and surface emissivity (ϵ), thermal cameras provide surface temperature (T_s) rather than apparent temperature (T_{ap}). In application, background temperatures can be accounted for directly or indirectly with an IRT sensitive to the same LWIR region as the thermal sensor (Maes & Steppe, 2012). Direct background temperatures of the sky are measured, while indirect background temperature can be measured from a horizontal lambert radiator, blotted aluminum foil.

1.2.2 Emissivity (ϵ)

Emissivity must be identified in order to accurately quantify kinetic temperature from emitted radiant temperature (Hecker, et al., 2013). Thermal sensing accounts for emissivity using empirical laboratory and/or field measurements (Hecker, et al., 2013). Surface emissivity reduces emitted radiant energy, as shown in Figure 1.4.

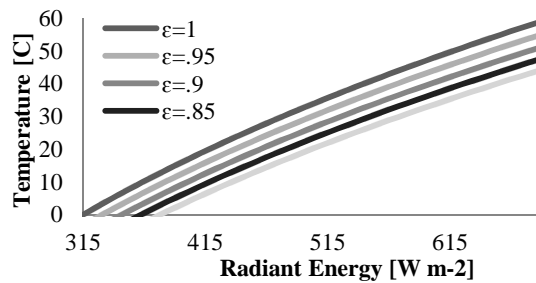


Figure 1.4. Simulated temperature from emitted radiant energy based on varying surface emissivity

Emissivity correction is crucial when analyzing thermal imagery because objects with identical kinetic temperature and different emissivity will emit and reflect different levels of radiant temperature (Kuenzer, 2014). Because plant leaves consist primarily of water, plant leaves closely emit and absorb thermal radiation as near-blackbodies with a general emissivity (ϵ) of 0.95 (Berni, et al., 2009; Hecker, et al., 2013). Actual emissivity of vegetation should be validated because of complex chemical interactions within the leaf and varying leaf structures that

consequently produce subtle differences in emissivity between vegetation species types (Hecker, et al., 2013; Jones, 1999; Vasterling & Meyer, 2013). If surface temperature (T_s), apparent temperature (T_{ap}), and background temperature (T_{bg}) are known, emissivity can be estimated, as defined by Equation 1.5:

$$\varepsilon = \frac{T_{ap}^4 - T_{bg}^4}{T_s^4 - T_{bg}^4} \quad (1.5)$$

In addition to empirical emissivity measurements, accurate background and surface temperature can reduce measurement error (Maes & Steppe, 2012). Idso et al. (1969) empirically determined crop leaf emissivity for a range of species, as shown in Table 1.1.

Table 1.1. Emissivity ($\varepsilon \pm$ standard deviation) of determined crops leaves. Adapted from Idso, Jackson, Ehler, and Mitchell (1969).

Species	Infrared Emittance
Aralia - <i>Aralia seboldi</i>	0.968 \pm 0.006
Avocado - <i>Persea drymifolia</i>	0.979 \pm 0.009
Beavertail Cactus - <i>Opuntia basilaris</i>	0.978 \pm 0.002
Blind Prickly pear - <i>Opuntia rufida</i>	0.977 \pm 0.002
Cactus Pear - <i>Opuntia ficus indica</i>	0.957 \pm 0.002
Chili Pepper - <i>Capsicum frutescens</i> cv. Long Green	0.979 \pm 0.005
Common Bean - <i>Phaseolus vulgaris</i> cv. Bountiful (center leaflet)	0.938 \pm 0.008
Common Bean - <i>Phaseolus vulgaris</i> cv. Bountiful (lateral leaflet)	0.964 \pm 0.005
Cordyline - <i>Cordyline terminalis</i>	0.967 \pm 0.003
Cotton - <i>Gossypium hirsutum</i> cv. Deltapine	0.964 \pm 0.007
Cottonwood - <i>Populus Fremontii</i>	0.977 \pm 0.004
Crested Cactus - <i>Lophocereus schottii</i>	0.973 \pm 0.004
Geranium - <i>Pelargonium domesticum</i> var. Martha Washington	0.992 \pm 0.002
Ivy - <i>Hedera helix</i> var. Algerian	0.969 \pm 0.005
Lacy Tree Philodendron - <i>Philodendron selloum</i>	0.990 \pm 0.010
Long Cotton - <i>Gossypium barbadense</i> cv. Pima S-4	0.979 \pm 0.008
Maize - <i>Zea mays</i> cv. Mexican June	0.944 \pm 0.004
Orange - <i>Citrus aurantium</i>	0.972 \pm 0.008
Papaya - <i>Carica papaya</i>	0.982 \pm 0.004
Prickle pear - <i>Opuntia engelmannii</i>	0.961 \pm 0.004
Purple Prickly pear - <i>Opuntia orbicular</i>	0.971 \pm 0.006
Rose - <i>Rosa</i>	0.993 \pm 0.006
Rough Lemon - <i>Citrus jambhiri</i>	0.975 \pm 0.008
San Pedro Cactus - <i>Cereus bridgesii</i>	0.973 \pm 0.001
San Rita Prickly pear - <i>Opuntia santa rita</i>	0.969 \pm 0.002
Snailseed - <i>Cocculus laurifolius</i>	0.973 \pm 0.003
Sugarcane - <i>Saccharum officinarum</i>	0.995 \pm 0.004
Tobacco - <i>Nicotiana tabacum</i>	0.972 \pm 0.006
Tomato - <i>Lycopersicon esculentum</i> cv. Pearson Improved	0.982 \pm 0.004
Tongue Prickly pear - <i>Opuntia linguiformis</i>	0.965 \pm 0.001
Upland Cotton - <i>Gossypium hirsutum</i> cv. Hopicala	0.967 \pm 0.011
Water Lily - <i>Nymphaea odorata</i>	0.957 \pm 0.006
White Mulberry - <i>Morus alba</i>	0.976 \pm 0.008
Wild Privet - <i>Ligustrum vulgare</i> cv. Japanese	0.964 \pm 0.003

Based on Table 1.1 and empirical tests, Idso et al. (1969) found no apparent correlation between species and corresponding emissivity, thereby suggesting necessary measurements are required for emissivity correction. Detailed surface emissivity correction is recommended when

attempting to retrieve exact surface temperature (Maes & Steppe, 2012). This can complicate thermography because each image pixel could be comprised of multiple surfaces of varying emissivity. However, emissivity correction can be performed with image processing techniques.

1.2.3 Natural Physics in Crop Sensing

Land surface objects, vegetation, soil, and water all have diurnal (i.e., day and night cycle) temperature characteristics throughout a 24 h period. This dynamic temperature change is dependent on the object's material properties (regarding thermal inertia), season (strength of illumination), atmospheric conditions, and orientation to the sun (aspect, slope) (Kuenzer, 2014). In addition, the microclimate surrounding an object is highly dependent on the incident radiation, as shown in Figure 1.5.

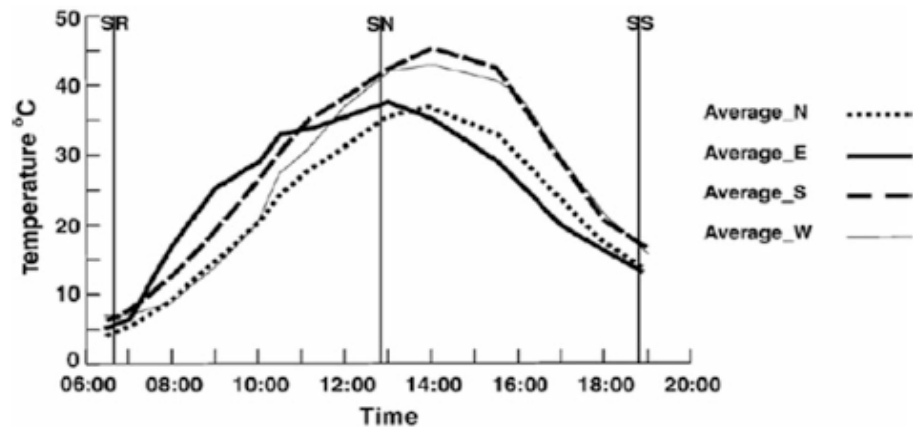


Figure 1.5. Diurnal temperature variation of desert sand depending on aspect ratio to the sun. Adapted from Kuenzer (2014).

Solar illumination time, intensity, and orientation must be accounted for in order to compare vegetative temperature for real-time decisions (Evans, et al., 2000). Therefore, vegetative characteristic data sets depicting leaf surface temperature should only be compared with comparable circumstances (i.e., day of year, acquisition time, sensor configuration, and calibration methods) (Kuenzer, 2014). In addition, site-specific attributes contribute to dynamic leaf and canopy energy balance based on leaf orientation (Kuenzer, 2014), water requirement for the crop species, and current water status. This fundamental suggests that air temperature is not an accurate predictor of leaf temperature when typical air temperature measurements are remote and cannot account for field and crop variability (Luvall & Holbo, 1991). The following sections include brief discussion of aspects of natural physics in crop sensing including thermal inertia (TI), artifacts of wind, and atmospheric corrections.

1.2.4 Thermal Inertia

Materials heat up at varying rates based on material properties primarily determined by TI. TI is the material's ability to store and conduct heat (Kuenzer, 2014; Notarnicola, et al., 2013), as expressed in Equation 1.6.

$$TI = \sqrt{c \times \rho \times k} \quad (1.6)$$

Where:

TI = thermal inertia [$\text{J m}^{-2} \text{K}^{-1} \text{s}^{-0.5}$]

c = heat capacity [$\text{J kg}^{-1} \text{K}^{-1}$]

ρ = density [kg m^{-3}]

k = thermal conductivity [$\text{W m}^{-1} \text{K}^{-1}$].

Variations in TI result in changes in maximum and minimum temperature (ΔT) during a diurnal solar cycle (Kuenzer, 2014). Low TI results in a high fluctuation temperature ΔT (e.g., rocks); whereas, a high TI resists temperature change with a low ΔT (e.g. water) (Kuenzer, 2014; Wooster, et al., 2013). Figure 1.6 illustrates differences between TI.

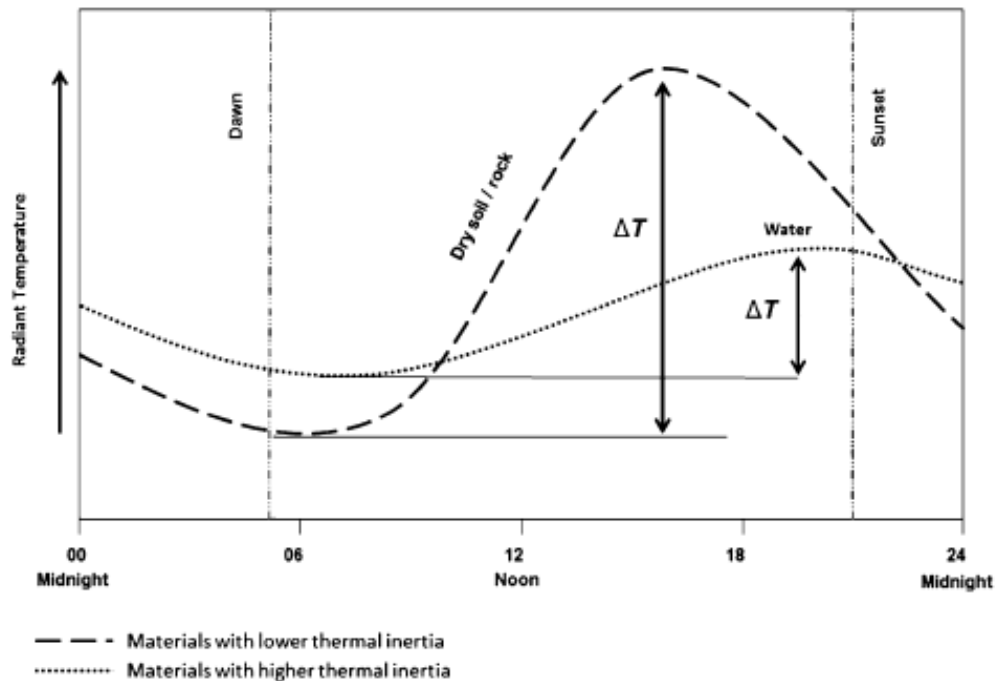


Figure 1.6. Diurnal temperatures of natural objects determined by thermal inertia. Adapted from Kuenzer (2014)

Spatial and temporal resolution provide opportunities for moisture content variability, such as soil moisture estimation, watershed management, irrigation scheduling for precision farming, environmental health monitoring, and climate analysis (Notarnicola, et al., 2013). Idso et al. (1975) used diurnal ΔT to derive soil moisture in the first 0-2 cm of a soil profile with temporal

measurements and the TI concept. Soil moisture analysis has been proven in studies of bare and vegetative cover based only on surface TI (Kuenzer, 2014).

The strongest correlation between water stress and canopy temperature occurs after solar noon, a period from 12:00 to 16:00 h, when crop canopy-to-air temperature deficit is highest, regardless of crop growth stage (Ayeneh, et al., 2002). As suggested by Ayeneh et al. (2002), measuring crop leaf temperatures at solar noon limit error in assessing crop water status. Extensive research has been conducted to create models and methods that utilize a more flexible time schedule (Alves & Pereira, 2000; Zia, et al., 2013). Models created to prove a flexible sensing time period have been suggested by Alves et al. (2000), as shown in the Figure 1.7.

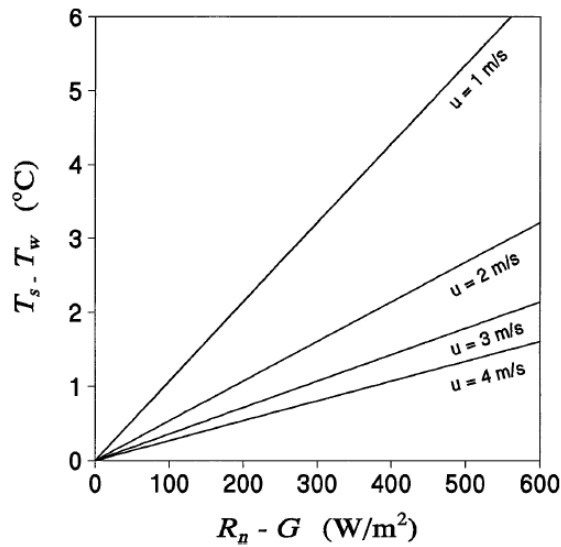


Figure 1.7. Graphical representation of baselines accounting for wind and solar intensity with fixed temperature depression ($T_s - T_w$). Adapted from Alves and Pereira (2000).

O'Shaughnessy et al. (2012) investigated a technique to increase the time window for crop stress characteristic assessment based on diurnal temperature measurements to estimate a temperature-scale algorithm, as shown in Equation 1.7:

$$T_{\text{canopy,time}} = T_{\text{dawn}} + \frac{(T_{\text{remote,time}} - T_{\text{dawn canopy}})(T_{\text{real-time reference}} - T_{\text{dawn canopy}})}{T_{\text{reference,time}} - T_{\text{dawn canopy}}} \quad (1.7)$$

The temperature scaling algorithm was implemented aboard a center pivot system in which one fixed reference canopy temperature was scaled compared to the canopy temperature measurement from the sprinkler section in a remote location within the field (O'Shaughnessy, et al., 2012). In similar research by Peters et al. (2004), linear correlation among diurnal canopy temperature scaling provided significant support for minimal canopy temperatures throughout the

day for crop stress assessment (Peters & Evett, 2004). Figure 1.8 illustrates the ability of the scaling method to measure remote crop canopy temperatures.

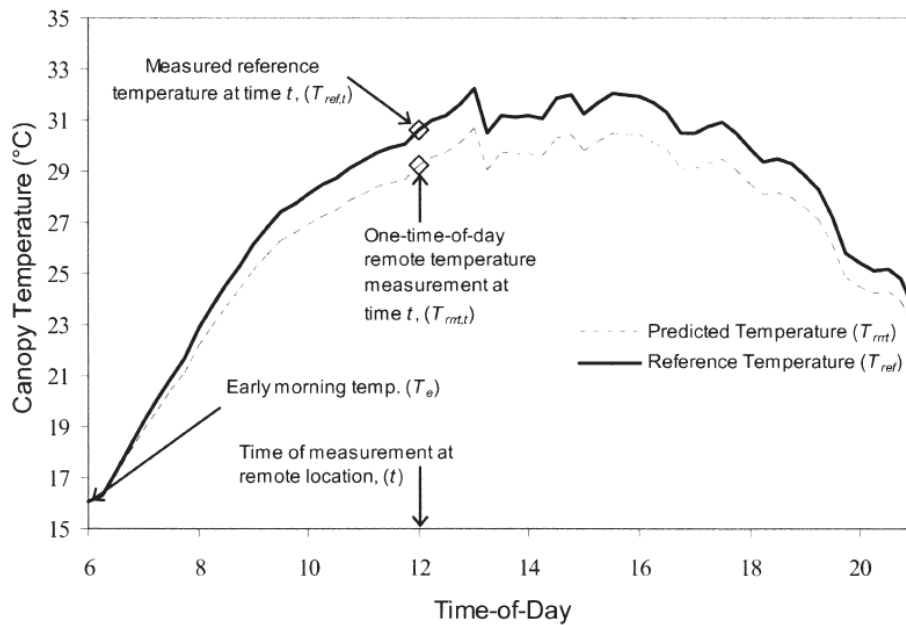


Figure 1.8. Temperature scaling algorithm’s prediction of canopy temperature at remote locations with one daily measurement. Reproduced from Peters and Evett (2004).

1.2.5 Wind Artifacts

When considering heat loss from convection, the rate in which heat is lost from or to an object depends on the surface geometry, air speed, and the temperature gradient between the air temperature and leaf surface (Monteith & Unsworth, 2013). Regardless of the sensing platform, wind create artifacts within thermal imagery of crop vegetation to varying degrees based on wind speed, direction, and flow characteristics, as illustrated in Figure 1.9. Wind influences thermal imagery with wind smear and streaks.

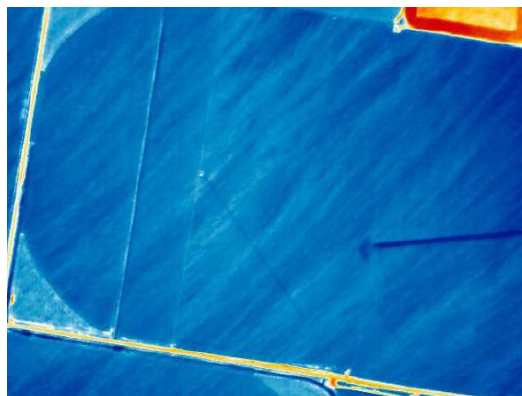


Figure 1.9. Wind artifacts within a thermal image. Reproduced from Schepers (2012).

For objects with a small surface area, such as a leaf, heating from radiation is dramatically overshadowed with convective heat transfer, thereby making temperature fluctuations more dependent on air conditions than incident radiation (Monteith & Unsworth, 2013).

1.2.6 Atmospheric Correction

In addition to surface emissivity, diurnal temperature change, and wind artifacts, environmental conditions such as water vapor and sensing distance can influence temperature measurement of thermographic systems for path radiances between the target surface and sensor detector, as shown in Table 1.2.

Table 1.2. Atmospheric conditions that influence thermographic systems. Adapted from Kuenzer (2014).

Factors Influencing Time Series	Observations
Water Vapor Disturbance	Skews actual temperature
Aerosols	Skews actual temperature
Clouds	Cannot Measure Through
Cloud Shadows	Crop within shadow will be cooler
Topography	Uneven solar heating
Emissivity	Actual measurements

Clouds artifact satellite imagery and create shadows that can impact ground and aerial-based thermal imagery. Atmospheric corrections are based on sensing elevation. To account for varying absorption characteristics of atmospheric water vapor, the use of MODTRAN, an online application, provides atmospheric corrections that improve calculations of solar and thermal scattering from clouds and aerosols (Berk, et al., 1998), as shown in Figure 1.10.

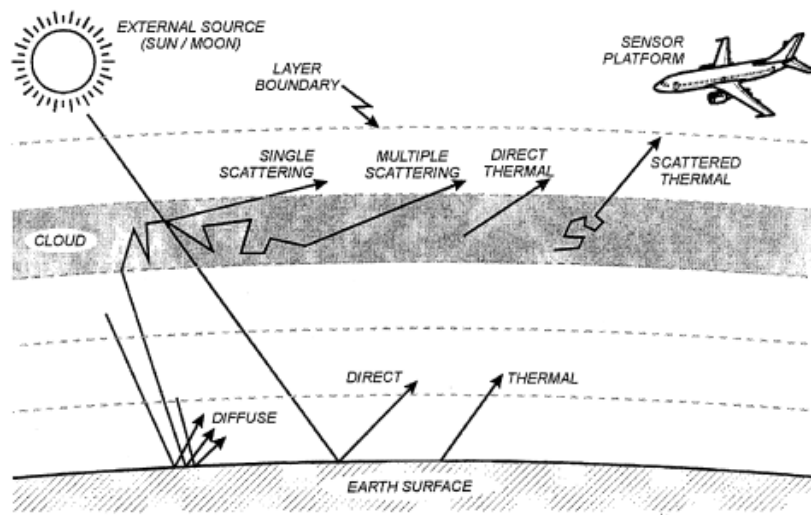


Figure 1.10. Diagram for atmospheric correction for sensing platforms. Recreated from Berk et al. (1998)

The MODTRAN atmospheric radiation technique improves accuracy of radiance measurements with influence from clouds and thick aerosols.

1.3 THERMOGRAPHY

Thermography has been an advantageous thermal sensing technique because a thermal image provides spatial temperature to measure subtle characteristics of a sensing target. The spatial resolution and image processing functionality of low-resolution thermography increase the use of crop canopy temperature characteristics in agriculture (Luquet, et al., 2003) in order to provide qualitative and quantitative crop characteristics that support management decisions (Colaizzi, et al., 2012; Evans, et al., 2000). The following section includes a brief discussion of techniques to increase thermographic sensitivity related to intrinsic properties of thermal cameras and image analysis, as well as future development needs in thermography.

1.3.1 Intrinsic Properties of Thermal Cameras

Due to the fractional cost compared to previous cooled TIR cameras, minimal size and weight, and lack of moving parts, uncooled TIR cameras are emphasized because of their potential use aboard sUAS, thereby increasing coverage area and crop stress assessments not previously possible in agricultural remote sensing. Thermal infrared (TIR) cameras have physical components and capabilities that influence temperature sensitivity, increase measurement error, and limit camera use in agricultural environments. Fundamentals of uncooled TIR cameras, including intrinsic properties, are briefly discussed in the following sections.

1.3.2 Thermal Image Sensor and Sensitivity

Uncooled TIR cameras use a thermal detector, or microbolometer, in order to generate an image with the change of electrical properties (e.g., resistance) due to temperature change within the thermal detector pixel (Kuenzer, 2014). A single thermal detector, also referred to as a pixel, measures temperature intensity that is transformed into a raw digital number (DN). For thermography, the thermal image sensor measures temperature intensity at each pixel in order to generate a digital image, as shown in Figure 1.11.

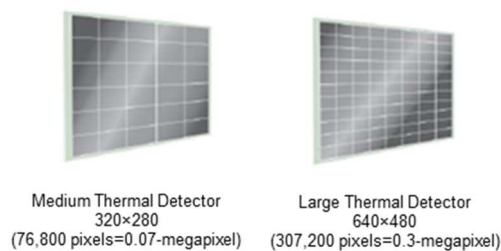


Figure 1.11. Comparison between medium and large pixel arrays for a microbolometer. Reproduced from Schepers (2012)

Because uncooled TIR cameras have a low signal-to-noise ratio, their thermal detectors are less sensitive ($\pm 0.1^{\circ}\text{C}$) than other temperature sensors (Kuenzer, 2014); however, this accuracy make microbolometers sensitive to the subtle temperature differences ($<0.5^{\circ}\text{C}$) necessary for accurate crop stress assessment (Blonquist & Bugbee, n.d.; Sepulcre-Canto, et al., 2007). For utility in agricultural sensing applications, TIR cameras are sensitive to the 7 to 14 μm longwave infrared (LWIR) which is the temperature range from -66°C to 150°C . Microbolometer pixel arrays are sensitive to LWIR radiation that strike the detector material, changing its electrical resistance from a temperature change, and transforming a temperature intensity into a raw digital value (DV) (Kuenzer, 2014).

1.3.3 Microbolometer Temperature Drift and Warm-Up Time

Since uncooled TIR cameras do not have heavy cooling jackets, uncooled TIR cameras regulate their microbolometer thermal detectors with automatic re-calibration to maintain sensor accuracy while limiting measurement drift caused by temperature fluctuations of the thermal detector from internal circuit and external environmental temperatures (DRS Technologies, Network and Imaging Systems Group, n.d.). As a result, a shutter is used to recalibrate the thermal detector at a user defined time interval or based on an internal temperature change of the thermal detector (DRS Technologies, Network and Imaging Systems Group, n.d.). When the shutter closes, it blocks thermal energy to create a uniform thermal reference for the thermal detector. A recalibration algorithm is performed to ensure a uniform pixel intensity is measured across the whole sensor with the uniform shutter temperature. Such techniques are required for uncooled thermal cameras to maintain accurate temperature measurement due to their inability to regulate their internal temperatures (DRS Technologies, Network and Imaging Systems Group, n.d.).

Limited literature test uncooled TIR camera measurement accuracies, provide standard operating protocol, and give general guidelines for practical sensing scenarios. Internal circuitry and ambient temperature conditions cause TIR cameras to have necessary warm-up periods in order to reach a steady-state operating temperature, as shown in Figure 1.12.

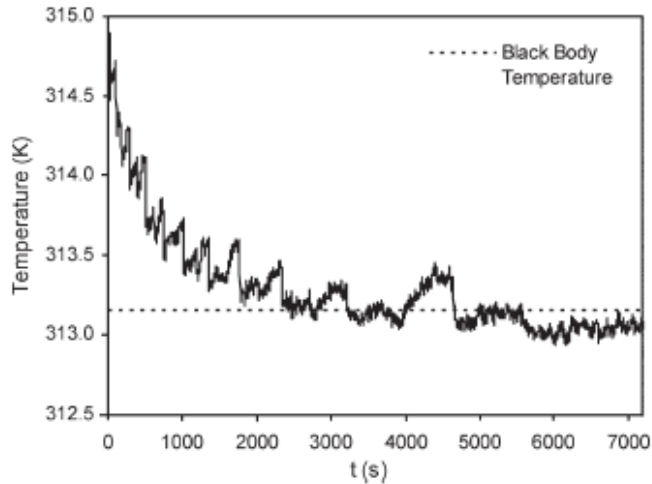


Figure 1.12. Radiometric temperature changes measured by a TIR camera during warm-up period. Adapted from Berni et al. (2009).

The TIR camera studied by Berni et al. (2009) had a recommended warm-up period of 2 h before the measured temperature converged to a steady-state black body temperature, as illustrated in Figure 1.12. Therefore, adhering to the warm-up time would reduce inaccuracy as the TIR camera reaching operating temperature.

1.3.4 Lens Distortion

Maintained lens focus over a wide range of temperatures is essential for sensing platform utility and image quality. An athermalized lens maintains performance using optical passivity through ranging scene temperatures. Compared to visible imagery, TIR camera lenses are subject to the same physical calibration parameters for distance, focal point, and radial image distortion (Kuenzer, 2014). Because thermal radiation does not transfer through glass, TIR camera lenses are made from germanium, a material that is transparent to thermal radiation (Kuenzer, 2014). Germanium lenses in TIR cameras have intrinsic properties identical to glass lenses in regards to geometric precision. These lenses are optimized for radiometric resolution, thereby are subject to varied degrees of lens distortion (Berni, et al., 2009) from short focal lengths and radial and tangential distortion (Lagueta, et al., 2013). When a TIR camera captures an image, the image does not fully represent real spatial points but a distorted pixel location that is a function of the position within the lens' field of view (FOV) (x_1, y_1) , as defined by Equations 1.8 and 1.9 (The Mathworks, Inc., 2015):

$$x_2 = x_1(1 + k_1r^2 + k_2r^4) + 2p_1x_1y_1 + p_2(r^2 + 2x_1^2) \quad (1.8)$$

$$y_2 = y_1(1 + k_1r^2 + k_2r^4) + 2p_2x_1y_1 + p_1(r^2 + 2y_1^2) \quad (1.9)$$

Where:

x_1, y_1 = distorted pixel locations

x_2, y_2 = undistorted pixel locations

k_1, k_2 = radial distortion coefficients of the lens

p_1, p_2 = tangential distortion coefficients of the lens

$$r = \sqrt{x_1^2 + y_1^2}$$

Resulting lens distortion coefficients act as a basis for an image processing algorithm. Imaging processing automate batch processing in order to undistort images for spatial accuracy for precise location of actual points using Equations 1.8 and 1.9 for respective lens. Figure 1.13 shows radial distortion of a germanium camera lens.

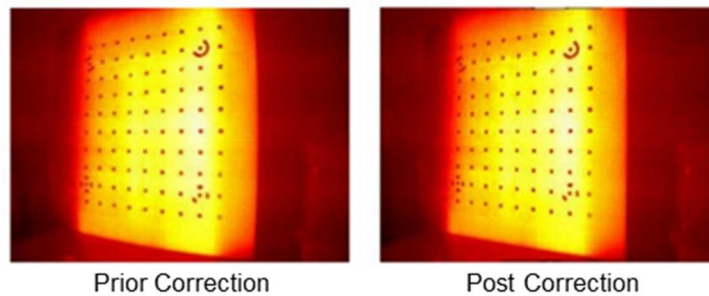


Figure 1.13. Lens distortion prior to correction (left) and with correction (right). Adapted from Lagueta et al. (2013).

A comparison of handheld TIR cameras revealed a high level of geometric distortion for all TIR cameras, thereby requiring correction for further image processing (Taghvaeian, et al., 2013).

1.3.5 Image Processing

Thermography has demonstrated advantages over thermometrics and other crop sensors because it provides spatial temperatures, thereby allowing image processing not previously possible. Unlike thermometrics, thermography outputs images with the combination of spatial and temperature data. Techniques to capture, analyze, and interpret images also apply to thermal imagery, giving thermography an advantage over conventional thermal sensing techniques and crop stress assessment techniques. Manual image capture and processing can be labor intensive and are subject to user-based processing thresholds. Ballester et al. (2013) asserted that automatic imaging and analysis of individual trees has saved processing time with more uniformity and confidence in results due to automatic imaging (Ballester, et al., 2013). Image processing has been

widely used in remote sensing but has been rarely used in small research studies (Leinonen & Jones, 2004).

Although slow processing speed, large memory requirements, and a high cost of hardware once limited imaging, it is being restudied for utility in precision agriculture (Wang, N., personal communication, November 1, 2013). Industrial application of thermography for automation and adoption have decreased hardware costs and increased sensing capabilities of image sensors. However, automatic image capture and analysis are needed to account for error incurred with manual measurements such as setup and capture inconsistencies and latency between images, leading to small microclimate changes. Therefore, automatic thermography captures temperature information with high spatial (ground distant measurement) and temporal (repeat frequency) coverage crucial for monitoring dynamics of crop phenomena (Kuenzer, 2014; Luquet, et al., 2003). A thermal image allows plant vegetation to be identified and isolated for analysis based on the following types of segmentation:

Temperature – Individual crop vegetation pixels within the FOV can be extracted based primarily on temperature emitted onto the TIR image sensor. Crop leaf temperature typically vary from that of soil within the FOV. In fact, the soil itself can greatly influence temperature measurement at partial canopy coverage (Luvall & Holbo, 1991). In addition, TIR imaging is independent of an illumination source, such as the sun, so TIR data can be measured during the nighttime when VIS and NIR imagery is not possible (Kuenzer, 2014).

Shape – Differences in leaf and stem shape can be used to identify plant species (Zhang, et al., 2006). Zhang et al. (2006) explained that this type of segmentation is based on physical leaf traits such as “elongation, size, curvature, center moment of inertia, and principal-axis moment of inertia.”

Location – Location segmentation uses spatial knowledge of row spacing and population rates to identify where crop vegetation should be located. Application of this principle can segment soil from crop by identifying soil material between rows.

Numerous physical characteristics of crop sensing limit thermometry adoption due to crop surface parameters that cannot be easily measured without extensive hardware, setup, and extensive thermal indices. According to Luquet et al. (2003) and Grant et al. (2007), thermography can identify the following crop characteristics:

- 1) Partial crop cover from exposed bare soil
- 2) Plant variability due to growth stage and senescence
- 3) Subtle difference across plant leaf

New thermal imaging technologies advance integration into data loggers and microcomputer equipment, increasing ease of data collection and timely response of results (Evans, et al., 2000; Leinonen & Jones, 2004). Image processing is briefly discussed in this section in order to increase understanding of analysis and considerations necessary to ensure that thermal imagery data is accurate for well-informed decision making. Correction methods discussed in the following sections pertain to radiometric conversion, atmospheric corrections, and ground truthing.

1.3.5.1 Radiometric Conversion

Radiometric conversion functions are linear transfer functions applied to images in order to convert digital values into temperature values. TIR camera calibration is necessary when saturation occurs with high and low temperatures beyond the temperature threshold of applied settings (Kuenzer, 2014). Accurate measurements typically modify transfer function coefficients for thermal camera settings and calibrations (Kuenzer, 2014). With radiometric conversion, each digital image pixel converts to a temperature value, as defined in Equation 1.10:

$$T_{(i,j)} = T_{min} + \frac{I(i,j)}{2^N - 1} T_{span} \quad (1.10)$$

where:

- $T_{(i,j)}$ = Pixel temperature (°C) at row i and column j ,
- T_{min} = Lowest temperature within the image (°C),
- $I_{(i,j)}$ = Pixel intensity at row I and column j ,
- N = Number of bits for pixel intensity (e.g., $N=8$ for 8-bit images), and
- T_{span} = Span of temperature captured in the image.

1.3.5.2 Atmospheric Correction

Physical atmospheric conditions apply accurate radiometric correction (Kuenzer, 2014). One method typically used for atmospheric corrections is derived from the MORTRAN radiative transfer model using inputs of air temperature, humidity, and barometric pressure (Berni, et al., 2009). Figure 1.14 shows simulated atmospheric influence.

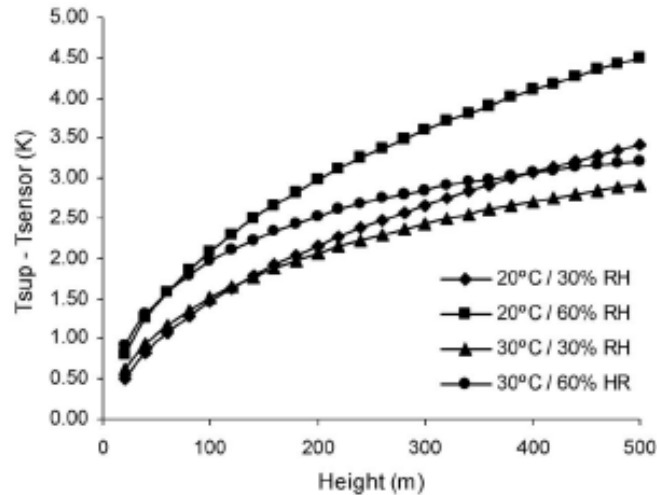


Figure 1.14. Simulated atmospheric conditions and flight altitude. Reproduced from Berni et al. (2009).

Simulations shown in Figure 1.14 illustrate temperature differences between actual surface temperature measurements and measured surface temperature for atmospheric corrections with sensing elevation. Environmental correction techniques allow ground referenced land surface temperature at measurement accuracies less than 1 K (Berni, et al., 2009).

1.3.5.3 Image Management

Image management is an important fundamental in order to process the data influx from imagery, thereby increasing image throughput for faster interpretation and quality. Image management aboard a sUAS consists of either on-board storage or wireless data-link to a ground station for storage. Zen et al. (2008) found that a continuous high-speed storage device on an aircraft can store images at 150 MB s⁻¹ on a 280 GB disk for high resolution aerial photography surveying. On the other hand, Jones et al. (1999) used an on-board microprocessor to send compressed images and commands to the sUAS via digital data-link at a speed of 10.71 MB s⁻¹ to the ground station at altitudes up to 7,500 m. Imagery data size and permissible sUAS payload determines the necessary image management solution while considering the weight of the storage device compared to the digital data-link hardware weight. Digital data-link communication is subject to signal noise or line-of-sight obstruction interference; however, increased sUAS platform flight duration and range advances wireless data transfer technology for extended range and signal quality. In addition, digital data-link allows on-the-go sensor and/or sUAS control changes based on the data-link feedback.

1.3.5.4 Image Fusion

Image manipulation using image fusion combines two images from the same or different sources to create one image that typically enhances automatic detection (Bulanon, et al., 2009), thereby supporting utility aboard satellite, aerial, and ground-based remote sensing. Pixel-level (two or more image pixels fused into one), feature-level (combination of specific shape, extent, and neighborhood pixels), and decision-level (separately analyzed images for extraction followed by a decision-based, weighted combination) techniques combine two or more images (Pohl & Van Genderen, 1998). Image information, such as topography, global positioning system (GPS) location, and time, are also combined into the resulting image. In application, pixel-level image fusion is more commonly used (Bulanon, et al., 2009). Image fusion has been used in medicine, military surveillance, and human identification and only recently investigated for agricultural use (Leinonen & Jones, 2004).

Because VIS cameras typically have higher image sensor resolutions than thermal cameras, a critical aspect of image fusion is overlapping FOVs. A FOV within images must initially be defined before images can be fused in order to limit pixel combination errors. Physical control points typically are placed in the FOV of each camera (Leinonen & Jones, 2004). However, the assumption that a VIS camera and TIR camera image's FOV directly overlap and align for image processing commonly leads to error (Wang, et al., 2010). One effective, consistent approach compares the mean canopy temperature and the thermal image exclusively and the mean canopy temperature of the fused image (Wang, et al., 2010).

One source of error using image fusion is the subjectively manual user inputs. To address these concerns, features within an image can be isolated or discovered using practices such as standard deviation, wavelet transform, entropy change, and pixel variance changes. Nevertheless, robust image software requires a level of logical user input to set thresholds, input functions, and weight importance in order to reduce misidentified objects or features (Bulanon, et al., 2009), thereby requiring complex combinations of crop and soil elements in the sensors' FOV for crop sensing (Wanjura, et al., 1992). From early growth stages until full canopy coverage, crop health characteristics require high spatial resolution to mask soil temperature influence in the thermal image (Hackl, et al., 2012; Rodriguez, et al., 2005).

An advantage of image fusion is related to the synergy of the two image sources. Thermal imaging is able to detect LWIR radiant energy emitted from an object regardless of illumination,

whereas VIS imaging is able to detect differences in reflected visible radiant light (Pohl & Van Genderen, 1998) as shown in Figure 1.15.

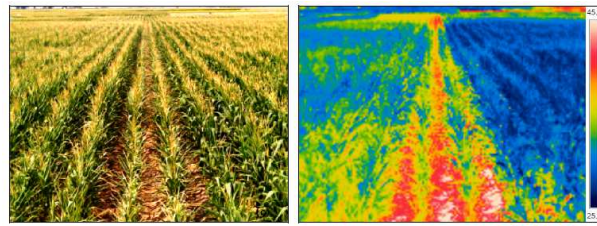


Figure 1.15. Visible color and thermal image comparison. Adapted from Taghvaeian et al. (2013).

Image fusion demonstrates that together these sensor platforms can create automatic imaging tools to isolate objects of interest (i.e., fruit, leaves, stems) and exclude unwanted features (i.e., soil, shaded leaves, background features) (Bulanon, et al., 2009). In addition, together the two imaging sources isolate and detect objects at an increased confidence rate (Bulanon, et al., 2009; Leinonen & Jones, 2004). Image fusion has been successfully used to compensate for soil temperature influence (Leinonen & Jones, 2004; Tilling, et al., 2007; Wang, et al., 2010). Application of image fusion allows identification of leaves in the VIS image to discriminate pixels in order to extract TIR image pixels by overlaying images with corresponding spatial location within an image (Luquet, et al., 2003).

Wang et al. (2010) used VIS images to identify the amount of leaf area distributed in the AOI. Based on this leaf area, canopy temperature was associated with leaf area to calculate statistical analysis. Figure 1.16 shows temperature extraction with leaf color.

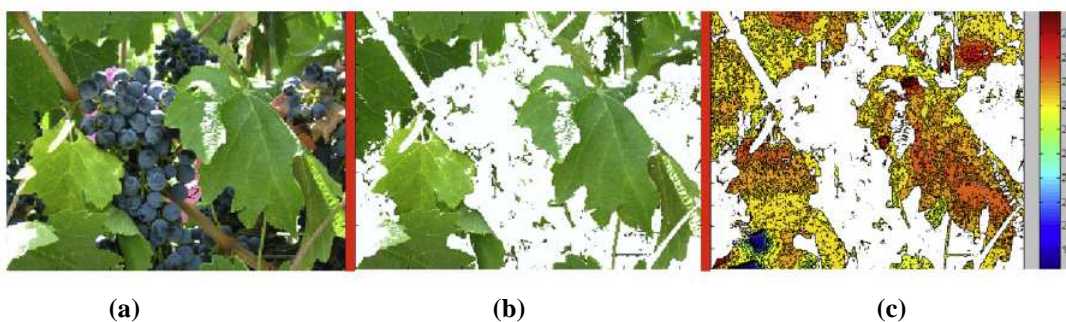


Figure 1.16. Typical plant canopy temperature extraction (b) demonstrating color from the (a) visible color image and the resulting temperature association (c). Reproduced from Wang et al. (2010).

Wang et al. (2010) used image processing to extract leaf material by color; yet, color alone can cause non-vegetation to be classified as leaves, thereby creating error with associated temperature. Typical image fusion discriminates sunlit and shaded bare soil and leaves while

allowing leaf canopy coverage percentage to be quantified for temperature analysis (Luquet, et al., 2003; Zia, et al., 2013).

A similar approach is the combination of normalized difference vegetative index (NDVI) values with TIR imagery. However, TIR and NDVI measurements are both subject to measurement error when used in partial canopy coverage (Moran, et al., 1994). Temperature relationships based on the partial canopy coverage have been investigated to reduce the influence from background temperatures. Figure 1.17 shows differences in the measured temperature of the actual canopy temperature and the FOV average temperature based on the partial canopy coverage.

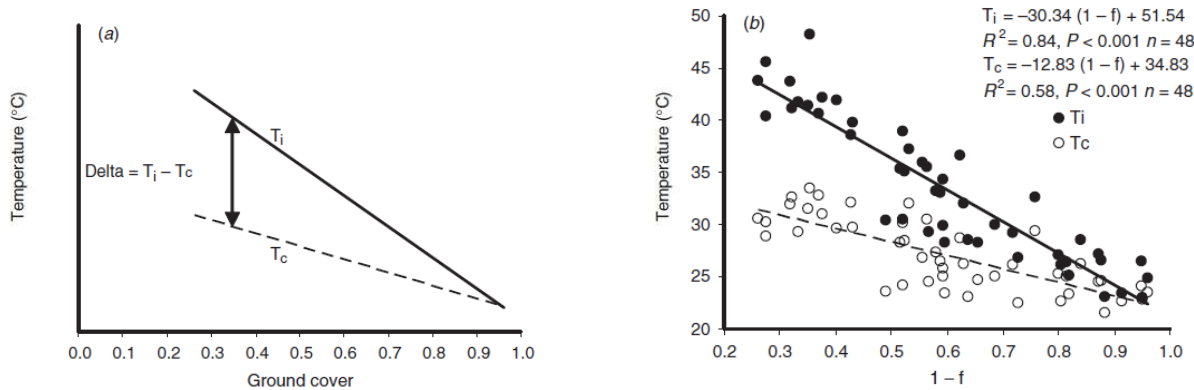


Figure 1.17. Difference between the characterized vegetation temperature of the actual crop canopy temperature (T_c) and the averaged FOV temperature (T_i) versus crop canopy coverage (a), and measured vegetation temperature of the actual crop canopy temperature (T_c) and the averaged FOV temperature (T_i) versus crop canopy coverage (b). Reproduced from Rodriguez et al. (2005).

In Figure 1.17, the actual temperature of the leaf is shown (T_c) compared to the average temperature of the camera FOV (T_i) regression curve versus the partial canopy coverage. This illustration demonstrates the inaccuracy of temperature measurement when vegetation temperatures cannot be extracted from the background temperatures. By using Equation 1.11 derived by Rodriguez et al. (2005), the difference ($\Delta^\circ\text{C}$) in terms of inaccuracy can be solved.

$$T_c = T_i - \Delta(^\circ\text{C}) \quad (1.11)$$

Partial canopy coverage measurement is critical in sensing applications to limit the temperature influence from a warm soil background and shaded lower leaves (Ayeneh, et al., 2002; Luquet, et al., 2003; Maes & Steppe, 2012). Because biological crop material is unique, physical differences in plant architecture, such as color, leaf size, relative orientation to the sun, and field variability, cause temperature differences between any two plants (Ayeneh, et al., 2002; Luquet, et al., 2003), as shown in Figure 1.18.

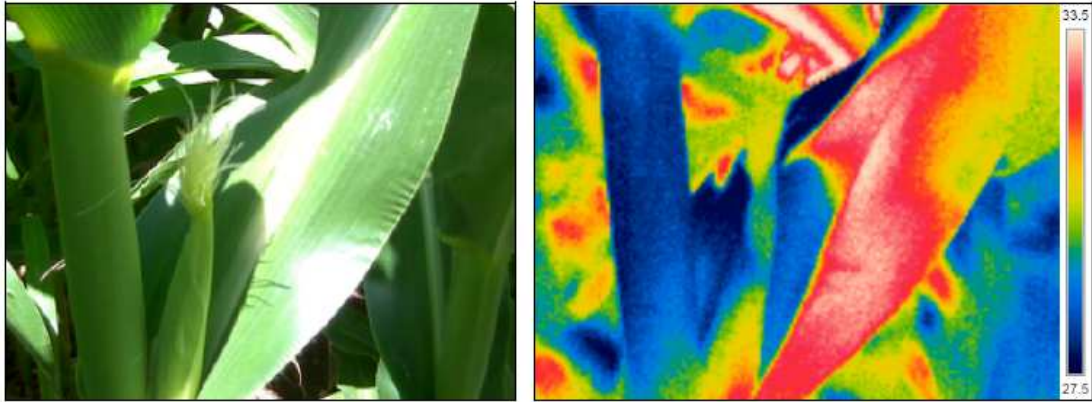


Figure 1.18. Macro image of visible color and thermal image comparing leaf temperatures under sunlit and shaded regions. Adapted from Taghvaeian et al. 2013.

As demonstrated in Figure 1.18, whole canopy temperature averages can differ from single leaf temperatures (Grant, et al., 2007). At high spatial resolutions and plant-by-plant analysis, inherent variability between each plant complicates crop health assessments. Subtle differences exist from plant to plant and at locations within each leaf (Cohen, et al., 2005; Grant, et al., 2007). When a high spatial resolution image is maintained, image processing can segment and exclude pixel intensities corresponding to a certain temperature range or object of interest. Figure 1.19 illustrates soil at a warmer temperature than crop vegetation (peach orchard).

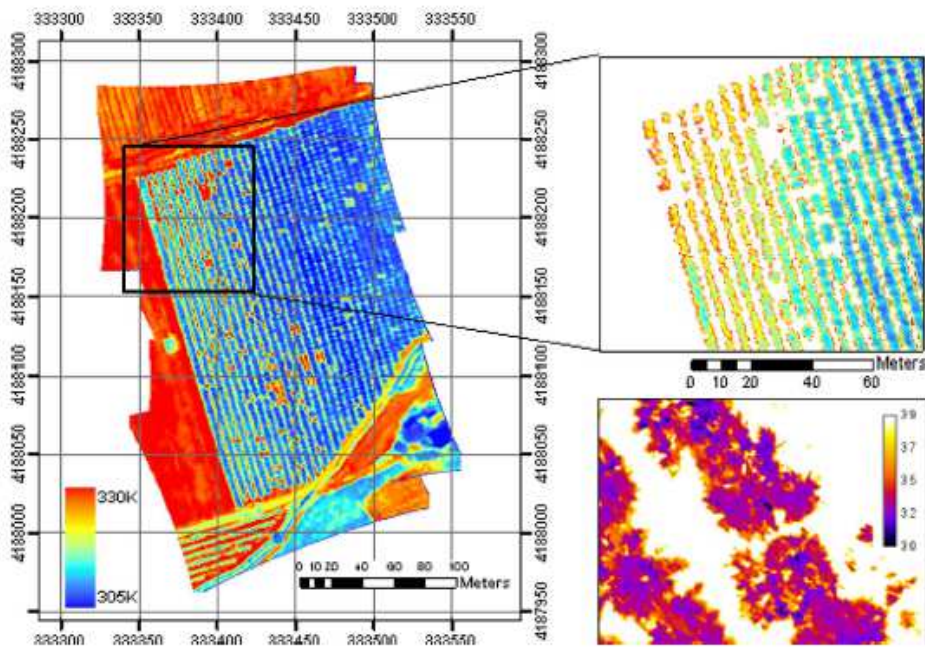


Figure 1.19. Thermal orthomosaic image (left) from a sUAS over a peach orchard where vegetation is extracted from soil (lower right). Reproduced from Berni et al. (2009).

As shown in Figure 1.19, image segmentation isolates the crop foliage temperature (low pixel intensity) of the peach orchard.

With the aforementioned capabilities of image combination, image fusion requires a TIR, visible camera, accurate algorithms, and a computer with imaging software and processors to efficiently perform the task of automating image capture, analysis, and interpretation for tactical irrigation.

1.3.5.5 Ground Truthing

Ground truthing ensures accuracy of measured temperature from the sensing platform. Temperature ground truthing involves measuring radiant and kinetic temperatures of an object in order to determine emissivity and environmental correction factors. Typical ground truthing consists of handheld thermometers that use noncontact infrared readings and contact readings with thermistors (Ayeneh, et al., 2002; Berni, et al., 2009). Comparisons between sensing platforms are subject to measurement error from accuracy calibration, calibration errors, and time between measurements (Berni, et al., 2009). Automated thermography supports the inclusion of wet and dry temperature references for real-time thermal indices (discussed in Section 5.4.1). Reference temperatures can be automatically detected for analysis with treated leaves or artificial reference surfaces viewable within the AOI.

Validation during a time series relies on permanently installed noncontact or contact (ground or air) measurement devices with data loggers capable of simultaneous measurements of wind speed and direction, humidity (Kuenzer, 2014), air temperature, and solar radiance. Optimal surfaces for ground truthing are high thermal inertia substances that resist temporal temperature changes. Items used for ground truthing should be viewable and recognizable from the sensing platform. Thermography ground truthing helps to reduce the influence from partial canopy coverage as soil dominates temperature measurement before a crop achieves full canopy cover (Rodriguez, et al., 2005). As provided from thermography, unprecedented measurements of bare soil and shaded and sunlit conditions aid in analyzing image view and orientation (Colaizzi, et al., 2012 ; El-Shikha, et al., 2007 ; Luquet, et al., 2003).

1.3.5.6 Whole-field Coverage and Image Mapping

Providing an accurate whole-field crop canopy temperature map has been a challenge in the past for each thermal sensing platforms because of the tradeoff between coverage area,

measurable crop characteristics, and sensing frequency. TIR cameras are inherently limited by their spatial resolution, therefore a compromise between resolution and efficiency exist dictating sensing distance and platform. Sensing distance and on-board sensor FOV must be considered in order to overlap neighboring pictures in order to limit environmental correction error from wide angle and bidirectional effects from lens distortion and incident radiant energy. Dynamic camera platforms capture a volume of images across the field covering more vegetation area in order to create high definition temperature maps using only the central image portion, nadir, in order to improve overall image quality (Berni, et al., 2009; Vasterling & Meyer, 2013).

For whole-field coverage, individual images are stitched together to generate an orthomosaic image of the entire coverage area. Manual or automatic image processing software stitches images together while automatically georectifying images from common points within individual pictures, ground control points or by utilizing camera or platform GPS coordinates (Berni, et al., 2009). In images taken in a forward and lateral direction, common graphical features can be traced over several images in which neighboring images can be referenced (Vasterling & Meyer, 2013), therefore, an orthomosaic image is generated to form a whole-field composite image collected at a similar sensing distance.

1.3.6 Development Opportunities

Thermography has been emphasized in crop sensing applications because of development opportunities over thermometry due to visible patterns revealed with image processing techniques (Grant, et al., 2007; Rodriguez, et al., 2005). Yet, thermography has only become widespread and investigated over the last decade (Hackl, et al., 2012) as a result of being declassified from the United States Military for civilian use (Maes & Steppe, 2012; Schepers, 2012). As a result, technical and physical barriers still limit thermal remote sensing, including image sensor resolution, image data capture and transmission, practical agricultural operating experience, thermal sensor cost, image processing software designed specifically for thermography, and complex image composition dominated by soil, leaf differences, and environmental temperature influence (Colaizzi, et al., 2012; Evett, et al., 2014; Rodriguez, et al., 2005). In addition, thermography should be a complementary crop characterization technology due to complex leaf dynamics “strongly influenced by morphological, physiological, and biochemical traits as well as environmental factors and their interactions” (Liu, et al., 2011). Agricultural studies that use thermographic systems have been limited because of the expense, unfamiliar use and operating

guidelines, system integration and complexity, and lack of proven durability in agricultural conditions, thereby restricting their use to laboratories, greenhouses, and intermittent use in prolonged field studies. Listed below are opportunities for thermography development:

Influence from Soil - Directional influence from soil significantly impacts current thermal indices. Medium resolution thermal images cause pixels within the image to inevitably capture mixed soil-foliage pixels (Hackl, et al., 2012). Opportunity exists for advanced indices that are less impacted by background temperature influence from partially covering crops.

Advancements in Weight, Cost Reduction, Durability, and System Hardware -

Thermography research has been limited because of size, weight, and cost of TIR cameras. However, uncooled thermal imaging shows utility in agriculture because of their fractional cost to that of cooled thermal imagers, integration into automatic imaging systems, small envelope size and weight, and ability to collect data in sunny, cloudy, and slightly windy conditions. As a result, uncooled thermal cameras have increased thermography's adoptability for large ground coverage (Kuenzer, 2014) and monitoring time studies (Sobrino & Julien, 2013).

Thermal Camera Control Software -

A limitation of TIR cameras is the accompanying software required to perform image analysis. While image combination with VIS images is conducted, automatic image conversion-to-radiometric images with temperature-based pixel intensities would improve post-processing ease (Taghvaeian, et al., 2013). Increased confidence in thermography techniques and hardware will ensure accurate crop health during all measurements to effectively assess plant growth parameters.

TIR cameras' cost, size, and weight and their ability to quickly assess crop stress characteristics potentially offset limitations. Therefore, proliferation of thermography and its capabilities provides opportunity for technological advancements to assist agricultural producers (Taghvaeian, et al., 2013). Although thermography has been implemented in laboratory research, practical research with thermal imaging in agricultural fields has been limited (Grant, et al., 2007). However, TIR cameras include features to meet the monitoring needs of non-agricultural uses, thereby providing incentive for TIR camera manufacturers to develop modified cameras intended for operation within agricultural fields and conditions (Taghvaeian, et al., 2013).

1.4 THERMAL SENSING PLATFORMS

Thermal imaging sensors can be ground, aerial, or satellite-based (Kuenzer, 2014). Ground-based observations are statically or dynamically performed with handheld or rigidly mounted TIR cameras in order to detect, study, and manage high definition crop phenomena; airborne and satellite thermography assess whole-field temperature fluctuations. This range of capabilities relates crop temperature and water status at various scales in order to measure water supply (Jackson, et al., 1981; Moran, et al., 1994). As a result, large crop coverage areas and throughput need seamless monitoring from automatic or semi-automatic sensing platforms (Ballester, et al., 2013; Evett, et al., 2014; Romano, et al., 2011). In addition, the amount of measurable data has a practical threshold level dependent on physical processing means of the equipment used (i.e., data storage space, intrinsic sensor capability, sampling frequency, sensor sensitivity, data processing speed, sensing platform limitations, etc.). TIRIS measure a large volume of data within each image (e.g., 1 megapixel image = 1,000,000 samples), but imaging systems typically have a slow sampling frequency (e.g., <30 Hertz). On the other hand, thermometric systems capture less data in one sample at a very high sampling rate (e.g., >100 Hertz). However, equipment limitations can only capture an influx threshold of data. In other words, a distinct trade-off between the level of measurable crop characteristics and desired coverage area exist when selecting a sensing platform for the amount of data desired from the producer. As a result, increased use of thermal sensing in precision agriculture has been dependent on increased spatial and temporal resolution in order to increase effectiveness in aiding actionable decisions for precisely monitoring crop health (Sobrino & Julien, 2013) for the right agricultural input at the right time (Taghvaeian, et al., 2013).

With ground-based thermal imagery, crop stress measurements are achieved on a plant-by-plant basis with dynamic or stationary platforms. Until recently, TIR cameras have been used in preventative maintenance and when operating conditions are more regulated, unlike agricultural studies. In typical agricultural studies, ground-based systems assess crop stress variability for variable rate irrigation (Colaizzi, et al., 2012; El-Shikha, et al., 2007; Erdem, et al., 2010), water stress (Cohen, et al., 2005; Fitzgerald, et al., 2007; Grant, et al., 2007; Moller, et al., 2007; O'Shaughnessy, et al., 2011; Wang, et al., 2010), biomass estimation Hackl, et al., 2012; Liu, et al., 2011), indirect stomatal conductance (Grant, et al., 2006; Hashimoto, et al., 1984; Zia, et al., 2013), phenotype screening for water stress and/or heat stress (Merlot, et al., 2002; Prashar, et al.,

2013; Romano, et al., 2011; Zia, et al., 2013), automatic leaf geometry and extraction (Luquet, et al., 2003), nutrient influence on leaf temperature (Fitzgerald, et al., 2007), and disease detection (Chaerle, et al., 1999; Hashimoto, et al., 1984). Most thermographic applications have been used manually to complement thermometric systems; but, manual measurements increase sensing time, inconsistent setup errors, and latency between images, thereby leading to small leaf microclimate changes.

Satellite-based platforms, the first application of remote sensing, carry multiple imaging sensors capable of multispectral or hyperspectral imaging of objects in the VIS, NIR, and TIR electromagnetic spectrum (Luvall & Holbo, 1991; Zhang & Kovacs, 2012). Satellite remote sensing uses high spectral cameras that capture multiple bandwidths measuring coarse thermal imagery to monitor crop health, soil characteristics (Goel, et al., 2000; Zhang & Kovacs, 2012), and agricultural market forecasting (Luvall & Holbo, 1991). However, accounting for low resolution of thermal imaging systems poses challenges. Current satellite imagery is limited to moderate resolution imaging spectroradiometer (MODIS) or advanced very high resolution radiometer (AVHRR) with spatial resolutions of 1 km (Colaizzi, et al., 2012), whereas the Landsat Thematic Mapper (TM) and advanced space borne thermal emission and reflection radiometer (ASTER) thermal scanners provide 120 m and 90 m, respectively (Berni, et al., 2009).

Radio detection and ranging (RADAR), multi-spectral imager (MSI), MODIS, AVHRR, and Landsat TM satellite platforms are limited in practical use due to low sensing frequency incapable of producer demand and resolution (Brown, et al., 1994; Colaizzi, et al., 2012). As previously discussed, ground truthing and environmental correction for satellites imagery reduces the influence from obstructions such as cloud cover and atmospheric conditions (Notarnicola, et al., 2013), which require extensive attention in order to interpret crop characteristics. Although satellite-based remote sensing cover a broad ground area, it is expensive, has high operational complexity, and operates at unfavorably low spatial and temporal resolutions for precision agriculture applications (Berni, et al., 2009; Zhang, et al., 2006).

Current satellite-based and ground-based products have limited thermography in commercial agriculture because of producer demand for a combination of measurable crop characteristics and coverage area. In order to meet this demand, TIRIS are flown aboard piloted aircrafts and sUAS. Recent advancements in uncooled TIR camera sensor technology have emphasized remote sensing and expanded its role in tactical farm management (Herwitz, et al.,

2004) because thermography provide high spatial resolution (< 2 m) (Berni, et al., 2009) and has flexible revisit times for whole-field temperature mapping (Berni, et al., 2009; Cohen, et al., 2005; Zhang & Kovacs, 2012). In addition, aerial imagery resolves several ground-based and satellite-based platform limitations because it exceeds the coverage area of ground-based platforms and low resolution of satellite-based platforms (Kuenzer, 2014), thereby providing whole-field crop stress assessment with spatial resolutions up to 2 m (Berni, et al., 2009; Sepulcre-Canto, et al., 2007). In conducted studies, thermography aboard piloted aircrafts has been used to assess crop water stress (Scherrer, et al., 2011; Taghvaeian, et al., 2013; Tilling, et al., 2007; Wang, et al., 2010), phenotype screening (Zhao, et al., 2005), soil compaction monitoring, and irrigation maintenance (Schepers, 2012). Even aboard piloted airplanes, the primary limitation is the spatial resolution of TIR cameras. In addition, the aircraft expense, fuel limitations, pilot fatigue, infrequent revisit times, and unfamiliar complexity of flying and hiring manned aerial imagery limit extensive commercial use (Berni, et al., 2009; Goel, et al., 2000; Herwitz, et al., 2004). In response, advancements in sUAS has increased their use in aerial imagery (Herwitz, et al., 2004). The sUAS industry is evolving rapidly to expand as a complementary platform to satellites and manned aerial imagery for tactical farm management (Zia, et al., 2013). Producers have supported adoption of this type of aerial imagery because sUAS platforms provide low-altitude imagery for high-definition images, on-demand response times, and low investment costs (Goel, et al., 2000).

SUAS are capable of on-demand sensing and have analysis response times more suitable for commercial agricultural applications with results comparable, if not better, than applications using manned airborne missions (Berni, et al., 2009). SUASs can fly at low airspeeds (30 km h⁻¹) under manual control or autopilot flight campaigns with predetermined flight routes for operation ease (Laliberte, et al., 2011; Rango, et al., 2009) in order to sense area not previously accessible based on distance, time, or terrain (Luvall & Holbo, 1991). These sensing platforms also fly at altitudes that provide spatial resolution necessary for characterizing pertinent features in agronomic decision management (Figure 1.20)

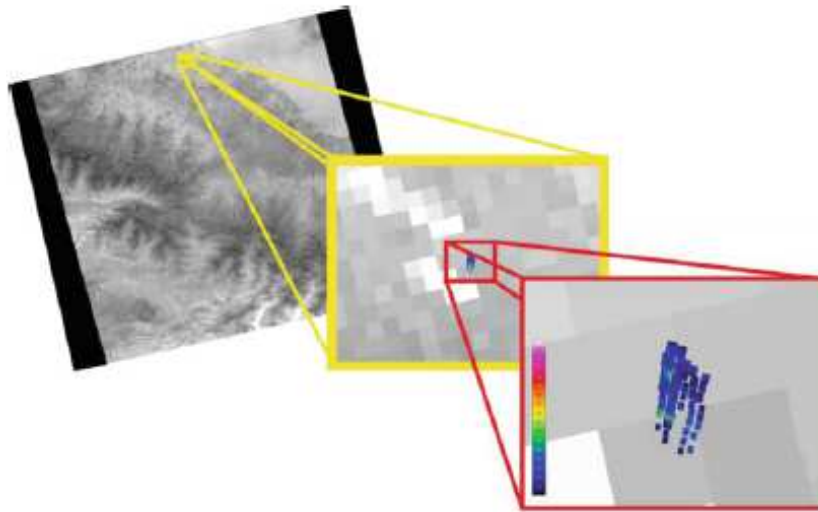


Figure 1.20. Thermal satellite imagery with overlay of sUAS imagery demonstrating the spatial resolution of satellite (90 m) to sUAS (<2m) aerial imagery. Adapted from Kuenzer (2014).

Because of technological advancements focused on unprecedented performance and endurance (Hecker, et al., 2013), sUAS platforms have conducted long-duration flight campaigns that provide valuable contribution to tactical agriculture management. Herwitz et al. (2004) demonstrated advanced sUAS technology with NASA’s solar-powered Pathfinder-Plus by proving prolonged flight times (12 h) loitering over coffee production in Hawaii. The slow-flying aircraft was designed to be flown under pilot and air traffic control supervision while up-linking mission commands and down-linking on-demand imagery (Herwitz, et al., 2004).

Currently, commercial autopilot control, cost-effective telemetry, and semi-automated image georectification systems promote the feasible use of sUAS in precision agriculture (Berni, et al., 2009; Wooster, et al., 2013). Commercialized sUAS systems, seamless imaging integration, GPS, and autopilot systems provide ready-to-fly (RTF) systems for operator ease at an inexpensive price compared to manned imagery that provide a sensible low-cost platform for high resolution imagery at sub-meter increments (Berni, et al., 2009; Herwitz, et al., 2004). As demonstrated with automated machine control, advances in technology will replace the human capacity for observation and decision making. Similarly, commercial sUAS will continue to employ automatic machine control to simplify the operation, regulate application uniformity and imaging quality, and increase the size of managed machinery. Nevertheless, field scouting and manual processing is still needed if growers are to understand and implement management zones (Goel, et al., 2000). However, sUAS are controlled from a remote control operator present in the field, thereby

allowing direct crop health characteristics to be measured for unprecedented ground truthing of the remote imagery prior to or after the flight campaign.

Although low flight altitudes (40 to 200 m) increase thermography’s ability to measure crop health characteristics at scales more adoptable for agricultural production, sUAS are still subject to the same atmospheric effects of other thermography sensing platforms (Berni, et al., 2009; Maes & Steppe, 2012). Thermography is prone to varying extents of artifacts related to varying degrees of wind, shadows, and clouds (Kuenzer, 2014). Table 1.3 compares the sensing platforms capabilities while Table 1.4 summarized the thermographic research conducted in agriculture.

Table 1.3. Platform comparison between satellite, piloted aircraft, sUAS, and ground thermography.

Platform	Satellite	Piloted Aircraft	sUAS	Ground
Survey Area/Coverage	Very Large Area	Whole Field(s)	Whole-Field / Small	Small
Resolution	Coarse	Medium	Medium-to-Fine	Fine
Revisit Time	Weekly / Daily	Pilot Availability	On-Demand	On-Demand
Sensing Time	Very High	Fast/Medium	Fast/Medium/Slow	Very Slow
Data Processing	Georeference Orthorectification Atmospheric Correction Emissivity Correction	Image Mosaic Georeference Orthorectification Atmospheric Correction Emissivity Correction	Image Mosaic Georeference Orthorectification Atmospheric Correction Emissivity Correction	Emissivity Correction Interpolation

Table 1.4. Summary of thermography use, thermal camera, sensing platform, imagery software, temperature sensitivity, and source.

Use (Crop)	Camera (Manufacturer)	Platform Sensing distance/altitude	Image Pixels (Spatial Resolution/pixel) Sensitivity	Imaging Processing	(LWIR) Range (FOV) Emissivity	Citation
Field CWSI mapping (Maize)	FLIR IR E30 (FLIR Systems, USA) Uncooled	Aerial (Nadir)	- 0.2°C	ArcGIS 10.0 Convert image to radiometric	7.5 to 13 μm NA NA	(Taghvaeian, et al., 2013)
Field Mapping Nitrogen & Water Stress (Wheat)	ThermaCAM P40 (FLIR Systems, USA)	Aerial (Nadir)	1 meter -	Mean Canopy Temperature	7.5 to 13 μm NA NA	(Tilling, et al., 2007)
Correlate canopy temperature to soil water potential (Mixed Forrest)	VarioCAM (Infra Tech, Germany)	Aerial (Nadir) 100 meters	3.5 meters 0.1°C	Compare with Visible imagery to isolate tree canopy	NA NA NA	(Scherrer, et al., 2011)
Automate CWSI Measurements (Grapevines)	FLIR PM570	Aerial / Ground (Nadir)	320/240 -	ThermaCAM Research Pro Isolate reference temperatures for CWSI	NA NA NA	(Wang, et al., 2010)
Estimate daily ET (Wheat)	SC2000 Thermal Camera (FLIR Systems)	Airborne Nadir 760 meters	0.5 m -	NA	NA	(French, et al., 2005)
Automated leaf temperature extraction (Broad Bean)	SnapShot 225 (Infrared Solutions)	Greenhouse - 0.25 to 10 meters	0.63 to 25.2 mm NA	ENVI remote sensing (Research Systems) Automatically Segment leaves	8 to 12 μm 17.2° 0.95	(Leinonen & Jones, 2004)
influence from soil, sunlit versus shaded leaves, and sun/sensor orientation (Cotton)	760 IR Imaging Radiometer (FLIR)	Ground (11 viewing angles) 2 meters radius over canopy	10 mm NA	Matlab™ software transform digital image to temperature scale and geo-reference pixel	8 to 12 μm 70° Na	(Luquet, et al., 2003)

Mean Canopy Temperature and Variability (Citrus Tree Crops)	IR Thermal Camera TH9100 WR (NEC Avio Infrared Tech. Co., Ltd., Japan)	Ground (Frontal) 1-3 meters	51 mm NA	ArcGIS 9.3 Average temperature and variability	8 to 14 μm 42° .98	(Ballester, et al., 2013)
Water Status Estimation (Cotton)	ThermaCAM PM545 (FLIR systems)	Ground (Nadir)	5 mm 0.1°C	ThermaCAM Explorer Matlab™ Apply Radiometric temperature scale to image pixel	7.5 to 13 μm 24° NA	(Cohen, et al., 2005)
Compare Nitrogen content to water stress (Wheat)	ThermaCAM P40 (FLIR, Sweden)	Ground (nadir) 2.5 meters	- NA	ThermaCAM Reporter Pro 7 Extract full temperature of canopy, soil, and foliage	7.5 to 13 μm 24° NA	(Fitzgerald, et al., 2007)
Distinguish water stress Stomatal Conductance (Grapevines, Beans, & Lupins)	IR Snapshot 525 (Infrared Solutions, Minneapolis, USA)	Ground (Horizontal)	2.5 mm 0.1°C	SnapView Pro Test spatial camera drift Segment background temperature	8 to 12 μm NA 0.96, 0.95	(Grant, et al., 2007) (Grant, et al., 2006)
Biomass Estimation (Wheat)	T335 Thermal Camera (FLIR Systems, Wilsonville, USA)	Ground (Nadir) 0.5-0.8 meters	- 0.05°C	FLIR QuickReport 1.2 Segment soil and non-plant material	7.5 to 13 μm 34° 0.96	(Hackl, et al., 2012)
Seedling biomass and drought during early growth stage	ThermaCAM SC3000 (FLIR Systems)	Ground (Nadir) 1.8 meters	<3 mm .002°C	ThermaCAM Researcher Measure overall leaf temperature	8 to 9 μm 20° 0.95	(Liu, et al., 2011)
Water Stress (Grapevine)	ThermaCAM SC2000 (FLIR Systems)	Ground (Nadir) 15 meters	17 mm NA	Matlab (Mathworks) Combine thermal and digital images Segment soil and shaded leaves	7.5 to 13 μm 24° NA	(Moller, et al., 2007)
Correlate CWSI to Leaf Water Potential (Cotton/Soybeans)	ThermaCAM SC2000 (FLIR System)	Ground (Nadir) 7 meters	- NA	ThermaCAM Software	7.5 to 13 μm 24° NA	(O'Shaughnessy, et al., 2011)
High Throughput Phenotyping (Potato)	ThermaCAM P25 (FLIR Systems)	Ground (Off to one side) 8 meters	320-240 NA	ThermaCAM Research Pro Estimate mean plot canopy temperature	7.5 to 13 μm NA NA	(Prashar, et al., 2013)
High Throughput Phenotyping for water stress (Maize)	Midas 320L (Dias Infrared, Germany)	Ground (Nadir) 8 meters	320*240 NA	Extract canopy leaves for average canopy temperature	NA NA 0.94	(Romano, et al., 2011)
Fruit Identification (Orange Orchard)	ThermaCAM P65HS (FLIR Systems)	Ground (Horizontal) 2 meters	320*240 NA	ThermaCAM Researcher (Mathworks, USA) Radiometric Conversion Image Fusion	NA NA 0.90	(Bulanon, et al., 2009)
Drought Tolerant Genotype Screening Relate stomatal closure & yield (Maize)	VarioCAM (Infra Tech, Germany)	Ground (Nadir) >5 meters	- NA	IRBIS-Professional Object emissivity, distance, and temperature. Merge VIS with TIR	NA Wide Angle	(Zia, et al., 2013)
Localized Stomatal Conductance and Disease (Sunflowers)	JTG-MD Thermal Camera (JTG-MD, Japan)	Laboratory (Macro)	<3 mm 0.05°C	Image distribution for measuring localized photosynthesis	NA NA NA	(Hashimoto, et al., 1984)
Spatial and temporal stomatal conductance (French Bean Leaves)	Thermovision 900 LW/ST (NEED)	Laboratory (Macro)	0.2 to 0.7 mm 0.08°C	IRWinRes	8 to 12 μm 10° 0.93	(Jones, 1999)
Crop Breeding for Drought Tolerance	ThermaCAM PM250 (FLIR Systems, USA)	Laboratory (Nadir) 0.4 meters	320*240 0.1°C	Image Analysis Relative temperature differences	3.4 to 5 μm 16° 1	(Merlot, et al., 2002)
Disease Detection (Tobacco)	Agerna THV900LW (FSI, USA)	Laboratory (Macro)	- NA	Observe temporal change in tobacco leaves after infections	8 to 12 μm NA NA	(Chaerle, et al., 1999)
Detect range of water stress (Peach/Olive Orchard)	SnapShot (Infrared Solutions, USA)	Manned Aerial (Nadir) 1000 meters	2 m NA	Detect the tree crown temperature within irrigation regimes	8 to 14 μm NA NA	(Sepulcre-Canto, et al., 2007)
Map spatial CWSI with site-specific environment parameters (Olive Orchards)	Thermovision A40 M (FLIR, USA)	sUAS (Nadir) 150-200 meters	40 cm 0.08°C	Segment soil and detect mean canopy temperatures	7.5 to 13 μm 40° 0.98	(Berni, et al., 2009); (Berni, et al., 2009)

1.5 THERMAL SENSING FOR CROP STRESS

The following sections include descriptions of thermal sensing for crop stress with regards to early crop sensing, alternative crop sensing, crop stress indicators, thermal indices, ground truthing, and cost versus benefit.

1.5.1 Early Crop Sensing

As producers strive for increased output from available land, techniques and technologies are needed to accurately classify spatial crop water need or crop water stress to gain economic and environment advantages (Herwitz, et al., 2004; Taghvaeian, et al., 2013). Several crop health monitoring methods that rely on a combination of single-point soil and atmospheric measurements are available to monitor crop water stress (Alves & Pereira, 2000; Cohen, et al., 2005). In addition, current methods require multiple sensors that are subject to localized, placement error and do not account for spatial crop variability that exist within a field (Moller, et al., 2007). As a result, site-specific techniques that utilize input parameters from the plant instead of the soil to assess spatial crop water stress have been investigated (Jackson, et al., 1986).

Established methods exist for detecting crop water stress which utilize pressure chambers and leaf diffusion porometers to measure individual leaf stomatal conductance and leaf and stem water potential, respectively (Ballester, et al., 2013; Berni, et al., 2009; Grant, et al., 2007; Idso, et al., 1977). However, these techniques are destructive, labor intensive, subject to placement error, limited by small sample size and unsuitable for automation (Ballester, et al., 2013; Berni, et al., 2009; Cohen, et al., 2005; Gontia & Tiwari, 2008; Jones, 1999; Leinonen & Jones, 2004). Consequently, these drawbacks make invasive plant-based crop monitoring impractical in commercial applications, thereby limiting producer adoption for irrigation decision management (Ballester, et al., 2013).

To address these concerns, thermal sensing approaches have been investigated because they are non-contact, less labor intensive, and offer non-destructive monitoring to assess crop stress from leaf canopy temperatures (Grant, et al., 2006; Leinonen & Jones, 2004). Since the 1970s, crop canopy temperature has been accepted as a health indicator of crop water stress because plants close their leaf stomata, or leaf openings, when they experience water stress in order to retain water, thereby lowering stomatal conductance, reducing transpiration, and increasing leaf temperatures (Ballester, et al., 2013; Grant, et al., 2006; Idso, et al., 1977; Jones, 1999; Leinonen & Jones, 2004; Rodriguez, et al., 2005). On the other hand, when leaf stomata are open, water in

the leaf evaporates through transpiration which cools the leaf (Maes & Steppe, 2012). During transpiration, energy from the leaf is used to evaporate the water from a liquid to a vapor, inducing latent heat loss and cooling the leaf. In addition to transpiration, leaf temperature depends on ambient conditions such as relative humidity, wind speed, ambient temperature, and radiation incident on the leaf surface (Leinonen & Jones, 2004). As a result, canopy and leaf temperatures are controlled by a combination of thermal energy balances, vegetative genetics, and natural site-specific elements (Luvall & Holbo, 1991). Although these environmental elements influence leaf temperature, they can be readily measured in real-time using commercially available sensors (Udompetaikul, et al., 2010).

Current growth studies have primarily used ground-based thermometry to take canopy temperature measurements and develop thermal indices that account for canopy characteristics, soil temperature, and atmospheric conditions for site-specific irrigation management and breeding programs (Idso, et al., 1981; Jackson, et al., 1981; O'Toole & Real, 1986). According to Zia et al. (2013), growth stage does not significantly impact canopy leaf temperature, thereby promoting leaf temperature as a viable crop characteristic in growth performance. Highly integrated thermometric systems use an array of infrared thermometers (IRTs) mounted in fixed positions within the field and on center pivot irrigation systems to measure crop canopy temperatures and provide a means of irrigation scheduling (O'Shaughnessy, et al., 2012). However, because of their single-point measurement, IRTs are limited to ground-based systems because they lack the ability of measuring subtle heterogeneity characteristics of leaf dynamics which are readily enabled with thermography (Liu, et al., 2011).

Because thermal sensing is primarily used to detect crop water stress, several robust indices have been proposed to aid irrigation scheduling, such as Stress Degree Day (SDD) (Idso, et al., 1981), CWSI (Jackson, et al., 1981), Water Deficiency Index (WDI) (Moran, et al., 1994), Temperature-Time Threshold (TTT) (Wanjura, et al., 1992), and more recently, the Crop Stress Index (CSI) (Rodriguez, et al., 2005). Thermal-based indices have shown significant correlation between crop canopy temperature and stomatal conductance and leaf water potential with stronger correlations with increased stress intensity (Hackl, et al., 2012). Increasing availability of sensitive TIRIS support high definition studies that assess canopy temperature in relation to dynamic leaf stomatal conductance and crop stress assessment (Jones, 1999; Liu, et al., 2011). Numerous studies prove thermography's ability to distinguish between irrigated and water-limited stress of

grapevines (Grant, et al., 2006; Grant, et al., 2007), cotton (Luquet, et al., 2003), citrus trees (Ballester, et al., 2013), olive orchards (Berni, et al., 2009), and sunflowers (Hashimoto, et al., 1984) while supporting the development of greenhouse model comparisons (Grant, et al., 2006; Leinonen & Jones, 2004), genetic-based drought tolerance in maize (Liu, et al., 2011), leaf temperature association with biomass accumulation (Liu, et al., 2011), spatial awareness of different leaf architecture (Ballester, et al., 2013; Grant, et al., 2007). In addition, laboratory studies using TIRIS show an increase of understanding in the physiological utility while studying localized stomatal conductance of leaf material at the macro-scale (Hashimoto, et al., 1984; Jones, 1999). Localized infections and damage demonstrate themselves as areas of warm or cold spots due to change in transpiration rate at the localized leaf stomata (Chaerle, et al., 1999; Maes & Steppe, 2012), as shown in Figure 1.21.

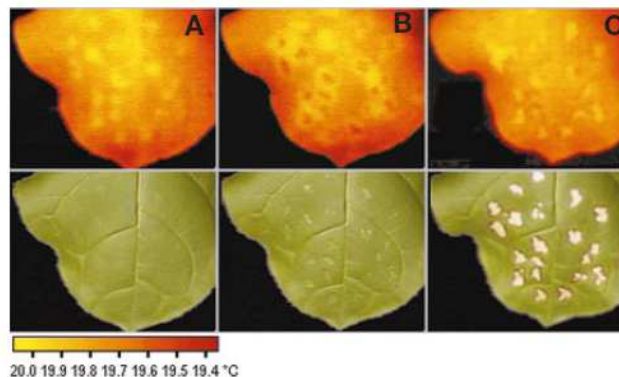


Figure 1.21. Infected tobacco interaction Chaerle et al. (1999).

Thermography has shown utility in correlating stomatal conductance and leaf temperatures in monitoring crop performance for genetic screening (Merlot, et al., 2002). As a form of high spatial sensing, a leaf's response to temperature change can be used as an indicator while screening crop varieties for differences in stomatal response. Because it is non-invasive and easily automated, leaf stomatal function is not inhibited, thereby enabling analysis for undisturbed relationships between photosynthesis and stomatal conductance (Jones, 1999). Crop variety screening methods highly favor commercial traits for crop yield (Prashar, et al., 2013; Zia, et al., 2013). However, expressed traits are a complex combination of genetics and chemical and physical reactions, and for advancing technologies in precision agriculture, phenotyping has been a bottleneck in breeding programs (Prashar, et al., 2013). A desire of any breeding program is to carry out breeding experiments under natural conditions outside of a greenhouse and

environmental chamber (Zia, et al., 2013). However, field trials place different constraints on crop sensing equipment due to large population sample size (Prashar, et al., 2013).

Stomatal conductance is one trait directly linked to crop performance and photosynthesis while maintaining water use efficiency. Thermography offers the ability to screen for mutant populations at a higher throughput and scale that exhibit optimal stomatal response to water stress (Prashar, et al., 2013), as shown in Figure 1.22.

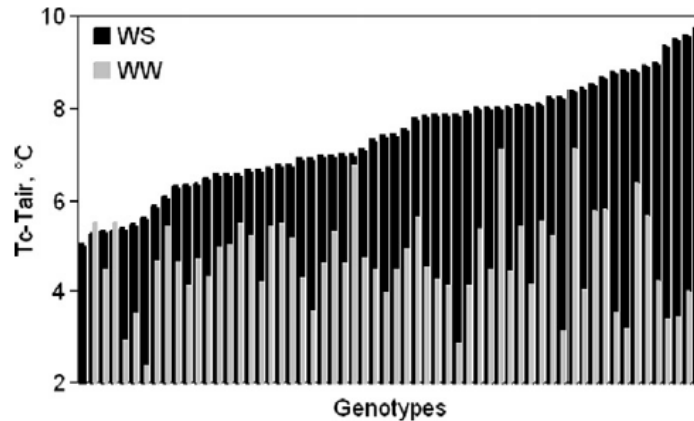


Figure 1.22. Canopy temperature differences between canopy (Tc) and ambient air (Tair) of 61 maize genotypes in water stress and well-watered plants. Romano et al. (2011).

As demonstrated in Figure 1.22, implementation of automated thermography in screening programs capable of sensing individual leaf differences can be a rapid and responsive tool for screening phenotypes and disease (Chaerle, et al., 1999). Similarly, Rodriguez et al. (2005) and Tilling et al. (2007) compared crop canopy temperature with respect to nitrogen treatments. Table 1.5 illustrates the CSI from specific nitrogen applications to wheat.

Table 1.5. Applied nitrogen rate versus crop stress index of wheat samples. Adapted from Rodriguez et al. (2005).

Nitrogen Rate (lbs. acre-1)	Normalized Difference Vegetative Index (NDVI)		Crop Stress Index (CSI) (°C kPa-1)	
	Rain fed	Irrigated	Rain fed	Irrigated
0	0.32	0.43	3.43	1.67
16	0.29	0.51	4.57	2.07
39	0.47	0.63	3.50	1.60
163	0.44	0.78	3.10	1.10

As shown in Table 1.5, canopy temperature is more sensitive to water stress than nitrogen deficiencies, thereby supporting the use of canopy temperature as an indicator of a plant's ability to utilize inputs such as nitrogen fertilizers (Rodriguez, et al., 2005; Tilling, et al., 2007).

1.5.2 Alternatives to Thermal Crop Sensing

Plant crop characteristics have been widely studied using multispectral and hyperspectral sensors for qualitative and quantitative analysis in the VIS and NIR light spectrum (400 to 2500 nm spectral range) (Berni, et al., 2009). VIS sensors detect chemical differences of the plant material that interact with light between molecules and atoms on a micron scale within the plant material (Miller, n.d.). Based on this light interaction, monitoring select wavelengths can provide insight as to chemical compounds present in the sample specimen. This evidence has been repeatedly used to monitor plant phenology (Zia, et al., 2013) and crop vigor and yield (Berni, et al., 2009) and estimate biomass (El-Shikha, et al., 2007), fractional ground cover, chlorophyll content (Fitzgerald, et al., 2007), crop evapotranspiration (El-Shikha, et al., 2007), and nutrients (Fitzgerald, et al., 2007; Tilling, et al., 2007). Although VIS sensors quantify relative variation in crop growth performance, crop characteristics such as water stress limit their utility (El-Shikha, et al., 2007) because the first signs of measureable water stress assessments with VIS and NIR light sensors are due to the change in detected leaf angle from wilting when potential yields have most likely already been affected (Fitzgerald, et al., 2007).

1.5.3 Crop Stress Characteristics

Precise crop stress characterization for tactical management conserves resources and reduces expensive growing costs while optimizing plant performance and quality growth parameters (Jackson, et al., 1986). Research continues to show that crop growth and yield is directly affected by crop water stress and only indirectly and partially affected by soil-water interaction (Sepulcre-Canto, et al., 2011; Zhang & Kovacs, 2012). For most crops, quality and quantity of production is directly related to efficient crop water use. More specifically, heat stress induced from lack of water is a abiotic stress factor that influences crop growth performance (Ayeneh, et al., 2002) hindering complex biological systems that impact transpiration, photosynthesis, leaf senescence, and grain development, consequently reducing economic return (Ballester, et al., 2013). For example, grain protein is largely dependent on the utilization of plant nitrogen accumulation and concentration in the grain during the filling stage (Zhao, et al., 2005). In addition, water stress during the filling stage influences the resulting grain protein content. As discussed, leaf temperatures are dependent on stomatal closure in order to provide nutrient delivery through water transport during critical periods during the growing season (Zhao, et al., 2005). As

a result, crops have periods during development in which they become more susceptible to stress; hence, tactical management can intervene to maintain yield potential (Taghaeian, et al., 2013).

With the aforementioned potential for measuring spatial crop stress, thermography applied to the homogeneous nature of cropland reduced the complexity experienced in studies conducted in orchards with sparse canopy (Maes & Steppe, 2012) without spatial resolutions below 2 m (Sepulcre-Canto, et al., 2007). As previously mentioned, plants close the leaf stomata, thereby lowering stomatal conductance and reducing transpiration (Liu, et al., 2011) in response to ambient conditions, as defined by Equation 1.12:

$$(T_{\text{predicted canopy}} - T_{\text{air}})_{\text{wet}} = r_a(R_{\text{net}})/\rho C_p \quad (1.12)$$

Where:

$T_{\text{predicted canopy}}$ = Estimated temperature of the non-stressed leaf

T_{air} = Temperature of the air (°C)

r_a = Aerodynamic resistance ambient temperature

ρ = Air density

C_p = Heat capacity of air

R_{net} = Net radiation incident on the leaf surface.

By applying a fundamental energy budget, microclimates (i.e., interactions between other vegetation and bare soil) can account for environmental inputs for crop characteristic comparisons between species and varying climates (Luvall & Holbo, 1991), as shown in Figure 1.23.

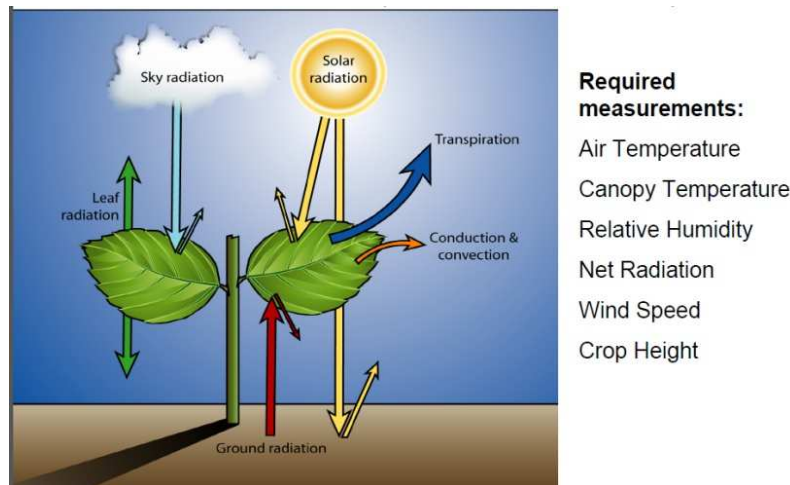


Figure 1.23. Generalized energy balance of vegetation. Adapted from Blonquist and Bugbee (n.d.).

1.5.4 Thermal Indices and Techniques

Thermography has been utilized to develop thermal indices and crop sensing techniques. The most commonly used thermal index, the CWSI, is discussed because of its utility by all sensing

platforms while the stress degree day (SDD), temperature time threshold (TTT), and canopy stress index (CSI) are also briefly discussed in the following sections.

1.5.4.1 Crop Water Stress Index

Idso et al. (1981) found a direct relationship between ambient air conditions and the influenced transpiration rate of non-water stress crops. For example, a leaf temperature at or below predicted leaf temperature indicates a non-stressed plant, whereas leaf temperature above the non-water stress baseline (NWSB) indicates a gradient level of water stress (Figure 1.24). Idso investigated the correlation between non-water stressed leaf temperatures under the same net radiation, similar vapor pressure deficit (VPD), and wind speed.

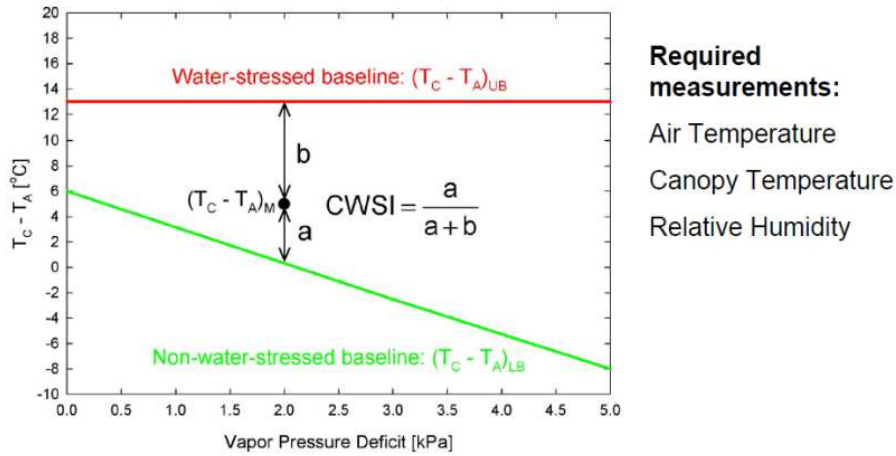


Figure 1.24. ($T_c - T_a$) versus Vapor Pressure Deficit comparison. Reproduced from Blonquist and Bugbee (n.d.).

Shown in Figure 1.24, the non-water stressed leaf canopy-to-air temperature deficit can be found versus specific VPD for the same net radiation and wind speed, as defined by Equation 1.13:

$$T_{\text{canopy}} - T_{\text{air}} = a - b \times \text{VPD} \quad (1.13)$$

Where:

- T_{canopy} = Canopy Temperature ($^{\circ}\text{C}$)
- T_{air} = Measured air temperature ($^{\circ}\text{C}$)
- a = Crop specific intercept for NWSB
- b = Crop specific coefficient
- VPD = Vapor pressure deficit [kPa]

The NWSB coefficients are empirically measured with daily leaf temperature measurements over a full growing season or with diurnal leaf temperature measurements over the course of several days. The relationship between canopy temperature and transpiration rate is defined as the normalized difference of the measured air-to-leaf canopy temperature deficit

between the lower base line (i.e., NWSB) and the upper base line, or water-stressed baseline (WSB), on a plot of air-to-leaf canopy temperature deficit vs. VPD as depicted in Equation 1.14 (Idso, et al., 1981; Jackson, et al., 1981; Jackson, 1982):

$$CWSI = \frac{\Delta T_{predicted} - \Delta T_1}{\Delta T_{predicted} - \Delta T_{dry\ leaf}} \quad (1.14)$$

Where:

$$\Delta T_{predicted} = (T_{predicted} - T_{air})$$

$$\Delta T_{dry} = (T_{dry} - T_{air})$$

$$\Delta T_1 = (T_{actual} - T_{air})$$

For example, stressed leaf (T_{dry}) and non-stress leaf ($T_{predicted}$) boundary temperatures for a leaf are 25°C and 20°C, respectively. Air temperature is 23°C and actual temperature of the leaf is 22°C. In this example, the CWSI is 0.4.

This aforementioned crop-based relationship was used by Jackson et al. 1981 to indirectly measure soil moisture and apparent crop health through transpiration. As a result, the CWSI has been successfully developed and implemented using IRTs in order to base variable rate irrigation needs (Taghvaeian, et al., 2013). An advantage of the CWSI is the scale at which it can be implemented. With the addition of upper and lower boundaries for predicted leaf temperature, the CWSI approach has been the most used index aboard all thermal sensing platforms in various climate regions because of the inclusion of VPD, solar radiation, and wind speed (Maes & Steppe, 2012; Rodriguez, et al., 2005). Figure 1.25 shows simulated relationships between solar radiation (R_{net}), wind speed (U), and VPD.

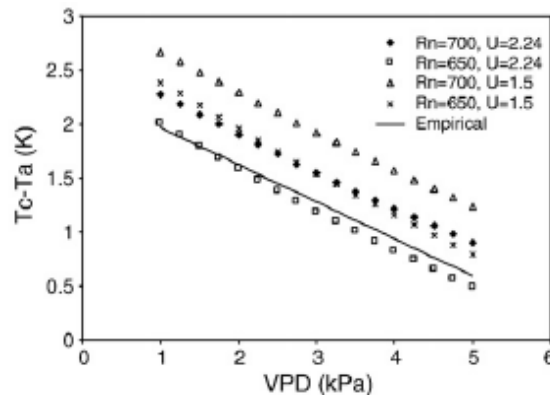


Figure 1.25. Simulated relationships of non-water stress baselines from varied environmental conditions compared to theoretical baselines. Reproduced from Berni et al. (2009).

Various approaches have been suggested to compute CWSI for a particular crop species in actual environment parameters. In all platform types, theoretical CWSI relies on baseline temperature deficits, assuming that environmental conditions remain constant, thereby requiring

measurements of crop canopy temperatures, wet/dry reference temperatures, and environment conditions (Grant, et al., 2007; Luquet, et al., 2003). A robust technique relies on empirical NWSB during a particular research study that directly accounts for net radiation, aerodynamic resistance, and the particular crop's microclimate (Ballester, et al., 2013; Blonquist & Bugbee, n.d.; El-Shikha, et al., 2007; Erdem, et al., 2010; Fitzgerald, et al., 2007; Gontia & Tiwari, 2008; Grant, et al., 2007; Maes & Steppe, 2012). In order to directly measure upper and lower reference temperature bounds, leaves are wetted with water for a fully transpiring leaf (lower limit) and covered with petroleum jelly to indicate a non-transpiring leaf (upper limit). However, preparation of wet/dry leaf surfaces for reference leaf temperatures is not practical and subject to repeatability errors.

Many studies have investigated the use of standardized measurements without manually preparing reference temperatures achieving similar CWSI results (Berni, et al., 2009b; Cohen, et al., 2005; Grant, et al., 2006; Grant, et al., 2007; Jones, 1999). Standard dry reference temperature recommendations include the use of an upper temperature bound of 5°C above air temperature (Alves & Pereira, 2000; Cohen, et al., 2005; Erdem, et al., 2010; Moller, et al., 2007; Moran, et al., 1994; Wanjura, et al., 2006). Standard wet reference temperature recommendations include measuring leaf temperature of well-watered plants (Ballester, et al., 2013; Blonquist & Bugbee, n.d.; El-Shikha, et al., 2007; Erdem, et al., 2010; Fitzgerald, et al., 2007; Gontia & Tiwari, 2008; Grant, et al., 2007; Maes & Steppe, 2012). These studies support crop water stress monitoring at any time of day regardless of incoming solar radiation and aerodynamic resistance, thereby increasing the ease of use for site-specific farm management (Alves & Pereira, 2000; Berni, et al., 2009) where changing weather conditions may complicate acquisition of comparative sensing data (Luvall & Holbo, 1991). Blonquist and Bugbee (n.d) monitored crop water stress to allow for increased practical knowledge regarding sensitivity necessary to measure crop stress under various environmental conditions. Table 1.6 shows recommended sensor sensitivity to monitor CWSI to an accuracy of ± 0.05 .

Table 1.6. Recommended sensor accuracies to limit CWSI measurement error (Blonquist & Bugbee, n.d.).

Parameter	Sunny, Warm, Dry	Cloudy, Cool, Humid
Net Radiation	$\pm 100 \text{ W m}^{-2}$	$\pm 15 \text{ W m}^{-2}$
Relative Humidity	$\pm 9 \%$	$\pm 4 \%$
T _{air}	$\pm 2^\circ\text{C}$	$\pm 0.2^\circ\text{C}$
T _{canopy}	$\pm 1^\circ\text{C}$	$\pm 0.2^\circ\text{C}$
Wind	$\pm 0.6 \text{ m s}^{-1}$	$\pm 0.3 \text{ m s}^{-1}$
Canopy Height	$\pm 0.06 \text{ m}$	$\pm 0.03 \text{ m}$

Automated measurements with image processing increase thermography's appeal as a sensing tool because instantaneous measurements can be used to account for consistent crop water stress (Maes & Steppe, 2012). Artificial measurements have provided a repeatable standard for applications of a higher scale when used in conjunction with thermal imaging (Moller, et al., 2007). Artificial wet reference surface targets are viewable within a FOV for significant pixel coverage and mounting height within the plant canopy to optimally capture leaf microclimate (Wang, et al., 2010). However, no artificial dry reference exists to measure dry leaf (Prashar, et al., 2013).

In order to overcome soil influence in thermometric sensor readings, Moran et al. (1994) developed the water deficit index (WDI) that applied a two-dimensional CWSI theory to partially covered canopies. This index relies on soil surface temperature measurements in order to evaluate crop water stress from partial to full crop canopies, making reference temperatures difficult to maintain and reducing index adoptability.

In comparison studies between thermography and thermometry, thermometry inherently creates baseline temperature data over sunlight and shaded leaves as well as soil background. However, thermography can extract leaf vegetation, creating more accurate baselines for leaf canopy-to-air temperature deficit versus VPD (Taghvaeian, et al., 2013). Future studies must investigate thermal indices analyzed with thermography. For example, sunflower vegetative indices analyzed with thermography demonstrated slightly different slopes and intercepts (Nielsen, 1994). A main contributor to limited commercial adoption of CWSI as a stress indicator is because the current sensing platforms (i.e., ground-based, aerial, and satellite) lack necessary temporal and spatial resolution for accurate and timely separation of sunlit and shaded soil and lower leaf backgrounds. In addition, CWSI values cannot account for differing net radiation and aerodynamic resistance without repeated empirical calibrations without non-water stressed plant samples (Berni, et al., 2009; Colaizzi, et al., 2012; Cohen, et al., 2005; El-Shikha, et al., 2007; Jackson, et al., 1986; Jones, 1999).

1.5.4.2 Stress Degree Day

Irrigation scheduling based on canopy temperature depression ($T_{\text{canopy}} - T_{\text{air}}$) is a method widely used as an indicator of crop health in regards to heat stress and drought stress in crops between irrigation regimes (Ehrler, 1973). With a canopy-to-air temperature deficits, automated irrigation occurs in accordance to the SSD when crop canopy temperatures rise above air

temperatures at 1 to 2 h following solar noon during a duration of days (n), as defined by Equation 1.15 (Idso, et al., 1977):

$$\text{Stress Degree Day} = \sum_{i=1}^n (T_{\text{canopy}} - T_{\text{air}})_i \quad (1.15)$$

When SDD = 0, irrigation was automated. Because environmental conditions change, the CWSI has been widely adopted, thereby replacing SDD in most irrigation scheduling. However, SDD stills acts as a significant correlation to stomatal conductance as an estimator of yield and water use (Maes & Steppe, 2012).

1.5.4.3 Temperature-Time Threshold

Similar to SDD proposed by Idso et al. (1977), the TTT concept is based on the correlation between crop performance and the amount of time the crop canopy surpasses a narrow temperature range. Temperature threshold concepts are also known as the biological identified optimal temperature interactive console (BIOTIC) protocol (Wanjura, et al., 2006). In practice, when the crop exceeds the threshold temperature for a certain period of time, irrigation is signaled (O'Shaughnessy, et al., 2012). Thermometric systems utilize an array of IRTs integrated onto a center pivot irrigation system for crops such as corn, soybeans, (Evet, et al., 2014), and cotton (Wanjura, et al., 2006). Ongoing irrigation studies suggest that the TTT approach is more robust than the more commonly known CWSI for assessing water stress and estimating yield (Wanjura, et al., 2006). Limitations of the TTT, however, include continuously monitoring crop temperatures and soil water potential to assess crop water stress and water deficit, respectively.

1.5.4.4 Canopy Stress Index

With the availability of thermography, Rodriquez et al. (2005) introduced the CSI to normalize the leaf-to-air temperature deficit ($T_{\text{canopy}} - T_{\text{air}}$) under a specific VPD, as defined by Equation 1.16:

$$CSI = \frac{(T_{\text{canopy}} - T_{\text{air}})}{VPD} [\text{°C kPa}^{-1}] \quad (1.16)$$

Approaches such as CSI attempt to reduce necessary sensors for instantaneous canopy stress assessment in precision agriculture. As reported by Rodriquez, CSI accounts for 80% of yield variation over that of the 46% correlation to NDVI values. As a result, most variation in crop performance was more correlated to water stress. Aside from this example, thermography provides

a unique opportunity to measure only canopy leaves reducing background temperature influence, allowing for new and advances relationships to be investigated not previously possible.

1.5.5 Precision Agriculture Cost/Benefit

The importance of performance, cost/benefit, and increased yield potential for a particular actionable decision is only briefly discussed in this paper. Actionable decisions in precision agriculture rely on useful thermal sensing software and hardware with the capacity to use on-demand imagery for actionable decisions while the level of incremental knowledge complements the practical management zone permitted by mechanical intervention (e.g., sprayer nozzle coverage, seeding row control, irrigation zones) (Cohen, et al., 2005; Herwitz, et al., 2004). Before implementing precision technology, the producer must first answer these questions:

1. **What is my goal?** (i.e., I will change irrigation scheduling with this crop water assessment.)
2. **What type of data do I need to capture?** (i.e., I need whole-field canopy temperature.)
3. **What is the best technique to achieve that information?** (i.e., remote sensing platforms)
4. **Will it be useful, quick, and accurate?** (i.e., actionable irrigation prescription, on-demand, and based on crop need)
5. **What is my minimal management zone I can change?** (i.e., individual nozzle/section/boom)
6. **How will I know I made a difference?** (i.e., yield production data, resample)

For precision agriculture, the more specific the application, the better a technology can be configured for the producers' operation (Pohl & Van Genderen, 1998). In addition, the type of data the customer needs will suggest the type of sensor and platform necessary. The return on investment (ROI) of a tactical site-specific management must reduce (1) input costs, (2) machinery wear, and (3) loss in yield potential. Increased crop stress awareness for tactical management will rely on new technologies to capture on-demand information to support intervention within minimal management zones permitted by practical hardware. Advancing imaging platforms for sUAS increase crop characteristics assessment and will continue to evolve in capabilities regarding 1) high resolution images of entire fields, 2) automatic analysis from acquired images, and 3) practical needs or adjustment at a high spatial scale.

1.6 CONCLUSION

Producers know their land and its productivity and therefore require on-demand information to increase actionable management. Thermography is well-suited for agriculture crop sensing because of its ability to provide imagery of whole-field assessment, automated analysis, and tactical decisions at a high level of precision. However, agricultural studies using thermography have been limited due to expense of past thermal camera systems, unfamiliar use and operation, system complexity, and unknown performance in agricultural conditions that restrict their use to laboratories, greenhouses, and intermittent use in prolonged field studies.

TIR cameras, however, contain features that currently only meet the needs of non-agricultural uses, thereby providing an incentive for TIR camera manufacturers to develop modified cameras intended for operation within agricultural fields and conditions. Due to their low cost compared to cooled TIR camera, minimal size and weight, and lack of moving parts, uncooled TIR cameras have been emphasized and utilized aboard sUAS platforms for unprecedented ground coverage and high spatial crop stress assessments.

Crop temperature plays a fundamental and often limiting role in many biological processes that control the rate of chemical reactions between plants and surrounding microclimates. Therefore, most variation in crop performance is found to be related to water stress. The decision to irrigate is critical, but accurate determination of irrigation amount and location is as equally important for site-specific irrigation, or irrigation that matches precise crop need at manageable increments to achieve desired crop performance. However, extensive variability exists within commercial agricultural fields, including soil type and depth, topography, climate, crop growth stage, and variance in operation methods. Effective assessment of plant growth parameters requires confidence in thermography techniques and hardware in order to accurately assess crop stress during all measurements.

Chapter 2 - Selection and Utility of Uncooled Thermal Cameras for Spatial Crop Temperature Measurement within Precision Agriculture

2.1 ABSTRACT

Since previous research used local, single-point measurements to indicate crop water stress, thermography is presented as a technique capable of measuring spatial temperatures supporting its use for monitoring crop water stress. This study investigated measurement accuracy of uncooled thermal cameras under strict environmental conditions, developed hardware and software to implement uncooled thermal cameras and quantified intrinsic properties that impact measurement accuracy and repeatability. A DRS Tamarisk® 320 (CAM1) and FLIR® Tau 2 (CAM2) were selected for this study. Results indicated that wide and medium angle lens distortion was 19% for CAM1 and 30% for CAM2. A minimum of four pixels were recommended to maintain surface temperature integrity and maximize image coverage area. A 19 and 7 min warm-up was necessary for CAM1 and CAM2 respectively. A real-time (RT) and one-time (OT) radiometric calibration provided absolute surface temperatures with environmental compensation. CAM1 analog output yielded a configurable temperature span from 5°C-156°C, resolution from 0.02°C-0.61°C, and measurement accuracy of $\pm 0.82^{\circ}\text{C}$ or 0.62°C with OT or RT radiometric calibration, respectively, whereas digital output yielded a fixed temperature span of 156°C, resolution of 0.01°C and measurement accuracy of ± 0.43 or 0.29°C with OT or RT radiometric calibration, respectively. CAM2 yielded a controllable temperature span of 18°C-206°C, resolution of 0.07°C-0.80°C, and measurement accuracy of ± 0.87 or 0.63°C with OT or RT radiometric calibration, respectively. Both cameras were sensitive to surface temperatures ($R^2=0.99$); but, CAM1 was more controllable. Results highlight that uncooled thermal cameras can measure spatial temperatures, thereby measuring subtle crop dynamics for water resource management.

2.2 INTRODUCTION

In the midst of recent droughts, increased water demand, and the implementation of water allocations for conservation, irrigated acreage throughout the United States increased by nearly 1.3 million acres from 2002 to 2007 (USDA, 2014). The largest percentage of irrigated farms is located in the western United States where competition for irrigation water availability has

escalated in the past two decades (Taghaeian, et al., 2013). In the Midwest, for example, average irrigated corn yield has increased approximately 2.5 bushels per acre per year since the early 1970s. Diminishing irrigation water requires efficient water management practices using monitoring and control for sustainable water management (Adeuya, 2007). Other water conservation projects have developed smart-water systems that use less water from aquifers and above-ground freshwater sources while investigating soil-improving strategies in which drought-tolerant crop varieties are chosen according to a climate's available water (Berton, 2006). Although these and other advances in precision irrigation technologies are becoming available to producers, adoption of these systems for commercial applications requires producers to monitor crop water stress at increased spatial (ground sample distance (e.g., 1 cm/pixel)) and temporal (revisit frequency) resolution.

Research shows that crop growth and yield are directly affected by water stress but only partially affected by soil-water interaction (Zhang & Kovacs, 2012). Current irrigation schedules are typically based on soil moisture deficits; however, localized soil moisture sensors are not representative of spatial moisture variability that may exist throughout the field. As a result, direct measurement of canopy temperatures with manual or mounted infrared thermometers (IRTs) on pivot systems have been used to quantify crop water stress because plants close their leaf stomata under periods of water stress, thereby reducing transpiration and causing proportionally increased leaf temperatures (Evans, et al., 2000).

Although irrigation scheduling has used canopy temperature and soil moisture monitoring, these tedious and time-consuming methods yield limited samples at less resolution than is required to perform precision irrigation, consequently proving the methods to be impractical for commercial applications (Jones, 2004). While an IRT can take quick measurements, a thermal infrared imaging system (TIRIS) can monitor multiple crop profiles per image. This novice, less studied technology can monitor spatial crop temperatures in irrigation applications and in periods of drought, weed infestation, heat tolerant phenotype trait expression, and herbicide and nutrient applications. Limited publications describe United States studies of thermal infrared (TIR) cameras for measuring crop temperature profiles, specifically crops whose yield significantly increases with irrigation in the water-stressed Midwest.

Increased interest among United States agricultural producers regarding small unmanned aerial systems (sUAS) allows possibility for a TIRIS designed for lightweight, high-throughput sensing that could measure crop temperature variability and assess spatial crop water stress in

agricultural production. However, available knowledge regarding thermal sensing platform performance in agricultural field studies is limited, and producers are skeptical of technology that has demonstrated potential for measuring crop temperature profiles and enabling site-specific water management in orchards, vineyards, and other specialty crops in areas outside of the United States (Sepulcre-Canto, et al., 2011). Lack of knowledge can be attributed to the expense of cooled TIR cameras which has made crop temperature measurements in commercial agriculture economically unfeasible. However, innovation of the uncooled thermal sensor has led to development of new, lightweight TIR cameras that have no moving parts and require no cooling package, thereby providing extended operating life at a fraction of the cost of previous cooled TIR cameras.

Because microbolometer thermal detectors are uncooled, they have a low signal-to-noise ratio, the amount of usable signal compared to noise signal. Consequently, uncooled TIR detectors are less accurate ($\pm 0.1^{\circ}\text{C}$) than other temperature sensors (Kuenzer, 2014); however, this accuracy, also known as sensor measurement confidence, make microbolometers' sensitive to subtle temperature differences ($< 0.5^{\circ}\text{C}$) necessary for accurate crop health stress assessment (Blonquist & Bugbee, n.d.; Sepulcre-Canto, et al., 2007). In agricultural and environmental studies, natural objects have been found to emit long wave infrared (LWIR) radiation, a region of 7 to 14 μm wavelength bandwidth (-66.2°C to 140.0°C). Microbolometer image sensors are sensitive to LWIR radiation that strikes the detector material, changing the detectors' electrical resistance from a change in temperature, thereby transforming temperature intensity into a raw digital value (DV) generating a thermal image (Kuenzer, 2014).

Internal circuitry heat and external temperature exposure require uncooled TIR cameras to regulate their microbolometer sensors with automatic temperature recalibration. Consequently, TIR camera warm-up time can alter measurement accuracy (i.e., closeness to the true value) by microbolometer recalibration thereby requiring warm-up periods in order to reach a steady-state operating temperature (Figure 2.1).

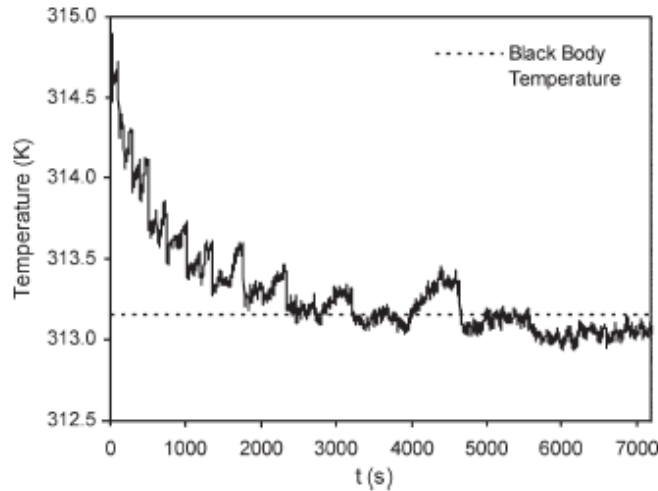


Figure 2.1 Changes of radiometric temperature measured by TIR camera during warm-up period. Adapted from Berni et al. (2009).

As shown in Figure 2.1, Berni et al. (2009) studied a TIR camera with a recommended warm-up period of 2 h before the measured temperature converged to a steady-state blackbody (i.e., object or system that absorbs and emits electromagnetic radiation equal to its internal kinetic temperature (Kuenzer, 2014)) temperature. As a result, limited literature exists testing uncooled TIR cameras in order to create standard operating protocols under practical scenarios.

For a camera, the sensed object and desired sensing distance determines the choice of lens (Elfaki, et al., 2000). Maintained focus over a wide range of temperatures is essential for system performance, stability, and imaging quality. An athermalized lens maintains performance using optical passivity over the sensitive temperature span. Unlike typical visible cameras, the TIR camera lens focal length may need to be adjusted to focus on particular sensing distances (DRS Technologies A Finmeccanica Company, 2013). However, TIR camera lenses are subject to the same geometric calibration parameters as visible imagery including focal distance, point coordinates, and radial distortion (Berni, et al., 2009; Kuenzer, 2014). Because thermal radiation does not transfer through glass, TIR camera lenses are made from germanium that allows the transmission of TIR radiation (Kuenzer, 2014). Germanium lenses are optimized for radiant heat transmission, consequently making them more susceptible to geometric distortion. According to Laguela et al. (2013), increased lens distortion is more common for TIR cameras compared to glass lenses because of their short focal length and germanium material.

Expectations associated with TIRIS rely on accurate temperature measurement, high imaging speed, limited image noise, and optimized storage of raw images. This research will

support future studies to develop a full system package for capturing accurate spatial canopy temperatures aboard sUAS and ground-based sensing platforms in order to create high definition canopy temperature maps and aid variable rate irrigation decision management. As stated, increased irrigated acres in the Midwest depend primarily on declining fresh water reserves. Significant studies have indicated that a very high level of management is required in order to maintain or improve irrigation water productivity and economic return with decreasing water resources. Researchers, TIR and sUAS manufacturers, agricultural service providers, and producers in the Midwest are eager to adopt thermal technologies in precision agriculture, such as a TIRIS aboard sUAS and ground-based platforms to assist with efficient and accurate water utilization. Therefore, this study investigated industry-leading TIR camera cores under strict laboratory conditions (i.e., air temperature, relative humidity, incident radiant heat) to determine measurement accuracy under anticipated field conditions. In addition to thermography potential, **core objectives of this research were to** (1) quantify measurement accuracy and intrinsic properties of two commercially available uncooled TIR camera cores, (2) investigate impact of physical properties and environmental conditions on measurement accuracy, and (3) determine necessary equipment and considerations when integrating an uncooled TIR camera core into a TIRIS for accurate crop temperature measurement.

2.3 METHODS AND MATERIALS

Strict laboratory experiments were conducted at the Department of Biological and Agricultural Engineering at Kansas State University, Manhattan, Kansas. A DRS Tamarisk® 320 (DRS Technologies, Inc., Dallas, Texas) and FLIR® Tau 2-324 (FLIR® Systems, Inc., Boston, Massachusetts), hereafter referred as CAM1 and CAM2, were studied to benchmark their utility in precision agriculture. These cameras were selected because of their minimal size, lightweight design, and limited power consumption. Utility was investigated with regards to integration hardware and software, camera controllability for changing applications, and radiometric measurement accuracies. CAM1 was further investigated to determine environmental conditions that impact temperature measurement.

2.3.1 Determining Physical Properties of TIR Camera

Cameras have physical parts and capabilities that influence their sensitivity to temperature differences, increase their measurement error, and limit their use in agricultural environments. Due to their relatively low cost compared to cooled thermal cameras, minimal size and weight, and no

moving parts, uncooled TIR cameras provide increased coverage area and crop stress assessments aboard different sensing platforms not possible with cooled TIR cameras and IRTs. The identified physical properties that restrict practical use of TIR cameras include:

1. Lens selection and distortion
2. Image resolution and measurement
3. Radiometric characterization and measurement accuracy
4. Warm-up time and automatic recalibration
5. Connection ease, software, and controllability

Considering these physical properties and their influence on accurate measurement may allow for their influence to be reduced or eliminated with proper camera configuration, hardware, standard operating protocol, and sensing platform. Therefore, intrinsic fundamentals of uncooled TIR cameras were investigated using the methods discussed in the following sections.

2.3.1.1 Lens Selection and Distortion

Lens selection was investigated because specific target size and sensing distance determines the lens and resulting image size for a specific application. TIR cameras have germanium lenses that are factory-installed and calibrated, consequently increasing the cost of additional lenses and requiring expensive equipment for recalibration. Due to the small lens focal length, both TIR camera lens distortions were investigated in order to correct lens distortion for spatial integrity. A distorted image does not fully represent real spatial points but a distorted location dependent on the position within the lens' field of view (FOV) (x_1, y_2) , as defined by Equations 2.1 and 2.2 (The Mathworks, Inc., 2015):

$$x_2 = x_1(1 + k_1r^2 + k_2r^4) + 2p_1x_1y_1 + p_2(r^2 + 2x_1^2) \quad (2.1)$$

$$y_2 = y_1(1 + k_1r^2 + k_2r^4) + 2p_2x_1y_1 + p_1(r^2 + 2y_1^2) \quad (2.2)$$

Where:

x_1, y_1 = distorted pixel locations

x_2, y_2 = undistorted pixel locations

k_1, k_2 = radial distortion coefficients of the lens

p_1, p_2 = tangential distortion coefficients of the lens

$$r = \sqrt{x_1^2 + y_1^2}$$

CAM1 features an 11 mm, medium angle lens with a 27°×20° degree angle FOV and CAM2 features a 7.5 mm, wide angle lens with a 63°×50° degree angle FOV. Using a distortion model (grid) calibration approach (Sun, et al., 2013), each TIR camera lens distortion was

corrected based on multiple calibration grid images using a heated grid pattern tool, as shown in Figure 2.2.

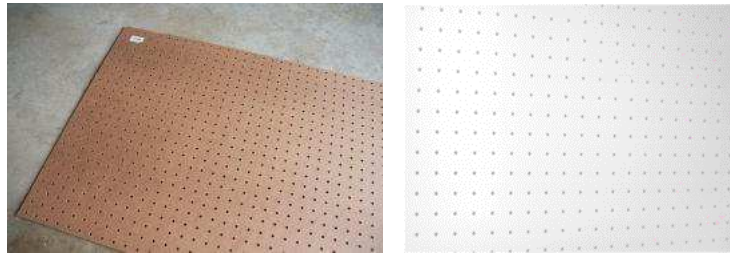


Figure 2.2. Grid pattern tool (left) and thermal image (right) used for lens distortion

A wooden pegboard was warmed and placed on a cool flat surface to produce a distinguishable temperature difference (Figure 2.2). The grid distortion model required at least five images from different orientations in order to calibrate radial and tangential distortion coefficients. Thermal images were imported into the NI LabVIEW™ Vision Assistant (National Instruments Corporation, Austin, Texas) for lens distortion analysis.

2.3.1.2 Image Resolution and Measurement

Since TIR cameras typically have lower resolution image sensors than visible cameras, the target size and sensing distance is more critical when determining the lens focal length (distance from the lens to the thermal detector) and resulting FOV degree angle. Critical pixel resolution was investigated by using a known target size and determining the necessary number of incident pixels in order to limit inaccuracies. A target measuring 16 mm in diameter was heated and placed on a flat surface at a stable temperature for TIR camera visibility (Figure 2.3).

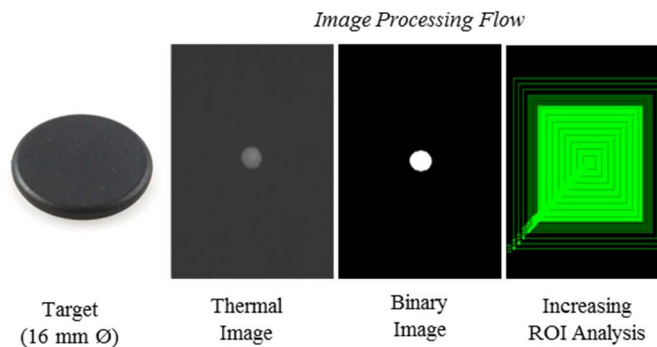


Figure 2.3. Investigation of necessary spatial resolution for temperature accuracy

As shown in Figure 2.3, the thermal image was altered into a binary image (i.e., white=1 | black=0) in order to maximize the contrast between the accurate and inaccurate measured value of 1 and 0, respectively. As the last image processing step, a series of increasing regions of interest

(ROI) were designated by increasing the offset pixel resolution by 1 pixel (i.e., 1×1, 3×3, 5×5, 7×7, ..., 333×333 pixel resolution) centered directly over the target. Increasing the spatial resolution by 1 pixel (or 0.33 mm/pixel) around the outer perimeter for each subsequent ROI allowed the average DV to be calculated with the LabVIEW™ Vision Assistant™.

2.3.1.3 Radiometric Characterization and Measurement Accuracy

Uncooled TIR cameras measure LWIR energy intensity present on the image sensor, thereby generating a thermal image of radiated surface temperatures. CAM1 is sensitive to 8 to 14 μm LWIR, or a theoretical temperature span from -66°C to 90°C (~Δ156°C), while CAM2 is sensitive to 7 to 14 μm LWIR, or a theoretical temperature span from -66°C to 140°C (~Δ206°C). However, the uncooled TIR camera cores only measure relative temperature values, leaving temperature measurements unquantified. Therefore, a calibration method was developed to characterize pixel intensity-to-actual temperature using reference temperature panels viewable within a camera's FOV in order to create a radiometric calibration transfer function. A near-perfect blackbody enclosure, hereafter termed as "BB enclosure", was built from wood and painted flat black to isolate the camera and target surfaces from outside influences while investigating this radiometric calibration method (Figure 2.4).

Three reference surfaces were used to provide temperature differentials necessary for the radiometric calibration (Figure 2.4 c). An isolated 0.10×0.10 m piece of 8 mm thick wood, painted flat black, was used as a box reference that fluctuated with ambient air temperature. A 0.30×0.60 m piece of 1.52 mm thick (14 gauge) aluminum sheet metal was fabricated for use as the heated target surface. An electric heating element in the BB enclosure was capable of heating the aluminum panel up to 65°C at a manual or automatic rate determined by the BB enclosure heating element and air exchange vent controller, as shown in Figure 2.5. The third reference panel is identified as the wet reference. To make the wet reference, a highly evaporative cloth (Chilly Padd, Arab, Alabama) was placed around a solid wooden dowel and placed in a bottle of water for continuous wicking and evaporation, thereby creating a stable, cool reference temperature.

For apparent temperature correction, a commercial IRT (Fluke 62 MAX, Fluke Corporation, Everett, Washington) with a measurement accuracy of ±1°C and an adjustable emissivity correction from 0.1 to 1 was used to determine the emissivity of the reference targets. To determine emissivity, surface temperatures measured with the IRT were corrected to match actual surface temperatures measured with the thermistors. Emissivities of 0.82, 0.88, and 0.96

were found for the flat-black painted wooden box and aluminum panel and wet reference, respectively.

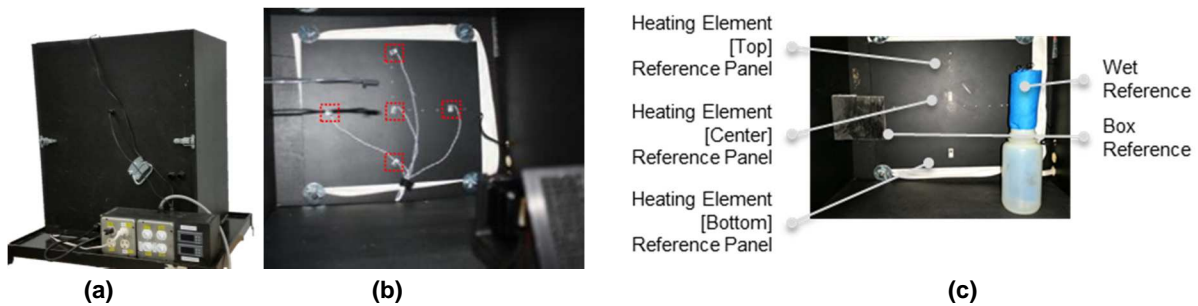


Figure 2.4. (a) BB enclosure constructed to limit outside influence. (b) Surface mount thermistors measured actual target surface temperatures within an ROI (shown in red) to characterize pixel intensities. (c) Heating element, box reference equal to air temperature and a cool, wet reference.

In addition to controlling the heating element, the BB enclosure regulates air exchange within the chamber until set air conditions are automatically or manually reached by using the vent controller (Figure 2.5). This function is directly used to determine the environmental influence as described in Section 2.3.2, below.

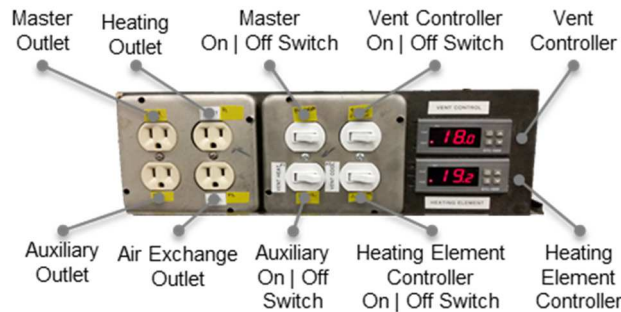


Figure 2.5. BB enclosure heating element and air exchange vent controller user interface.

Actual surface temperatures were measured with five surface-mounted thermistors (ON-930-44033, OMEGA, Stamford, Connecticut) with a measurement accuracy of $\pm 0.1^{\circ}\text{C}$ (See Appendix A, Figure A.4 for more details). In addition, a surface-mount thermistor was attached to the camera housing, shown in Figure 2.6, to monitor operating camera housing temperatures during TIR camera evaluations.



Figure 2.6. Thermistor mounted to camera housing temperature for subsequent testing

Thermistors were wired into a voltage divider to sense the change in voltage due to the temperature-based resistance (Figure 2.7 a). The resulting voltage (V_{out}) was used to determine temperature using a calibration curve provided by the manufacturer (Figure 2.7 b).

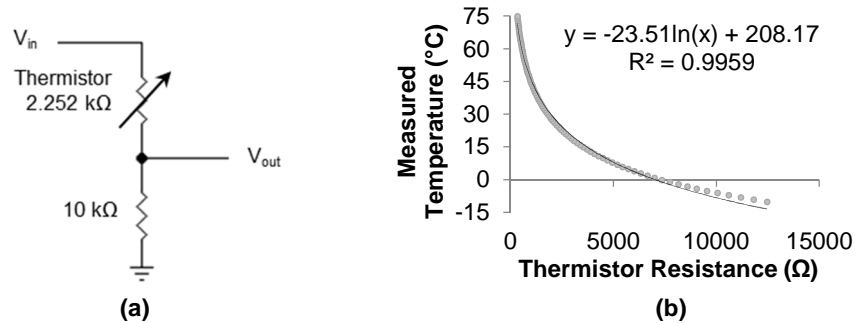


Figure 2.7. (a) Voltage divider wiring diagram used to measure changing voltage from the corresponding change in the thermistor resistance. (b) Thermistor calibration curve used to quantify temperature with a change in voltage. (See Appendix A, Figure A.4 for more details)

Relative humidity and air temperature within the BB enclosure were measured with a combination sensor (Omega Engineering Inc., Stamford, Connecticut) with an accuracy of $\pm 3\%$ and $\pm 0.2^{\circ}\text{C}$, respectively. A data acquisition system was built using a NI myRIO (National Instruments Corporation, Austin, Texas) to monitor the surface mount thermistors, air temperature, and relative humidity inputs from sensors within the BB enclosure (Figure 2.8).

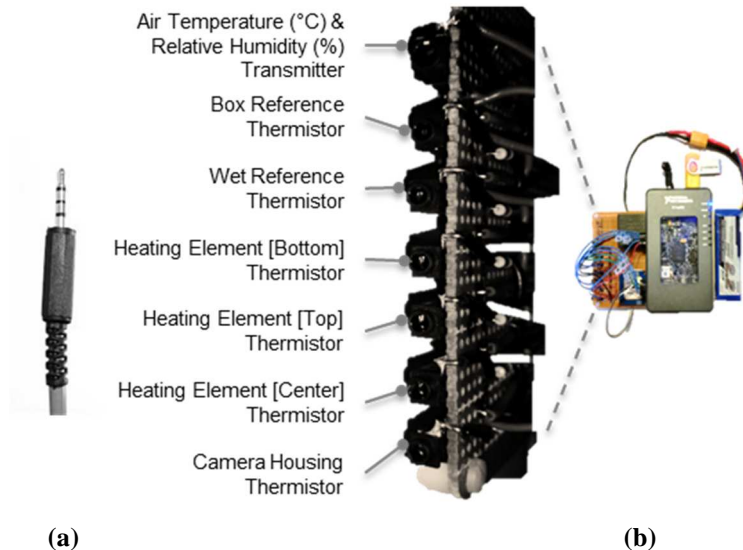


Figure 2.8. (b) Data acquisition (DAQ) system used to monitor BB enclosure sensors with (a) stereo plug connectors.

A TIR Camera Evaluation Software program (Figure 2.9) was developed using NI LabVIEWTM (National Instruments Corporation, Austin, Texas) to acquire real-time image data, camera housing temperature, actual reference surface temperatures, air temperature, and relative

humidity while controlling test length and file specifications (Figure 2.10). Raw data was monitored at a sampling frequency of 9 Hz to match the frame rate of the TIR camera cores.

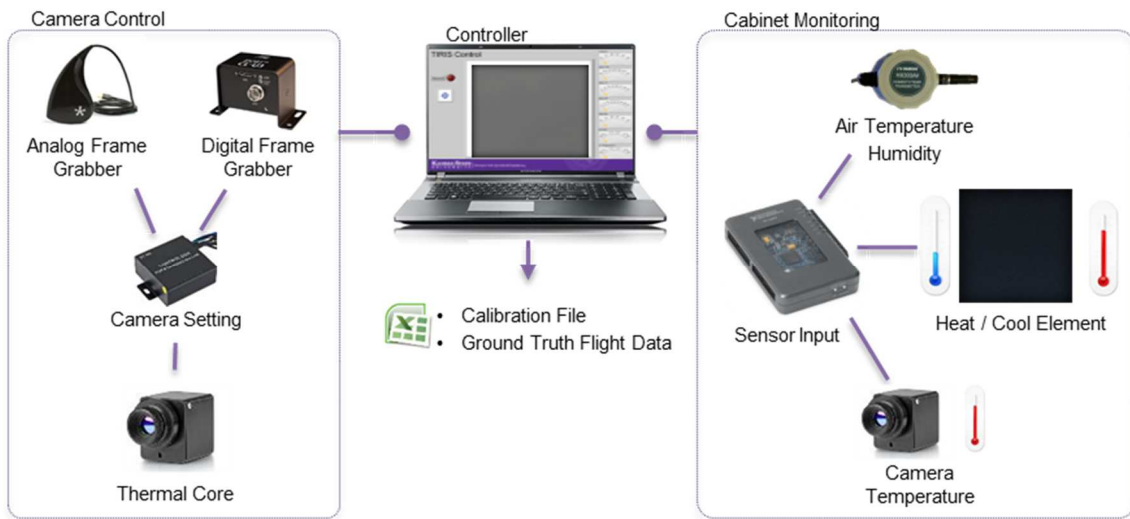


Figure 2.9. TIR Camera Evaluation system diagram used to control cameras, monitor BB enclosure conditions, and output test data.

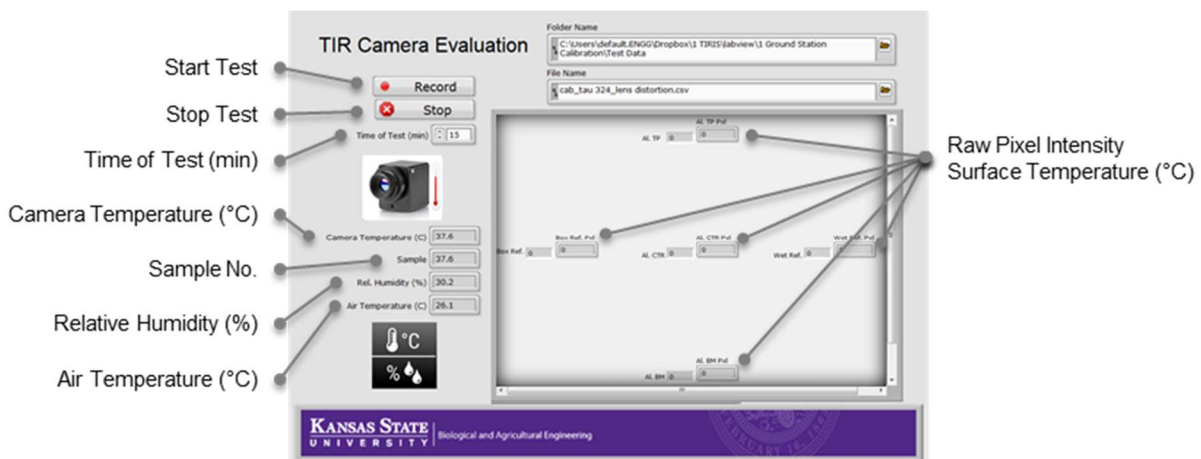


Figure 2.10. TIR Camera Evaluation Software VI used to conduct radiometric calibrations while recording raw data. (See Appendix A, Figure A.7 for more details)

The TIR Camera Evaluation Software program averaged multiple image pixels within static ROIs within the TIR camera FOV to correlate pixel intensity-to-actual surface temperature (Figure 2.10, above). Raw pixel intensities (X_1, X_2) were combined with actual surface temperature (Y_1, Y_2) to determine the radiometric transfer function slope, as defined by Equation 2.3:

$$m = \frac{Y_2 - Y_1}{X_2 - X_1} \quad (2.3)$$

By using the slope found in Equation 2.3 and a raw pixel and coinciding surface temperature (X_1, Y_1), the y-intercept of the radiometric transfer function was determined using Equation 2.4:

$$Y - Y_1 = m(X - X_1) \quad (2.4)$$

When a radiometric transfer function was found, each digital image pixel was converted to a temperature value defined by Equation 2.5:

$$T_{(i,j)} = T_{min} + \frac{I(i,j)}{2^N - 1} T_{span} \quad (2.5)$$

where:

- $T_{(i,j)}$ = Pixel temperature ($^{\circ}\text{C}$) at row i and column j ,
- T_{min} = Lowest temperature within the image ($^{\circ}\text{C}$),
- $I_{(i,j)}$ = Pixel intensity at row I and column j ,
- N = Number of bits for pixel intensity (e.g., $N=8$ for 8-bit images), and
- T_{span} = Span of temperature captured in the image.

The radiometric calibration method developed above was segmented into two methods in order to compare temperature measurement accuracies. The first method was referred to as the real-time (RT) radiometric calibration, in which RT image pixels are correlated to RT surface temperatures defined with Equations 2.3, 2.4, and 2.5. Similarly, the second method was termed the one-time (OT) radiometric calibration that utilized one calibration image to determine the radiometric transfer function. The RT radiometric calibration method was developed to test the measurement accuracy of the uncooled TIR cameras where reference temperature panels are consistently viewable within the camera FOV like a fixed platform. On the other hand, the OT radiometric calibration method was developed to test the measurement accuracy of the uncooled TIR camera when reference panels cannot be continuously viewed for practical reasons such as a dynamic sensing platform.

2.3.1.4 Warm-up Time and Automatic Recalibration

Uncooled TIR cameras account for microbolometer temperature fluctuations without heavy cooling systems with automatic recalibration. A shutter recalibration technique is activated to conduct a non-uniformity correction (NUC) across the thermal detector at either a user-defined time interval and/or in the event of an internal temperature change of the thermal detector (DRS Technologies, Network and Imaging Systems Group, n.d.). During a NUC, the camera shutter closes to block incoming thermal energy, thereby providing a uniform thermal reference for the

detector. At that time, a recalibration algorithm ensures a uniform pixel intensity is measured across the entire microbolometer. Once powered on, an uncooled TIR camera begins to reach a steady state operating temperature as a result of internal circuitry temperature and ambient air conditions.

To determine the amount of time needed to reach the steady state operating temperature from ambient conditions, the TIR cameras were operated in the BB enclosure with steady target temperature for 45 minutes while the video pixel intensities, target surface temperatures, camera housing temperature, and ambient air conditions were monitored. The resulting warm-up time was determined when the measured pixel intensity was within 5% of the stable target pixel intensity.

Because automatic NUC is recommended during regular operation, additional tests were conducted to investigate the influence on temperature measurement accuracy from a 1 min, 5 min, and no NUC. Each test was run for 60 minutes because typical thermography applications occur in a short time span in order to limit time between samples (Maes & Steppe, 2012). Images for these tests were monitored using the DAQ system described above in Section 2.3.1.3 to determine the temperature measurement accuracy under the specific scenarios listed in Table 2.1.

Table 2.1. Non-uniformity correction influence on measurement accuracy ($\pm^{\circ}\text{C}$) with OT and RT radiometric correction

Video Output	Correction Time		
	No Correction (Sensing Time)	5-minute NUC (Sensing Time)	1-minute NUC (Sensing Time)
Analog	60 minutes	60 minutes	60 minutes
Analog	30 minutes	-	-
Analog	15 minutes	-	-
Digital	60 minutes	60 minutes	60 minutes
Digital	30 minutes	-	-
Digital	15 minutes	-	-

2.3.1.5 Connection Ease, Software, and Controllability

The TIR camera cores provide analog and digital video outputs. Analog output provides an 8-bit (256 discrete pixel intensity DV) thermal video, whereas digital output is 8-bit or 14-bit (256 or 16,384 discrete pixel intensity DV) video. These two modes of video output were investigated in regards to measurement accuracy, temperature resolution (i.e., smallest measurable temperature difference), and ease of image capture regarding necessary hardware and software functionality. Each TIR camera control software’s graphical user interface (GUI) configured the camera for video output and frame rate, user-defined NUC, and thermal detector sensitivity. Although both camera control softwares have distinguishing features, they are not discussed in

detail. However, both softwares adjust the thermal detector gain sensitivity (i.e., detectable scene temperature span) and level control (i.e., shift offset of the center temperature within the temperature span), thereby adjusting the slope (m) and level offset (b), respectively, defining a $y=(m)x+(b)$ format (Figure 2.11). More specifically, the thermal detector gain sensitivity adjusts the upper and lower pixel saturation and temperature measurement resolution, thereby improving the visibility of desired scene temperatures. For example, a temperature span of 20°C is set by the camera gain control whereas a center temperature of 25°C is controlled by the level control. In this example, the lower and upper saturation temperatures would be at 15°C and 35°C , respectively. In addition, the temperature resolution of the resulting 8-bit image of a 20°C span would equal 0.08°C , as defined by Equation 2.6:

$$T_{\text{resolution}} (^{\circ}\text{C}) = \frac{T_{\text{span}} (^{\circ}\text{C})}{2^n} \quad (2.6)$$

where:

T_{span} =Span of temperatures ($^{\circ}\text{C}$) measurable by the thermal detector

N =bits of resolution (e.g., $N=8$ for 8-bit images), and

$T_{\text{resolution}}$ =theoretical temperature resolution

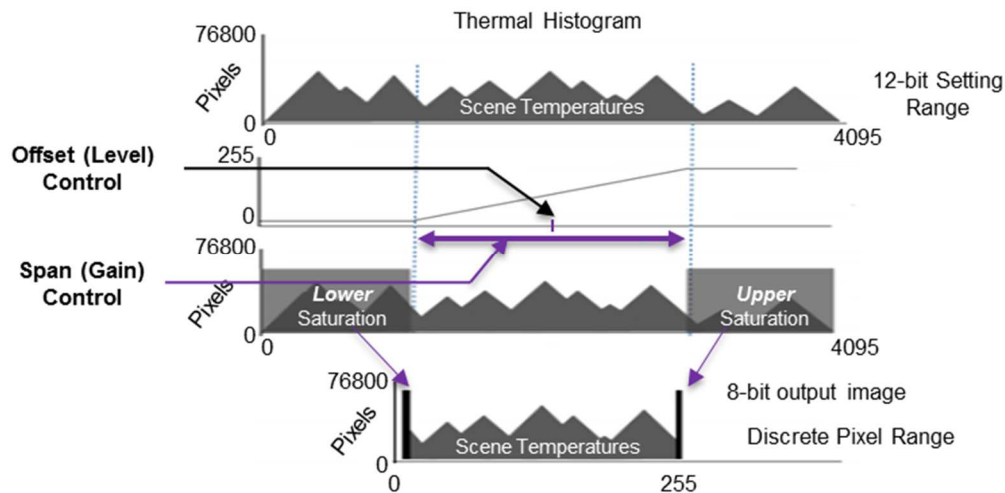


Figure 2.11. Camera settings from level and gain control for a thermal detector. The gain control adjusts the thermal detector sensitivity to LWIR energy thereby adjusting the temperature span. Level control adjusts the center offset temperature to adjust the offset of the temperature span. Adapted from DRS Tamarisk® 320 Camera Control Software User Guide (2013).

A DRS breakout board module (Breakout Box 1003785-001, DRS Technologies, Inc., Dallas, Texas) controlled CAM1 by adjusting the gain and level for the span and center temperature offset. Similarly, CAM2 was controlled via the FLIR® VNC module (FLIR® Systems, Inc., Boston, Massachusetts) (Figure 2.12).

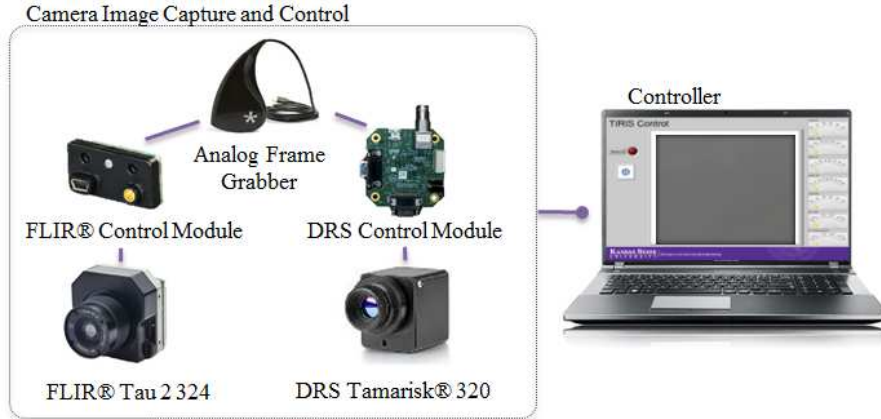


Figure 2.12. Hardware used to control, capture, and process thermal images from the TIR camera cores

Analog video from both uncooled TIR cameras was streamed at 9 Hz into an analog-to-digital video converter (Dazzle DVD Recorder HD, Corel Corporation, USA) (Figure 2.12). This raw analog video signal was streamed into a host computer using LabVIEW™ (National Instruments Corporation, Austin, Texas) image acquisition and processing software that captured, processed, and stored each video frame using a developed virtual interface (VI).

In order to reduce signal loss and noise introduced with analog video signal transmission, digital video feed from CAM1 was captured with an external digital frame grabber (iPORT CL-U3, Pleora Technologies, Ontario, Canada). The frame grabber acquired digital images directly from the TIR camera, as shown in Figure 2.13.

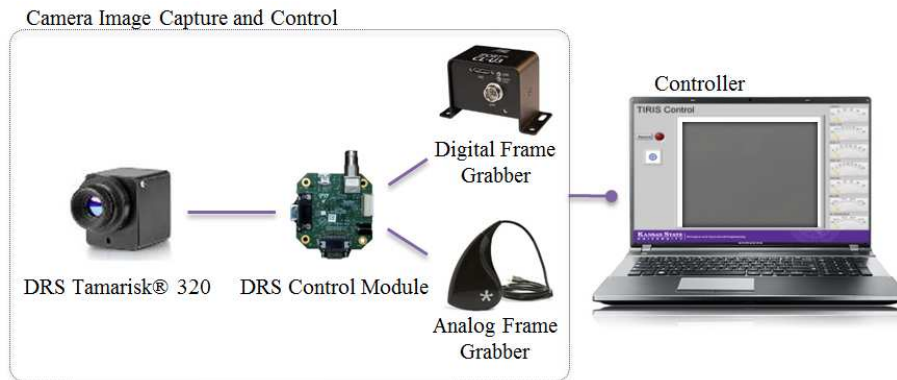


Figure 2.13. Hardware to capture digital and analog video outputs

Controllability was studied using digital video feed from CAM1 in order to investigate added functionality (i.e., measurement accuracy, temperature span and resolution) of the digital output configuration. CAM1 was used because the DRS breakout board supported digital video feed while CAM2 required additional breakout boards beyond the FLIR® VNC module.

Using the developed RT and OT radiometric calibration methods described above, the resulting temperature span and offset temperature increment were investigated for each gain and level control setting. In order to determine the temperature span, the aluminum reference target was chilled to 0°C and attached to the heating element held at 65°C. Through convective heat transfer, the aluminum reference target rose from 0°C to 65°C in under 10 minutes. This rise in temperatures were used to determine the thermal detector sensitivity of each TIR camera core under a discrete range of low to high gain settings. In order to determine the level control characteristics, RT pixel intensity of a stable reference temperature was recorded as the camera level control was adjusted from lower to upper pixel saturation for each respective gain setting. With a stable target temperature, the change in the pixel intensity value for each level offset increment was used to characterize the controllability and determine the temperature difference for each level control increment.

2.3.2 Environmental Influence on Measurement Accuracy and Repeatability

In addition to controlling the heating element, the BB enclosure regulates air exchange within the chamber to pull air from outside the cabinet until equilibrium is automatically or manually reached (Figure 2.14 b). The BB enclosure was operated within an environmental growth chamber (EGC15, Chagrin, Ohio) in order to investigate the repeatability of the TIR camera under changing environmental conditions (i.e., air temperature and relative humidity) typical in agricultural studies (Figure 2.14).

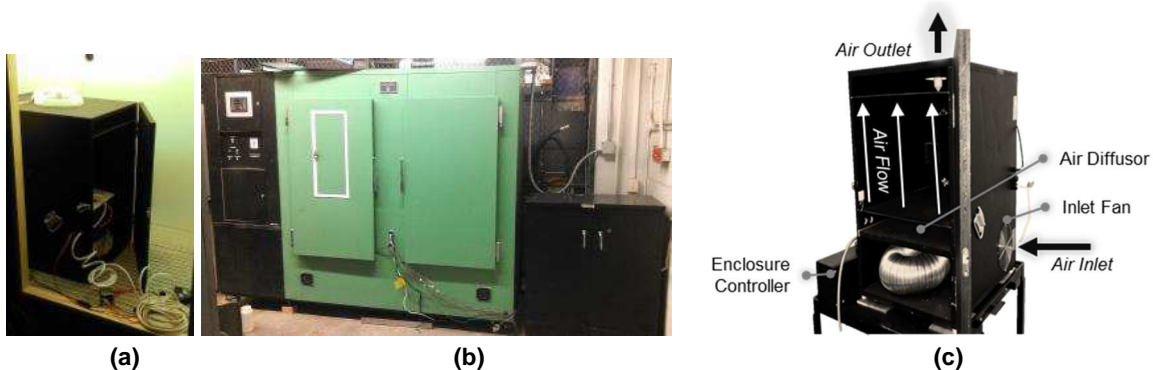


Figure 2.14. (a) BB enclosure installed in the (b) environmental chamber for strictly controlled environmental conditions. (c) Air exchange through the BB enclosure controls internal air parameters

Strict laboratory tests regulated air temperature and relative humidity, providing an evaluation of the measurement accuracy under diverse laboratory conditions (i.e., 15-45°C \pm 0.3°C, and 25-75%RH \pm 2.5%). The BB enclosure pulled outside air from the environmental chamber

until the set air condition parameters were reached (Figure 2.14). Eight air temperature namely 10, 15, 20, 25, 30, 35, 40, and 45°C were selected. For each test, the desired air temperature was set while humidity was set at 25% relative humidity. When the specific air conditions were achieved within the BB enclosure, an OT radiometric calibration was performed as the relative humidity on the environmental chamber was set to change from 25% to 75% which occurred over a period of 10 minutes. The change in relative humidity was induced to observe radiant heat attenuation due to increased water vapor between the target and the TIR camera (Monteith & Unsworth, 2013). Environmental attenuation would be consistent between the two camera cores; therefore, only CAM1 was testing in the environmental chamber. An OT radiometric calibration was used because RT radiometric calibration was developed to compensate for changes in ambient conditions.

2.4 RESULTS AND DISCUSSION

2.4.1 Lens Selection and Distortion

The medium angle lens of CAM1 has less visible distortion than the wide angle lens of CAM2 (Figure 2.15). The wide angle lens (7.5 mm) and medium angle lens (11mm) distortion was 30% and 19%, respectively. However, both distortions were corrected with the resulting lens correction coefficients shown in Table 2.2. The distortion comparison is not meant to distinguish differences between TIR camera cores, but the difference between medium to wide angle lens focal length and resulting lens FOV degree angle. Distortion coefficients of both camera lenses had to be determined because they were not provided by the TIR camera manufacturer. The results reveal a significant distortion occurs within the germanium lens of each TIR camera core. This will have practical implications where spatial accuracy is critical especially in whole-field temperature mapping and site-specific crop health monitoring. In application, batch image processing would use the resulting lens distortion coefficients within an algorithm in order to undistort images for spatial accuracy for actual location using Equation 2.1 and 2.2, above. In addition, since each TIR camera and lens are factory calibrated, a TIR camera and lens combination may have subtle variations in distortion characteristics. As a result, identical camera-lens configurations may not be interchangeable; therefore, each individual TIR camera may need to be calibrated in order to determine specific lens distortion coefficients.

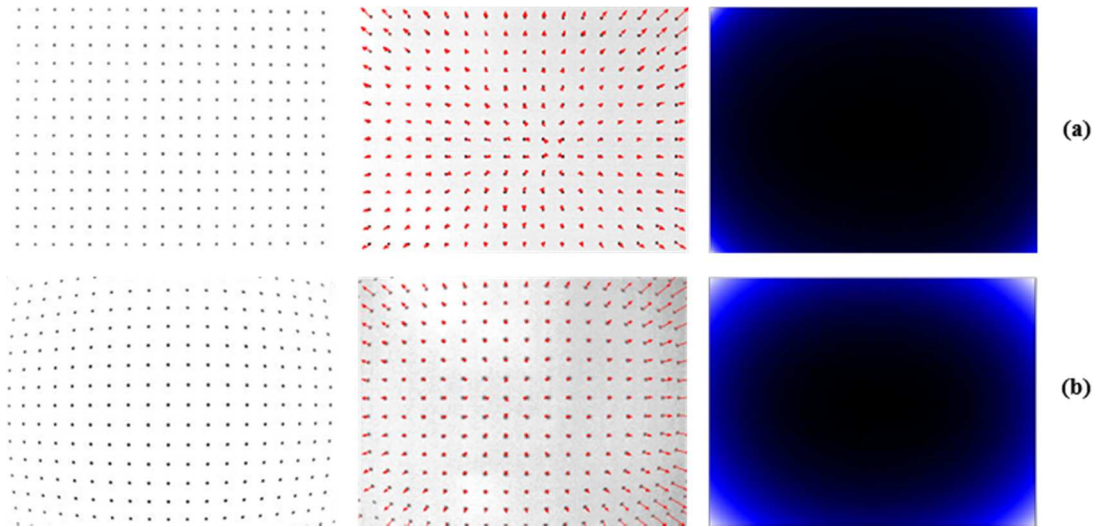


Figure 2.15. (a) CAM1 with 11 mm and (b) CAM2 with 7.5 mm lens distortion results from the point distortion (grid) model with grid pattern with known point distances (left) point vector map (middle), and visual distortion map (right)

Table 2.2 Lens distortion results including radial and tangential correction coefficients. (See Appendix A, Figure A.8 and A.9 for more details)

TIR Camera Core	% Distortion	Radial		Tangential	
		k_1	k_2	p_1	p_2
CAM1 11 mm lens	19.1	-0.24992	-0.74306	-0.000177	0.002740
CAM2 7.5 mm lens	30.4	-0.43814	0.20181	0.001486	-0.000493

2.4.2 Image Resolution and Measurement

The increasing pixel-by-pixel-resolution ROI analysis provided necessary spatial resolution to limit false measurements. As shown in Figure 2.16 a, a 9 mm/pixel spatial resolution was necessary to measure 100% of the DV of the target when the ROI was directly centered on the target normal to the camera. In actual in-field applications, however, a target will seldom be normal to the camera and aligned to the fixed pixel array. Consequently, target orientation and location variation will inherently cause pixels to measure a mixture of background/target temperature (Figure 2.16 b).

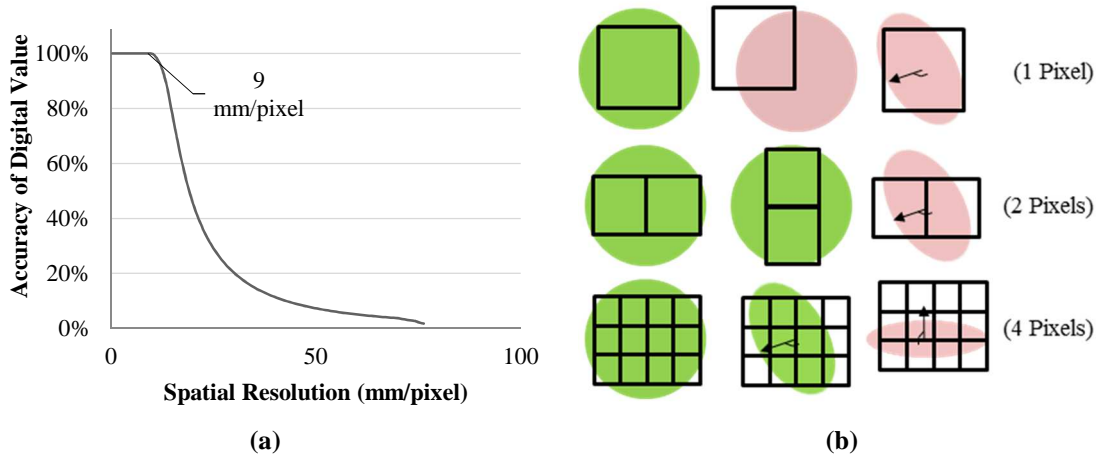


Figure 2.16. (a) Spatial resolution versus the digital value accuracy. (b) Generalized pixel orientations and spatial resolutions of 1 pixel, 2 pixel, and 4 pixels incident on a target. Black boxes represent the individual pixel's FOV. Green objects represent an object that can be accurately measured with the pixel orientation and spatial resolution. Pink objects represent an object that is measured with error.

The first response would be to increase the number of pixels incident on a target by positioning the camera closer. However, this reduces the overall image coverage area and requires a larger volume of images in order to cover the desired ground area at the specific level of detail. For example, 4 pixels on a target, as shown Figure 2.16 b, better capture a representative value but cannot entirely reduce the inaccuracy from extreme target orientation and shape irregularity (Figure 2.16 b). At the same time, 4 pixels versus 2 pixels present on a target reduces the overall image coverage area by 75% and requires 4 times the images in order to cover the same surface area. As a result, a tradeoff exists between the coverage area and level of measurable detail possible from a sensing platform. This will be especially important in the case of uncooled TIR camera when the image resolution (i.e., number of pixels in the fixed pixel array) are small compared to typical visible camera image resolutions. This relationship is critical when matching the camera's fixed pixel resolution and lens combination to the necessary spatial resolution because of the volume of data generated in order to achieve the desired application ground coverage and specific level of detail.

2.4.3 Warm-up Time

The warm-up time for each camera was determined as shown Figure 2.17. Results show warm-up times of 19 min and 7 min were necessary for CAM1 and CAM2, respectively, in order to reach within 5% of the stable pixel intensity measurement. Timely fluctuations in the first minutes are due to NUC triggered by the change in the thermal detector temperature and/or after the user-defined timed interval of 1 min. During the warmup period, multiple NUC were activated

from a temperature change of the microbolometer as shown by the drastic change in measured pixel intensity during the first 5 minutes. Once the camera housing temperature began to level off, less erratic pixel intensities were observed past 5 minutes which may suggest NUC is activated from the timed interval of 1 min rather than the temperature change.

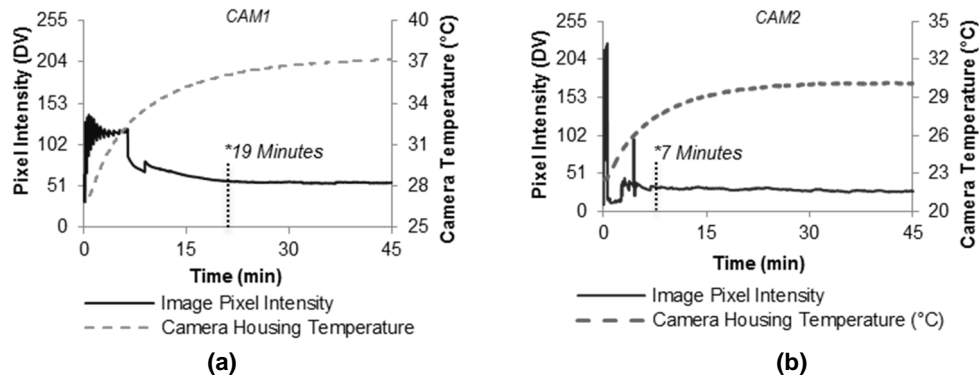


Figure 2.17. Raw image intensity and housing temperature versus camera ‘on-time’ of (a) CAM1 and (b) CAM2. The dotted vertical line indicates the time when measured pixel intensity was within 5% of the stable pixel intensity.

Prior to the designated warm-up period, inaccuracy exists as the camera reached a stable operating temperature. Camera warm-up time will have implications on how quickly a system can be deployed and is important when considering a standard operating protocol. Furthermore, warm-up time is dependent on the storage temperature prior to operation. In the scenario producing the results shown in Figure 2.17, the cameras were equal to ambient temperature prior to operation. As a result, warm-up time is dependent on ambient conditions; therefore, allowing TIR cameras to operate beyond the warm-up time will ensure the camera reach a stable operating temperature to limit inaccurate measurements. In application, starting the camera may be the first step in a standard operating procedure when taking data.

2.4.4 Radiometric Characterization and Measurement Accuracy

The developed radiometric calibration methods yielded radiometric curves demonstrated in Figure 2.18. Linear regression analysis showed significant correlation between actual surface temperature and image pixel intensity ($R^2 = .99$) for both TIR camera cores. The resulting linear transfer functions would be directly used to convert image pixel intensities into surface temperature measurements for each camera. Between the two TIR camera cores, the sensitivity to incoming LWIR is comparable. This sensitivity demonstrates uncooled thermal cameras’ ability to measure absolute temperatures with additional hardware and software, standard operating protocol for radiometric calibration, and strict camera configurations.

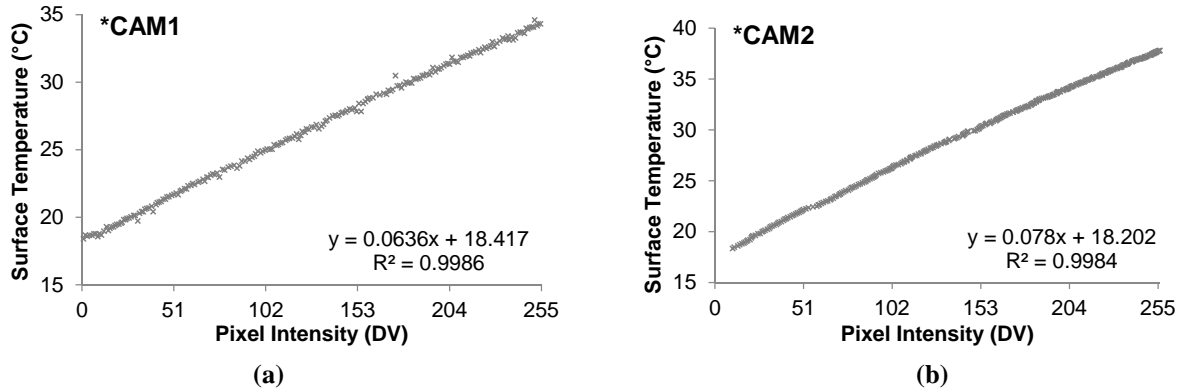


Figure 2.18. Radiometric calibration performed on the CAM1 (a) and CAM2 (b) at 25°C air temperature and 35% relative humidity after reaching a steady operating temperature.

Because the OT and the RT radiometric calibration methods were developed for different applications, a comparison in Figure 2.19 shows the measurement accuracy of the two calibration methods. The absolute difference between the actual and measured temperature showed the measurement accuracy was $\pm 0.38^{\circ}\text{C}$ or 0.62°C ($\alpha=0.05$) with RT and OT radiometric calibration, respectively. RT radiometric calibration had a higher measurement accuracy because of the fixed reference panels within the FOV for RT calibration, whereas the same OT radiometric calibration was used throughout the sensing period. As a result, the OT calibration has a diminishing measurement accuracy as the camera continuously conducts a NUC generating slight pixel-to-pixel variation caused by the correction algorithm.

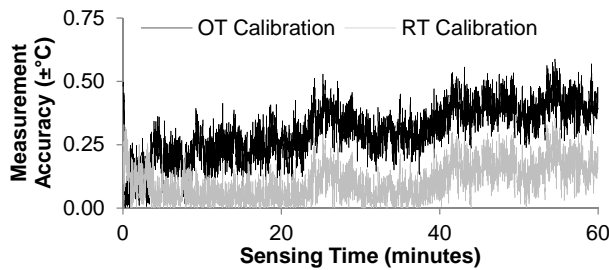


Figure 2.19. CAM1 measurement accuracy ($\pm^{\circ}\text{C}$) of OT and RT radiometric calibration process over 1 h. The absolute difference between the actual and measured temperature is shown. CAM1 operated at a stable temperature prior to comparison.

In applications needing a high accuracy with a fixed sensing platform, the RT radiometric calibration would be most applicable. On the other hand, the OT radiometric calibration would be better suited for dynamic sensing platforms in field studies. Most importantly, when considering a TIR camera core and complementary hardware and software, choosing relative versus absolute temperature measurements may reduce the necessary hardware and software, but limit quantifiable temperature measurements. For consistency, the sensing distance was held constant throughout all

tests. However, in typical field applications, larger sensing distances beyond that of the BB enclosure may influence the measurement accuracy. As a result, future studies should be conducted that test multiple sensing distances to validate the developed radiometric calibration methods.

2.4.5 Automatic Recalibration

Because NUC recalibrates the thermal sensor, measurement accuracy with and without NUC is summarized in Table 2.3.

Table 2.3. Measurement accuracy ($\pm^\circ\text{C}$) with OT and RT radiometric correction. (Accuracies shown represent an 95% confidence interval)

	Video Output	NUC Timed Interval	OT Calibration			RT Calibration		
			15 min	30 min	60 min	15 min	30 min	60 min
CAM2	Analog	1 min	-	-	0.87	-	-	0.63
		5 min	-	-	1.00	-	-	0.72
		^[a] W/O	0.67	0.80	0.92	0.47	0.53	0.74
CAM1	Analog	1 min	-	-	0.82	-	-	0.62
		5 min	-	-	1.15	-	-	0.65
		^[a] W/O	0.60	0.73	0.87	0.38	0.49	0.62
	Digital	1 min	-	-	0.43	-	-	0.29
		5 min	-	-	0.95	-	-	0.54
		^[a] W/O	0.30	0.35	0.64	0.29	0.30	0.35

^[a]Subject to thermal detector sensor drift from internal and external temperature inaccuracy. Not recommended from TIR camera manufacturer

Under operation with and without NUC, measurement accuracy decreased with increased sensing time which is most likely attributed to the slight pixel variation of the NUC. Results showed that a camera configured for a NUC at a user-defined time interval of 1 min yielded the highest measurement accuracy for both analog and digital video systems (Table 2.3). However, a RT calibration for a sensing time of 60 min with a 1 min NUC provided similar measurement accuracy as with no NUC with CAM1, thereby suggesting the use of no NUC. However, the strict environmental conditions that produced these results are impractical in agricultural applications. In addition, TIR camera manufacturers do not recommend camera operation without NUC due to potential temperature drift previously discussed in 2.4.3. Throughout tests, maximum sensing time used to evaluate the two TIR camera cores was set at 60 minutes. Extended sensing times may need to be investigated for high temporal studies and performance under constant operation.

2.4.6 Connection Ease, Software, and Controllability

Required evaluation hardware for analog video capture was enabled with off-the-shelf (OTS) equipment with camera control software from TIR manufacturers for full evaluation of camera controls and features. As observed, manual control of the thermal detector through the

camera control software with radiometric calibrations revealed the characteristic linear transfer functions of gain and level controls, as shown in Figure 2.20 and Figure 2.21. This knowledge is important in order to set the cameras for a particular temperature span and offset the center temperature. As observed, a configured temperature span has a direct influence on the discrete temperature resolution measurable from the thermal detector. As a result, the ability to set a specific temperature span could result in the ability in order to better assess discrete spatial crop temperature differences.

For application in crop sensing, a minimum temperature resolution of 0.5°C is suggested to measure the subtle temperature differences for crop health assessment (Sepulcre-Canto, et al., 2007). As a result, a limitation of the 8-bit image data is the coarse temperature resolution with large temperature spans. As shown in Table 2.4, the minimum temperature resolution suggested by Sepulcre-Canto et al. (2007) of 0.5°C would result in a temperature span close to 120°C . In order to cover twice the suggested temperature resolution, a minimum temperature resolution of 0.25°C was chosen to determine the maximum temperature span (60°C) in Figures 2.20 and 2.21 by rearranging Equation 2.6.

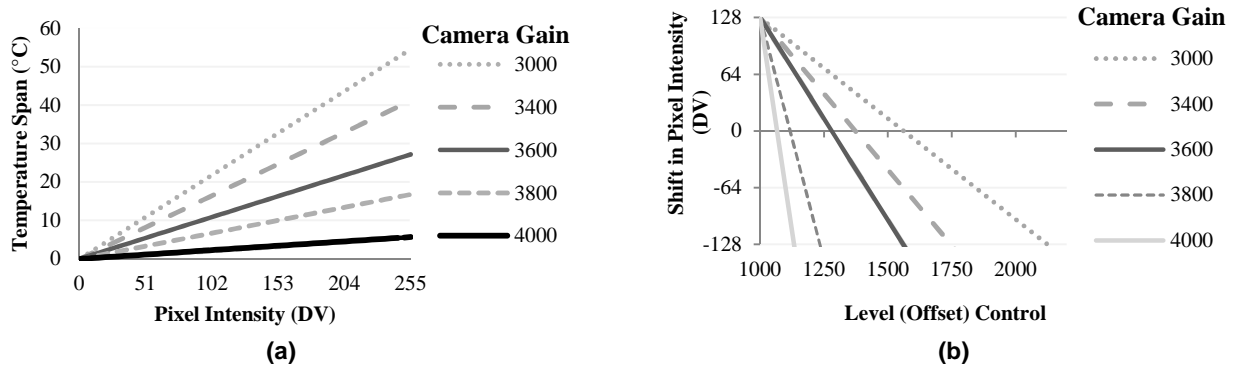


Figure 2.20. CAM1 camera (a) gain for temperature span and (b) level setting characteristics for offset temperature bias.

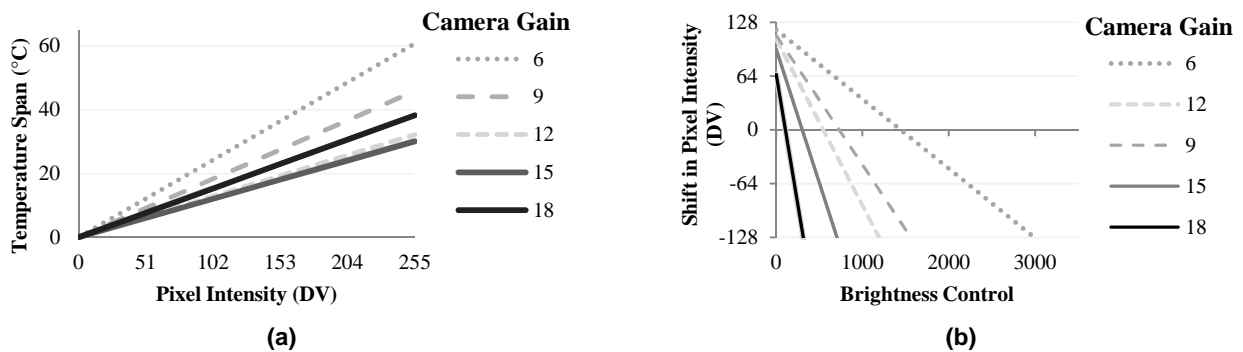


Figure 2.21. CAM2 camera (a) gain for temperature span and (b) level setting characteristics for offset temperature bias.

With Equation 2.6, Table 2.4 demonstrates theoretical temperature resolution of selected temperature spans of the analog and digital output. By using Equation 2.6, digital output from CAM1 resulted in a fixed temperature span of 156°C with a fixed 0.01°C temperature resolution. Similarly, analog output from CAM1 resulted in a configurable temperature span from 5°C to 156°C and resolution from 0.02°C to 0.61°C. Analog output from CAM2 yielded a controllable temperature span of 18°C to 206°C and resolution of 0.07°C to 0.80°C.

Table 2.4. Temperature resolution (°C) of specific temperature span

Video Type (bits)	Span (°C)							
	^[a] 200	150	100	50	40	30	20	10
Analog (256)	0.78	0.59	0.39	0.20	0.16	0.12	0.08	0.04
Digital (16,384)	-	0.01	^[b] 0.01	^[b] 0.01	^[b] 0.01	^[b] 0.01	^[b] 0.01	^[b] 0.01

^[a]Only the FLIR® Tau 2 (324) is sensitive to a temperature span of 200°C

^[b]Based on fixed temperature span and resolution of the digital output

Results in Table 2.4 will have implications on a sensing application that requires a large temperature span and high temperature resolution. Therefore, a digital output would provide the full temperature span and resolution of the thermal detectors. In addition, TIR cameras have a low signal-to-noise ratio that neither digital nor analog video equipment can reduce. However, digital video hardware eliminated noise introduced with analog video transmission (Figure 2.22) while streaming 14-bit video data.

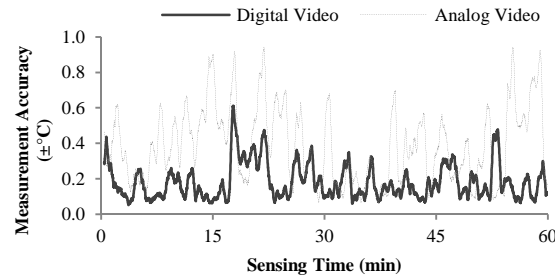


Figure 2.22. Accuracy comparison of analog and digital video output over a 1 h sensing time of CAM1. The absolute difference between actual and measured temperature is shown with a 1 min NUC. Results demonstrate the digital and analog measurement accuracy to be 0.43°C or 0.82°C ($\alpha=0.05$), respectively. The TIR camera core operated at a stable temperature prior to the comparison.

2.4.7 Environment Influence

Due to the unregulated temperature of the microbolometer, a change in thermal detector temperature during the warm-up period caused a decrease in measurement inaccuracy (Figure 2.17, above). Similarly, evaluation within the environmental chamber revealed a change in ambient air temperature caused a proportional change in camera housing temperature, thereby causing similar measurement inaccuracy (Figure 2.23).

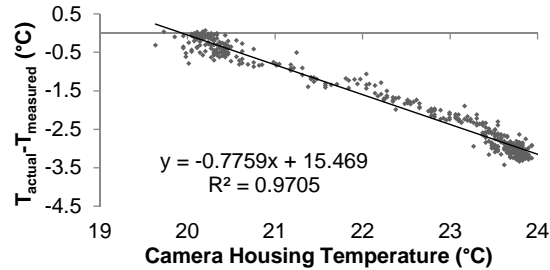


Figure 2.23. Measurement inaccuracy due to a change in camera housing temperature over a 10 min time span. OT radiometric calibration was performed when the TIR camera housing was at 20°C. CAM1 was configured for 1 min NUC, analog video output and a temperature span of 20°C. Ambient air temperature was 10°C and relative humidity was 25%. CAM1 operated at a stable temperature prior to inducing a change in ambient air temperature.

As camera housing temperature increased, the measured temperature was consistently higher than the actual temperature. This consistent temperature increase could be attributed to how the microbolometer quantifies a pixel intensity due to a change in resistance of an individual pixel detector. As the camera housing temperature increases, the heat transfer to the microbolometer would cause individual pixel resistances to increase resulting in a higher measured temperature. Results from an increased relative humidity was investigated and the resulting influence to measurement accuracy is shown in Figure 2.24. As shown in Figure 2.24 a, a target with a stable temperature above air temperature resulted in a decreased measured temperature that appeared to attenuate towards ambient air temperature with increasing relative humidity. Similarly, a target with a stable temperature below air temperature (Figure 2.24 c) resulted in an increased measured temperature that appeared to attenuate towards ambient air temperature with increasing relative humidity. Lastly, a target with a stable temperature equal to air temperature (Figure 2.24 b) resulted in a measured temperature that remained closely centered to air temperature but with diminished accuracy. With stable targets not equal to air temperature, the apparent attenuation towards ambient air temperature is most likely due to ambient air particles in-between the target surface and camera. In the scenario with the stable target equal to air temperature, some inaccuracy may be contributed to air particles that are not in equilibrium with the ambient air, thereby causing the apparent decrease in measurement accuracy.

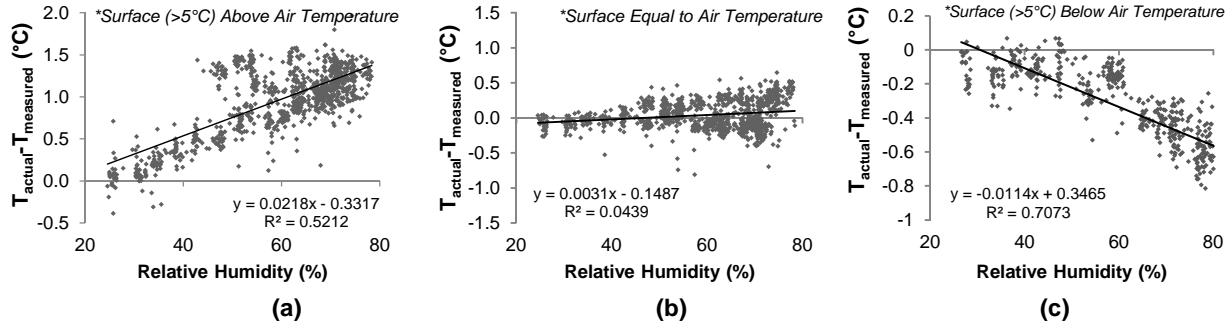


Figure 2.24. Influence of relative humidity changes to measurement accuracy between the TIR camera and the stable target whose temperature is (a) above (>5°C) ambient air temperature, (b) equal to air temperature, and (c) below (>5°C) air temperature. CAM1 was configured for 1 min NUC, analog video output, and a temperature span of 20°C. CAM1 operated at a stable temperature prior to the inducing a change in relative humidity.

Results indicate air temperature and relative humidity can impact measurement accuracy of the TIR camera systems. The R^2 values for plots in Figure 2.23 and 2.24 indicated that regression curves can be generated to compensate for temperature and humidity changes. However, further research needs to be conducted to understand these affects with the TIR camera system at different sensing distances especially aboard sUAS platforms.

To account for changing environmental conditions, an OT radiometric calibration at a specific air temperature, relative humidity, and camera housing temperature produced an accurate surface temperature measurement (Figure 2.25). Similarly, a RT radiometric calibration maintained measurement accuracy from changing environmental conditions. Depending on the application, the OT radiometric calibration method may be appropriate if conditions such as air temperature, relative humidity, and camera thermal detector temperature go unchanged, while the RT calibration accounts for the instantaneous environmental conditions.

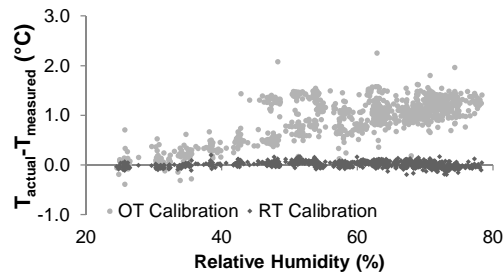


Figure 2.25. RT versus OT radiometric calibration under changing relative humidity. OT radiometric calibration was conducted when chamber was at a relative humidity of 25%. CAM1 was configured for 1 min NUC, analog video output, and a temperature span of 20°C. CAM1 operated at a stable temperature prior to the inducing a change in relative humidity.

Further studies should be conducted with TIR camera cores within semi-regulated and unregulated environmental settings in order to fully investigate TIR camera core utility and the robustness of the developed calibration methods in dynamic field operations.

2.5 CONCLUSION

Uncooled TIR camera core evaluations were conducted to answer questions on use and standard operating protocol, system complexity, and measurement accuracy in changing environmental conditions, which has restricted previous use. More specifically, this study determined the necessary hardware and influences to measurement accuracy from physical properties and some environmental conditions present in agricultural applications. As studied, physical properties that reduce practical use of TIR cameras for temperature measurement include lens distortion, image pixel resolution, warm-up time, camera controllability, and repeatability. However, negative influences on measurement accuracy can be reduced with camera configuration settings, a camera-lens combination selected for sensing distance and target dimensions, post-processing lens calibrations, and standard operating protocol.

In this study, the wide angle lens (7.5 mm) and medium angle lens (11mm) distortion was 30% and 19%, respectively, that image distortion correction resolved for precise spatial integrity. At least 4 pixels are recommended on the target in order to capture a representative value from the target and maximize the image coverage area while accounting for slight inconsistencies in target orientation and shape. Warm-up times of 7 and 19 min are necessary for a stable temperature measurement of CAM2 and CAM1, respectively.

With a 1 min timed-interval NUC over a sensing period of 1 h, OT or RT radiometric calibration provided absolute surface temperatures with environmental compensation in which the TIR camera was calibrated. The CAM1 analog output yielded a configurable temperature span from 5°C to 156°C, resolution from 0.02°C to 0.61°C, and measurement accuracy of $\pm 0.82^\circ\text{C}$ or 0.62°C with OT or RT radiometric calibration, respectively. CAM 1 digital output yielded a fixed temperature span of 156°C, resolution of 0.01°C and measurement accuracy of ± 0.43 or 0.29°C with OT or RT radiometric calibration, respectively. CAM2 yielded a controllable temperature span of 18°C to 206°C, resolution of 0.07°C to 0.80°C, and measurement accuracy of ± 0.87 or 0.63°C with OT or RT radiometric calibration, respectively. Both TIR camera cores had a thermal detector that was sensitive and directly correlated to the temperature within the FOV ($R^2 = 0.99$), thereby resulting in comparable measurement accuracies between the two TIR cameras.

Increased measurement temperature accuracy, resolution, and added control was achieved by integrating a digital frame grabber to reduce analog signal loss and noise introduced with analog video signal transmission. The DRS Breakout Box in conjunction with CAM1 was advantageous because it acts as the analog and digital module while doubling as the control interface. Both cameras were configurable for a span of temperatures, but CAM1 had more discrete settings in order to make fine adjustments to span and offset temperature.

Findings of this research support future studies to capture spatial temperatures aboard ground and aerial-based sensing platforms to generate high-spatial thermal images for unique monitoring of crop health for new and advanced relationships.

Chapter 3 - Deploying a Thermal Infrared Imaging System for High Spatial and Temporal Resolution Crop Water Stress Monitoring of Corn within a Greenhouse

3.1 ABSTRACT

Inadequate water application often decreases yield and product quality. Existing methods using single, localized soil moisture or canopy temperature measurements that do not account for crop water stress on a high spatial basis to assist irrigation scheduling. This study was conducted to understand the feasibility of thermal cameras in order to quantify high spatial canopy temperatures in relation to soil moisture. Study objectives included the deployment of a thermal infrared imaging system (TIRIS) for high spatial and temporal monitoring to test camera durability and measurement accuracy during full-season crop development, remove background temperatures with image segmentation, and sample individual plants to investigate full-season crop water stress versus soil moisture content. A developed TIRIS using a lightweight uncooled thermal camera maintained measurement accuracy below $\pm 0.62^{\circ}\text{C}$ ($\alpha=0.05$) while compensating for changing greenhouse conditions. Corn plants were segmented into well-watered and water-stressed irrigation zones to observe stress from water deficits. Canopy temperatures were used to develop empirical canopy-to-air temperature deficit versus vapor pressure deficit linear regressions that revealed predicted canopy temperature are closely related to characteristic water use. Results of the 80-day study demonstrated that 82% of decreased soil moisture variation was explained when the CWSI increased above 0.6. Results support the use of the CWSI as an alternate irrigation scheduling method in order to quantify spatial soil moisture by remotely measuring canopy temperature.

3.2 INTRODUCTION

In the United States, agriculture annually uses approximately 80% of the consumptive ground and surface water use (USDA, 2014). The potential to conserve water relies heavily on decision support tools (Rodriguez, et al., 2005) to increase water use efficiency using precision irrigation technologies (Ballester, et al., 2013; Cohen, et al., 2005; Gontia & Tiwari, 2008). Quantity of irrigation water and application time are among critical decisions producers need to make to develop site-specific irrigation plans (Alves & Pereira, 2000; Cohen, et al., 2005; Wanjura,

et al., 1992). Precision irrigation technologies can be used to precisely apply desired water at a controllable increment for desired crop performance (Cohen, et al., 2005; Taghvaeian, et al., 2013). However, large variability may exist in commercial agricultural fields due to variability in soil type and depth, topography, climate, specific crop growth period and producer's operation (Cohen, et al., 2005; Evett, et al., 2014). Therefore, techniques and technologies are needed to accurately classify spatial crop water need or crop water stress to gain economic and environment advantages (Herwitz, et al., 2004; Taghvaeian, et al., 2013). Of the many types of crop stress, water stress is the most common and restrictive factor impacting crop yield (Jackson, et al., 1981; Luvall & Holbo, 1991; Scherrer, et al., 2011; Zia, et al., 2013) where water stress severity depends on timing and duration.

Several existing methods to monitor crop water stress rely on a combination of single-point soil, plant and atmospheric measurements (Alves & Pereira, 2000; Cohen, et al., 2005). Soil moisture sensors are one of the most common tools being utilized to make irrigation decisions. One soil moisture probe is typically installed for a whole field due to the installation cost and maintenance. Soil moisture probes, more recently, quantify moisture at multiple soil depths. Soil moisture probes, however, are subject to localized placement error and do not account for spatial crop variability that exists within a field (Moller, et al., 2007). Alternative methods for detecting crop water stress utilize pressure chambers and leaf diffusion porometers to measure individual leaf stomatal conductance and leaf and stem water potential, respectively (Ballester, et al., 2013; Berni, et al., 2009a; Grant, et al., 2007; Idso, et al., 1977). However, these techniques are destructive, labor intensive, localized, limited by small sample size and unsuitable for automation (Ballester, et al., 2013; Berni, et al., 2009a; Cohen, et al., 2005; Gontia & Tiwari, 2008; Jones, 1999; Leinonen & Jones, 2004). Consequently, these drawbacks make invasive plant-based crop monitoring impractical in commercial applications, thereby limiting producer adoption for irrigation decision management (Ballester, et al., 2013).

To address these concerns, thermal sensing approaches have been investigated because they are non-contact and less labor intensive, and offer non-destructive monitoring to assess crop stress from leaf canopy temperatures (Grant, et al., 2006; Leinonen & Jones, 2004). Since the 1970s, crop canopy temperature has been accepted as a health indicator of crop water stress because plants close their leaf stomata, or leaf openings, when they experience water stress in order to retain water, thereby lowering stomatal conductance, reducing transpiration, and increasing leaf

temperatures (Ballester, et al., 2013; Grant, et al., 2006; Idso, et al., 1977; Jones, 1999; Leinonen & Jones, 2004; Rodriguez, et al., 2005). On the other hand, when leaf stomata are open, water in the leaf evaporates through transpiration which cools the leaf (Maes & Steppe, 2012). During transpiration, energy from the leaf is used to evaporate the water from liquid to vapor, inducing latent heat loss and cooling the leaf. In addition to transpiration, leaf temperature depends on ambient conditions such as relative humidity, wind speed, ambient temperature, and radiation incident on the leaf surface (Leinonen & Jones, 2004). As a result, canopy and leaf temperatures are controlled by a combination of thermal energy balances, vegetative genetics, and natural site-specific elements (Luvall & Holbo, 1991). Although these environmental elements influence leaf temperature, they can be readily measured in real-time using commercially available sensors (Udompetaikul, et al., 2010).

Current crop growth studies have primarily used ground-based thermometry to take canopy temperature measurements and develop thermal indices that account for canopy characteristics, soil temperature, and atmospheric conditions for site-specific irrigation management and breeding programs (Idso, et al., 1981; Jackson, et al., 1981; O'Toole & Real, 1986). According to Zia et al. (2013), crop growth stage does not significantly impact canopy leaf temperature, thereby supporting the use of leaf temperature as a viable indicator of full-season crop health characteristic. Highly integrated thermometric systems use an array of infrared thermometers (IRTs) mounted in fixed field locations and on dynamic center pivot irrigation systems to measure crop canopy temperatures and provide a means of irrigation scheduling (O'Shaughnessy, et al., 2012).

However, crop temperature must be segmented from the measured temperature influence of soil background and shaded lower leaves (Ayeneh, et al., 2002; Luquet, et al., 2003; Maes & Steppe, 2012). Unfortunately, this segmentation is not possible with IRTs without additional sensor measurements potentially adding to measurement inaccuracies and automation complexity. In general, IRT inaccuracy from background temperatures limit their use until the crop reaches a particular growth stage because when plants are small, soil covers a majority of the measurable surface, thereby dominating the temperature measurement. Moreover, IRTs cannot measure spatial temperature difference between shaded and sunlit leaves where temperature differences can drastically differ. Due to the uniqueness of biological crop material, any two plants exhibit temperature differences as a result of physical variation in plant architecture, such as color, leaf size, relative orientation to the sun, and field variability (Ayeneh, et al., 2002; Luquet, et al., 2003).

In addition, IRTs are limited to ground-based systems because of their single-point measurement, small measurement area, time requirement for field mapping, and inability to segment crop from a soil background. Overall, IRT technology lack both spatial (ground sample distance (e.g., 1 cm/pixel)) and temporal (revisit frequency) resolution to quantify crop variability (Colaizzi, et al., 2012) critical for making weekly irrigation decisions.

An alternate to IRTs are thermal infrared imaging systems (TIRIS). TIRIS are advantageous because they can spatially map temperatures via a thermal image to measure subtle, heterogeneous characteristics of leaf dynamics (Liu, et al., 2011). The spatial resolution and image processing functionality of low-resolution thermography increase the use of crop canopy temperature characteristics in agriculture (Luquet, et al., 2003) in order to provide qualitative and quantitative crop characteristics that support management decisions (Colaizzi, et al., 2012; Evans, et al., 2000). Crop stress monitoring with thermography allows producers to use thermal sensing for crop canopy temperature mapping (Alves & Pereira, 2000; Ayeneh, et al., 2002; Berni, et al., 2009b; Taghvaeian, et al., 2013; Wang, et al., 2010), individual crop temperature profiling (Leinonen & Jones, 2004), variable rate irrigation scheduling (Cohen, et al., 2005; Colaizzi, et al., 2012; Fitzgerald, et al., 2007), crop breeding (Grant, et al., 2006; Liu, et al., 2011; Zia, et al., 2013), fruit detection and quality assessing (Bulanon, et al., 2009; Sepulcre-Canto, et al., 2007; Zhao, et al., 2005), biomass estimation (Wooster, et al., 2013), yield prediction (Hackl, et al., 2012), and disease and nutrient deficiency detection (Chaerle, et al., 1999; Hashimoto, et al., 1984; Tilling, et al., 2007).

Progressive agriculture management with on-demand thermal sensing relies on accurate measurements, rapid response times, inexpensive sensor platforms, and user-intuitive techniques in order to achieve well-informed decisions. Thermography has been utilized to further develop thermal indices and crop sensing techniques originally developed with IRTs. Temperature-based indices have shown significant correlations among crop canopy temperature, stomatal conductance, and leaf water potential. The correlations become more significant as stress intensity increased (Hackl, et al., 2012). Idso et al. (1981) investigated the hypothesis that non-water stressed crops transpire to a predictable leaf temperature dependent on ambient air conditions, such as wind speed, net radiation, and vapor pressure deficit (VPD). For example, a leaf temperature at or below the predicted leaf temperature indicates a non-stressed plant, whereas a leaf temperature above the non-water stress baseline (NWSB) indicates a level of water stress.

This aforementioned predictable leaf temperature relationship was used by Jackson et al. (1981) to indirectly measure soil moisture and apparent crop health through transpiration. The crop water stress index (CWSI) has been successfully developed and implemented using IRTs that measure canopy temperatures in order to determine variable rate irrigation needs (Taghvaeian, et al., 2013). The CWSI is the normalized difference of the measured air-to-leaf canopy temperature deficit between the lower base line (i.e., NWSB) and the upper base line, or water-stressed baseline (WSB), on a plot of air-to-leaf canopy temperature deficit vs. VPD. Therefore, the robustness of the CWSI is attributed to the scale at which it can be implemented. With the addition of upper and lower boundaries for predicted leaf temperature, the CWSI approach has been the most used index aboard all thermal sensing platforms in various climate regions because of the inclusion of VPD, solar radiation, and wind speed (Maes & Steppe, 2012; Rodriguez, et al., 2005).

A limitation of thermal indices includes the need for measuring several environmental parameters. Measurements necessary for CWSI include crop canopy temperatures, wet/dry leaf reference temperatures, and environment conditions (Grant, et al., 2007; Luquet, et al., 2003). A robust technique relies on empirically determined NWSBs and water stress baselines (WSBs) that directly account for present net radiation, aerodynamic resistance, and the particular crop's microclimate (Ballester, et al., 2013; Blonquist & Bugbee, n.d.; El-Shikha, et al., 2007; Erdem, et al., 2010; Fitzgerald, et al., 2007; Gontia & Tiwari, 2008; Grant, et al., 2007). In order to directly measure lower and upper reference temperature bounds, select leaves are wetted with water to represent a fully transpiring leaf while leaves are covered with petroleum jelly to reach a non-transpiring stage. Temperatures of these leaves are measured to provide the lower and upper limits, respectively. However, preparation of wet/dry leaf surfaces for reference leaf temperatures is not practical and subject to repeatability errors. Many studies have investigated the use of standardized measurements without manually preparing reference temperatures achieving similar CWSI results (Berni, et al., 2009b; Cohen, et al., 2005; Grant, et al., 2006; Grant, et al., 2007; Jones, 1999). Standard dry reference temperature recommendations include the use of an upper temperature bound of 5°C above air temperature (Alves & Pereira, 2000; Cohen, et al., 2005; Erdem, et al., 2010; Moller, et al., 2007; Moran, et al., 1994; Wanjura, et al., 2006). Standard wet reference temperature recommendations include measuring leaf temperature of well-watered plants (Ballester, et al., 2013; Blonquist & Bugbee, n.d.; El-Shikha, et al., 2007; Erdem, et al., 2010; Fitzgerald, et al., 2007; Gontia & Tiwari, 2008; Grant, et al., 2007; Maes & Steppe, 2012). CWSI

measurement strength is reduced in climates with high humidity in which the VPD approaches zero as differences between water-stressed and well-watered leaf temperatures diminish. Near zero VPDs, consequently, increase the chance of inaccurate CWSI assessment because of the requirements for high temperature measurement resolution and accuracy. Artificial dry/wet reference measurements have provided a repeatable standard for applications of a larger scale when used in conjunction with thermography (Moller, et al., 2007). The use of artificial reference surfaces requires a viewable reference within the camera's field of view (FOV) mounted near the plant canopy to most accurately match the leaf's microclimate. Thermography is an appealing sensing technology because consistent crop water stress can be accounted for by automatically measuring an artificial wet reference (Maes & Steppe, 2012) viewable from within the camera's FOV (Wang, et al., 2010).

Considering the limitations and drawbacks of IRT sensors, a TIRIS may provide high spatial and temporal resolutions for canopy temperature measurement that are needed for advanced crop health monitoring and CWSI-based irrigation scheduling. With single-point measurements, present and past studies used IRTs to derive CWSI values. However, limited studies have been conducted to measure crop temperature with high spatial and temporal resolutions. Canopy temperatures of corn obtained throughout the growth season, especially during periods of irrigation deficits and replenishment, could provide necessary knowledge on crop stress to assist in practical adoption of crop water stress for deciding irrigation management. Thermal imaging could show the spatial canopy temperatures from varying nighttime and daytime vapor pressure deficits. More specifically, thermal imaging can segment canopy vegetation from soil, lower leaves, and inner to outer canopy spatial temperatures to further correlate canopy temperatures with VPDs. With high spatial temperature resolution, upper and lower limits for the CWSI can be further investigated with real-time soil moisture at growth stages not previously studied. Diurnal conditions of the greenhouse and empirical NWSB can be used for an investigation of VPD-to-canopy temperature deficit transfer functions for a full growth season.

Based on the limitations of current crop water stress monitoring methods, objectives for this study included:

1. Develop and deploy a thermal imaging system for monitoring corn canopy at high spatial and temporal resolutions in a greenhouse,

2. Evaluate the accuracy of the thermal imaging system in measuring crop canopy temperatures during a full growth season of corn, and
3. Investigate full-season air-to-canopy temperature deficit versus VPD transfer functions for direct relationships between crop water stress index (CWSI) values and soil moisture by automatically evaluating canopy temperature images.

3.3 METHODS AND MATERIALS

Laboratory experiments were conducted at the Department of Biological and Agricultural Engineering at Kansas State University, Manhattan, Kansas, to evaluate TIRIS accuracy and requirements for measuring corn canopy temperatures in precision agriculture applications. An uncooled Tamarisk® 320 thermal infrared (TIR) camera core (DRS Technologies, Inc., Dallas, Texas) was selected for this study. On 10 May 2014, corn (*Zea mays*) seeds were planted in pot containers with 20 cm diameter in 30 replications at the Throckmorton Greenhouses at Kansas State University, coordinates of 39.1917° N, 96.5917° W. For a full-season growth study (80 days), the plants were separated into two irrigation regimes of well-watered (WW) and water-stressed (WS), as shown in Figure 3.1.

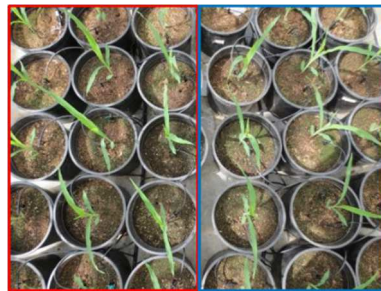


Figure 3.1. Water stressed plant orientation (left) and well-watered plants (right)

Corn was selected as the crop of choice because it is a major irrigated crop in the Midwest and has demonstrated high yield potential with subsequent irrigation (Schlegel, et al., 2014). Compost material with high organic and plant nutrient content was used as potting media with a water-holding capacity of 3.4 ml per gram of soil, as determined in an oven drying method (Texas Department of Transportation, 2014). All corn seed was planted 4 cm deep, fertilized with slow-release nitrogen pellets, and imposed with water treatments directly after emergence. Greenhouse temperature was set to 27°C during the day from 6:00 to 18:00 h and 20°C at night from 18:00 to 6:00 h on the following day (Hoeft, et al., 2004).

As specified by Rogers (1998), a characteristic amount of water use (Figure 3.2) was used to irrigate the well-watered corn plants while inducing water stress in the water-stressed regime. Consequently, periods of analysis were split into growth periods of 1) germination and seedling stage, 2) rapid growth stage, 3) reproductive stage, and 4) maturity stage.

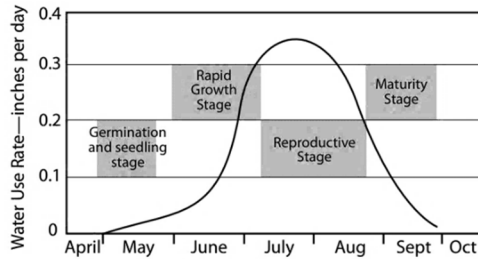


Figure 3.2. Characteristic water use of corn. Reproduced from Rogers and Alam (1998).

Irrigation was applied according to recommended water needs as specified in Table 3.1. Based on the size of pot containers used in this study, Table 3.1 depicts the water amount applied to each corn plant during the respective growth stage based on findings of Rogers and Alam (1998).

Table 3.1. Average recommended water-use rate for irrigated corn

Time	*Recommended Water Use Per Day [ml]	Water Applied to Well-Watered Per Day [ml]	Water Applied to Water-Stressed Per Day [ml]
Germination and Seedling	453	500	225
Rapid Growth	907	900	450
Reproductive	1058	1100	550
Maturity	605	625	300

*Does not account for evaporation or pot drainage

3.3.1 Irrigation Setup

Water was applied via commercial drip-line irrigation under constant pressure from a regulating solenoid valve (Production Series Sprinkler Valve, Orbit Irrigation Products, Inc., Bountiful, Utah) controlled by a zone irrigation controller (Zone Indoor/Outdoor Irrigation Controller, Orbit Irrigation Products, Inc., Bountiful, Utah) to maintain drip uniformity and repeatability. Precise and timely irrigation regimes were applied at increments of 25 ml at 6:00 h. Figure 3.3 shows the irrigation setup and plants under growth period 1.

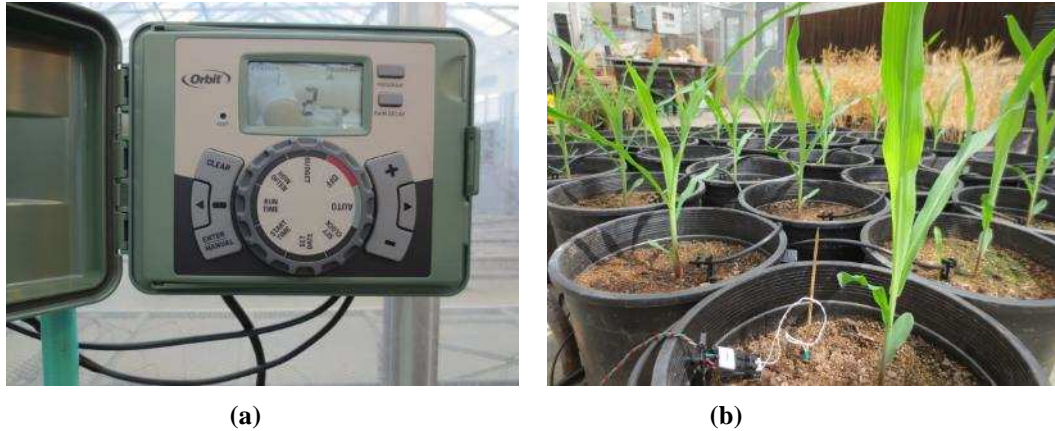


Figure 3.3. (a) Automated irrigation system and (b) corn during growth period 1.

3.3.2 Thermal Imaging and Environmental Monitoring

An automated TIRIS was developed and deployed that featured components for remote control, camera control, environmental monitoring sensors, and computer for capturing, storing, and analyzing image and environmental data (Figure 3.4). For functionality, wireless control was enabled using a virtual private network (VPN) connection which provided remote monitoring and direct control of the TIRIS.

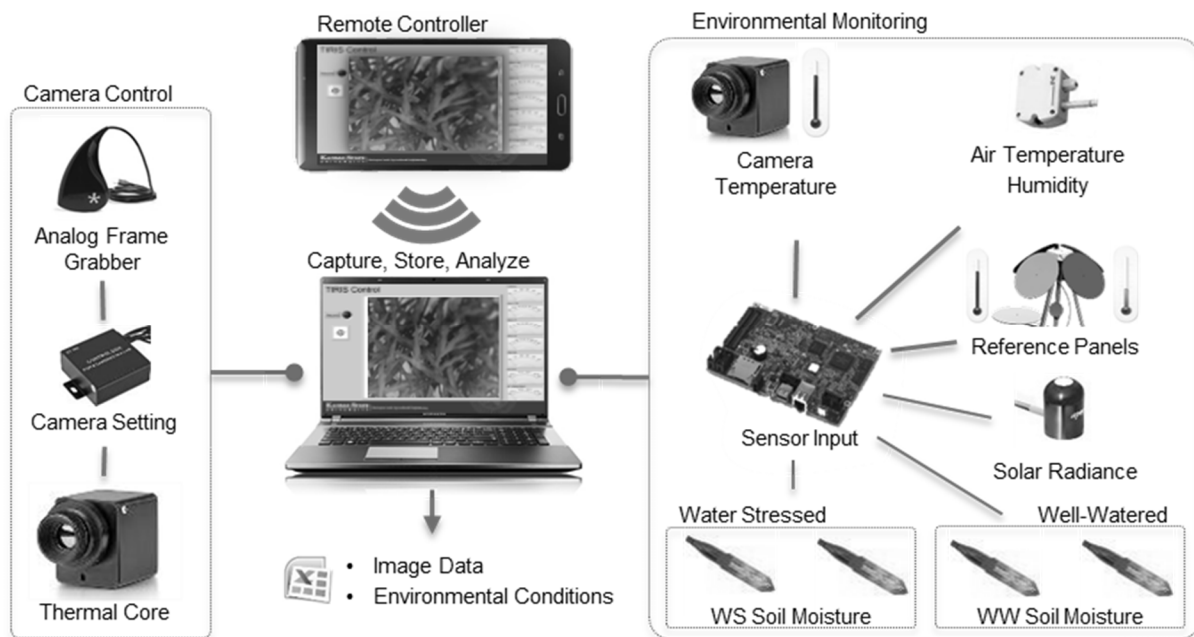


Figure 3.4. Component diagram for TIRIS

Thermal images were obtained with an uncooled Tamarisk® 320 thermal infrared (TIR) camera core (DRS Technologies, Inc., Dallas, Texas) with a focal length of 11 mm and a 27°×20° FOV lens. The camera has a maximum frame rate of 60 Hz, sensitive the long wave infrared

(LWIR) electromagnetic radiation from 8 to 14 μm corresponding to a temperature span of -66 to 90°C, and an uncooled microbolometer sensor with a 320×280 fixed pixel array. The camera was mounted at a 4.5 m height nadir to the corn plants, thereby providing a spatial resolution of 7.7 mm/pixel, limiting the FOV to 3 × 2 m. A critical aspect of any TIRIS is the amount of pixels on the target. As previously studied, at least four pixels are recommended on a target in order to limit inaccurate temperature measurement and maximize spatial image coverage while accounting for slight inconsistencies in target orientation. For example, the smallest object the TIRIS in this study was able to accurately measure was an object of 15.4 mm (7.7 mm × 4 = 30.8 mm). The TIR camera core provided an 8-bit (256 discrete pixel intensity digital value (DV)) thermal video. The DRS Camera Control Software controlled each camera's functions and features. Within the software's graphical user interface (GUI), the TIR camera core was configured for video output and frame rate, and thermal detector sensitivity settings. In order to set the TIR camera core, a DRS breakout board module (Breakout Box 1003785-001, DRS Technologies, Inc., Dallas, Texas) adjusted the thermal detector gain sensitivity (i.e., detectable scene temperature span) and level control (i.e., shift offset of the center temperature within the temperature span), thereby improving detected thermal energy of the scene temperatures. Auto gain and level contrast were enabled via the DRS Camera Control Software (DRS Technologies, Dallas, Texas) to account for continuously changing operating camera housing temperatures within the greenhouse. Auto gain and contrast maintains distinguishable scene temperatures and high and low temperatures within saturation threshold limits (Kuenzer, 2014).

Analog video output was streamed at 60 Hz into an analog-to-digital video converter (Dazzle DVD Recorder HD, Corel Corporation, USA). This raw analog video signal was streamed into a host computer using LabVIEW™ (National Instruments Corporation, Austin, TX) image acquisition and processing software. When sampled, the developed Greenhouse TIRIS virtual interface (VI) would grab the image, assign a timestamp, and store within the appropriate storage folder (Figure 3.5).



Figure 3.5 Greenhouse TIRIS VI front panel for controlling loop time and camera control while monitoring and saving soil moisture of irrigation regimes, air temperature, relative humidity, solar radiance, reference panels, camera temperature, sample number, and time stamp.

Parallel environmental conditions were captured over 2.5 min with a single-board microcontroller (Single Board RIO 9633, National Instruments Corporation, Austin, Texas) and placed into a measurement file denoted with the corresponding image number. Relative humidity and air temperature were measured with an ambient air sensor (HX303AV, Omega Engineering Inc., Stamford, Connecticut) with an accuracy of $\pm 3\%$ and $\pm 0.2^\circ\text{C}$, respectively. Solar radiance was measured with a pyranometer (SP115, Apogee Instruments, Logan, Utah) with an accuracy of $\pm 0.25 \text{ W m}^{-2}$. To compensate for the influence of environmental conditions on the accuracy of the TIR camera, surface mount thermistors (ON-930-44004, Omega Engineering Inc., Stamford, Connecticut) with an accuracy of $\pm 0.2^\circ\text{C}$ measured temperature of reference panels within the camera's FOV.

Reference panels used in the experiment were 10 x 10 cm wooden pads with an empirical emissivity of 0.9, whereas corn has an emissivity of about 0.95 (Idso, et al., 1981). Reference temperature panels were sized accordingly to the camera's spatial resolution and constructed of materials with a low thermal inertia in order to resist temperature changes. A reference panel was placed on shaded concrete, well-watered soil, and water-stressed soil to generate temperature differentials. Thermistors were wired into a voltage divider to sense the change in voltage due to the temperature-based resistance (Figure 3.6 a). The resulting voltage (V_{out}) was used to determine temperature using a calibration curve provided by the manufacturer (Figure 3.6 b).

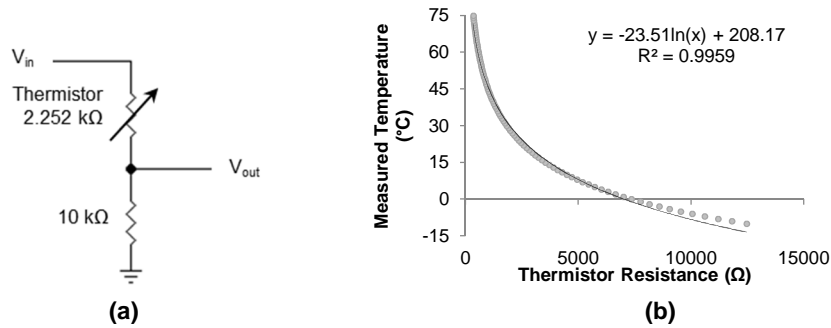


Figure 3.6. (a) Voltage divider wiring diagram used to measure changing voltage from the corresponding change in the thermistor resistance. (b) Thermistor calibration curve used to quantify temperature with a change in voltage. (See Appendix A, Figure A.4 for more details)

In order to ensure the two irrigation regimes were imposed, soil moisture was monitored with four capacitance soil moisture probes (Waterscout SM 100, Spectrum Technologies, Aurora, Illinois) with an accuracy of $\pm 3\%$ soil moisture content (SMC) with two sensors in each irrigation regime. Soil moisture content of the WW and WS plants were monitored throughout the season to validate the extent of crop water stress.

3.3.3 Radiometric Calibration

The uncooled TIR camera core measures LWIR energy that strikes the detector material, altering the electrical resistance from a temperature change, transforming LWIR radiation intensity into a raw DV, thereby generating a thermal image (Kuenzer, 2014). A limitation of uncooled TIR cameras, however, is their inability to quantify absolute temperatures. Therefore, a real-time (RT) radiometric calibration method was developed to quantify absolute surface temperature at environmental conditions in which the TIR camera was calibrated. A RT radiometric calibration uses RT image pixel intensities of a viewable reference panel within the camera's FOV and the actual surface temperatures to characterize pixel-to-temperature intensity functions. This RT radiometric calibration is covered in more detail in Section 2.4.4. At any one sampling, the three reference panels would naturally produce a low, in-between, and high temperature. As a result, the low and high reference panel was used for the RT radiometric calibration, whereas the in-between reference panel acted as a crosscheck for assessing RT measurement accuracy. Static regions of interest (ROI), as specified in the automatic imaging program, averaged multiple image pixels to correlate to one surface temperature measurement.

Raw pixel intensities (X_1, X_2) from the video feed were correlated to actual surface temperature (Y_1, Y_2) to determine the radiometric transfer function slope, as defined by Equation 3.1:

$$m = \frac{Y_2 - Y_1}{X_2 - X_1} \quad (3.1)$$

By using the slope found in Equation 3.1 and a raw pixel and coinciding surface temperature (X_1, Y_1), the y-intercept of the RT radiometric transfer function was determined using Equation 3.2:

$$Y - Y_1 = m(X - X_1) \quad (3.2)$$

Using results from Equation 3.2, instantaneous temperature span was defined by Equation 3.3:

$$\text{Temperature Span } (^{\circ}\text{C}) = \text{Bits of Resolution} \times \text{Radiometric Slope}[m] \quad (3.3)$$

Using the resulting $y=mx+b$ radiometric calibration function from Equation 3.1 and 3.2, the TIR camera core was found to be directly sensitive ($R^2 = 0.9986$) to the scene temperatures within the FOV (Figure 3.7).

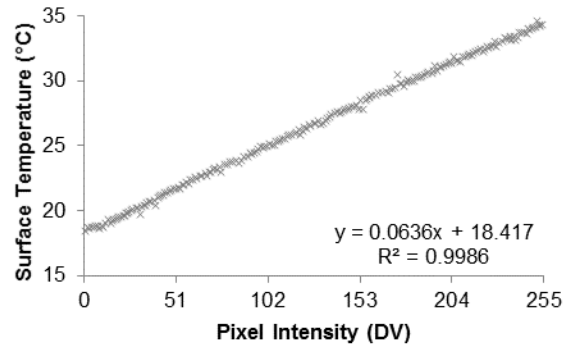


Figure 3.7. Real-time radiometric calibration performed on the DRS Tamarisk® 320 at a 25°C air temperature, 45% relative humidity, and steady-state operating temperature.

The RT radiometric conversion was applied to each image to convert DV into temperature values as defined by Equation 3.4:

$$T_{(i,j)} = T_{min} + \frac{I(i,j)}{2^N - 1} T_{span} \quad (3.4)$$

where:

$T_{(i,j)}$ = Pixel temperature ($^{\circ}\text{C}$) at row i and column j ,

T_{min} = Lowest temperature within the image ($^{\circ}\text{C}$),

$I_{(i,j)}$ = Pixel intensity at row i and column j ,

N = Number of bits for pixel intensity (e.g., $N=8$ for 8-bit images), and

T_{span} = Span of temperature captured in the image.

The developed radiometric calibration method enables the uncooled TIR camera core to use the sensitivity of the thermal detector, as shown Figure 3.7, to quantify surface temperatures. To determine the TIR camera's ability to measure temperatures, the absolute difference between

actual and measured temperature is shown in Figure 3.8. Results reveal the maximum measurement accuracy is 0.62°C ($\alpha=0.05$).

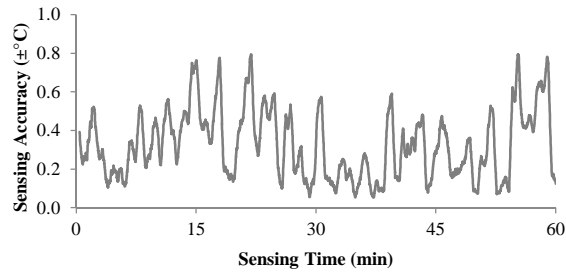


Figure 3.8. Absolute difference between actual minus measured temperature.

As previously studied, the RT radiometric calibration’s ability to compensate for environment conditions while maintaining measurement accuracy is illustrated in Figure 3.9. See Section 2.4.7 for more details on environmental compensation.

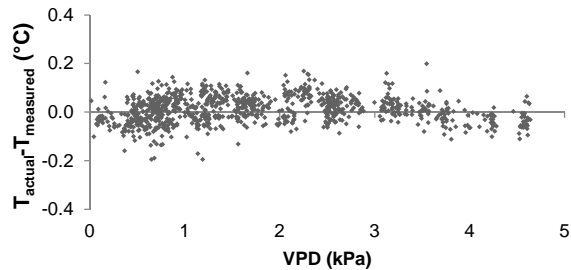


Figure 3.9. RT radiometric calibration under changing vapor pressure deficit (VPD)

Figure 3.9 shows the TIR camera core’s measurement inaccuracy remains below 0.28°C under changing VPD within strict laboratory conditions as described in Section 2.3.2. However, the RT radiometric calibration method was investigated to determine the potential influence to the measurement accuracy from semi-controlled environmental conditions within a greenhouse.

3.3.4 Automated Thermal Imaging and Processing

For subsequent analysis, an Image Processing VI was developed to process the image data and environmental data (Figure 3.10) using the process flow as shown in Figure 3.11. When started, the Image Processing VI would reference the greenhouse reference data for the specific image to process. The image would be pulled from the file storage and corrected for len distortion as described in Section 2.4.1 and would have a basic variance filter applied to reduce analog signal noise within the image. A variance filter was found to reduce visible noise in the image that would cause inconsistencies in the static ROIs.

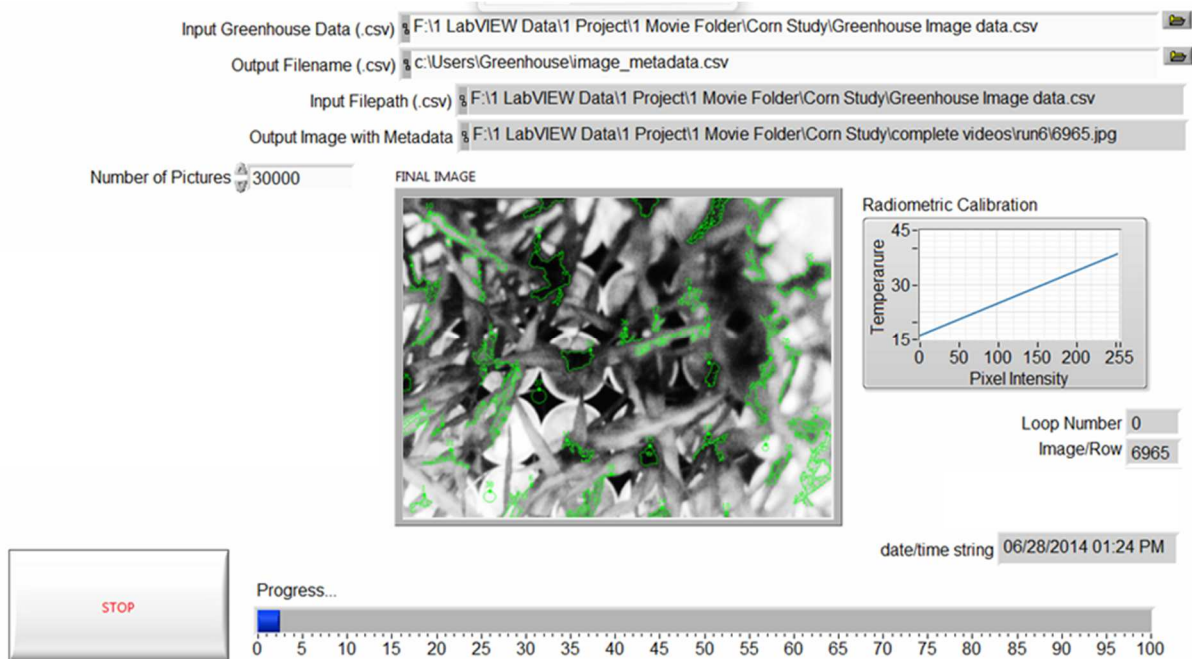


Figure 3.10. Image Processing VI for analyzing greenhouse data controlling input data, output metadata filename, the number of processed images and monitoring output image RT radiometric calibration, image number, and timestamp.

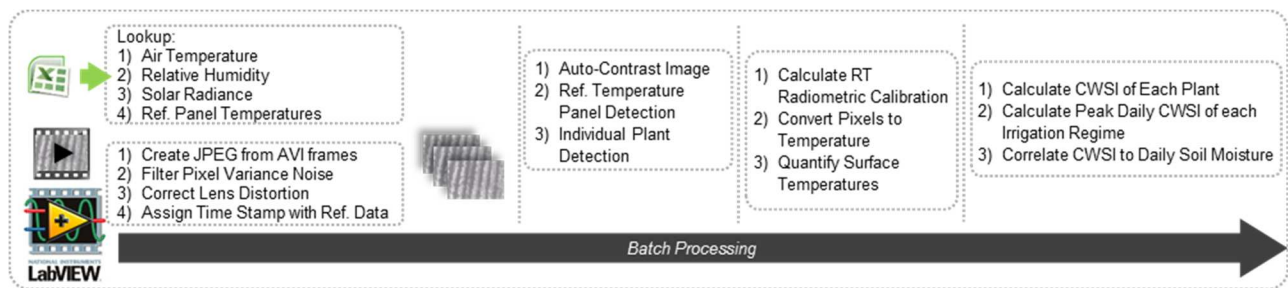


Figure 3.11. Flow chart of batch processing for image and environmental data flow

Within a single image, plant vegetation was identified and isolated for analysis based on location within the image. ROI were designated on each plant to isolate crop vegetation, thereby segmenting crop vegetation from soil and concrete (Figure 3.12). Similarly, ROI were designated on each reference panels in order to extract reference panel pixel intensities.

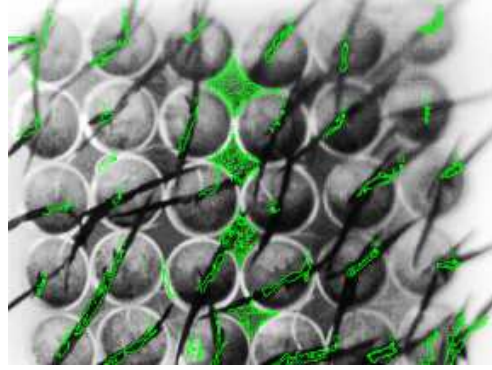


Figure 3.12. Automated TIRIS segmented individual corn foliage, shown in green, from background soil, cement, and pot containers. Black pixels indicate a cold surface while white pixels indicate hot surface. ROIs, shown in green, captured the individual crop intensity and reference panel temperatures.

Location was the only parameter used to isolate vegetation, but shape and texture could be utilized for image pixel segmentation. Location was similarly used to look at spatial temperature differences from the stem and leaf. As a result, the correlation was compared between the predicted stem-to-air temperature deficit versus VPD and the predicted canopy-to-air temperature deficit versus VPD.

3.3.5 Crop Water Stress Monitoring

Because previous studies have found crop stress to be highest at periods following solar noon, temperature measurements from 12:00 to 17:00 h were monitored for peak canopy temperatures (Idso, et al., 1977). Relative humidity, air temperature, solar radiance, and crop temperatures were combined to quantify instantaneous crop water stress. In all measurements, the VPD was calculated from the air temperature and relative humidity as defined in Equation 3.5 (Monteith & Unsworth, 2013):

$$VPD = \left(1 - \left(\frac{RH}{100}\right)\right) \times \left(0.6108 \times 10^{\left(\frac{7.5 \times T_{air}}{237.3 + T_{air}}\right)}\right) \quad (3.5)$$

where:

T_{air} = Measured air temperature (°C),

RH = Relative humidity (%), and

VPD = Vapor pressure deficit [kPa].

Equation 3.5 was used to deduce a non-water stressed baseline (NWSB) leaf canopy-to-air temperature deficit from VPD for similar solar radiation as defined in Equation 3.6:

$$T_{WW \text{ canopy}} - T_{air} = a - b \times VPD \quad (3.6)$$

where:

$T_{ww \text{ canopy}}$ = Well-watered canopy temperature (°C),

T_{air} = Measured air temperature (°C),

a = Crop specific intercept for NWSB,
b = Crop specific slope for NWSB, and
VPD= Vapor pressure deficit [kPa].

NWSB coefficients were empirically measured from RT canopy temperatures of the well-watered irrigation regime ($T_{ww \text{ canopy}}$) over the full growing season starting with the germination and seedling stage (growth period 1), rapid growth stage (growth period 2), reproductive stage (growth period 3), and maturity stage (growth period 4). The RT CWSI was calculated as depicted in Equation 3.7 (Idso, et al., 1981; Jackson, et al., 1981; Jackson, 1982):

$$CWSI = \frac{\Delta T_{predicted} - \Delta T_1}{\Delta T_{predicted} - \Delta T_{dry \text{ leaf}}} \quad (3.7)$$

where:

$$\Delta T_{predicted} = (T_{ww \text{ canopy}} - T_{air}),$$

$$\Delta T_{dry} = (T_{dry} - T_{air}), \text{ and}$$

$$\Delta T_1 = (T_{actual} - T_{air}).$$

For example, water stressed leaf (T_{dry}) and non-water stress leaf ($T_{ww \text{ canopy}}$) boundary temperatures were 25°C and 20°C, respectively. Air temperature was 23°C and actual leaf temperature was 22°C. In this example, CWSI is 0.4. For comparison, daily CWSI values were measured for each plant.

An instantaneous CWSI was derived from the air temperature, relative humidity, and solar radiance for each thermal image. Because wet and dry leaves are not practical within a prolonged monitoring study, wet reference temperatures were empirically found using well-watered plants in the WW regime. Similarly, standardized dry reference temperature of 5°C above air temperature was utilized to represent the WSBs (upper leaf temperature bounds). Empirical NWSBs (lower leaf temperatures) were determined using WW regime leaf temperatures in order to develop RT CWSI values.

3.4 RESULTS AND DISCUSSION

The TIRIS was designed to quantify absolute surface temperature with RT radiometric calibration, thereby maintaining measurement accuracy by compensating for environmental influences from air temperature, relative humidity, solar radiance, and temperature of the uncooled TIR camera. Thermography was used as a crop water stress monitoring tool with high spatial and temporal resolutions. The confidence in assessing crop water stress is directly related to inherent sensor accuracy and calibration protocol. By enabling auto gain and level, the uncooled TIR camera maintained upper and lower pixel saturation to maximize the detected thermal imagery for

temperature span throughout the study. RT environmental correction with temperature reference panels provided temperature measurement accuracy, as shown in Figure 3.13.

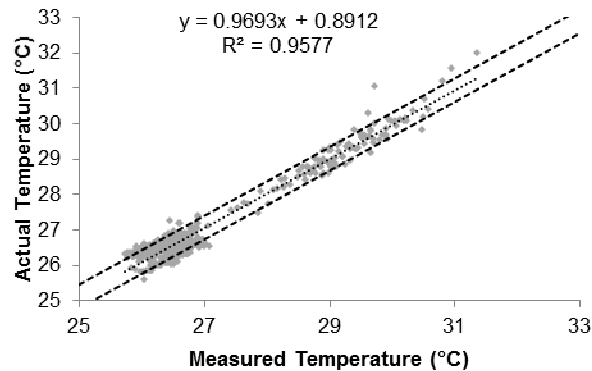


Figure 3.13. Comparison between the measured and actual temperature of the in-between reference panel temperature in the greenhouse from 6:00 to 19:00 h.

As shown in Figure 3.13, the measured-to-actual temperature comparison revealed a 95% confidence that the measurement accuracy is $\pm 0.62^{\circ}\text{C}$ in the semi-controlled greenhouse environment. Because RT temperature measurement accuracy was determined for each image, the RT confidence interval was calculated throughout the day of one well-watered corn plant sample, as shown in Figure 3.14.

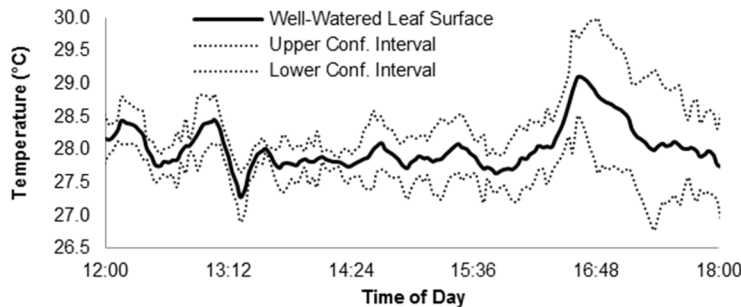


Figure 3.14. Real-time confidence interval of a well-watered corn plant from 12:00 to 18:00 h

By quantifying surface temperatures, Figure 3.15 shows the empirically derived leaf canopy-to-air temperature deficit versus VPD during the four growth stages. Table 3.2 shows coefficients derived from the regression analysis; and, Figure 3.16 shows the simulated canopy-to-air temperature deficit versus VPD regression curves. The R^2 values of the plots in Figure 3.15 show that a correlation exists between the VPD and the predicted leaf canopy temperature. This fundamental relationship is important as the results are directly used to determine the normalized CWSI. Lower plot R^2 values during the last three growth stages could be contributed to the high humidity within the greenhouse which create a concentration of data samples from a VPD of 0 to 2 kPa. In applications in the field, these concentrations may not be as prevalent. As a result, future

studies using high spatial and temporal resolution TIRIS should be investigated in order to observe the full-season leaf canopy-to-air temperature deficit versus VPDs of corn in actual field conditions.

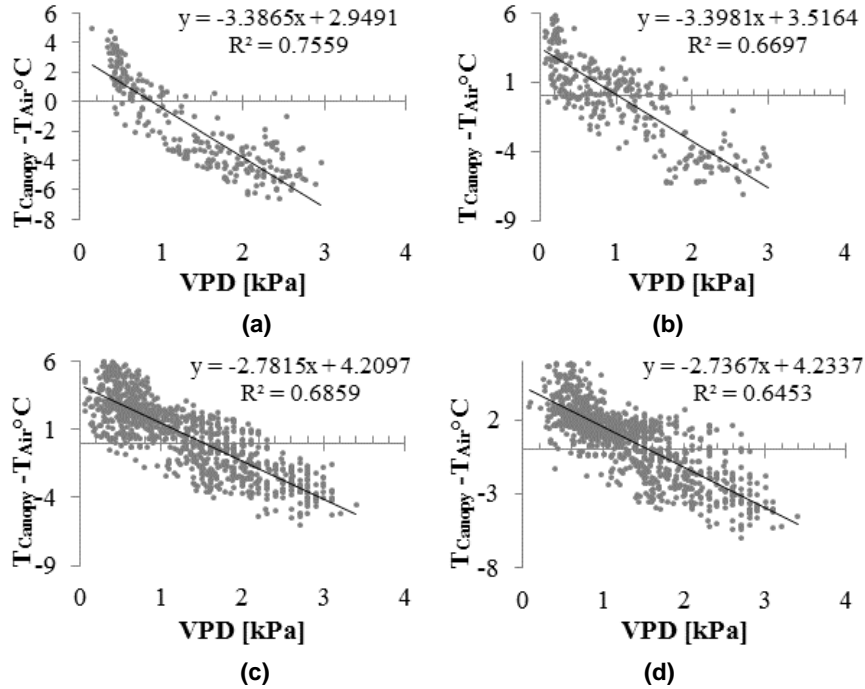


Figure 3.15. Empirical leaf canopy-to-air temperature deficit versus VPD during (a) germination and seedling stage, (b) rapid growth stage, (c) reproductive stage, and (d) maturity stage

Table 3.2. Predicted canopy-to-air temperature deficit-to-VPD

Growth Stage	Slope [m]	Intercept [b]
1	-3.3865	2.9491
2	-3.3981	3.5164
3	-2.7815	4.2097
4	-2.7367	4.2337

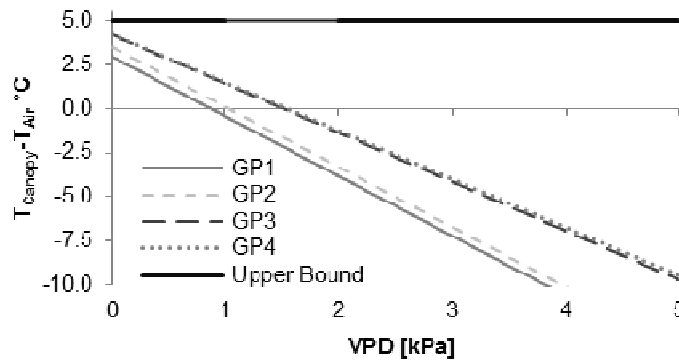


Figure 3.16. Predicted canopy-to-air temperature deficit versus VPD through four growth stages

Figure 3.16 demonstrates the canopy-to-air temperature deficit regression curve only slightly changed from the first growth period (GP1) to the second growth period (GP2). As observed in Figure 3.2, in Section 3.3.1, the recommended daily water use shows a peak followed

by a decline in water use during the third growth stage. Similarly, during the third growth period (GP3), predicted leaf temperatures were warmer, suggesting that corn uses less water for transpiration as the plant utilized energy to grow fruit during the reproductive growth stage. Finally, reduced water uptake resulted in warmer leaf canopy temperatures during the final growth stage (GP4) closely resembling characteristic water use specified in Figure 3.2.

Aside from segmenting soil and background temperatures from vegetation, the stem and leaf temperatures were isolated from within the FOV using location based ROIs. The canopy-to-air temperature deficit was compared to the stem-to-air temperature deficit versus VPD, as shown in Figure 3.17. These values were collected throughout the full-season and represent the WW plant sample average. The canopy-to-air temperature deficit versus VPD produced a stronger correlation ($R^2=0.7364$) versus the stem-to-air temperature deficit versus VPD ($R^2=0.6592$). This observation supports the use of the VPD to better predict the NWSB canopy temperature. This will have practical implications on what portion of the plant is a better indicator of the leaf transpiration. For practical adoption purposes, measuring the canopy temperature aboard different sensing platforms would be less of a challenge because the canopy typically has a large surface area and is the upmost point on the plant. At the same time, being the upmost portion of the plant, the canopy is more exposed to environmental conditions, thereby is more subject to larger diurnal temperature changes. As a result, high temporal ground truthing will be critical to limit error in crop based thermal sensing.

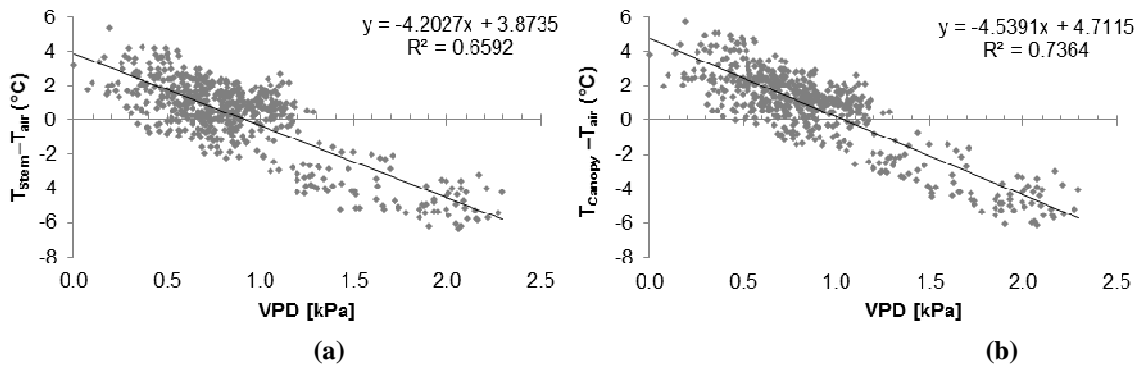


Figure 3.17. Comparison of (a) non-water stressed stem-to-air temperature deficit to VPD and (b) non-water stressed canopy-to-air temperature deficit versus VPD.

The TIRIS measured daily peak CWSI and soil moisture of the WS and WW irrigation regimes in the critical time period between 12:00 and 18:00 h (Figure 3.18).

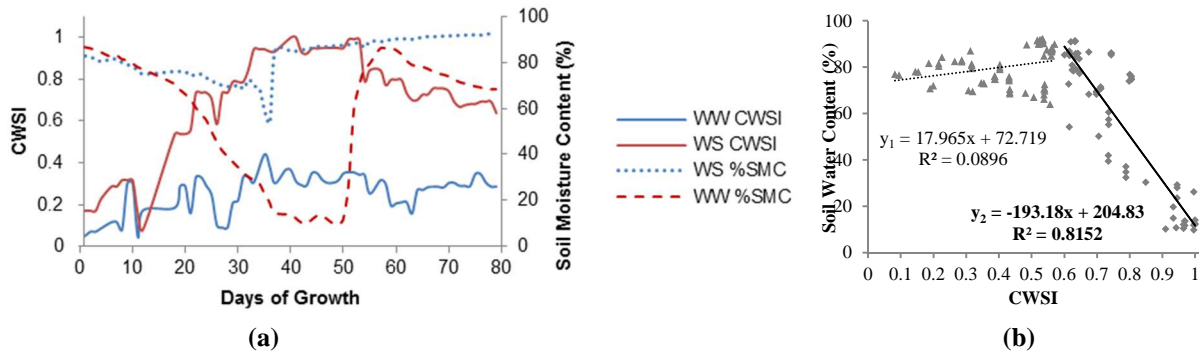


Figure 3.18. (a) Daily soil moisture content and peak daily CWSI throughout the experiment; (b) daily soil moisture content versus peak daily CWSI. A split plot shows the negative correction of the soil moisture versus CWSI from a CWSI value of 0.6 to 1.0 and no significant correlation from a CWSI value of 0 to 0.6.

In Figure 3.18 a, daily soil moisture measurements revealed a soil moisture deficit occurred from day 15 through day 50 in the WS regime. On day 50, the WS plants were watered in order to preserve the specimens and to observe the WS plants' response to irrigation following severe water stress. Peak CWSI of the WS corn did not, however, decrease until Day 52. This observation is important when interpreting and utilizing CWSI values for irrigation decisions because, immediately after watering, plants may have received an ample amount of water but did not have sufficient time to absorb water and transpire, thereby still reflecting a high CWSI. The level of crop water stress prior to irrigation seems to influence the amount of time required for the plants to absorb and transpire thus decreasing their CWSI. Further temporal studies should be considered in order to quantify this time response.

High temporal resolution revealed that the daily peak crop water stress occurred between 13:30 and 15:00 h. Daily peak CWSI closely followed solar noon when plants experienced maximum transpiration in order to adequately cool themselves. In actual field conditions, peak crop water stress could occur at different times depending on current environmental conditions; however, the most critical time to measure CWSI should closely coincide with the time of maximum transpiration.

As shown in Figure 3.18 b, soil moisture content at or above 72% (y_1 linear regression curve intercept) maintained a CWSI value below 0.6 whereas soil moisture content below 72% negatively correlated with CWSI values above 0.6. Results from the 80-day study revealed that 82% ($R^2=0.8152$ of the y_2 linear regression curve) of soil moisture variation was explained by a CWSI above 0.6. This relationship demonstrates the use of non-contact thermal sensing to

indirectly measure soil moisture. This supports the use of CWSI values in order to quantify spatial soil moisture deficits as an alternative irrigation scheduling method instead of soil moisture probes.

Thermography provides an unprecedented opportunity to study crop vegetation for new and advanced relationships. As observed from this study, thermal imaging systems could be considered for measuring crop water stress at scales required for large agricultural production systems. Simplification of image acquisition systems in order to capture full-season crop stress could allow producers, agricultural service providers, and researchers to have thermal sensing technology sensitive to crop water requirements for management decisions, leading to more efficient allocation of available resources for precision agriculture.

3.5 CONCLUSION

A TIRIS was developed for high spatial and temporal resolution monitoring of corn in order to observe crop stress from water deficits with concurrent soil moisture measurements in a greenhouse. The lightweight, low cost, and small size of the uncooled TIR camera used in this study maintained a measurement accuracy below $\pm 0.62^{\circ}\text{C}$ ($\alpha=0.05$) within a greenhouse. In addition, thermography hardware and techniques were investigated to increase crop based thermal relationships of isolated crop vegetation against a soil background with image processing. As observed, a stronger relationship was found regarding the predicted canopy-to-air temperature deficit versus VPD ($R^2=0.7364$) compared to the predicted stem-to-air temperature deficit versus VPD ($R^2=0.6592$).

Canopy temperatures were used to develop empirical canopy-to-air temperature deficits versus VPD regression curves for corn in order to quantify RT CWSI. Empirical NWSBs revealed that crop canopy temperature changed slightly throughout growth stages. Results indicated that canopy water deficit regression curves closely follow the characteristic water use curve throughout corn growth stages. Results from the 80-day study revealed that a significant decrease in soil moisture was measured only when the CWSI value increased past 0.6 with 82% of soil moisture variation explained by the CWSI. As observed, the CWSI was negatively correlated to soil moisture supporting the use of the CWSI as an alternate irrigation scheduling method in order to quantify spatial soil moisture by remotely measuring canopy temperature.

Chapter 4 - Developing a Thermal Infrared Imaging System for High Spatial Temperature Mapping aboard a Multirotor sUAS

4.1 ABSTRACT

Inadequate water application often decreases yield and product quality. Existing irrigation scheduling uses single, localized measurements that do not account for high-spatial crop water stress. Although quick, single-point sensors are impractical when covering large areas and measuring discrete variations, whereas thermal infrared (TIR) imaging, or thermography, is a novel approach for measuring high-spatial crop temperatures to quantify crop water stress. A small, lightweight thermal infrared imaging system (TIRIS) was developed using uncooled thermal cameras for a multirotor small unmanned aerial system (sUAS) providing imagery sensitive to spatial crop temperature variability. Imaging hardware and software was designed to provide uniform analysis advancing the ease of image capture, correction, throughput and storage management for subsequent thermal mapping. As studied, the Tamarisk® 320 (11 mm lens) and Tamarisk® 640 (25 mm lens) had 19% and 18% lens distortion, respectively, that image processing corrected. Adhering to a critical spatial resolution maximized surface data integrity and area coverage. A relationship between image overlap and camera views was created in order to determine a flight campaign that is capable of representing a target measurement with a given confidence. An image variance filter increased mapping efficiency by aligning 99% of images instead of 69%. A one-time radiometric calibration and real-time ground reference data provided absolute surface temperatures with environmental compensation yielding a $\pm 1.38^{\circ}\text{C}$ measurement accuracy. This research supports using uncooled thermal cameras to capture spatial crop temperatures, thereby allowing users to measure subtle crop dynamics for water resource management.

4.2 INTRODUCTION

In the midst of recent droughts, increased water demand, and implementation of water allocations for conservative purposes, irrigated acreage throughout the United States has increased by nearly 1.3 million acres from 2002 to 2007 (USDA, 2014). The largest percentage of irrigated farms is located in the Midwest where competition for available water resources has escalated in the past two decades (Taghaeian, et al., 2013). As a result, diminishing irrigated water requires efficient management practices that utilize monitoring and control in order to achieve sustainable

water management (Adeuya, 2007) from decision support tools (Rodriguez, et al., 2005) in order to increase water use efficiency (Ballester, et al., 2013; Cohen, et al., 2005; Gontia & Tiwari, 2008). Quantity of irrigated water and application time are among critical decisions producers need to make to develop site-specific irrigation plans (Alves & Pereira, 2000; Cohen, et al., 2005; Wanjura, et al., 1992) to precisely apply water to meet crop need at a controllable increment for desired crop performance (Cohen, et al., 2005; Taghvaeian, et al., 2013). Of the many types of crop stress, water stress is the most common and restrictive factor impacting crop yield (Colaizzi, et al., 2012; Jackson, et al., 1981; Scherrer, et al., 2011; Zia, et al., 2013) where water stress severity depends on timing and duration.

As a result, water use efficiency studies compare irrigated water use-to-yield, thereby resulting in management decisions that decrease water use from aquifers and above-ground freshwater sources while investigating soil-improving strategies where drought-tolerant crop varieties have been chosen for a climate's available water (Berton, 2006). Current irrigation schedules, however, are typically based on local, soil moisture sensors that do not account for the spatial moisture variability that may exist in commercial agricultural fields due to varying soil type and depth, topography, climate, specific crop growth period and a producer's operation (Cohen, et al., 2005; Evett, et al., 2014). Although advances in precision irrigation technologies are available for utilization, research shows that crop growth and yield is directly associated with crop water stress, and only partially related to soil-water interaction (Sepulcre-Canto, et al., 2011). More specifically, crops are more susceptible to stress during certain development periods when actionable intervention can maintain yield potential (Taghaeian, et al., 2013). Typical methods used to detect crop water stress utilize pressure chambers and leaf diffusion porometers to measure individual leaf stomatal conductance and leaf and stem water potential, respectively (Ballester, et al., 2013; Berni, et al., 2009; Grant, et al., 2007; Colaizzi, et al., 2012). However, these techniques are destructive, labor intensive, subject to placement error, limited by small sample size and unsuitable for automation (Ballester, et al., 2013; Berni, et al., 2009; Cohen, et al., 2005; Gontia & Tiwari, 2008; Jones, 1999; Leinonen & Jones, 2004), thereby limiting producer adoption for irrigation decision management (Ballester, et al., 2013).

To address these concerns, thermal sensing approaches have been investigated because they are non-contact and less labor intensive and offer non-destructive monitoring to assess crop stress from leaf canopy temperatures (Grant, et al., 2006; Leinonen & Jones, 2004). Crop water

stress is typically quantified by measuring canopy temperatures because plants close their leaf stomata during periods of water stress, thereby reducing transpiration and causing increased leaf temperatures (Evans, et al., 2000). Currently, static and/or dynamic arrays of infrared thermometers (IRTs) are used to measure canopy temperature (O'Shaughnessy, et al., 2012). Although single-point measurements are quick, IRT sensors are localized, whereas a thermal infrared imaging system (TIRIS), or thermography, monitors spatial crop temperatures via a thermal image. Thermography has only been investigated over the last decade (Hackl, et al., 2012) because the technology was only recently declassified by the military for civilian use (Schepers, 2012; Maes & Steppe, 2012).

Although once limited by slow processing speed, large memory requirements, and high hardware costs, imaging is being restudied for utility in precision agriculture (Wang, N., personal communication, November 1, 2013). With industrial applications using thermography for automation, TIRIS adoption has decreased the hardware cost while increasing sensing capabilities of thermal infrared (TIR) image sensors. Automatic image capture and analysis, however, are needed to account for error incurred with manual measurements such as setup and capture inconsistencies and latency that lead to small microclimate changes of the crop environment. Therefore, automatic imaging systems capture temperature information with high spatial (ground sample distance (e.g., 1 cm/pixel)) and temporal (repeat frequency) resolution essential for monitoring subtle crop dynamics (Kuenzer, 2014; Luquet, et al., 2003).

Thermal imaging studies that assess spatial canopy temperature in relation to dynamic crop stress assessment have become increasingly available (Jones, 1999; Liu, et al., 2011). Numerous studies prove thermography's ability to distinguish between irrigated and water-limited stress of grapevines (Grant, et al., 2006; Grant, et al., 2007), cotton (Luquet, et al., 2003), citrus trees (Ballester, et al., 2013), olive orchards (Berni, et al., 2009), and sunflowers (Hashimoto, et al., 1984) while supporting the development of greenhouse model comparisons (Grant, et al., 2006; Leinonen & Jones, 2004), genetic-based drought tolerance in maize (Liu, et al., 2011), leaf temperature association with biomass accumulation (Liu, et al., 2011), and spatial awareness of different leaf architecture (Ballester, et al., 2013; Grant, et al., 2007). This novel, less-studied technology has been discussed in limited publications that illustrate United States' research conducted with TIR cameras to measure spatial crop temperatures, specifically crops that experienced significant yield increase with irrigation. In conducted studies, orchards with sparse

canopy made thermal measurements difficult (Maes & Steppe, 2012) without spatial resolutions below 2 m (Sepulcre-Canto, et al., 2007), whereas applications with homogeneous cropland typical in agricultural production reduced imaging complexity. Increased use of thermography in agriculture, however, depends on increased spatial and temporal resolution in order to increase effectiveness and aid actionable decisions for precise, timely crop health monitoring (Sobrino & Julien, 2013; Taghvaeian, et al., 2013).

Current satellite and ground-based sensing platforms have limited the use of thermography in commercial agriculture because producers demand crop characteristics throughout entire fields with frequent revisit times. To meet this demand, TIRIS are flown aboard piloted aircrafts and small unmanned aerial systems (sUAS) with the advantage of high temporal and spatial resolution paired with on-demand analysis (Berni, et al., 2009; Zhang & Kovacs, 2012). Manned aerial imagery has shown potential in practical thermography because it solves previous platform limitations regarding the small coverage area of ground-based platforms and low spatial and temporal resolution of satellite-based platforms (Kuenzer, 2014). As a result, aerial imagery combines high measurable crop characteristics and increased ground coverage. In addition, aerial imagery can provide whole-field crop stress assessment with spatial resolutions up to 2 m (Berni, et al., 2009; Sepulcre-Canto, et al., 2007). In conducted studies, thermography aboard piloted aircrafts has been used to assess crop water stress (Scherrer, et al., 2011; Taghvaeian, et al., 2013; Tilling, et al., 2007; Wang, et al., 2010), screen phenotypes (Zhao, et al., 2005), and conduct irrigation maintenance (Schepers, 2012).

However, a trade-off exists between ground coverage area and measurable crop characteristics. Even aboard piloted airplanes, the primary limitation is spatial resolution of TIR cameras. In addition, expense, fuel limitations, pilot fatigue, infrequent revisit times, and unfamiliar complexity of flying and hiring aerial imagery limit widespread commercial use (Berni, et al., 2009; Goel, et al., 2000; Herwitz, et al., 2004). As a result, advancements in technical capabilities and regulatory standpoints for sUAS have increased interest in aerial imagery (Herwitz, et al., 2004). As a result, the sUAS industry is evolving rapidly to expand its role as a complementary platform to satellites and piloted aerial imagery for tactical farm management (Zia, et al., 2013).

Producers support sUAS adoption because sUAS platforms provide low-altitude imagery for high-definition images, on-demand response times, and low investment costs (Goel, et al.,

2000; Laliberte, et al., 2011; Rango, et al., 2009) for crop health characterization for agronomic decision management not previously possible. Another advantage of sUAS is their ability to fly at low airspeeds (30 km h^{-1}) under manual control or autopilot flight campaigns with predetermined flight routes for ease of operation and application mapping in order to sense areas not previously accessible because of distance, time, or terrain (Luvall & Holbo, 1991; Rango, et al., 2009). These advantages make sUAS the most promising sensing platform for spatial resolution crop assessment (Maes & Steppe, 2012; Rango, et al., 2009) at a fraction of the price of manned aerial platforms (Berni, et al., 2009). Currently, commercial autopilot control, cost-effective telemetry, and semi-automated image geo-rectification systems promote the feasibility of sUAS in precision agriculture (Berni, et al., 2009; Herwitz, et al., 2004; Laliberte, et al., 2011; Rango, et al., 2009; Wooster, et al., 2013).

Low-altitude image mapping captures a large series of images across a field over a quick timespan where manual or automatic image processing software stitches images together from common points within individual images, ground control points, or global position system (GPS) coordinates of the camera or sUAS flight controller (Berni, et al., 2009). With low flight speeds and high image capture, high spatial resolution imaging uses only the central portion, or nadir, of the image to improve composite image quality (Berni, et al., 2009; Vasterling & Meyer, 2013). As a result, an orthomosaic image is generated to form a whole-field composite image collected at a consistent altitude (Rango, et al., 2009).

Several sUAS platform configurations are available for agricultural use. Each platform configuration has different flight dynamics useful for specific coverage applications. Furthermore, flight characteristics of multirotor sUAS make them best suited for high-definition site-specific monitoring because of their ability to hover and capture quality imagery from different altitudes. Due to the design and weight of multirotor sUAS, flight times are typically less than other sUAS platforms, consequently requiring different payload considerations (Rango, et al., 2009). Regardless of the sUAS platform, commercial sUAS employ automatic machine control to simplify flight operation and regulate flight altitude and path uniformity (Rango, et al., 2009).

Although low flight altitudes increase thermography's ability to measure crop health characteristics at scales more suitable for commercial applications, sUAS are subject to the same atmospheric effects as other sensing platforms (Berni, et al., 2009; Maes & Steppe, 2012). In addition, field scouting and manual processing is still needed if growers are to understand

measured crop health response and implement management zones (Goel, et al., 2000). As a result, quality control of data from in-field flight operations make real-time ground truthing (i.e., provide correction to a remote measurement with ground-based measurement data) possible increasing the repeatability of estimates and assessments (Rango, et al., 2009). With on-the-ground measurements, aerial and ground truthed measurements support direct interpretation of plot-based indicators in detection studies (Rango, et al., 2009). Validation during a time series relies on permanently installed non-contact or contact (ground or air) measurement devices with data loggers capable of simultaneous wind speed and direction, humidity measurements, air temperature, and solar radiance (Kuenzer, 2014). Artificial reference measurements have provided a repeatable standard for increased application scales when used in conjunction with thermal imaging (Moller, et al., 2007) where real-time environmental measurements allow for consistent crop water stress assessment (Maes & Steppe, 2012).

Thermal cameras provide sub-meter spatial resolution aboard sUAS (< 2 m) (Berni, et al., 2009) and have flexible revisit times for whole-field temperature mapping (Cohen, et al., 2005). This potential to meet the needs of agricultural use provides an incentive for thermal camera manufacturers to develop modified cameras for operation within agricultural field conditions. However, available knowledge regarding thermal sensing platform performance in field studies aboard sUAS is limited. Consequently, producers are skeptical towards a technology that has enabled site-specific water management in orchards, vineyards, and other specialty crop fields in areas outside of the United States (Sepulcre-Canto, et al., 2011). Lack of knowledge is due primarily to the high cost of cooled TIR cameras, which has made measurement of spatial crop temperature in commercial agriculture economically unfeasible. However, innovation of the uncooled thermal sensor has allowed new uncooled TIR cameras to be small and lightweight, consume less power, and require no cooling package, thereby providing extended operating life at a fraction of the cost of previous cooled TIR cameras. Uncooled TIR cameras aboard sUAS have been emphasized because they demonstrate a potential for increased ground coverage and crop stress assessments beyond the range of previous remote sensing platforms for tactical farm management (Herwitz, et al., 2004).

With the aforementioned potential for high spatial and temporal temperature mapping from sUAS, studies using thermography have been limited due to camera expense, unfamiliar use and standard operating protocol, system complexity and calibration, and limited software for image

acquisition and high throughput processing for thermal imagery. Therefore, research objectives of this study were to (1) develop a small, lightweight TIRIS for temperature mapping aboard a multirotor sUAS, (2) develop a complementary hardware and software package to radiometrically calibrate TIRIS during infield setup while providing in-flight ground truthing, 3) develop a software program to upload and process imagery prior to image stitching, and 4) construct radiometric spatial temperature maps.

4.3 METHODS AND MATERIALS

A study was conducted to develop a small, lightweight TIRIS with an uncooled Tamarisk® 320 and 640 TIR cameras (DRS Technologies, Inc., Dallas, Texas) offering a low and high spatial resolution configuration. The development of a TIRIS for thermal mapping aboard a multirotor sUAS has been supported with preliminary studies that investigated the physical properties and environmental conditions that restrict the practical use of TIR cameras' in precision agriculture. During preliminary evaluations described in Chapter 2, hardware and software required to integrate an uncooled TIR camera core into an imaging system were identified and developed in order to measure surface temperatures. A TIRIS was built to include a sUAS thermal imaging acquisition system, in-field calibration system, and ground reference monitoring system for real-time environmental parameters during flight campaign. SUAS flight campaigns were conducted to investigate control ease, standard operating protocol, radiometric calibration, and measurement accuracy, thereby completing system validation. Resulting aerial temperature mapping efficiency was investigated regarding image quality and processing prior to creating a temperature map.

4.3.1 Intrinsic Camera Properties

TIR cameras contain physical parts and capabilities that influence their sensitivity to discrete temperature differences, increase their measurement error, and limit their use in agricultural environments. In preliminary studies, physical properties that restricted TIR camera use were identified and investigated as the following:

1. Image resolution and measurement
2. Lens distortion
3. Warm-up time and automatic recalibration
4. Radiometric characterization and measurement accuracy
5. Connection ease, software, and controllability

These physical properties and their influence on accurate surface measurement were considered in order to minimize influence by configuring the camera and hardware for use aboard sUAS, designing image processing software specifically for thermal imagery, generating standard operating protocol, and selecting a camera-lens combination suited for the sensing platform. System expectations for validation included maintained temperature measurement accuracy, camera controllability, limited image noise, and spatial accuracy.

4.3.1.1 Image resolution and measurement

The sensed target size and sensing distance determines a particular lens choice (Elfaki, et al., 2000). In addition, because of their particular role in preventative maintenance in non-agricultural roles and limited research studies, TIR sensor technology typically cannot compare to spatial resolutions of visible cameras. Because of the germanium lens, TIR camera lens are factory-installed and calibrated leaving no room for error when selecting the correct lens. For this study, two different TIR camera cores were chosen based on their small size, low weight, limited power consumption, capture framerate, and thermal detector, called a microbolometer, resolution. For coarse spatial resolution applications and lighter payload weight, a DRS Tamarisk® 320 TIR camera core with a 320×240 fixed pixel array microbolometer was chosen featuring an 11 mm lens with a 27°×20° field of view (FOV). For high spatial resolution applications, a DRS Tamarisk® 640 TIR camera core with a 640×480 fixed pixel array microbolometer was chosen featuring a 25 mm lens with a 24°×19° FOV. Table 4.1 illustrates the theoretical spatial resolutions and FOV with the chosen lens at select sensing distances.

Table 4.1. Spatial resolution with selected lens at various distances. Adapted from DRS Technologies A Finmeccanica Company, (2013).

Camera Core	Distance (m)	20	40	60	80	100	120
Tamarisk ® 320 (11 mm lens)	^[a] mm/pixel	31 [10×8]	62 [20×15]	93 [30×22]	124 [40×30]	155 [50×37]	186 [61×45]
Tamarisk ® 640 (25 mm lens)	^[a] [FOV m × m]	14 [9×7]	27 [18×13]	41 [27×20]	54 [35×26]	68 [44×33]	82 [53×36]

^[a] Round to nearest integer

Temperature mapping use the theoretical FOV, critical spatial resolution, and the desired level of detail specific to the sensing application in order to determine the sUAS autopilot flight program regarding altitude, flight speed, and flight orientation. These flight parameters have direct implications on the resulting orthomosaic from sufficient image overlap, camera stability, and the volume of images captured to sense the entire coverage area (Rango, et al., 2009). In addition, a sensing distance depicts the on ground coverage. For example, the Tamarisk® 640, flown at 40 m

with a nadir orientation, will have a spatial resolution of 27 mm/pixel and the resulting image will have an on-ground coverage of 18×13 m (Table 4.1).

In application, measurement error can be introduced from bidirectional reflectance due to varying incident radiation (Jones, et al., 2009). Unlike visible imagery that is subject to incident visible light radiation, thermal imagery is subject to bidirectional effects of thermodynamic heat transfer. Time and changing viewing angle between images may cause subtle temperature differences between targets from changes in convective, conductive, and radiant heat transfer due to changing air temperature, relative humidity, air drawn across the target surface, and incoming solar radiation. To account for bidirectional influence, multiple camera viewing angles provide a more representative sampling mean of a target’s temperature (Jones, et al., 2009). In general, each pixel intensity within an orthomosaic image is calculated from multiple camera views to represent an average target intensity. As a result, image overlap improve this representative pixel intensity by providing multiple camera views defined by the lateral and forward overlap as defined by Equation (4.1):

$$No. of Camera Views = \left(\frac{100}{100 - \% Overlap_{Forward}} \right) \times \left(\frac{100}{100 - \% Overlap_{Lateral}} \right) \quad (4.1)$$

Using Equation (4.1, for example, a forward and lateral overlap of 75% and 75%, respectively, results in 16 camera views of a specific target surface. Uniform forward and lateral image overlap is an important criteria when planning the flight campaign in order to increase the confidence level that a measurement truly represents the target surface. In addition, increased overlap produces more measurement samples of a target thereby reducing the standard error of the mean pixel intensity within the orthomosaic image.

4.3.1.2 Lens Distortion

Maintained lens focus over a wide span of temperatures is essential for quality thermography. Unlike autofocus of a typical visible camera, the lens focal length must be adjusted to focus on particular sensing distances (DRS Technologies A Finmeccanica Company, 2013). TIR camera lenses are constructed from an expensive material known as germanium, which is transparent to thermal radiation (Kuenzer, 2014). Germanium lenses are optimized for radiometric transmission, increasing the susceptibility to geometric distortion that causes spatial inaccuracy. A distorted image does not fully represent real spatial points but a distorted location dependent on

the position within the lens' field of view (FOV) (x_1, y_2), as defined by Equations 4.2 and 4.3 (The Mathworks, Inc., 2015):

$$x_2 = x_1(1 + k_1r^2 + k_2r^4) + 2p_1x_1y_1 + p_2(r^2 + 2x_1^2) \quad (4.2)$$

$$y_2 = y_1(1 + k_1r^2 + k_2r^4) + 2p_2x_1y_1 + p_1(r^2 + 2y_1^2) \quad (4.3)$$

Where:

x_1, y_1 = distorted pixel locations

x_2, y_2 = undistorted pixel locations

k_1, k_2 = radial distortion coefficients of the lens

p_1, p_2 = tangential distortion coefficients of the lens

$$r = \sqrt{x_1^2 + y_1^2}$$

Because the manufacturer does not provide lens distortion coefficients, lens distortion was investigated using a Grid Distortion Model calibration approach based on multiple grid calibration images and a heated grid pattern tool (Figure 4.1).

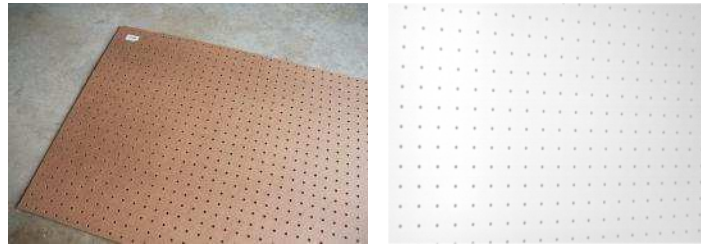


Figure 4.1. Grid pattern tool (left) and thermal image (right) used for lens distortion.

Thermal images were imported into the NI LabVIEW™ Vision Assistant (National Instruments Corporation, Austin, Texas) for lens distortion analysis. Resulting lens distortion coefficients were used in the image processing algorithm for batch processing in order to undistort images for precise location using Equation 4.2 and 4.3. See Section 2.4.1 for more details.

4.3.1.3 Warm-up Time and Camera Recalibration

Because uncooled TIR cameras operate without heavy cooling jackets, uncooled TIR cameras regulate their thermal detectors with automatic temperature re-calibration to maintain sensor accuracy and limit sensor measurement drift caused by temperature fluctuations (DRS Technologies, Network and Imaging Systems Group, n.d.). A shutter recalibration technique is activated to conduct a non-uniformity correction (NUC) across the thermal detector at either a user-defined time interval and/or in the event of an internal temperature change of the thermal detector (DRS Technologies, Network and Imaging Systems Group, n.d.). During a NUC, the camera shutter closes to block incoming thermal energy, thereby providing a uniform thermal reference for the detector. At that time, a recalibration algorithm ensures a uniform pixel intensity

is measured across the entire microbolometer. As a result, each TIR camera core's warm-up time was previously determined (Figure 4.2). Warm-up times of 19 and 18 min and a 1 minute timed-interval NUC were necessary for stable temperature measurement of the Tamarisk® 320 and 640, respectively. Adherence to the required warm-up period during standard operating protocol reduces inaccuracy as the camera reaches a stable operating temperature.

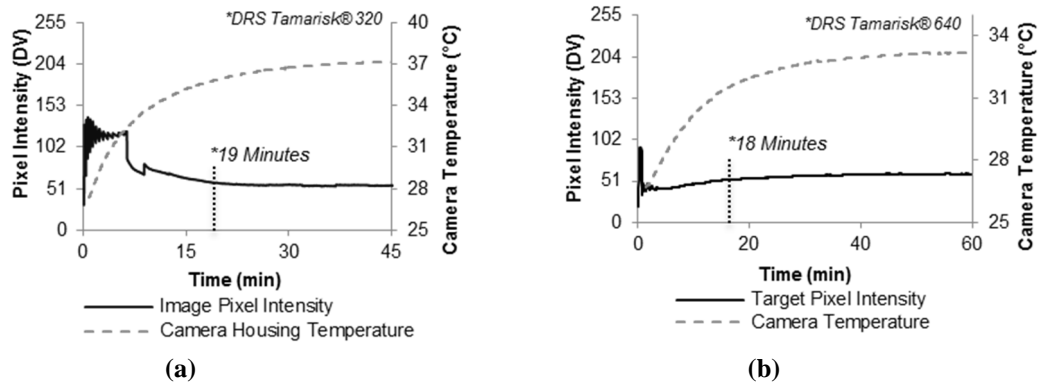


Figure 4.2. Image Intensity and housing temperature versus thermal camera on-time of (a) DRS Tamarisk® 320 and (b) DRS Tamarisk® 640. Indicated warm-up time was determined when the TIR camera measured with 5% of the stable pixel intensity. See Section 2.3.1.4 for more details.

4.3.1.4 Radiometric Calibration

Because uncooled TIR cameras have a low signal-to-noise ratio, their thermal detectors are less sensitive ($\pm 0.1^{\circ}\text{C}$) than other temperature sensors (Kuenzer, 2014). However, microbolometers are sensitive to subtle temperature differences ($< 0.5^{\circ}\text{C}$) necessary for accurate crop stress assessment (Blonquist & Bugbee, n.d.; Sepulcre-Canto, et al., 2007). In the context of agricultural sensing applications, the Tamarisk® 320 and 640 are sensitive to 8 to 14 μm longwave infrared (LWIR) radiation corresponding to a -66°C to 90°C temperature span. In operation, LWIR radiation strike the detector material, altering the electrical resistance from a temperature change, transforming LWIR radiation intensity into a raw digital value (DV), thereby generating a thermal image (Kuenzer, 2014).

A limitation of uncooled TIR cameras, however, is their inability to quantify absolute temperatures. Therefore, an one-time (OT) radiometric calibration method was used to quantify absolute surface temperature at environmental conditions in which the uncooled TIR camera was calibrated, as described Section 4.3.3. An OT radiometric calibration uses one calibration image to characterize pixel-to-temperature relationships, as shown below in Figure 4.3. For full description of the OT radiometric calibration method, see Section 2.3.1.3.

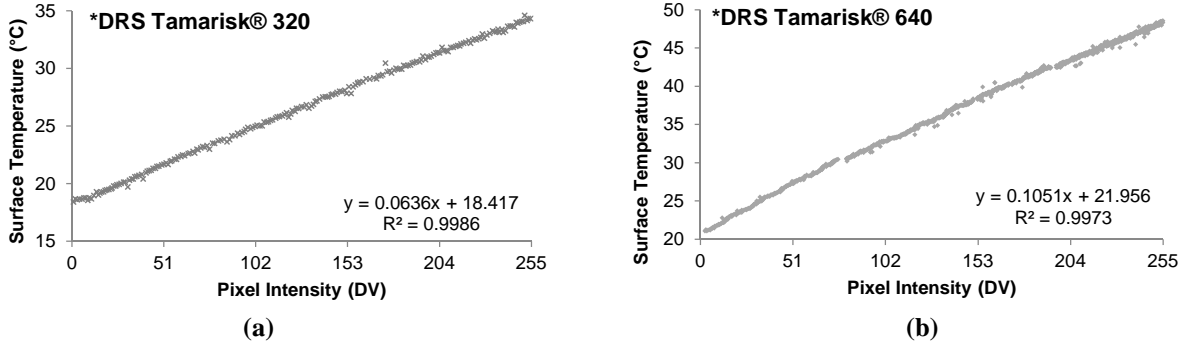


Figure 4.3. Radiometric calibration performed on (a) DRS Tamarisk® 320 and (b) DRS Tamarisk® 640 at 25°C air temperature and 35% relative humidity when each uncooled thermal camera reached a steady operating temperature.

Using the radiometric calibration transfer function, each uncooled TIR camera core was found to be directly sensitive ($R^2 = 0.99$) to the temperature within the FOV (Figure 4.3). Results demonstrate uncooled thermal cameras’ ability to measure absolute temperatures with additional hardware and software, standard operating protocol for radiometric calibration, and strict camera configurations.

As previously studied in Section 2.4.4, the OT radiometric calibration method was developed especially for quantifying temperatures aboard a dynamic sensing platform like a sUAS. To determine the TIR camera’s ability to measure temperatures, the absolute difference between actual and measured temperature is shown in Figure 4.4. Results reveal the maximum measurement accuracy is $\pm 0.82^\circ\text{C}$ and $\pm 0.81^\circ\text{C}$ ($\alpha=0.05$) for the Tamarisk® 320 and 640, respectively (Table 4.2). For application, a sensing time of 60 minutes demonstrates the maintained measurement accuracy throughout the typical flight time of a multirotor sUAS (Rango, et al., 2009).

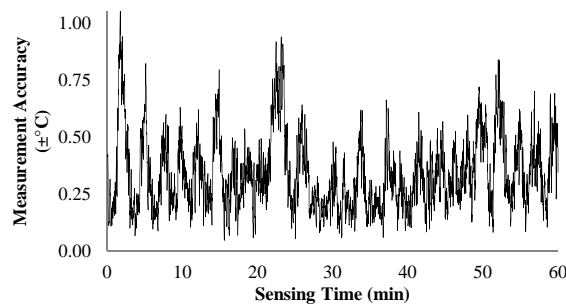


Figure 4.4. Measurement accuracy ($\pm^\circ\text{C}$) of the Tamarisk® 320 over 60 min. The absolute difference between the actual and measured temperature is shown.

<i>Tamarisk</i> ® 320	0.82
<i>Tamarisk</i> ® 640	0.81

4.3.1.5 Connection Ease, Software, and Controllability

Each TIR camera core provides an 8-bit (256 discrete pixel intensity DV) thermal video. Within the TIR camera control software, each camera was configured for video output and frame rate, and thermal detector sensitivity. In order to set the DRS Tamarisk® 320 and 640 camera cores, a DRS breakout board module (Breakout Box 1003785-001, DRS Technologies, Inc., Dallas, Texas) adjusts the thermal detector gain sensitivity (i.e., detectable scene temperature span) and level control (i.e., shift offset of the center temperature within the temperature span), thereby improving detected thermal energy of the scene temperatures (Figure 4.5).

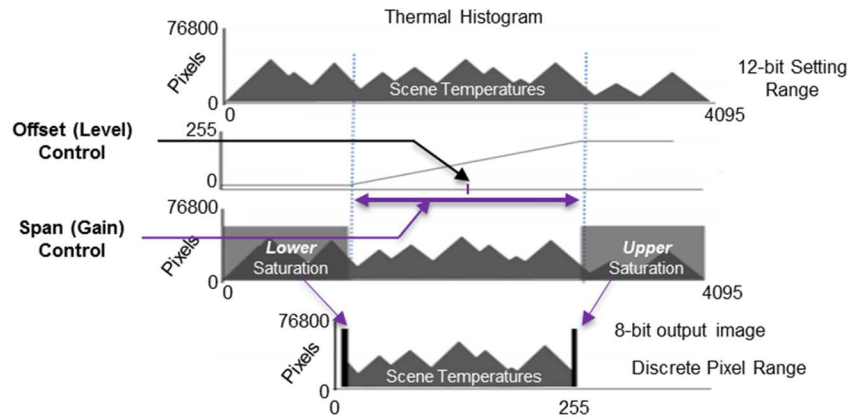


Figure 4.5. The gain control adjusts the thermal detector sensitivity to LWIR energy thereby adjusting the temperature span. Level control adjusts the center offset temperature to adjust the bias of the temperature span. Adapted from DRS Tamarisk® 320 Camera Control Software User Guide (2013).

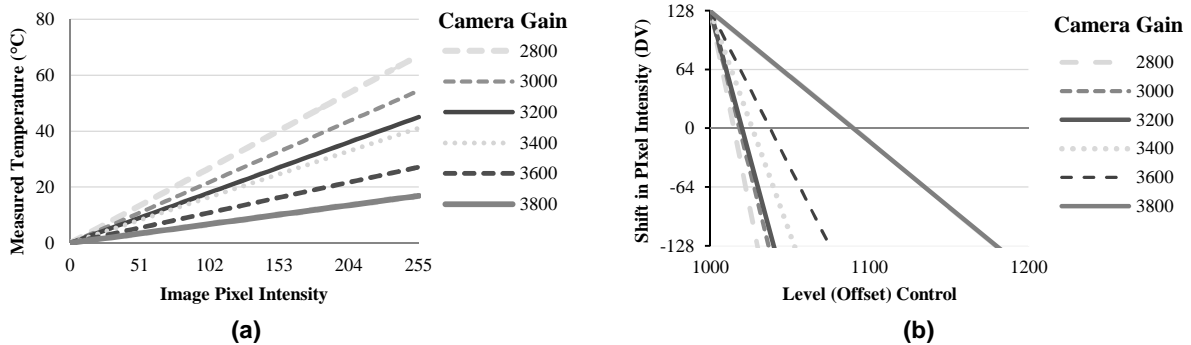


Figure 4.6. DRS Tamarisk® 320 Camera (a) camera (a) gain for temperature span and (b) level setting characteristics for offset temperature bias.

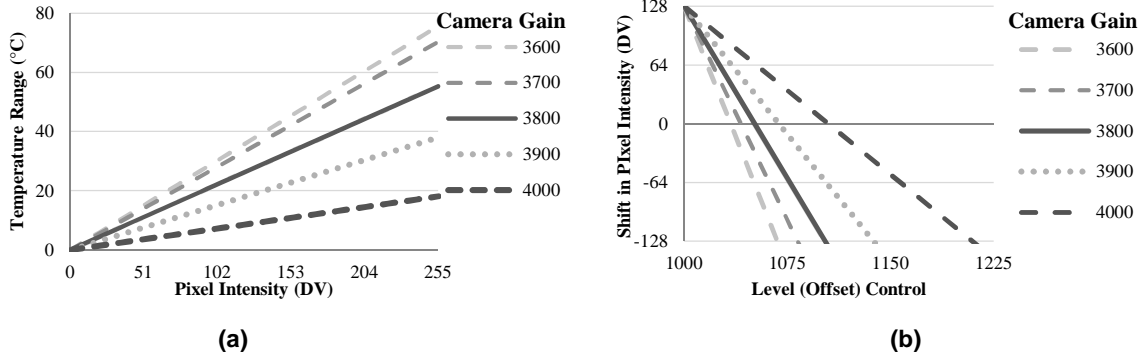


Figure 4.7. DRS Tamarisk® 640 camera (a) gain for temperature span and (b) level setting characteristics for offset temperature bias.

As previously studied in Section 2.4.6, manual control of the DRS Tamarisk® 320 and 640 thermal detector gain and level yielded a configurable temperature span from 5°C to 156°C and resolution from 0.02°C to 0.61°C. As shown in Figures 4.6 and 4.7, camera control software adjusted the limits of upper and lower pixel saturation while adjusting measurable temperature resolution on object targets. For example, a temperature span of 20°C is set by the camera gain control whereas a center temperature of 25°C is controlled by the level control. In this example, the lower and upper saturation temperatures would be at 15°C and 35°C, respectively. In addition, the temperature resolution of the resulting 8-bit image of a 20°C span would equal 0.08°C, as defined by Equation 4.4:

$$T_{resolution} (\text{°C}) = \frac{T_{span} (\text{°C})}{2^n} \quad (4.4)$$

where:

- T_{span} =Span of temperatures (°C) measureable by the thermal detector
- N =bits of resolution (e.g., $N=8$ for 8-bit images), and
- $T_{resolution}$ =theoretical temperature resolution

Combining temperature span and incremental offset level range reveal a significant relationship shown in Figure 4.8. Each level control increment offsets the temperature span by 0.107 °C, regardless of gain control. This was directly applicable for use in the field calibration software in order to provide suggested camera configurations for a particular temperature span and center temperature of interest as discussed below in the complementary TIR camera software detailed in Section 4.3.2.

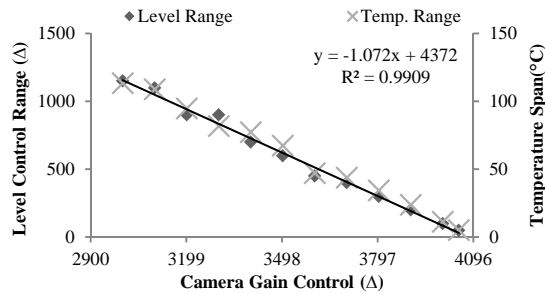


Figure 4.8. Relationship between level control range (Δ level) and temperature span ($^{\circ}\text{C}$).

4.3.2 Hardware and Software Development

Three distinct portions of the TIRIS are segmented into the sUAS TIRIS, OT calibration, and ground reference station. The system hardware and software was specifically developed to configure the TIR camera core within the sUAS TIRIS, provide OT radiometric calibration, and measure real-time environmental parameters for in-flight ground truthing in order to compensate for environmental conditions and maintain measurement accuracy (Figure 4.9).



Figure 4.9. TIRIS component system diagram for camera calibration and ground reference data

The sUAS TIRIS featured either the Tamarisk® 320 or 640 TIR camera core, depending on application and desired image resolution. The DRS breakout board module (Breakout Box 1003785-001, DRS Technologies, Inc., Dallas, Texas) functioned as the camera configuration board, video interface, and power input. Analog video was stored in video form using a miniature digital video recorder (RMRC FPV1000 DVR, ReadymadeRC, USA). The TIR camera cores and video recorder were set to record video at 30 frames per second. Power was supplied with an 11.1 volt battery (RMRC 1100mAh 3S 35C, ReadymadeRC, USA).

The ground reference station measured in-flight ground truthing reference data, such as air temperature and relative humidity, reference temperature panels, solar radiance, and global positioning from a GPS receiver. Air temperature and relative humidity were measured with an

Omega (HX303AV, Omega, Stamford, Connecticut) transmitter sensor with an accuracy of $\pm 3\%$ and $\pm 0.3^\circ\text{C}$. Solar radiance was measured with a pyranometer (SP115, Apogee Instruments, Logan, Utah) with accuracy of $\pm 0.25 \text{ W m}^{-2}$. Three surface mounted thermistors (ON-930-44004, Omega Engineering, Stamford, Connecticut) capable of temperature measurements with an accuracy of $\pm 0.1^\circ\text{C}$ were used to measure temperature panels in order to create reference surface temperatures. Thermistors were wired into a voltage divider to monitor a change in voltage due to temperature-based resistance (Figure 4.10 a) where analog thermistor signal inputs were programmed with LabVIEW™ sub-VIs using the factory supplied calibration curve, shown in Figure 4.10 b.

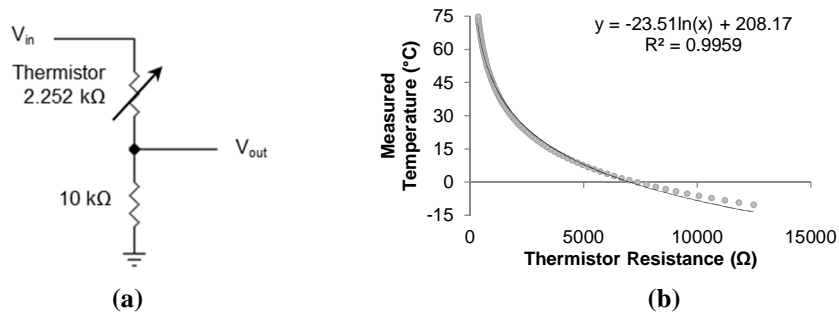


Figure 4.10. (a) Voltage divider wiring diagram used to measure voltage due to thermistor resistance change. (b) Thermistor calibration curve to quantify temperature with change in resistance. (See Appendix B, Figure A.4 for more details)

One of the three reference panels was fabricated from a $0.30 \times 0.60 \text{ m}$ piece of 1.52 mm thick (14 gauge) aluminum sheet metal and painted flat black. The second reference panel was fabricated from a $0.60 \times 1 \text{ m}$ piece of 6.35 mm thick wood that was painted flat black. The third reference panel was identified as a wet reference. To make the wet reference, a $0.30 \times 0.60 \text{ m}$ polystyrene foam pad was covered with a highly evaporative cloth (Chilly Padd, Arab, Alabama) that rapidly cooled when exposed to air. This foam piece was placed in a tub of water to allow continuous wicking and evaporation. In order to provide an emissivity correction, indirect background temperatures of the sky were measured from a viewable horizontal lambert radiator (i.e., crimped aluminum sheet metal). Differential temperatures provide visible reference temperatures within the TIR camera's FOV from aboard the sUAS (Figure 4.11 a).

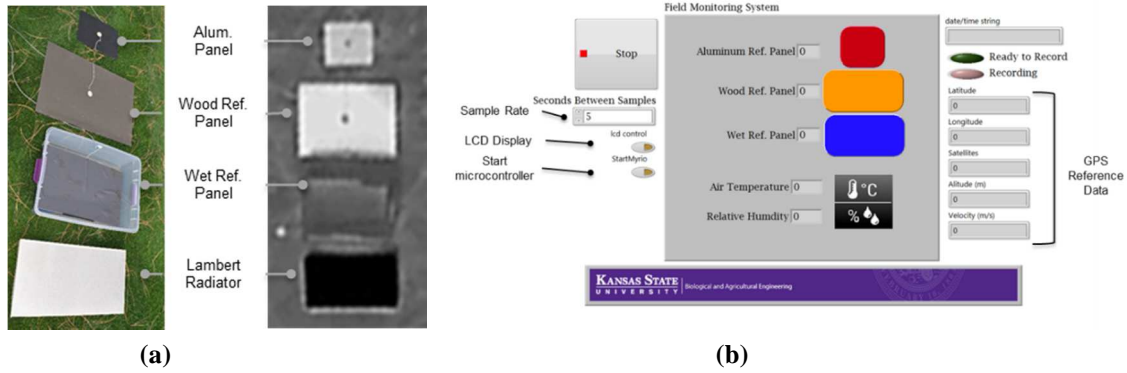


Figure 4.11. (a) Ground reference panels for temperature reference and cross-calibration from sensing distance and environmental influence in radiant heat transmission with (b) the virtual interface for control and visual awareness.

A commercial IRT (Fluke 62 MAX, Fluke Corporation, Everett, Washington) with an accuracy of $\pm 1^\circ\text{C}$ and emissivity adjustments from 0.1 to 1 found the emissivity (ϵ) of the lambert radiator, painted wood, aluminum, and wet reference surfaces to be 0.05, 0.82, 0.88, and 0.96, respectively (See Section 1.2.2 for more details on how this was performed). Reference temperature panels were sized to be viewable from aboard the sUAS and materials were constructed with a high surface emissivity in order to increase measurement accuracy (Figure 4.11 a). Since the reference targets are not perfect emitters or absorbers, the total LWIR radiation from a surface is part emitted and reflected LWIR radiation as defined in Equation 4.5 (Maes & Steppe, 2012):

$$LWIR_{out} = LWIR_{emitted} + LWIR_{reflected} \quad (4.5)$$

Where:

$LWIR_{out}$ = Outgoing radiant energy

$LWIR_{emitted}$ = Emitted radiant energy

$LWIR_{reflected}$ = Reflected radiant energy.

In Equation 4.5, the measured temperature from the TIR camera corresponds to the outgoing radiant energy ($LWIR_{out}$) which is measured as the apparent temperature (T_{ap}). As suggested by Maes et al. (2012), apparent temperature is influenced by background temperature (T_{bg}), surface temperature (T_s), and surface emissivity (ϵ), defined by Equation 4.6:

$$T_s = \sqrt[4]{\frac{T_{ap}^4 - (1 - \epsilon)T_{bg}^4}{\epsilon}} \quad (4.6)$$

Where:

T_s = Surface temperature $^\circ\text{C}$

T_{ap} = Apparent temperature $^\circ\text{C}$

ϵ = Emissivity

T_{bg} = Background temperature $^\circ\text{C}$

After accounting for background temperatures (T_{bg}) and surface emissivity (ϵ), the TIR camera provides surface temperature (T_s) rather than apparent temperature (T_{ap}).

A data acquisition (DAQ) system was built using a NI myRIO (National Instruments Corporation, Austin, Texas) in order to capture thermistors, air temperature, relative humidity, solar radiance, and global position and time, as shown in Figure 4.12. Data was captured at 5 hz matching the frequency of the GPS receiver (Crius CN-06 V3 GPS Receiver Module, Swiss U-Blox, Thalwil, Switzerland). The DAQ was programmed to store all sensor data files in a measurement file into a flash storage device. Each data sample in the ground reference measurement file had a corresponding time stamp that was parsed from a GPS national marine electronics association (NMEA) message string provided by a GPS receiver. Each thermal video had a corresponding ground reference measurement file.

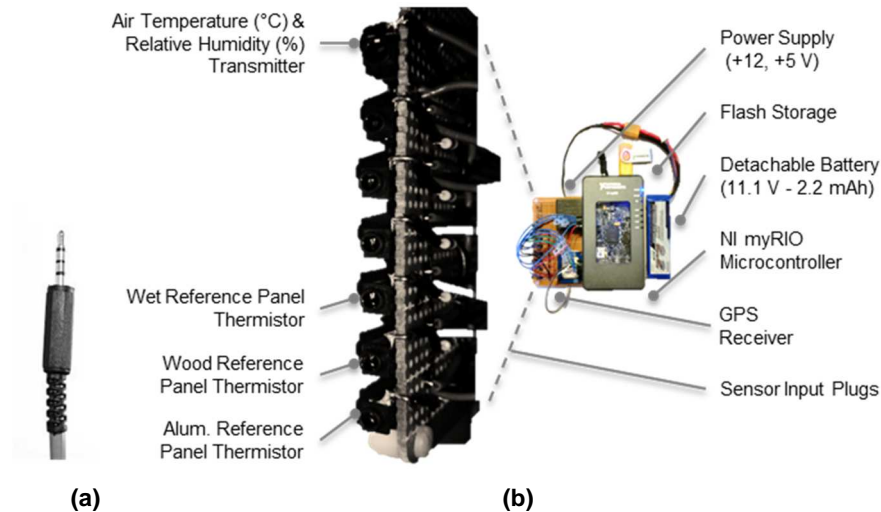


Figure 4.12. (b) Data acquisition system used to interface ground reference sensors with (a) plug-n-play sensor inputs

A lipo battery (RMRC 2200mAh 3S 35C, ReadymadeRC, USA) supplied power to a power supply in order to provide sensor excitation voltages and power to the microcontroller.

For the OT calibration components, analog video from the sUAS TIRIS was streamed at 30 Hz into an analog-to-digital video converter (Dazzle DVD Recorder HD, Corel Corporation, USA). This raw analog video signal was streamed into a host computer aboard sUAS using LabVIEW™ (National Instruments Corporation, Austin, TX) image acquisition and processing software in which each video frame was captured, processed, and stored using a developed virtual interface (VI) (Figure 4.14) to radiometrically calibrate the TIRIS and provide ground reference data. Ground reference data from the DAQ was wirelessly sent to the host computer using a

developed VI to perform on-ground OT radiometric calibration before flying the sUAS and monitor in-field data of the ground monitoring station.

4.3.3 Radiometric Calibration and Ground Reference Data

For an on-ground OT radiometric calibration, direct surface temperature measurements (Figure 4.13) and camera pixel intensity from the analog video stream were monitored with a TIR Field Calibration (TFC) software program developed with NI LabVIEW™ (National Instruments Corporation, Austin, TX) (Figure 4.14). The on-ground OT radiometric calibration was conducted by holding the camera to include the cold and warm reference panels in the camera FOV (As shown in Figure 4.13 c). Raw pixel intensities from the video feed (X_1 , X_2) were combined with actual surface temperature (Y_1 , Y_2) to determine the radiometric transfer function slope, as defined by Equation 4.7. By using the slope found in Equation 4.7 and a raw pixel and coinciding temperature (X_1 , Y_1), the y-intercept of the radiometric calibration curve was determined using Equation 4.8. When a radiometric transfer function was found, each digital image pixel was converted to a temperature value defined by Equation 4.9. Using results from Equation 4.9, upper and lower saturation temperatures were found by creating a visual temperature legend for the image (Figure 4.14). Instantaneous temperature span and center level was found as defined by Equation 4.10 and 4.11, respectively. For ease of camera configuration, characteristic gain and level responses (Equations 4.10 and 4.11) were used to set the cameras for a user-defined span and center level temperature as defined by Equations 4.12 and 4.13.

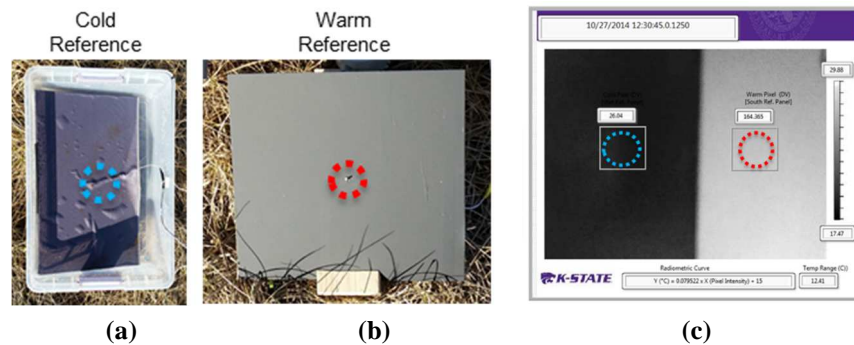


Figure 4.13. OT radiometric calibration use the cold and warm temperature differential created by (a) the wet reference panel and (b) the black aluminum panel measured with surface mount thermistors in the designated ROI shown in blue and red. (c) The corresponding TIR camera FOV is shown to demonstrate the temperature differential of the cold and warm reference.

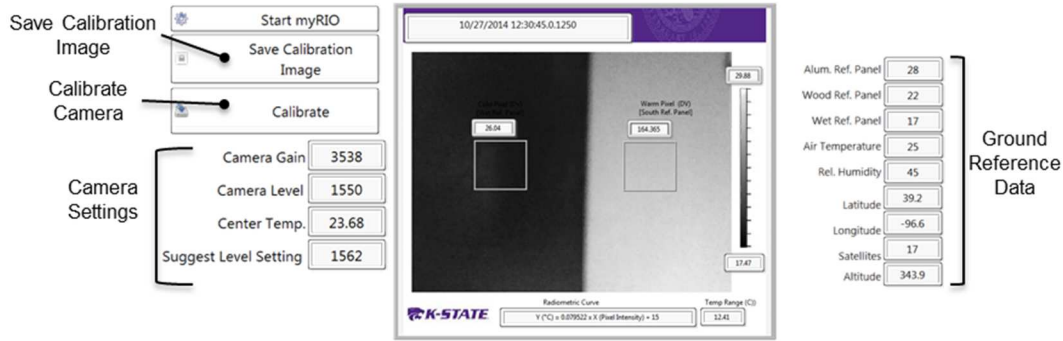


Figure 4.14. TIR Field Calibration (TCP) VI to create OT radiometric calibrations while recording ground reference data. The visual indicator shows the VI monitored RT ground reference data, raw video feed, and file storage specifications while providing controls to conduct a OT Calibration.

$$m = \frac{Y_2 - Y_1}{X_2 - X_1} \quad (4.7)$$

$$Y - Y_1 = m(X - X_1) \quad (4.8)$$

$$T_{(i,j)} = T_{min} + \frac{I(i,j)}{2^N - 1} T_{span} \quad (4.9)$$

where:

$T_{(i,j)}$ = Pixel temperature (°C) at row i and column j ,

T_{min} = Lowest temperature within the image (°C),

$I_{(i,j)}$ = Pixel intensity at row I and column j ,

N = Number of bits for pixel intensity (e.g., $N=8$ for 8-bit images), and

T_{span} = Span of temperature captured in the image.

$$\text{Temperature Span (}^\circ\text{C)} = \text{Bits of Resolution} \times \text{Radiometric Slope [m]} \quad (4.10)$$

$$\text{Center Temperature (}^\circ\text{C)} = 128 \times \text{Radiometric Slope [m]} \quad (4.11)$$

$$\text{Camera Gain Setting (}^\circ\text{C Range)} = -9.5289 \times \text{Desired Temperature Span} + 4109.34 \quad (4.12)$$

$$\text{Suggested Control Level} = \text{Current Center Temperature (}^\circ\text{C)} - \text{Desired Center Temperature (}^\circ\text{C)} \quad (4.13)$$

4.3.4 Camera Housing Design

The multirotor sUAS contained a gimbal camera mount below the main airframe to maintain stable nadir camera orientation for improved aerial thermography. A small, lightweight camera case was developed to house all sUAS TIRIS components and provide protection while aboard the sUAS. Each component of the camera case was generated using computer aided design (CAD) modeling (Pro/Engineer, PTC Inc., USA) (Figure 4.15). A 3D printer (Makergear™ LLC, Beachwood, Ohio) was used to print a camera case out of polyactic acid (PLA) plastic because of printing ease and UV protection for use in the field.

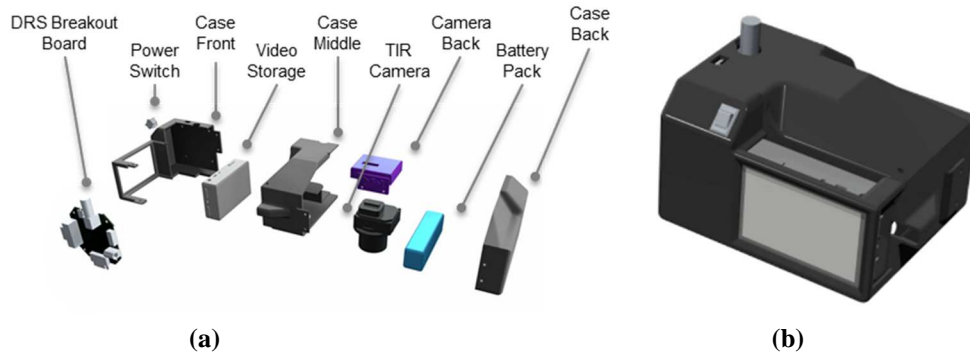


Figure 4.15. TIR camera case to hold sUAS TIRIS components in (a) the exploded view and (b) the collapsed view.

4.3.5 Flight Campaigns

The sUAS TIRIS was flown aboard a hexacopter multirotor sUAS (s800 Evo, DJI, China). The thermal camera was mounted on the gimbal for constant nadir orientation (Figure 4.16 b).

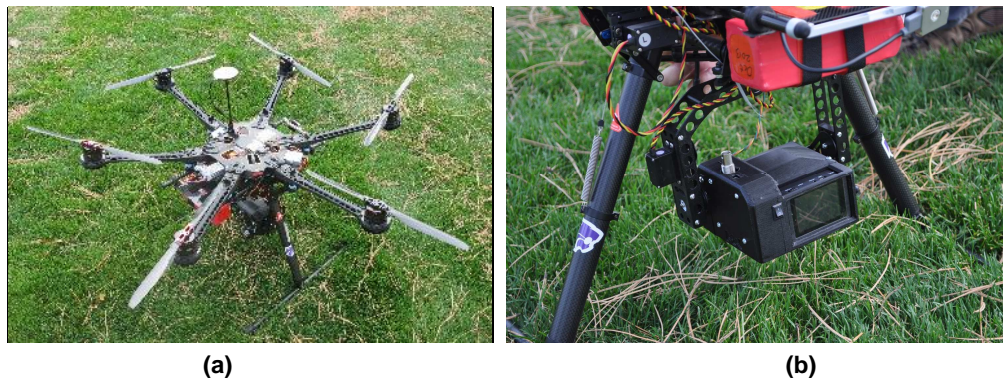


Figure 4.16. (a) DJI s800 Evo used for flight campaigns with sUAS TIRIS shown on (b) gimbal mount

Prior to a flight campaign, the standard operating procedures were as follows:

1. Unpack equipment
2. Power on the sUAS TIRIS to allow the TIR camera core to warm-up
3. Setup the ground reference station
4. Power on the ground monitoring station in order to achieve a GPS fix
5. Start laptop to program the multirotor sUAS and control the TIRIS
6. Conduct the pre-flight inspection for the multirotor sUAS and upload a flight program on the multirotor sUAS flight controller
7. Connect the sUAS TIRIS to the on-ground OT radiometric calibration hardware (Figure 4.9, above)
8. Configure the Tamarisk camera core using the TFC VI
9. Conduct an on-ground OT Radiometric Calibration
10. Start recording a simultaneous thermal video and ground measurement file
11. Mount the sUAS TIRIS on the multirotor sUAS

12. Conduct and complete flight campaign as specified in the autopilot flight program of the sUAS Flight Controller
13. Stop recording the measurement file and thermal video
14. Validate data was recorded
15. Finish testing and load equipment

The system was flown in 12 flight campaigns at low and high altitudes to access differences in spatial resolution and temperature measurement accuracies. Two specific flight campaigns at 40 and 80 m are described in detail below. For the flight campaign flown at 40 m, discussed in section 4.4.6, the TIRIS with the Tamarisk® 640 was flown over a golf course green to measure a fine resolution thermal map. For the 80 m flight campaign flown, the TIRIS with the Tamarisk® 640 was flown over a corn plot to measure a coarse resolution thermal map.

4.3.6 Image Processing

A batch processing procedure was developed to provide high-throughput thermal imagery, reduce manually subjective user control settings and provide uniform data handling. The standard operating procedure was used to parse thermal images and corresponding reference samples from raw data files, input processed images into image stitching software in order to generate a thermal map, and apply a radiometric transfer function to the resulting thermal map (Figure 4.17).

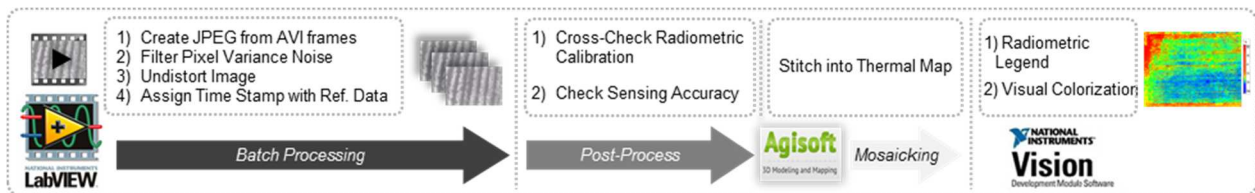


Figure 4.17. Image process flow as the analog video file is converted to the final stitched thermal map.

Two types of data was collected during a flight campaign. A raw thermal video was recorded on the mini-digital video recorder; and, a corresponding ground reference data file was recorded and stored on the MyRIO flash storage device. These two files would be downloaded for processing into a single folder on the processing computer.

For batch processing, a Thermal Video Processing (TVP) VI was developed with LabVIEW™ (National Instruments Corporation, Austin, Texas) to automatically parse images from the thermal video, correct lens distortion, apply a variance image filter, and align individual images with the coinciding ground reference data sample (Figure 4.18). Because the digital video recorder stored analog thermal video at 30 frames per second (FPS), the TVP VI controlled the captured frame rate in order to parse only a selected number of images for processing. For example,

for every second of video recording, 30 frames were available for processing, but a user-defined capture frame rate of 1 FPS would grab 1 image every 30 frames. As a result, only the images captured at the user-defined capture frame rate were processed.

At the beginning of the batch processing of the TVP VI, the user was prompted to select the raw video file (e.g., 0000155.avi) and the ground reference data file (i.e., corn_northfieldplot_flight_no1.csv). The TVP software would then pull the beginning time stamp from the ground reference data file to name the first image with the corresponding image number and time stamp. All subsequent images were then named based on the user-defined capture frame rate as controlled by the TVP VI and the time from that initial image. For example, the first image aligned with a ground reference data file started at '10.27.2014 10:30:00.000' would be named as '000001_10.27.2014.10.30.00.000.jpg'. In addition, if a user-defined capture frame rate was 1 FPS, the second image would be denoted as '000002_10.27.2014.10.30.01.000.jpg'. The TVP would then amend each individual sample of the ground reference data with the corresponding image number for the ease of manual cross-checking the on-ground OT radiometric calibration.

In the end, the TVP would output the filtered, undistorted images for subsequent image stitching and amended ground reference data in order to provide the ease of cross validating through ground truthing.

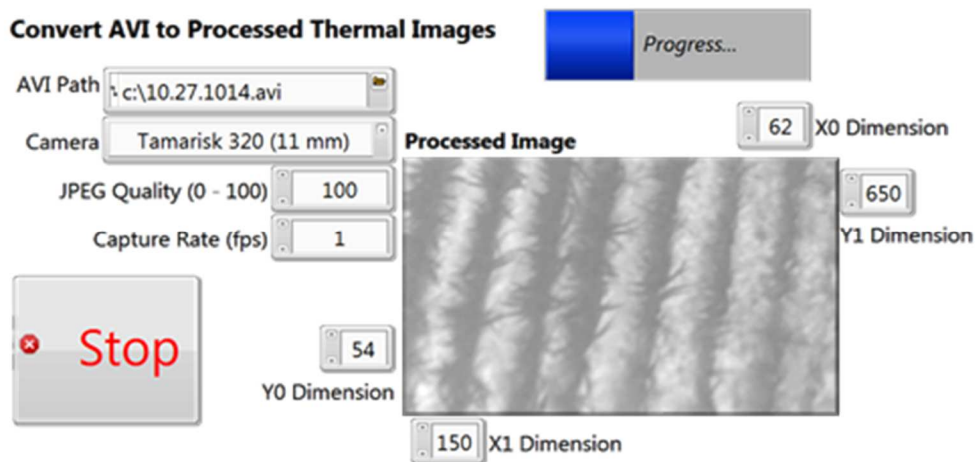


Figure 4.18. The TVP VI converts the thermal video file to filtered images featuring selective controls of file path, camera selection for specific lens distortion, image output quality, capture frame rate, cropping dimensions, and progress indicators.

4.3.6.1 Ground Truthing

Ground truthing was used to validate the on-ground OT radiometric calibration with an in-flight OT radiometric calibration from aboard the multirotor sUAS once flight altitude was reached. The in-flight OT radiometric calibration is manually conducted using RT surface temperatures from the ground monitoring station and image pixel intensity when the reference panels are present within the thermal images. This in-flight OT radiometric calibration correction would provide an environmental compensation to reduce LWIR energy attenuation from the influence of water vapor and aerosols present between the TIR camera and the reference panels as suggested by similar protocol conducted by Berni et al. (2009) and Monteith and Unsworth (2013).

Thermal images obtained after batch processing (Figure 4.18) were used to verify that image pixel intensity of the images remained within upper and lower saturation points of the thermal detector. This acts as a validation that the TFC VI suggested the correct camera configuration settings for the user-defined temperature span and center temperature. For example, correct camera configuration would mean that no vegetation temperatures would correspond to a pixel intensity of 0 (black saturation pixel intensity) or 255 (white saturation pixel intensity). As a result, all vegetation (or desired target) must remain within the scene temperatures for quality thermography.

4.3.6.2 Spatial Resolution

Temperature influences from a warm soil background and shaded lower leaves in partial canopy coverage can cause measurement error (Ayeneh, et al., 2002; Luquet, et al., 2003; Maes & Steppe, 2012). In order to investigate effects of spatial resolution on measured temperature, a series of increasing ROIs were designated within an image (Figure 4.19) by increasing offset spatial resolution by 1 pixel (i.e., 1×1 , 3×3 , 5×5 , 7×7 , ...) centered directly over a sensed target using the NI Vision Assistant™ (National Instruments Corporation, Austin, TX).

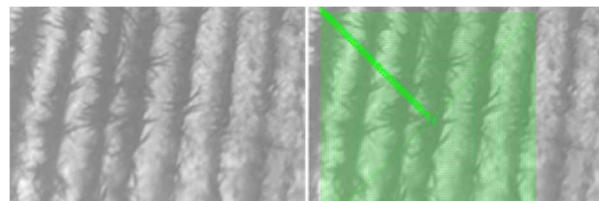


Figure 4.19. ROI analysis with increasing spatial resolution. The green boxes indicate the ROIs of increasing size.

By increasing spatial resolution by 1 pixel (or 0.5 cm/pixel) around the outer perimeter for each subsequent ROI, average DVs were calculated to illustrate quantified temperature at the respective spatial resolution. For example, the target corn leaf had a width of 6 cm, providing a theoretical 12 pixels on the target in the center of the ROI.

4.3.6.3 Thermal Mapping

Because the developed TVP software can capture images from the video stream at different capture rates, the capture frames per second (FPS) was investigated to determine necessary image overlap to improve mapping quality and efficiency. In order to reduce analog signal loss and noise introduced with analog video signal transmission, a basic variance image filter was applied to investigate its effect on mapping efficiency and quality.

After the still images were filtered for signal noise and corrected for lens distortion, thermal images were imported into Agisoft™ PhotoScan Professional (Agisoft LLC, St. Petersburg, Russia) software to generate an orthomosaic image for the entire coverage area from images collected at the same altitude. A pixel averaging method in the Agisoft software computed average individual temperature values from all overlapping pixels in order to reduce the effects of bidirectional temperature influence present in low-altitude mapping. The corresponding on-ground and in-flight OT radiometric calibration transfer function developed in the field was then used to convert each raw pixel DV to temperature in the orthomosaic image using Equation 4.8.

4.4 RESULTS AND DISCUSSION

A small, lightweight TIRIS was developed for thermal mapping aboard a multirotor sUAS. The TIRIS capabilities include one of the two TIR camera cores, ground measurement system to record and transmit environmental parameters, and on-ground OT calibration equipment (Table 4.3). An example of the sUAS TIRIS is shown in Figure 4.20. Between the low and high resolution TIRIS systems developed, the only substantial difference is the pixel resolution, video frame rate, resulting payload weight, and cost of the TIR camera core. When considering the application, the necessary spatial resolution, budget, and permissible payload determines which uncooled TIR camera core is appropriate. However, the sensitivity, controllability, measurement accuracy, and necessary hardware and software are identical for either systems.

Table 4.3. TIRIS Capabilities and Features

<i>sUAS TIRIS</i>		<i>Power</i>	
<i>Detector Type</i>	<i>Uncooled Vox Microbolometer</i>	<i>Input Voltage</i>	<i>5-18 Volts</i>
<i>Array Size</i>	<i>640 x 480 320 x 280</i>	<i>Power Usage</i>	<i>4 Watts</i>
<i>Pixel Pitch</i>	<i>17 μm</i>	<i>Battery Life</i>	<i>3 Hours</i>
<i>Spectral Band</i>	<i>8-14 μm</i>	<i>Battery Size</i>	<i>11.1 Volt (1100 mAh)</i>
<i>Video Format Options</i>		<i>Video Storage</i>	
<i>Frame Rates</i>	<i>9/30/60 fps</i>	<i>Video File Format</i>	<i>AVI @ 30 fps</i>
<i>Analog Video</i>	<i>NTSC (480p) PAL (576P)</i>	<i>Recording Time</i>	<i>2.5 h/1Gb</i>
<i>Image Resolution</i>	<i>8-Bit</i>	<i>Storage Memory</i>	<i>32 Gb</i>
<i>Camera Recalibration</i>		<i>Weight</i>	
<i>Video Record Time</i>	<i>1 Hour</i>	<i>TIRIS 320</i>	<i>250 g</i>
<i>Non-uniform Correction</i>	<i>Shutter calibration (Time/Temp.)</i>	<i>TIRIS 640</i>	<i>450 g</i>
<i>Ground Monitoring Station</i>		<i>Environmental</i>	
<i>Global Positioning Coordinates</i>	<i>1 Hz</i>	<i>Operating Temp. Span</i>	<i>0°C to 65°C</i>
<i>Solar Radiance</i>	<i>±1 W m⁻² or ±5%</i>	<i>Humidity</i>	<i>5 to 95%, non-condensing</i>
<i>Temperature Reference</i>	<i>±0.1°C</i>	<i>Power</i>	
<i>Air Temperature</i>	<i>±2°C</i>	<i>Input Voltage</i>	<i>9-24 Volts</i>
<i>Relative Humidity</i>	<i>±3%</i>	<i>Power Usage</i>	<i>6 Watts</i>
^[a] <i>Thermal Camera Core Accuracy</i>	<i>±0.82°C (T320) ±0.81°C (T640)</i>	<i>Battery Life</i>	<i>6 Hours</i>
		<i>Battery Size</i>	<i>11.1 Volt (3000 mAh)</i>

^[a] Measurement accuracy determined with a 1 min camera recalibration (NUC) and OT radiometric calibration

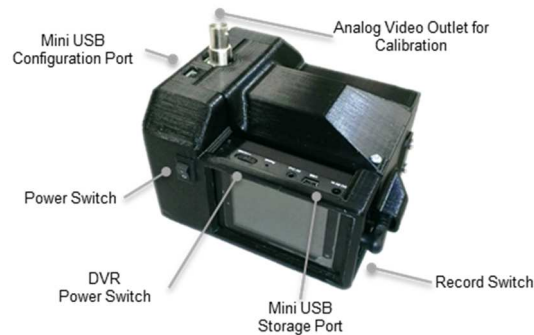


Figure 4.20. Resulting sUAS TIRIS featuring accessible control inputs and image acquisition ports.

4.4.1 Lens Distortion

The Tamarisk 640 with the 25 mm lens had 18% lens distortion; and, the Tamarisk 320 with the 11 mm lens had 19% lens distortion (Figure 4.21). Both lens distortion calibration results were used to correct lens distortion for spatial integrity, as shown in Table 4.4, within the TVP software.

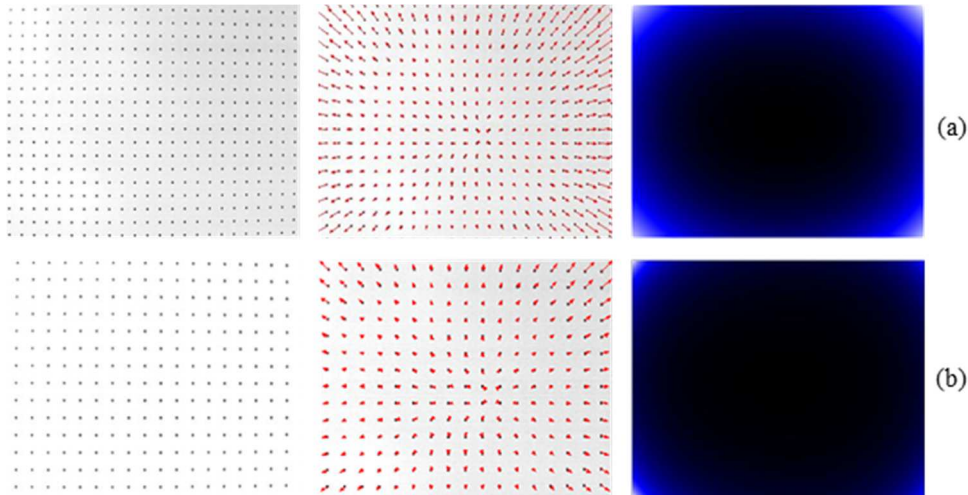


Figure 4.21 (a) Tamarisk® 640 with 25 mm and (b) Tamarisk® 320 with 11 mm lens distortion results from the point distortion grid model with the original image (left) point vector map (middle), and visual distortion map (right)

Table 4.4 Lens distortion analysis including radial and tangential correction coefficients

<i>TIR Camera Core</i>	<i>% Distortion</i>	<i>Radial</i>		<i>Tangential</i>	
		k_1	k_2	p_1	p_2
<i>DRS Tamarisk® 320 11 mm lens</i>	19.1	-0.24992	-0.74306	-0.000177	0.002740
<i>DRS Tamarisk® 640 25 mm lens</i>	18.6	-0.41780	0.11154	-0.002273	-0.007275

The percent lens distortion reveals significant distortion occurs within the germanium lens of each TIR camera core. This has implications in application where spatial integrity is critical especially in whole-field temperature mapping and site-specific crop health monitoring. In addition, since each TIR camera and lens are factory calibrated, a TIR camera and lens combination may have subtle variations in distortion characteristics. As a result, identical camera configurations may not be interchangeable; therefore, each individual TIR camera may need to be calibrated for its specific lens distortion coefficients.

4.4.2 Radiometric characterization and measurement accuracy

Once the sUAS TIRIS was calibrated, the TFC software created a calibration file including coinciding ground reference data, critical camera settings like the OT radiometric slope and intercept, scene temperature span, center temperature, calibration time, and the suggested camera level and gain configuration, as shown in Table 4.5.

Table 4.5. Sample TIRIS camera calibration file for a flight campaign

Time		Latitude	Longitude	Satellites	Elevation (m)
10/27/2014 12:42		39.194333	-96.597383	17	343.9
Cold Pixel (DV)	Warm Pixel (DV)	Cold Temp. (°C)	Warm Temp. (°C)	OT Rad. Slope (m)	OT Rad. Intercept (b)
76	166	10	48	0.422	-22.08
Camera Gain	Camera Level	Center Temp. (°C)	Span (°C)	Low Temp. (°C)	Hi Temp. (°C)
3450	1434	32	65.86	-8.57	57.288

For subsequent processing, the TFC program generated the calibration file name which was appended with the date and time coinciding with the ground reference data file described above in Section 4.3.6. As acquired from the calibration, the slope (m) and intercept (b) were used to apply a radiometric transfer function to the resulting thermal map, as described in Thermal Mapping section. The camera calibration naming conventions and file location is critical when managing the data generated with the TIRIS.

4.4.3 Ground Reference Data

Ground reference data monitored during the flight campaign was used to conduct on-ground and in-flight OT radiometric calibration. With a 5 Hz sample rate, subtle differences in reference temperature panels are shown in Figure 4.22. Results show the aluminum panel maintained the warmest temperature, whereas the wet reference panels had a temperature deficit of more than 10°C.

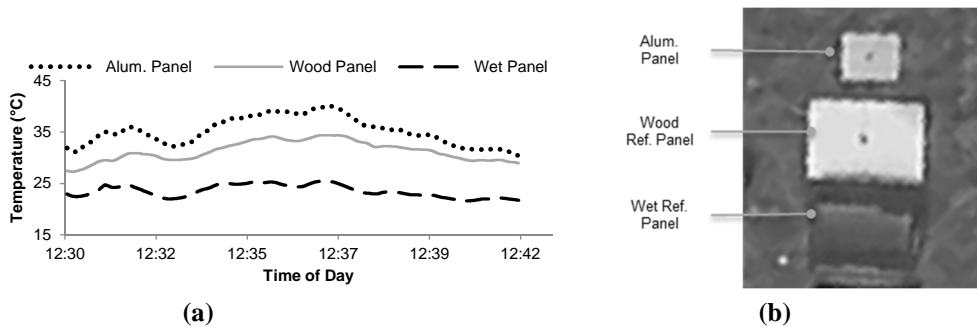


Figure 4.22. (a) Ground reference panel temperatures throughout flight campaign as recorded by the ground measurement station and (b) the ground reference panels viewable from the sUAS multirotor at an altitude of 40 m and a spatial resolution of 27 mm/pixel.

By ground truthing the thermal imagery, the TIRIS measurement accuracy during a flight campaign (Figure 4.23) was found to be $\pm 1.60^{\circ}\text{C}$ ($\alpha=0.05$) using the on-ground OT radiometric calibration. However, with an in-flight OT radiometric calibration conducted at flight altitude, the TIRIS yielded a measurement accuracy of $\pm 1.38^{\circ}\text{C}$ ($\alpha=0.05$), as shown in Figure 4.23.

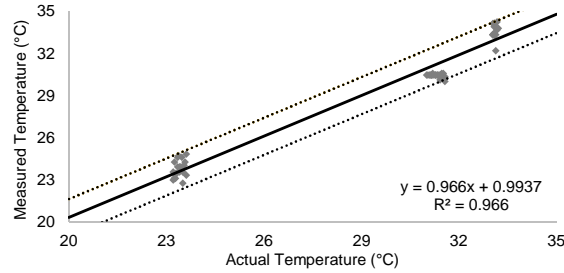


Figure 4.23. Measurement accuracy found from a flight campaign comparing the actual temperature versus the measured temperature as shown with a 95% confidence interval. Results reveal a TIRIS measurement accuracy of $\pm 1.38^{\circ}\text{C}$.

Because the reference temperature panels were unregulated and subject to the sensing environment, reference temperature deficits are a function of the sensing environment at the time of flight. This has implications on the temperature differential induced from a sensing environment. The temperature accuracy is increased with the use of the ground reference data correction. Even with ground reference correction, the measurement accuracy is diminished from laboratory accuracy measurements ($\pm 0.81^{\circ}\text{C}$). This could be contributed to environmental influence that cause temperature fluctuations of the reference panels reducing the accuracy of the radiometric transfer function. Further tests should consider testing reference materials of different thermal inertia in order to resist temperature fluctuations. With the image processing procedures discussed above, misalignment of images with the reference data time stamp may also introduce error due to incorrect reference data. Similarly, with every subsequent image, the time stamp was assigned based on the frame capture rate of the digital video recorder, which may fluctuate. Therefore, a future TIRIS should automatically assign each image with an instantaneous time stamp from a primary source.

4.4.4 Spatial Resolution and Measurement

Pixel-by-pixel resolution ROI analysis provided necessary spatial resolution in order to limit false measurements. The spatial resolution was adjusted within the developed ROI analysis program, and the corresponding quantified temperature is shown in Figure 4.24. Results show measurement accuracy diminished from increasing ROIs of spatial resolutions from influence from warm background soil temperature. At a spatial resolution of 200 cm/pixel, the measured temperature was 3.2°C above the measured temperature at 6 cm/pixel. Results reveal a spatial resolution above that of the critical target spatial resolution (6 cm/pixel in this scenario) significantly impacts the measurement accuracy of the TIRIS aboard sUAS.

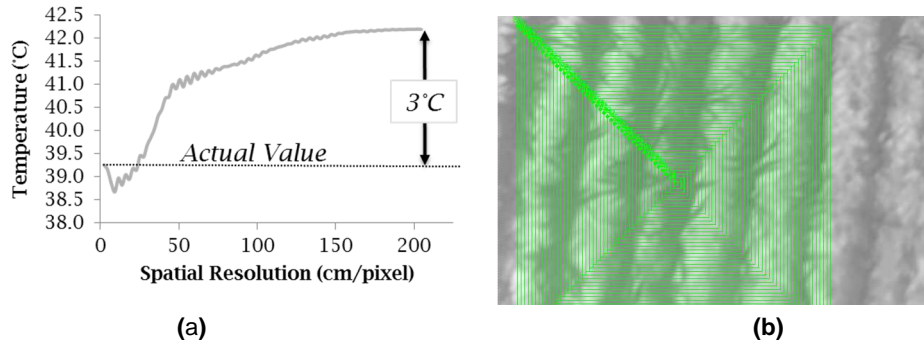


Figure 4.24. ROI analysis with measured temperature (a) with respective spatial resolution centered on a corn plant target with a spatial resolution of 0.5 cm/pixel (b).

The above influence could vary through crop development, where the largest influence may occur early in the growing season when soil dominates most of the measurement surface. Later in the growing season, a full canopy would reduce but may not eliminate this error. Therefore, future research needs to be conducted to develop advanced image analysis procedures; and, use a combination of visible and color infrared (CIR) cameras to accurately segment crop canopy from background soil. These additions could help accurately map canopy temperature at high spatial and temporal resolution throughout crop development.

4.4.5 Image Filtering

Because of noise introduced with analog video signal transmission, a pixel variance filter was applied to each image during batch image processing. The same image set was processed without the filter to compare thermal mapping quality and efficiency (Table 4.6). The first metric for comparison was the amount of images the stitching software was able to align with common points between images. Filtering each image with a pixel variance filter increased the amount of aligned photos of the given image set from 69% to 99%.

Table 4.6. Comparison of results from raw and filtered image stitching regarding aligned images, processing time, and developed point clouds

	Filtered Images	Raw Images
No. of aligned images	219/220= 99%	153/220= 69%
Processing Time	15 min 36 sec	12 min 18 sec
Initial Point Cloud	34,448	18,529
Dense Point Cloud	1,720,823	1,180,905

As expected, additional images resulted in increased processing time, but mapping efficiency improved by acquiring more data from filtered images, resulting in a higher quality orthomosaic image. Increased image data was reflected in the dense point cloud attained due to a greater number of aligned images. As the stitching software built initial and dense data point clouds, the filtered images almost doubled the data in the generated point clouds, thereby

increasing the resulting orthomosaic image data and overall quality displayed in the resulting thermal map (Figure 4.25).

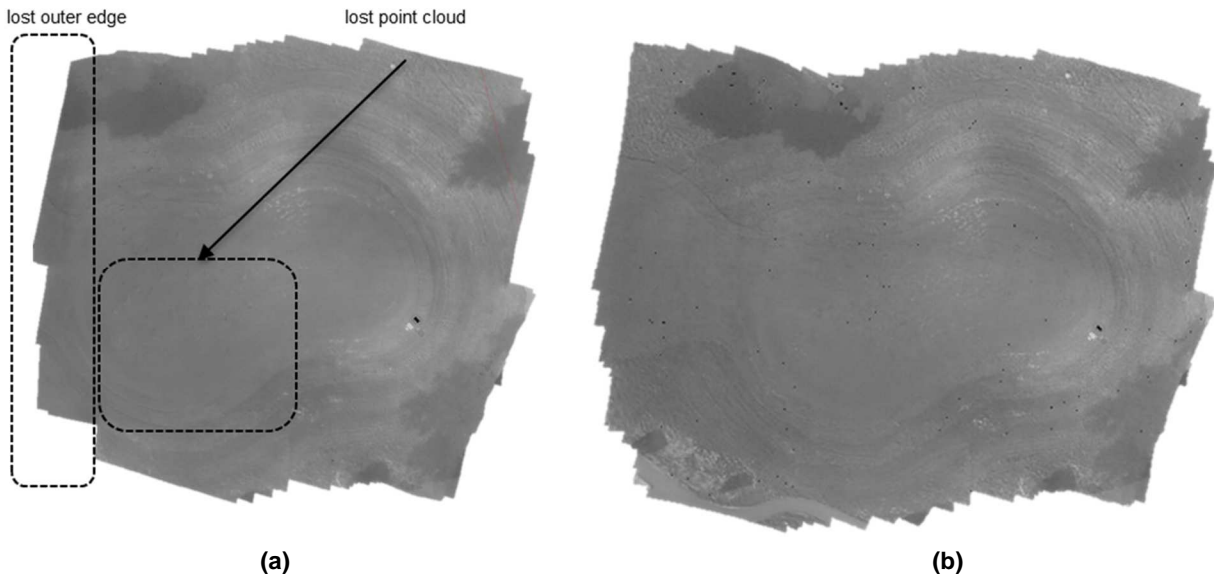


Figure 4.25. (a) Comparison of thermal map of raw images and (b) filtered images prior to image stitching. In the resulting raw image mosaic, the outer edge and inner portion (black boxes) of the image lacks detail represented in the resulting mosaic image captured by the filtered images.

As shown in the filtered images mosaic (Figure 4.25 b), points along the outer perimeter of the orthomosaic image increased the coverage of the image associated with more aligned images. More importantly, detail was lost in the thermal map of unfiltered images where subtle features are visible in the resulting thermal map of filtered images. This has implications on the quality of the resulting images. In addition, as images are processed with the stitching software, user defined software settings can alter mapping output from stitching algorithms producing potential error. Coarse settings and low quality parameters could result in faster mapping throughput but does not guarantee the resulting quality of the orthomosaic image. In addition, the stitching software may not be able to process low quality imagery. Similarly, low quality images may result in errors such as lost imagery coverage from limited point clouds and discrete data loss as the map is generated (Figure 4.25). As a result, quality of the resulting thermal map will inherently depend on the quality of individual images. Design considerations to improve and maintain captured image quality should be a deciding criteria for selecting system hardware and software.

4.4.6 Thermal Mapping

Five different capture rates were investigated and the resulting stitching parameters are shown in Table 4.7 and illustrated in Figure 4.26. With image stitching, the images with a denser point cloud resulted in a better thermal map featuring higher spatial accuracy. A capture frame rate of 1 FPS at the respective altitude and flight speed resulted in the highest quality thermal scan with an increased number of aligned images and the largest point cloud (Figure 4.26 c).

Table 4.7. Results from various frame capture rates and image stitching results related to processing time, developed point cloud, and common point matches between consecutive images

Capture frequency	3 frames s ⁻¹	2 frames s ⁻¹	^[a] 1 frames s⁻¹	1 frames 2 s ⁻¹	1 frames 3 s ⁻¹
No. of aligned images	355/635 = 56%	307/445 = 69%	219/220= 99%	108/111= 97%	60/74= 81%
Processing Time	35 min 18 sec	19 min 57 sec	15 min 36 sec	4 min 26 sec	2 min 15 sec
Point Cloud	15,563	31,846	34,448	16,681	6,592
Dense Point Cloud	225,270	1,031,577	1,720,823	1,228,590	539,457

[a] This capture frame rate provided the best mosaicked thermal map

Typical perception would be that more images would produce a better orthomosaic image from more overlap as a result of more common points between images. However, additional thermal images resulted in a less-efficient thermal map from less common points between images. This occurrence may be contributed to the thermal detector's integration time (time necessary for the microbolometer to measure incoming LWIR energy) which can create image blur in consecutive images from the resistance based temperature from the previous image frame (Vollmer & Mollmann, 2011).

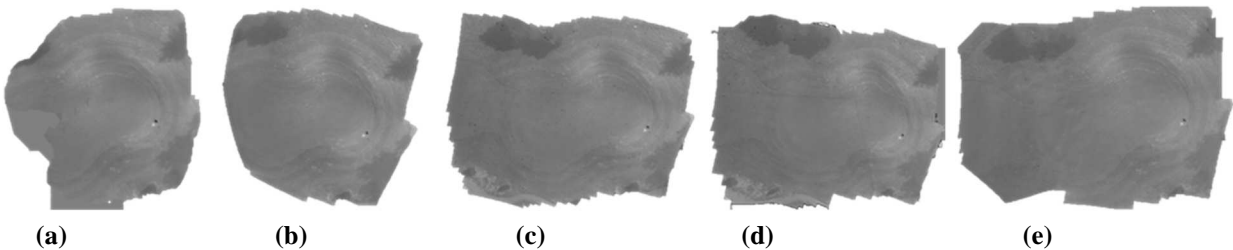


Figure 4.26. Mosaicked image resulting from capture frame rates illustrated in Table 4.7 at (a) 3 frames s⁻¹, (b) 2 frames s⁻¹, (c) 1 frame s⁻¹, (d) 1 frame 2 s⁻¹, and (e) 1 frame 3 s⁻¹.

Agisoft™ PhotoScan software aligns images based on common points, with or without the use of GPS coordinates, from neighboring images to determine the image layout and camera orientation (Figure 4.27). Common points, alone, were used as the alignment technique.

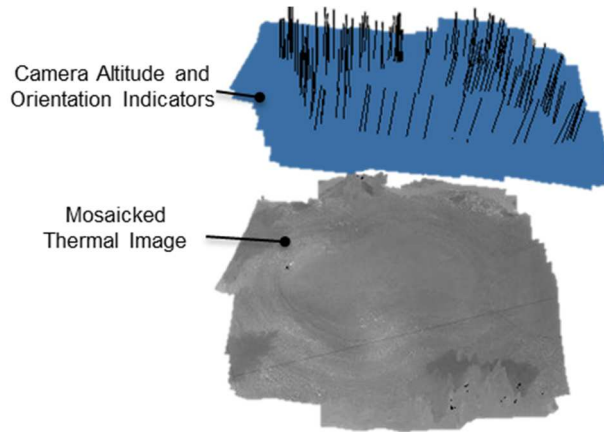


Figure 4.27. Camera orientation (black line normal to image) and respective image altitude. Parameters were deduced from image overlap and common pixel intensities between neighboring images.

From within the Agisoft™ PhotoScan software, a manual comparison between the forward and lateral images revealed the amount of overlap with a capture frame rate of 1 FPS. As shown in Figure 4.29, a low altitude thermal map of a golf course green had an overlap covering 81.4% of the forward image and 55.9% of the lateral image, as shown in Table 4.8. As a result, the average pixel intensity within the orthomosaic image is skewed from more camera views in the forward direction. In application, this skewed average could introduce mapping artifacts into the resulting orthomosaic image that closely follow the flight path orientation.

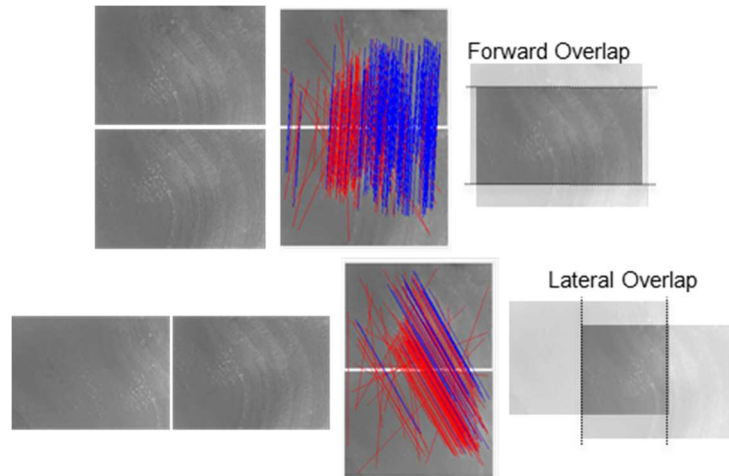


Figure 4.28. Forward and lateral overlap of stitched images. The red and blue lines indicate the invalid and valid, respectively, common points between the images.

Table 4.8 Image overlap percentage

	Image Size	Overlap	Camera Views
Original Image	610 × 441	-	
Forward Overlap	610 × 359	81.4%	5
Lateral Overlap	341 × 441	55.9%	2

As calculated from Table 4.8, a specific target surface was viewed, theoretically, by 10 different camera angles as found using Equation (4.1, above. However, the number of camera views could fluctuate due to sUAS platform's flight path variability from telemetry inaccuracy and wind influence.

As shown in Figure 4.29, the last step in image processing converted each image pixel into a quantified temperature intensity using the radiometric calibration transfer function generated by either the on-ground or in-flight OT radiometric calibration as defined by Equation 4.14:

$$T_{ij} = 0.1153 \times DV_{ij} + 5.17 \quad (4.14)$$

Where:

DV_{ij} = pixel brightness value at row i and column j

T_{ij} = corresponding temperature related to the pixel at row i and column j .

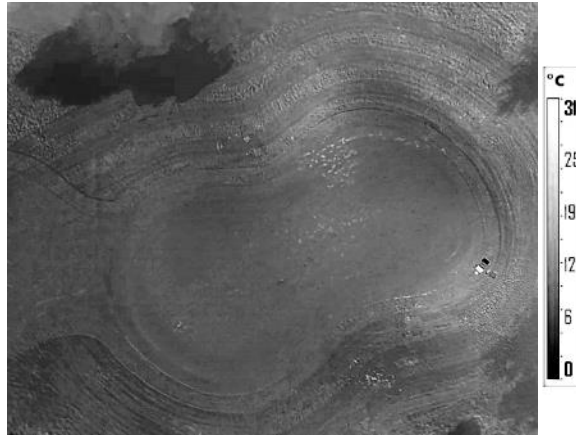


Figure 4.29. Thermal map of a golf course green at an altitude of 40 meters. This orthomosaic image is the result of 220 individual images taken at 1 FPS. After post-processing, measurement accuracy was $\pm 1.38^{\circ}\text{C}$ from an in-flight OT radiometric calibration with theoretical spatial resolution of 27 mm/pixel. A temperature legend is generated from the upper and lower temperatures found with the TIR Field Calibration software.

Similarly, a high altitude corn field thermal map was generated with a forward and lateral image overlap of 83.7% and 81.4%, respectively (Table 4.9). A specific target surface was viewed, theoretically, by 30 different camera angles as found using Equation (4.1, above. As a result, the average pixel intensity within the orthomosaic image represents a target from a more uniform distribution of camera views than the low altitude example, above.

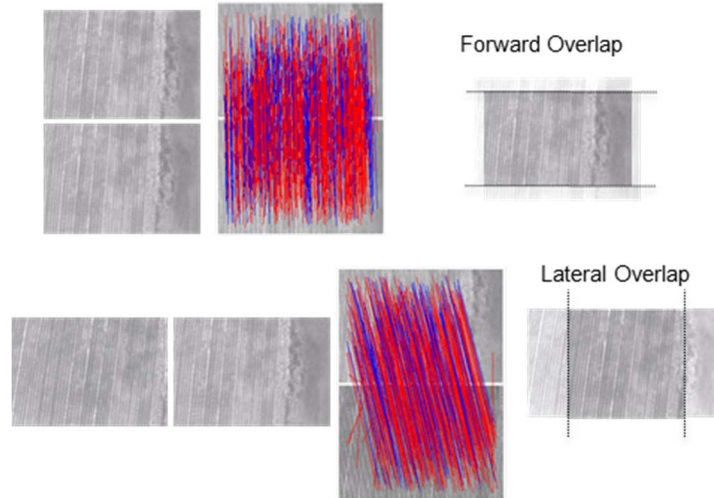


Figure 4.30 Forward and lateral overlap of stitched images. The red and blue lines indicate the invalid and valid, respectively, common points between the images.

Table 4.9. Image overlap percentage

	Image Size	Overlap	Camera Views
Original Image	610 × 441	-	-
Forward Overlap	575 × 387	87.8%	8
Lateral Overlap	497 × 441	81.4%	5

The corn field thermal map, as shown in Figure 4.31, was converted to temperature intensity using the radiometric transfer function generated by the TIR Field Calibration software as defined by Equation 4.15:

$$T_{ij} = 0.336 \times DV_{ij} + 7.23 \quad (4.15)$$

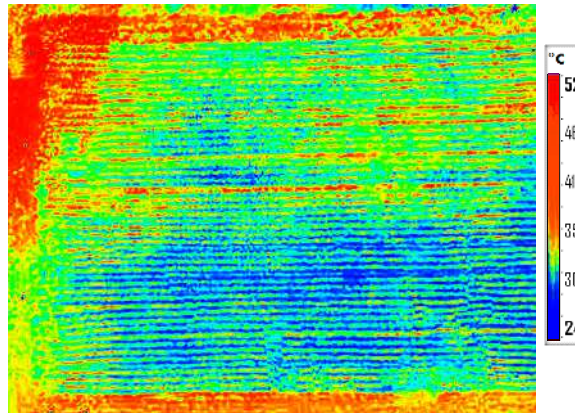


Figure 4.31. Thermal map of corn at an altitude of 80 meters. After post-processing, measurement accuracy was $\pm 1.60^\circ\text{C}$ from an on-ground OT radiometric calibration with theoretical spatial resolution of 54.4 mm/pixel. This orthomosaic image is the result of 180 individual images taken at 1 frame rate per second. A colorized mask is used to provide visual isotherms.

With environmental sensors utilized in this study, these micro-climates were assumed to be constant with RT measurement taken at the plant canopy level. Future studies should be

conducted to use the environmental sensors and temperature map in order to look at spatial crop water stress. Lastly, a feasibility study that investigates the use of a spatial crop water stress map for variable rate irrigation in order to provide a cost-benefit analysis need to be investigated in future studies.

4.5 CONCLUSION

A direct agricultural study using thermography was conducted to provide knowledge pertaining to specific operation and control, hardware configuration, and utility in precision agriculture in which limited studies have restricted thermography use to laboratories and controlled environments. A small, lightweight TIRIS was developed for a multirotor sUAS to provide high-throughput imagery sensitive to spatial crop temperature variability for radiometric temperature mapping. A complementary TIRIS software package allowed automatic image processing in order to limit manually subjective parameters and advance the ease of image capture, correct image distortion, and increase throughput and storage management for direct use in subsequent image stitching. The TIRIS was designed to quantify temperatures in environmental conditions typically observed under field conditions using either an on-ground or an in-flight OT radiometric calibration and RT ground reference station. RT ground reference data provided a specific time stamp and air parameters associated with each image and provided temperature measurement accuracy. Physical properties that typically increase inaccuracy were minimized with the TIRIS design by selecting TIR camera cores for the desired spatial resolution, creating standard operating protocol, and specifically designed software. As a result, the developed TIRIS is intended to add utility to uncooled thermal camera for direct use aboard sensing platforms in precision agriculture.

Results revealed adhering to critical spatial resolution maintains measurement accuracy while maximizing coverage area where critical spatial resolution depends on the current plant growth stage in order to limit background temperature exposure. The Tamarisk 320 with an 11 mm lens had 19% lens distortion; and, the Tamarisk 640 with a 25 mm lens had 18% lens distortion. Both lens distortions were automatically corrected in batch processing. A relationship between image overlap and camera views was created in order to determine a flight campaign that is capable of representing a target measurement with a given confidence. Similarly, an applied pixel variance filter increased mapping efficiency by increasing the amount of aligned photos from 69% to 99% of the given image set.

An OT radiometric calibration method was used to provide absolute surface temperature at calibrated environmental conditions. RT ground reference data provided the ability to make in-flight OT radiometric calibration corrections to thermal imagery flown aboard a multirotor sUAS in order to achieve a temperature measurement accuracy of $\pm 1.38^{\circ}\text{C}$, whereas an on-ground OT radiometric calibration yielded a measurement accuracy of $\pm 1.60^{\circ}\text{C}$.

Due to their low cost compared to cooled TIR cameras, minimal size and weight, and lack of moving parts, uncooled TIR cameras have been emphasized and utilized aboard sUAS platforms for coverage and spatial crop temperature assessments. Study results indicated that TIRIS could be further researched in order to produce temperature maps for spatial crop water stress at scales needed for large agricultural production systems. Producers, agricultural service providers, and researchers should consider TIRIS for crop water stress monitoring applications.

References

- Adeuya, R., 2007. Improving Agricultural Sustainability through drainage water management practices.. *Grants and Education to advance innovations in sustainable agriculture*, Volume GNV06-066.
- Alves, I. & Pereira, L. S., 2000. Non-water-stressed baselines for irrigation scheduling with infrared thermometers: a new approach. *Irrigation Science*, Volume 19, pp. 101-106.
- Ayeneh, A., van Ginkel, M., Reynolds, M. P. & Ammar, K., 2002. Comparison of leaf, spike, peduncle and canopy temperature depression in wheat under heat stress. *Fields Crops Research*, pp. 173-184.
- Ballester, C., Jimenez-Bello, M. A., Castel, J. R. & Intrigliolo, D. S., 2013. Usefulness of thermography for plant water stress detection in citrus and persimmon trees. *Agricultural and Forest Meteorology*, pp. 120-129.
- Berk, A. et al., 1998. MODTRAN Cloud and Multiple Scattering Upgrades with application to AVIRIS. *Remote Sensing Environment*, Volume 65, pp. 367-375.
- Berni, J. A. et al., 2009a. Mapping canopy conductance and CWSI in olive orchards using high resolution thermal remote sensing imagery. *Remote Sensing of Environment*, pp. 2380-2388.
- Berni, J. A. et al., 2009. Mapping canopy conductance and CWSI in olive orchards using high resolution thermal remote sensing imagery. *Remote Sensing of Environment*, pp. 2380-2388.
- Berni, J. A., Zarco-Tejada, P. J., Suarez, L. & Fereres, E., 2009b. Thermal and narrowband multispectral remote sensing for vegetation monitoring from an. *IEEE Transactions on Geoscience and Remote Sensing*, March, 47(3).
- Berni, J. A., Zarco-Tejada, P. J., Suarez, L. & Fereres, E., 2009. Thermal and narrowband multispectral remote sensing for vegetation monitoring from an. *IEEE Transactions on Geoscience and Remote Sensing*, March, 47(3).
- Berton, V., 2006. Smart water use on your farm or ranch. *Sustainable agriculture network*, pp. 12-15.
- Blonquist, M. & Bugbee, B., n.d. *Measuring Crop Water Stress Index: Empirical Versus Theoretical Approaches*, s.l.: Apogee Instruments.
- Brown, R. B., Steckler, G. A. & Anderson, G. W., 1994. Remote sensing for identification of weeds in no-till corn. *Transactions of the ASABE*, 37(1), pp. 297-302.
- Bulanon, D. M., Burks, T. F. & Alchanatis, V., 2009. Image fusion of visible and thermal images for fruit detection. *Biosystems engineering*, Volume 103, pp. 12-22.

- Chaerle, L. et al., 1999. Presymptomatic visualization of plant-virus interactions by thermography. *Nature Biotechnology*, August, pp. 813-816.
- Cohen, Y. et al., 2005. Estimation of leaf water potential by thermal imagery and spatial analysis. *Journal of Experimental Botany*, July, 56(417), pp. 1843-1852.
- Colaizzi, P. D. et al., 2003b. Water stress detection under high frequency sprinkler irrigation water deficit index. *Journal of Irrigation and Drainage Engineering*, Volume 129, pp. 215-229.
- Colaizzi, P. D., O'Shaughnessy, S. O., Evett, S. R. & Howell, T. A., 2012. *Using plant canopy temperature to improve irrigated crop management*. Colby, Kansas, s.n., pp. 203-223.
- DRS Technologies A Finmeccanica Company, 2013. *Tamarisk 320 Camera Control Software User Guide*. E ed. Dallas, TX: s.n.
- DRS Technologies, Network and Imaging Systems Group, n.d. *Benefits of a thermal camera shutter*, Dallas, TX: DRS Technologies.
- Ehrler, W. L., 1973. Cotton leaf temperatures as related to soil-water depletion and meteorological factors. *Agronomy Journal*, Volume 65, pp. 404-409.
- Elfaki, M. S., Zhang, N. & Peterson, D. E., 2000. Factors affecting color-based weed detection. *Transactions of the ASAE*, Volume 43, pp. 1001-1009.
- El-Shikha, D. M. et al., 2007. Ground-based remote sensing for assessing water and nitrogen status of broccoli. *Agricultural Water Management*, pp. 183-193.
- Erdem, Y. et al., 2010. Crop water stress index for assessing irrigation scheduling of drip irrigated broccoli. *Agricultural Water Management*, Volume 98, pp. 148-156.
- Evans, D. E., Sadler, E. J., Camp, C. R. & Millen, J. A., 2000. *Spatial canopy temperature measurements using center pivot mounted IRTS*. Madison, WI, s.n.
- Evett, S. R. et al., 2014. *The future of irrigation on the U.S. great Plains*. Burlington, CO, CPIA, pp. 2-25.
- Evett, S. R., Colaizzi, P. D., Schwartz, R. C. & O'Shaughnessy, S. A., 2014. *Soil Water Sensing-Focus on Variable Rate Irrigation*. Burlington, CO, CPIA, pp. 99-109.
- Fitzgerald, G. J. et al., 2007. Spectral and thermal sensing for nitrogen and water status in rainfed and irrigated wheat environments. *Precision Agriculture*, Volume 7, pp. 233-248.
- French, A. N., Hunsaker, D., Clarke, T. R. & Fitzgerald, G. J., 2005. *Estimation of spatially distributed evapotranspiration over wheat using thermal infrared images and ground-based radiometers*, Phoenix,: U.S. Arid Lands Agricultural Research Center.
- Gerhards, R. & Christensen, S., 2003. Real-time weed detection, decision making and patch spraying in maize, sugar beet, winter wheat and winter barley.. *European Weed Research Society*, 2003(43), pp. 385-392.
- Goel, P. K. et al., 2000. *Airborne optical remote sensing for detection of weed infestation in site specific management of field crops*. Milwaukee, United States, s.n., pp. 749-761.
- Gomide, R. L., Tian, L. & Pinto, F., 2003. *Thermal and color near-infrared spectral remotely sensed scanners to detect in-field soybean and corn water stress variability*., Las Vegas: s.n.
- Gontia, N. K. & Tiwari, K. N., 2008. Development of crop water stress index of wheat crop for scheduling irrigation using infrared thermometry. *Agricultural Water Management*, Volume 95, pp. 114-1152.
- Grant, O. M., Chaves, M. M. & Jones, H. G., 2006. Optimizing thermal imaging as a technique for detecting stomatal closure induced by drought stress under greenhouse conditions. *Physiological Plantarum*, Volume 127, pp. 507-518.
- Grant, O. M., Tronina, L., Jones, H. G. & Chaves, M. M., 2007. Exploring thermal imaging variables for the detection of stress responses in grapevine under different irrigation regimes. *Journal of Experimental Botany*, 58(4), pp. 815-825.
- Hackl, H. et al., 2012. A comparison of plant temperatures as measured by thermal imaging and infrared thermometry. *Journal of Agronomy and crop science*, Issue 198, pp. 415-429.

- Hashimoto, Y. et al., 1984. Dynamic Analysis of Water Stress of Sunflower Leaves by Means of a Thermal Image Processing System. *Plant Physiology*, Volume 76, pp. 266-269.
- Hecker, C. A., Smith, T. E., Ribeiro da Luz, B. & Wooster, M. J., 2013. Thermal Infrared Spectroscopy in the Laboratory and Field in Support of Land Surface Remote Sensing. In: *Thermal Infrared Remote Sensing*. s.l.:s.n., pp. 43-68.
- Herwitz, S. R. et al., 2004. Imaging from an unmanned aerial vehicle: agricultural surveillance and decision support. *Computers and Electronics in Agriculture*, Volume 44, pp. 49-61.
- Hoelt, R. G., Nafziger, E. D., Johnson, R. R. & Aldrich, S. R., 2004. *Modern Corn and Soybean*. First ed. Savoy, IL: MCSP Publications.
- Idso, S. B., Jackson, R. D., Ehrlert, W. L. & Mitchell, S. T., 1969. *A method for determination of infrared emittance of leaves*, Phoenix, Arizona: U.S. Water Conservation Laboratory.
- Idso, S. B. et al., 1981. Normalizing the stress-degree day parameter for environmental variability. *Agricultural Meteorology*, Volume 24, pp. 45-55.
- Idso, S. B., Jackson, R. D. & Reginato, R. J., 1975. Detection of Soil Moisture by Remote Surveillance. *American Scientist*, September, 63(5), p. 549.
- Idso, S. B., Jackson, R. D. & Reginato, R. J., 1977. Remote sensing of crop yields. *Science*, Volume 196, pp. 19-25.
- Jackson, R. D., 1982. Canopy Temperature and crop water stress. *Advances in Irrigation*, Volume 1, pp. 43-85.
- Jackson, R. D., Idso, S. B., Reginato, R. J. & Pinter Jr., P. J., 1981. Canopy Temperatures as a crop water stress indicator. *Water Resources*, Volume 17, pp. 1133-1138.
- Jackson, R. D., Pinter, P. J., Reginato, R. J. & Idso, S. B., 1986. *Detection and evaluation of plant stresses for crop management decisions..* s.l., IEEE Transactions, pp. 99-106.
- Jones, H. G., 1999. Use of thermography for quantitative studies of spatial and temporal variation of stomatal conductance over leaf surfaces. *Plant, Cell and Environment*, Volume 22, pp. 1043-1055.
- Jones, H. G., 2004. Irrigation scheduling: advantages and pitfalls of plant-based methods. *Journal of Experimental Botany*, Volume 55, pp. 2427-2436.
- Jones, T. L., Romanski, J. G., Buckley, J. J. & Girata, A. J., 1999. Demonstration of a multimode longwave infrared imaging system on an unmanned aerial vehicle. *Proceedings of SPIE*, Volume 510.
- Kargar, A. H. & Shirzadifar, A. M., 2013. *Automatic weed detection system and smart herbicide sprayer robot for corn fields*. s.l., s.n., pp. 468-473.
- Kuenzer, C., 2014. *Thermal Infrared Remote Sensing: Sensor, Methods, Applications*. New York(New York): Springer.
- Lagueta, S., Diaz-Vilarino, L., Roca, D. & Armesto, J., 2013. *Aerial thermography from low-cost UAV for the generation of thermographic digital terrain models*, University of Vigo: s.n.
- Laliberte, A. S., Winters, C. & Rango, A., 2011. UAS remote sensing missions for rangeland applications. *Geocarto International*, April, 26(2), pp. 141-156.
- Leinonen, I. & Jones, H. G., 2004. Combining thermal and visible imagery for estimating canopy temperature and identifying plant stress. *Journal of Experimental Botany*, June, 55(401), pp. 1423-1431.
- Liu, Y. et al., 2011. Maize leaf temperature responses to drought: thermal imaging and quantitative trait loci (QTL) mapping. *Environmental and Experimental Botany*, Volume 71, pp. 158-165.
- Luquet, D. et al., 2003. Using multidirectional thermography to characterize water status of cotton. *Remote Sensing of Environment*, Volume 84, pp. 411-421.
- Luvall, J. C. & Holbo, H. R., 1991. Thermal Remote Sensing Methods in Landscape Ecology. In: *Quantitative Methods in Landscape Ecology*. New York: Springer-Verlag, pp. 127-153.
- Luvall, J. C. & Holbo, H. R., 1991. Thermal Remote Sensing Methods in Landscape Ecology. In: *Quantitative Methods in Landscape Ecology*. New York: Springer-Verlag, pp. 127-153.

- Maes, W. H. & Steppe, K., 2012. Estimating evapotranspiration and drought stress with ground-based thermal remote sensing in agriculture: a review. *Journal of Experimental Botany*, 63(13), pp. 4670-4712.
- Merlot, S. et al., 2002. Use of infrared thermal imaging to isolate Arabidopsis mutants defective in stomatal regulation. *The plant journal*, 30(4), pp. 601-609.
- Miller, C. E., n.d.. Chemical Principles of Near-Infrared Technology. In: *Chemical Principles*. s.l.:s.n., pp. 1-37.
- Moller, M. et al., 2007. Use of thermal and visible imagery for estimating crop water status of irrigation grapevine. *Journal of Experimental Botany*, 58(4), pp. 827-838.
- Monteith, J. L. & Unsworth, M. H., 2013. *Principles of Environmental Physics*. Fourth ed. Oxford, UK: Academic Press.
- Monteith, J. L. & Unsworth, M. H., 2013. *Principles of Environmental Physics: Plants, Animals, and the Atmosphere*. Fourth ed. Oxford, UK: Elsevier Ltd..
- Moran, M. S., Clarke, T. R., Inoue, Y. & Vidal, A., 1994. Estimating crop water deficit using the relationship between surface-temperature and spectral vegetation index. *Remote Sensing Environment*, Volume 46, pp. 246-263.
- Nielsen, D. C., 1994. Non-water stressed baselines for sunflowers.. *Agricultural water management*, Volume 26, pp. 265-276.
- Notarnicola, C., Lewinska, K. E., Temini, M. & Zebisch, M., 2013. Application of the Apparent Thermal Inertia Concept for Soil Moisture Estimation in Agricultural Areas. In: *Thermal Infrared Remote Sensing*. Bolzano, Italy: Springer, pp. 331-346.
- O'Shaughnessy, S. A., Evett, S. R., Colaizzi, P. D. & Howell, T. A., 2011. Using radiation thermography and thermometry to evaluate crop water stress in soybean and cotton. *Agricultural Water Management*, Volume 98, pp. 1523-1535.
- O'Shaughnessy, S. A., Evett, S. R., Colaizzi, P. D. & Howell, T. A., 2012. A crop water stress index and time threshold for automatic irrigation scheduling of grain sorghum. *Agricultural Water Management*, 107(2012), pp. 122-132.
- O'Toole, J. C. & Real, J. G., 1986. Estimation of aerodynamic and crop resistances from canopy temperature. *Agronomy Journal*, Volume 78, pp. 305-310.
- Peters, R. T. & Evett, S. R., 2004. Modeling Diurnal Canopy Temperature Dynamics using one-time-of-day measurements and a reference temperature curve. *Agroclimatology*, Volume 96, pp. 1553-1561.
- Pohl, C. & Van Genderen, J. L., 1998. Multisensor image fusion in remote sensing; concepts, methods and applications. *International Journal of Remote Sensing*, 19(5), pp. 823-854.
- Prashar, A. et al., 2013. Infra-red Thermography for High Throughput Field Phenotyping in Solanum tuberosum. *PLoS ONE*, 8(6).
- Rango, A. et al., 2009. Unmanned aerial vehicle-based remote sensing for rangeland. *Journal of Applied Remote Sensing*, August.3(033542).
- Rodriguez, D., Sadras, V. O., Christensen, L. K. & Belford, R., 2005. Spatial assessment of the physiological status of wheat crops as affected by water and nitrogen supply using infrared thermal imagery. *Australian Journal of Agricultural Research*, Volume 56, pp. 983-993.
- Rogers, D. H. & Alam, M., 1998. Irrigation. In: *Grain Sorghum Production Handbook*. s.l.:Kansas State University Agricultural Experiment Station and Cooperative Extension Service, pp. 15-17.
- Romano, G. et al., 2011. Use of thermography for high throughput phenotyping of tropical maize adaption in water stress. *Computers and Electronics in Agriculture*, Volume 79, pp. 67-74.
- Schepers, A., 2012. *Using thermal imagery for agriculture*, Lincoln: s.n.
- Scherrer, D., Karl-Friedrich Bader, M. & Korner, C., 2011. Drought-sensitivity ranking of deciduous tree species based on thermal imaging of forest canopies. *Agricultural and Forest Meteorology*, Volume 151, pp. 1632-1640.
- Schlegel, A., Stone, L., Dumler, T. & Lamm, F., 2014. *No-till crop rotations with limited irrigation*. Burlington, Co., s.n., pp. 77-81.

- Sepulcre-Canto, G. F. et al., 2011. Estimating crop-specific evapotranspiration using remote sensing imagery at various spatial resolutions for improving crop growth modelling.. *International Journal of Remote Sensing*, 34(9-10), pp. 3274-3288.
- Sepulcre-Canto, G. et al., 2007. Monitoring yield and fruit quality parameters in open canopy tree crops under water stress.. *Remote Sensing of Environment*, Volume 107, pp. 455-470.
- Sobrino, J. A. & Julien, Y., 2013. Time Series Corrections and Analyses in Thermal Remote Sensing. In: *Thermal Infrared Remote Sensing*. Valencia, Spain: Springer, pp. 267-286.
- Sun, Q., Hou, Y., Tan, Q. & Li, G., 2013. A planar-dimensions machine vision measurement method based on lens distortion correction. *The scientific world journal*, 2013(963621).
- Taghvaeian, S. et al., 2013. Minimizing instrumentation requirement for estimating crop water stress index and transpiration of maize. *Irrigation Science*.
- Taghvaeian, S. et al., 2013. *Remote sensing for evaluating crop water stress at field scale using infrared thermography: potential and limitations*. s.l., s.n., pp. 73-83.
- Taghvaeian, S. et al., 2013. Remote sensing for evaluating crop water stress at field scale using infrared thermography: potential and limitations. *Hydrology Days*, pp. 73-83.
- Texas Department of Transportation, 2014. *Determining moisture content in soil materials*, s.l.: TxDOT.
- The Mathworks, Inc., 2015. *Developing an algorithm to undistort pixel locations of an image*, s.l.: Mathworks.
- Tilling, A. K. et al., 2007. Remote sensing of nitrogen and water stress in wheat. *Fields Crops Research*, Volume 104, pp. 77-85.
- Udompetaikul, V., Upadhyaya, S. K., Slaughter, D. & Lampinen, B., 2010. Development of sensor suite to determine plant water potential. *ASABE*, June.
- USDA, 2014. *Irrigation and Water Use*. [Online] Available at: <http://www.ers.usda.gov/topics/farm-practices-management/irrigation-water-use.aspx#UyfBjIUlotW>
- Vasterling, M. & Meyer, U., 2013. Imaging, Challenges and Opportunities for UAV-Borne Thermal. In: *Thermal Infrared Remote Sensing*. Hannover, Germany: Springer, pp. 69-92.
- Vollmer, M. & Mollmann, K.-P., 2011. *Infrared Thermal Imaging: Fundamentals, Research and Applications*. s.l.:John Wiley & Sons.
- Wang, X. et al., 2010. Automated canopy temperature estimation via infrared thermography: A first step towards automated plant water stress monitoring. *Computers and Electronics in Agriculture*, Volume 73, pp. 74-83.
- Wanjura, D. F., Upchurch, D. R. & Mahan, J. R., 1992. Automated Irrigation Based On Threshold Canopy Temperature. *ASAE*, September-October, 35(5), pp. 1411-1417.
- Wanjura, D. F., Upchurch, D. R. & Mahan, J. r., 2006. Behavior of temperature-based water stress indicators in BIOTIC-controlled irrigation. *Irrigation Science*, Volume 24, pp. 223-232.
- Wooster, M. J. et al., 2013. Thermal Remote Sensing of Active Vegetation Fires and Biomass Burning Events. In: *Thermal Infrared Remote Sensing*. s.l.:Springer, pp. 347-390.
- Zen, L., Tan, J. & Zhao, Z., 2008. Mass image data storage system for high resolution aerial photographic survey. *Proceedings of SPIE*, Volume 7133.
- Zhang, C. & Kovacs, J. M., 2012. The application of small unmanned aerial systems for precision agriculture:a review. *Precision Agriculture*, 2012(13), pp. 690-712.
- Zhang, N. et al., 2006. Weed identification using imaging technology and spectroscopy. *Environmental Control Biology*, Volume 3, pp. 161-171.
- Zhao, C. et al., 2005. Predicting grain protein content of winter wheat using remote sensing data based on nitrogen status and water stress. *International Journal of Applied Earth Observation and Geoinformation*, Volume 7, pp. 1-9.

Zia, S. et al., 2013. Infrared Thermal Imaging as a rapid tool for identifying water-stress tolerant maize genotypes of different phenology. *Journal of Agronomy and Crop Science*, pp. 75-84.

Appendix A - Supplemental Materials for Chapter 2

SYSTEM FEATURES

FOCAL PLANE ARRAY

Detector Type	Uncooled VOx Microbolometer
Array Size	320 x 240
Pixel Pitch	17 μm
Spectral Band	8-14 μm
Sensitivity (NE Δ T) @ f/1.0 @ Room Temperature	<50 mK

VIDEO FORMAT

Frame Rates	60 fps, 9 fps
Analog Video	NTSC (480i); PAL (576i) Field switchable
Digital Video	14-bit/8-bit LVCMOS or Camera Link®
Automatic Gain and Level	User defined and persistent through power cycles
Digital Zoom and Pan	Region of Interest, E-zoom from 1X - 4X
Non-Uniformity Correction	1-point with shutter or through lens
Time to First Image	< 2.0 seconds

MECHANICAL

Dimensions	See Configuration and Lens Data - Page 4
Camera Core Weight	See Configuration and Lens Data - Page 4

CONFIGURATIONS

Base	Detector, Bias Board, Processor Board
With Feature Board	Base with Feature Board (Back cover also available)

POWER

Input Voltage	3 - 5.5 V Base configuration 4.5 - 18 V Base configuration with Feature Board
Power Dissipation (nominal)	< 1.0 W Base configuration < 1.1 W Base configuration with Feature Board
PoUSB (Power over USB)	Requires Feature Board

FEATURES

Available Command Protocols	LVCMOS UART; RS-232; USB 2.0
Image Enhancement	Image Contrast Enhancement (ICE™)
External Sync	Yes
Color	24-bit RGB output via Camera Link®
Image Control	Polarity: White Hot / Black Hot Orientation: Invert / Revert
Symbology	User selectable options include: Zoom, Polarity and Shutter Notification
Custom Lens Configuration	Storage for up to 5 LUTs

ENVIRONMENTAL

Operating Temp Range	-40 °C to +80 °C
Shock / Vibration	70 G (all axis) / 4.3 G (three axis)
EMC Radiation	FCC Class A digital device
Humidity	5 to 95%, non-condensing
Standards Compliance	ROHS and WEEE Compliant
Sealed lens/lens mount	IP 67

TAMARISK® 320 CONFIGURATION AND LENS DATA

Product View	EFL f/# Focus Type ¹	FOV (H° x V°)	Weight ² (Camera + Lens)	Dimensions ³ H x W x D ±0.5 mm	Range ⁴ Performance Man Det. / Rec. Veh Det. / Rec.
	No Lens	No Lens	29 g	34 x 30 x 30	No Lens
	7.5 mm f/1.2 MF	40° x 30°	35 g	28 x 24 x 35	370 m / 70 m 930 m / 180 m
	7.5 mm f/1.2 A	40° x 30°	45 g	32 x 27 x 38	370 m / 70 m 930 m / 180 m
	11 mm f/1.2 MF	27° x 20°	49 g	31 x 26 x 40	540 m / 100 m 1,360 m / 260 m
	21 mm f/1.2 MF	15° x 11°	51 g	34 x 29 x 40	990 m / 190 m 2,380 m / 490 m
	19 mm f/1.2 A	16° x 12°	65 g	36 x 35 x 41	990 m / 190 m 2,380 m / 490 m
	35 mm f/1.2 MF	9° x 6.7°	64 g	37 x 32 x 49	1,620 m / 320 m 3,750 m / 810 m
	35 mm f/1.2 A	9° x 6.7°	134 g	47 x 47 x 58	1,620 m / 320 m 3,750 m / 810 m

- ¹ Focus Type A = Athermalized, MF = Manual Focus
² Weight Weights provided above are for the OEA configuration. Add 7 grams for OEAX configurations with the optional Feature Board. Add 5 grams when the optional back shell is included.
³ Dimensions Sizes provided above are for the OEA configuration. Add 7.5 mm to the depth for OEAX configurations with the optional Feature Board.
⁴ Range Data 50% probability of detection and recognition on a clear day, other factors apply

TAMARISK® 320 ACCESSORIES





Product Documentation CD Part #: 1013165 includes the following: User Manual, Mechanical ICD, Mechanical Drawing Source Files, Electrical ICD, Software ICD, Camera Control Software, Camera Control Software User's Guide and Application Notes	
Camera Interface Cable Terminated Part #: 1002775-001 12" 30-pin cable terminated on both ends	
Camera Interface Cable Un-terminated Part #: 1010590-001 12" 30-pin cable terminated on one end	
Breakout Box Part #: 1003785-001 For use with camera modules equipped with the optional Feature Board	
Back Shell Part #: 1012462-001 Custom fit for the OEAX configuration (open electronics architecture with feature board)	
Tripod Mounting Bracket for cameras: 40° A; 15°; 9° MF and no lens Part #: 1003631-001 for camera: 40° MF Part #: 1003631-002 for camera: 27° MF Part #: 1003631-003 Anodized aluminum with 1/4-20 thread in base	
Retaining Rings for cameras: 40° A; 15°; 9° MF and no lens Part #: 1002419-001 for camera: 40° MF Part #: 1002417-001 for camera: 27° MF Part #: 1003145-001 Anodized aluminum retaining ring	

Figure A.1 Tamarisk® 320 Data Specifications

Specifications

Overview	Tau 640	Tau 336	Tau 324
Thermal Imager	Uncooled VOx Microbolometer		
FPA / Digital Video Display Formats	640 × 512	336 × 256	324 × 256
Analog Video Display Formats	640 × 480 (NTSC); 640 × 512 (PAL) ¹		
Pixel Pitch	17 μm		25 μm
Spectral Band	7.5 - 13.5 μm		
Full Frame Rates	30 Hz (NTSC) 25 Hz (PAL)	30/60 Hz (NTSC) 25/50 Hz (PAL)	
Exportable Frame Rates	7.5 Hz NTSC; 8.3 Hz PAL		
Sensitivity (NEΔT)	<50 mK at f/1.0		
Scene Range (High Gain)	-25°C to +135°C	-25°C to +100°C	-25°C to +135°C
Scene Range (Low Gain)	-40°C to +550°C		
Time to Image	<5.0 sec	<4.0 sec	
Factory Optimized Video	Yes		
Physical Attributes	Tau 640	Tau 336	Tau 324
Size (w/o lens)	1.75" x 1.75" x 1.18"		
Lensed & Lensless Configurations Available	Yes		
Precision Mounting Holes (M2x0.4) on 3 sides (2 per side)	Yes		
Sealable Bulkhead Mounting Feature on Lens Barrel (M29x1.0), WFOV Only	Yes		
Radiometric Features	Tau 640	Tau 336	Tau 324
Isotherms	See Product Spec page 34 Section 3.3.3.1		
Spot Meter	Temperatures measured in central 4x4 Improved accuracy, moveable spot meter, image metric data, T-		
Advanced Radiometry	 Linear (digital output) (OEM part number required, additional charge)		
Image Processing & Display Controls	Tau 640	Tau 336	Tau 324
NTSC/PAL (field switchable)	Yes		
Image Optimization	Yes		
Digital Detail Enhancement	Yes		
Invert/Revert (analog and 8-bit digital)	Yes		
Polarity Control (black hot/white hot)	Yes		
Color & Monochrome Palettes (LUTs)	Yes		
Digital Zoom	2x, 4x, 8x	2x, 4x	
Continuous Zoom	Yes		
Symbology (256 gray & 256 color)	Yes, single-pixel resolution for all models		
Digital Video	Tau 640	Tau 336	Tau 324
LVDS (14-bit or 8-bit)	Yes		
CMOS (14-bit or 8-bit)	Yes		
BT.656 (8-bit)	Yes		
Camera Link (Expansion Bus Accessory Module)	Yes		
Slow Video Option (factory configured)	Yes		

Interfacing	Tau 640	Tau 336	Tau 324
Primary Electrical Connector	50-pin Hirose		
Input Power (max 2.5 amp during shutter)	4.0 - 6.0 VDC		
Power Dissipation, steady state	<1.2 W	~1.0 W	
Flat-Field Correction (FFC) Duration	<0.5 sec		
Power Reduction Switch (disables analog video)	Yes		
RS-232 Compatible Communication	57,600 & 921,600 baud		
External Sync Input/Output	Yes		
Discrete I/O Controls Available	Yes (10-camera minimum)		
Settable Splash Screens	Yes (10-camera minimum)		
User Configurability via SDK & GUI	Yes		
Dynamic Range Switching	No	Yes	

Figure A.2 FLIR® Tau 2 Data Specifications

IPORT CL-U3 External Frame Grabbers

Video Connectivity Solutions

iPORT External Frame Grabber	<ul style="list-style-type: none"> Highly reliable, 3 Gb/s data transfer rate with low, end-to-end latency Surface-mountable enclosure
eBUS SDK	<ul style="list-style-type: none"> eBUS Universal Pro driver Sample applications and documentation Support for CLProtocol
USB3 Vision and GenICam	<ul style="list-style-type: none"> Fully compatible firmware load Guarantees delivery of all packets Comprehensive data transfer diagnostics

Video Formats

Tap Support	<ul style="list-style-type: none"> Base mode: 1 and 2 taps Medium mode: 1,2, and 4 taps
Tap Geometry	<ul style="list-style-type: none"> 1X_1Y, 1X, 1X2_1Y, 1X2, 1X4_1Y, 1X4
Video Modes	<ul style="list-style-type: none"> Mono, BayerGR, BayerRG, BayerGB, BayerBG, RGB, BGR, Sparse Color Filter pattern
Pixel Depth	<ul style="list-style-type: none"> 8, 10, 12, 14, 16 bits, 24-bit RGB

Features

Pixel Clock	<ul style="list-style-type: none"> 20 MHz to 85 MHz
Frame Buffer	<ul style="list-style-type: none"> 120 MB
USB 3.0 based	<ul style="list-style-type: none"> Connection to low-cost, easy-to-use equipment USB3 Vision 1.0 compliant
Programmable Logic Controller	<ul style="list-style-type: none"> Advanced image capture control Integrated with GPIO
GPIO	<ul style="list-style-type: none"> 4 TTL/LVCMOS inputs 3 TTL/LVCMOS outputs
GPIO (CL-U3 industrial models only)	<ul style="list-style-type: none"> 2 LVDS/RS-422/HVTTL/±24V/±30V differential or single-ended inputs 2 TTL/LVCMOS inputs 3 TTL/LVCMOS outputs

Characteristics

Size (L x W x H) and Weight	<ul style="list-style-type: none"> 38 mm X 83 mm X 51 mm Up to 132 g
Operating temperature	<ul style="list-style-type: none"> 0°C to 45°C -20°C to 60°C (CL-U3 industrial models only)
Storage temperature	<ul style="list-style-type: none"> -40°C to 85°C
External power supply	<ul style="list-style-type: none"> 11.6V to 13.0V (CL-U3 industrial models only)
Power consumption	<ul style="list-style-type: none"> 3.5 W maximum for all models

Pleora Technologies Inc.
 340 Terry Fox Drive, Suite 300
 Kanata, Ontario
 Canada, K2K 3A2

Tel: +1.613.270.0625
 Fax: +1.613.270.1425
 Email: info@pleora.com

Connectors

Video	<ul style="list-style-type: none"> SDR-26 (Mini CL) for Camera Link
USB	<ul style="list-style-type: none"> 10-pin USB 3.0 micro-B Receptacle with locking screw connectors
GPIO	<ul style="list-style-type: none"> 12-pin circular connector
Power In	<ul style="list-style-type: none"> Power over USB cable GPIO Connector (CL-U3 industrial models only)
Power Out (CL-U3 industrial models only)	<ul style="list-style-type: none"> PoCL SDR-26 Connector

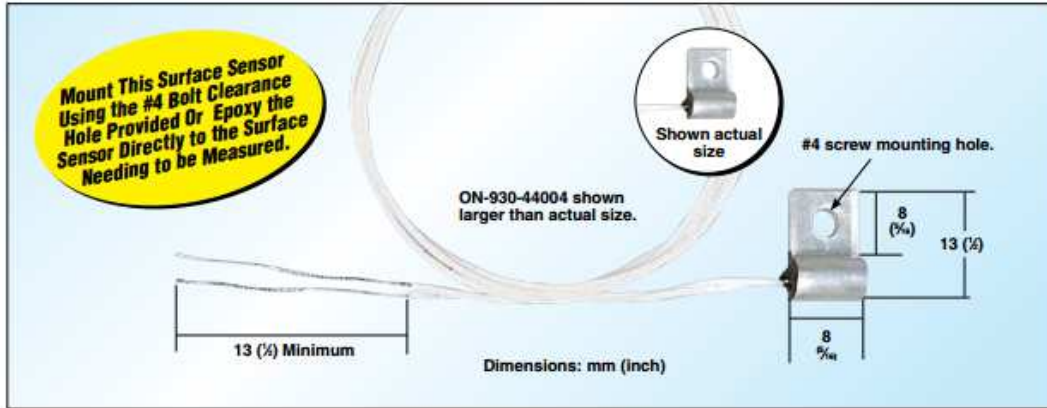
Ordering Information

903-0007	<ul style="list-style-type: none"> iPORT CL-U3B External Frame Grabber for Camera Link Base mode.
903-0011	<ul style="list-style-type: none"> iPORT CL-U3B Development Kit including 903-0007, USB 3.0 cable, and eBUS SDK USB stick.
903-0009	<ul style="list-style-type: none"> iPORT CL-U3B-IND External Frame Grabber (Industrial use) for Camera Link Base mode, extended operating temperature range, extensive GPIO, and power over Camera Link (PoCL).
903-0013	<ul style="list-style-type: none"> iPORT CL-U3B-IND Development Kit including 903-0009, power supply, USB 3.0 cable, and eBUS SDK USB stick.
903-0008	<ul style="list-style-type: none"> iPORT CL-U3M External Frame Grabber for Camera Link Medium mode.
903-0012	<ul style="list-style-type: none"> iPORT CL-U3M Development Kit including 903-0008, USB 3.0 cable, and eBUS SDK USB stick.
903-0010	<ul style="list-style-type: none"> iPORT CL-U3M-IND External Frame Grabber (Industrial use) for Camera Link Medium mode, extended operating temperature range, extensive GPIO, and power over Camera Link (PoCL).
903-0014	<ul style="list-style-type: none"> iPORT CL-U3M-IND Development Kit including 903-0010, power supply, USB 3.0 cable, and eBUS SDK USB stick.



© 2014 Pleora Technologies Inc. iPORT, vDisplay, eBUS, AutoGEV, and NetCommand are trademarks of Pleora Technologies Inc. Information in this document is provided in connection with Pleora Technologies products. No license, express or implied, by estoppel or otherwise, to any intellectual property rights is granted by this document. Pleora may make changes to specifications and product descriptions at any time, without notice. Other names and brands may be claimed as the property of others. EX002-023-0004 Rev 7.2 04/12/14

Figure A.3 iPORT CL-U3 External Frame Grabber



ON-930 Series

✓ Aluminum Housing Provides Rapid Heat Transfer Between the Sensor and Mounting Surface for Accurate Measurements

✓ Available in 5 Resistance Values to Fit Your Instrumentation Needs
 ✓ 28 AWG Stranded PFA Insulated Wire with Stripped Leads Standard (See Table for Length)

To Order					
Model No.	Resistance @ 25°C	Interchangeability @ 0 to 70°C	Temperature Rating	Cable Length mm (inch)	Cable Termination
ON-930-44004	2252 Ω	±0.2°C	100°C (212°F)	300 mm (12")	Stripped
ON-930-44005	3000 Ω	±0.2°C	100°C (212°F)	300 mm (12")	Stripped
ON-930-44007	5000 Ω	±0.2°C	100°C (212°F)	300 mm (12")	Stripped
ON-930-44006	10000 Ω	±0.2°C	100°C (212°F)	300 mm (12")	Stripped
ON-930-44008	30000 Ω	±0.2°C	100°C (212°F)	300 mm (12")	Stripped
ON-930-44004-40	2252 Ω	±0.2°C	100°C (212°F)	1 m (40")	Stripped
ON-930-44005-40	3000 Ω	±0.2°C	100°C (212°F)	1 m (40")	Stripped
ON-930-44007-40	5000 Ω	±0.2°C	100°C (212°F)	1 m (40")	Stripped
ON-930-44006-40	10000 Ω	±0.2°C	100°C (212°F)	1 m (40")	Stripped
ON-930-44008-40	30000 Ω	±0.2°C	100°C (212°F)	1 m (40")	Stripped

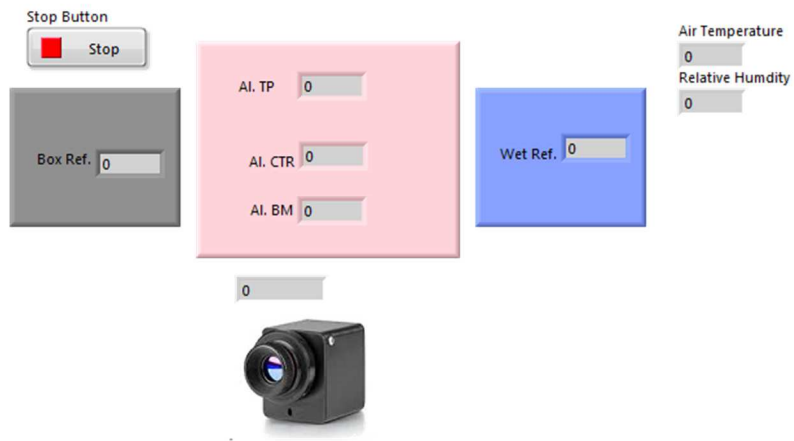
Notes: For additional cable length, add required length (in inches) to end of the model number for additional cost. For a phone plug, add "-PP" to the model number for additional cost. For tighter interchangeability, substitute the thermistor part number from the table below.
Ordering Examples: ON-930-44004, flag-mount thermistor sensor with a resistance of 2252 Ω at 25°C and an interchangeability of ±0.2°C, 300 mm (12") of cable.
 ON-930-44034-40-PP, flag-mount thermistor sensor with a resistance of 5000 Ω at 25°C and an interchangeability of ±0.1°C, 1 m (40") of cable and a phone plug connector.

Optional Thermistors

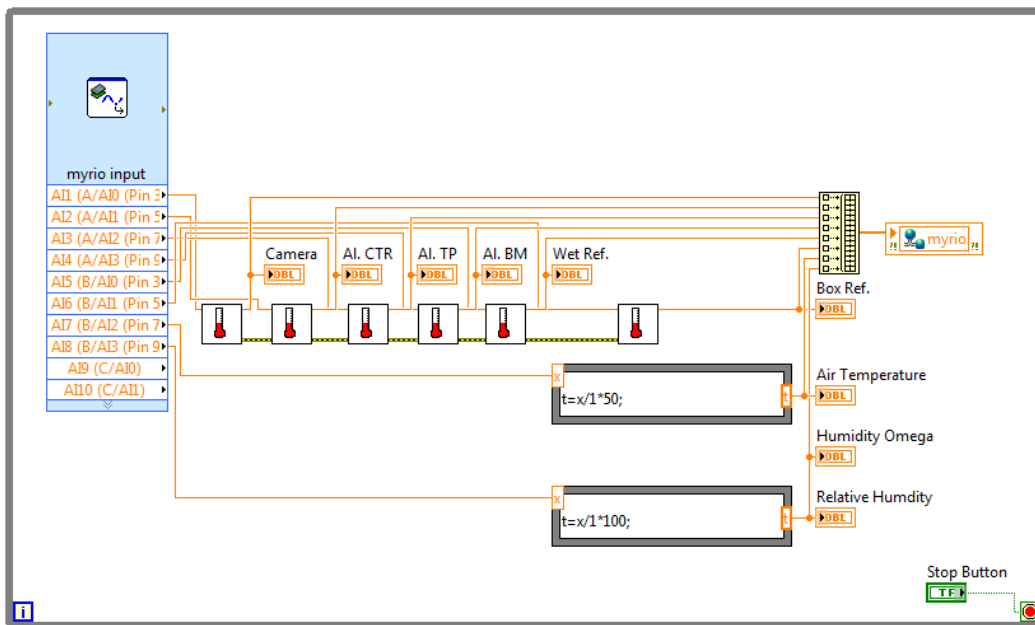
Model Number	Resistance @ 25°C (Ω)	Maximum Working Temp	Interchangeability @ 0 to 70°C	Storage and Working Temp for Best Stability
44033	2252	75°C (165°F)	±0.1°C	-80 to 75°C (-110 to 165°F)
44030	3000	75°C (165°F)	±0.1°C	-80 to 75°C (-110 to 165°F)
44034	5000	75°C (165°F)	±0.1°C	-80 to 75°C (-110 to 165°F)
44031	10,000	75°C (165°F)	±0.1°C	-80 to 75°C (-110 to 165°F)
44032	30,000	75°C (165°F)	±0.1°C	-80 to 75°C (-110 to 165°F)

Figure A.4 Surface mount thermistors produced by Omega Engineering. ON-930-44005-40 and ON-930-44033 were used for research covered in Chapter 2, 3, and 4.

TIR Camera Chamber Monitor

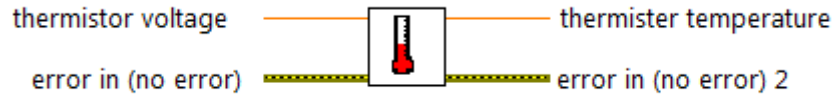


(a)

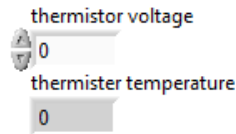


(b)

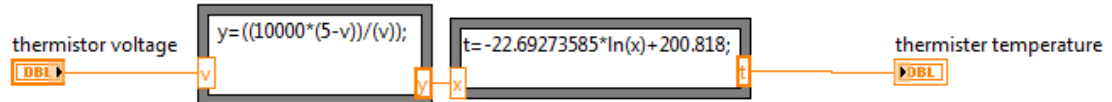
Figure A.5 Near-Perfect Black-Body Enclosure Monitoring VI front panel (a) and back panel (b)



(a)



(b)



(c)

Figure A.6 The wiring of the Thermistor sub-VI (a), front panel (b), and block diagram (c) show the input from the logarithmic calibration curve in order to convert input voltage into temperature °C.

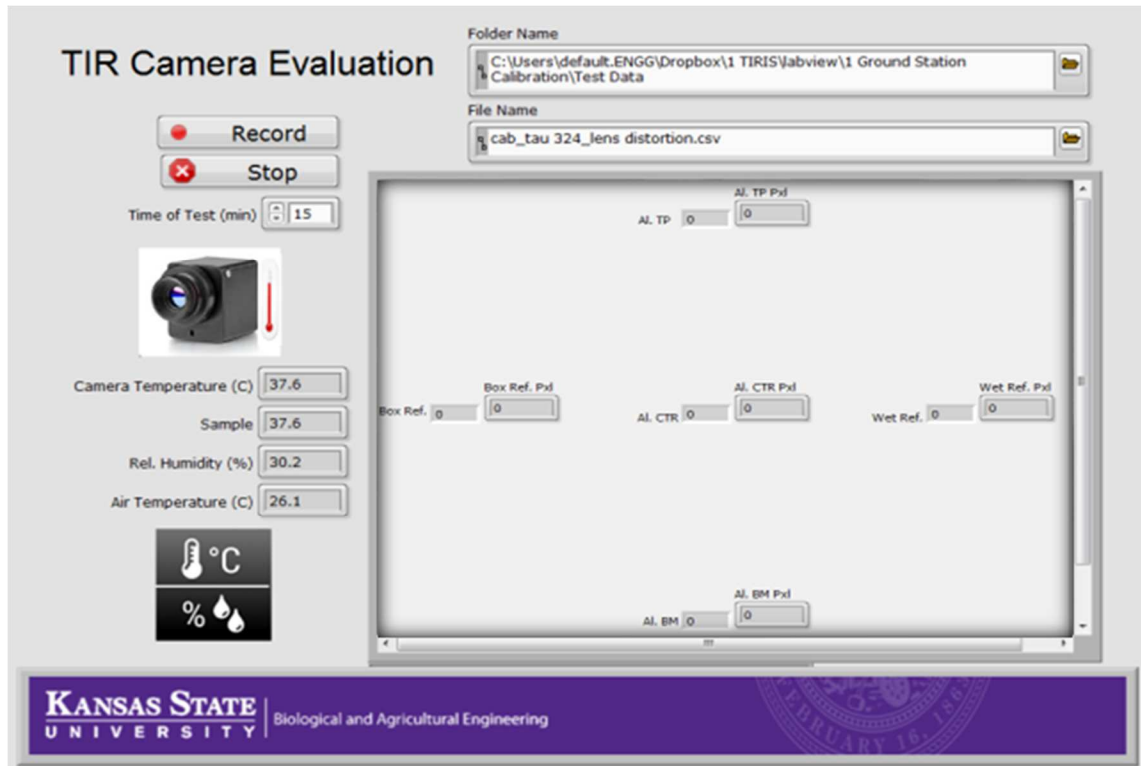


Figure A.7 TIR Camera Evaluation VI front panel

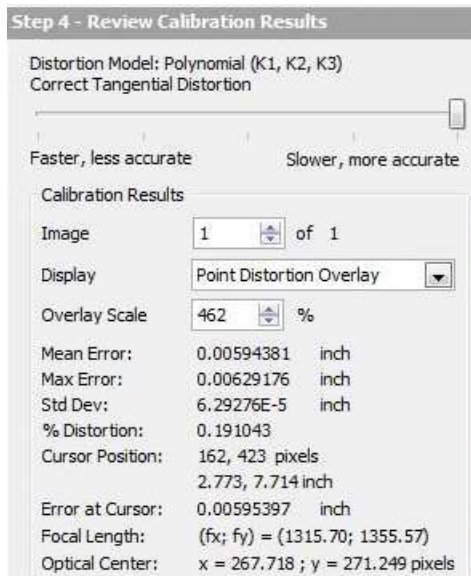


Figure A.8 Tamarisk® 320 lens distortion calibration results

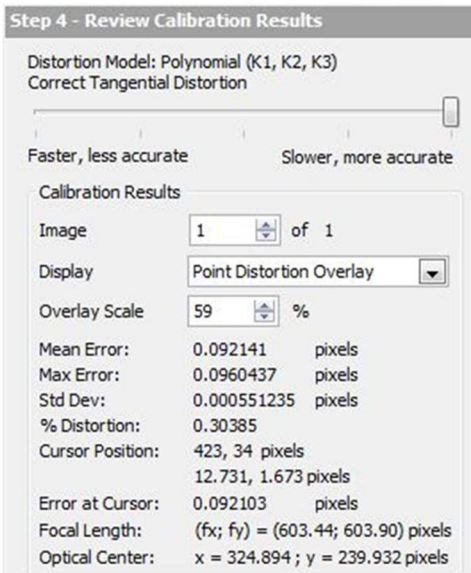


Figure A.9 FLIR® Tau 2 (324) lens distortion calibration results

Appendix B - Supplemental Materials for Chapter 4

SYSTEM FEATURES

FOCAL PLANE ARRAY

Detector Type	Uncooled VOx Microbolometer
Array Format	640 x 480
Pixel Size	17 μ m
Spectral Band	8 to 14 μ m
Sensitivity (NEDT) f/1.0 @ Room Temperature	< 50 mK

VIDEO FORMAT

Frame Rates	30 fps, 9 fps
Analog Video	NTSC (480i); PAL (576i) Field switchable
Digital Video	14/8-bit LVCMOS/Camera Link®
Automatic Gain and Level	User Defined, persistent through power cycles
Digital Zoom and Pan	Region of Interest; E-zoom from 1X - 4X
Non-Uniformity Correction	1-point with shutter or through lens
Time to First Image	< 2.5 seconds

MECHANICAL

Dimensions	See Configuration and Lens Data - Page 5
Camera Core Weight	See Configuration and Lens Data - Page 5

CONFIGURATIONS

Base	Detector, Bias Board, Processor Board
With Feature Board	Base with Feature Board (Back cover also available)

POWER

Input Voltage	3 - 5.5 V Base configuration 4.5 - 18 V Base configuration with Feature Board
Power Dissipation (nominal)	< 1.2 W Base configuration < 1.4 W Base configuration with Feature Board
PoUSB (Power over USB)	Requires Feature Board

FEATURES

Available Command Protocols	LVCMOS UART; RS-232; USB 2.0
Image Enhancement	Image Contrast Enhancement (ICE™)
External Sync	Yes
Color	24-bit RGB output via Camera Link®
Image Control	Polarity: White Hot / Black Hot Orientation: Invert / Revert
Symbology	User selectable options include: Zoom, Polarity and Shutter Notification
Custom Lens Configuration	Storage for up to 5 LUTs

ENVIRONMENTAL

Operating Temp Range	-40°C to +80°C
Shock / Vibration	75 G (all axis) / 4.43 G (all axis)
EMC Radiation	FCC Class A digital device
Humidity	5% and 95%, non-condensing
Standards Compliance	ROHS and WEEE
Sealed lens/lens mount	IP 67

TAMARISK® 640 CONFIGURATION AND LENS DATA

Effective Focal Length	Horizontal x Vertical FOV (H° x V°)	IFOV (mrad)	f/#	Weight ¹ (with lens in grams)	Dimensions ² H x W x D \pm 0.5 mm	Range ³ Performance Detection / Recognition (meters)	Focus Type
No Lens	No Lens	No Lens	No Lens	65	46 x 40 x 31	No Lens	No Lens
7.5 mm	90° x 67°	2.45	f/1.4	100	46 x 40 x 39	Man: 335 / 60 Vehicle: 855 / 160	Athermal
9 mm	70° x 52°	1.8	f/1.4	105	46 x 40 x 46	Man: 390 / 75 Vehicle: 900 / 180	Athermal
12.8 mm	49.8° x 37°	1.35	f/1.4	110	46 x 46 x 50	Man: 550 / 100 Vehicle: 1,260 / 260	Athermal
14.25 mm	44° x 33°	1.19	f/1.4	110	46 x 40 x 51	Man: 640 / 120 Vehicle: 1,580 / 310	Athermal
16.7 mm	37.5° x 28°	1.01	f/1.25	90	46 x 40 x 40	Man: 745 / 140 Vehicle: 1,825 / 365	Athermal
25 mm	24.8° x 18.6°	0.68	f/1.2	115	46 x 40 x 52	Man: 1,030 / 195 Vehicle: 2,475 / 505	Athermal
35 mm	17.6° x 13.2°	0.48	f/1.2	165	50 x 47 x 59	Man: 1,450 / 285 Vehicle: 3,390 / 725	Athermal
50 mm	12.4° x 9.3°	0.34	f/1.2	295	58 x 58 x 86	Man: 2,105 / 425 Vehicle: 4,740 / 1,070	Athermal
65 mm	9.6° x 7.2°	0.26	f/1.2	525	73 x 73 x 106	Man: 2,730 / 565 Vehicle: 5,950 / 1,405	Athermal

Figure B.10 Tamarisk® 640 Data Specifications

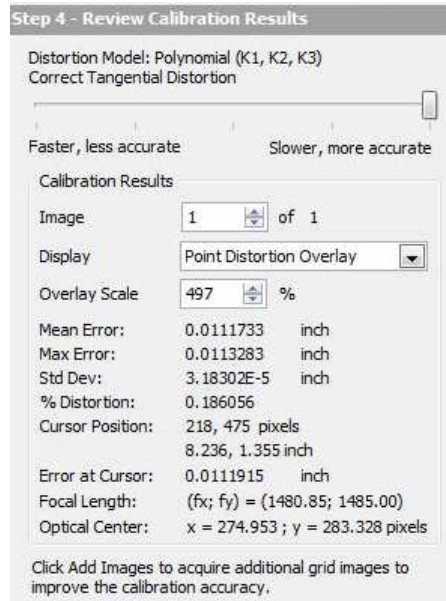


Figure B.11 Tamarisk® 640 lens calibration results

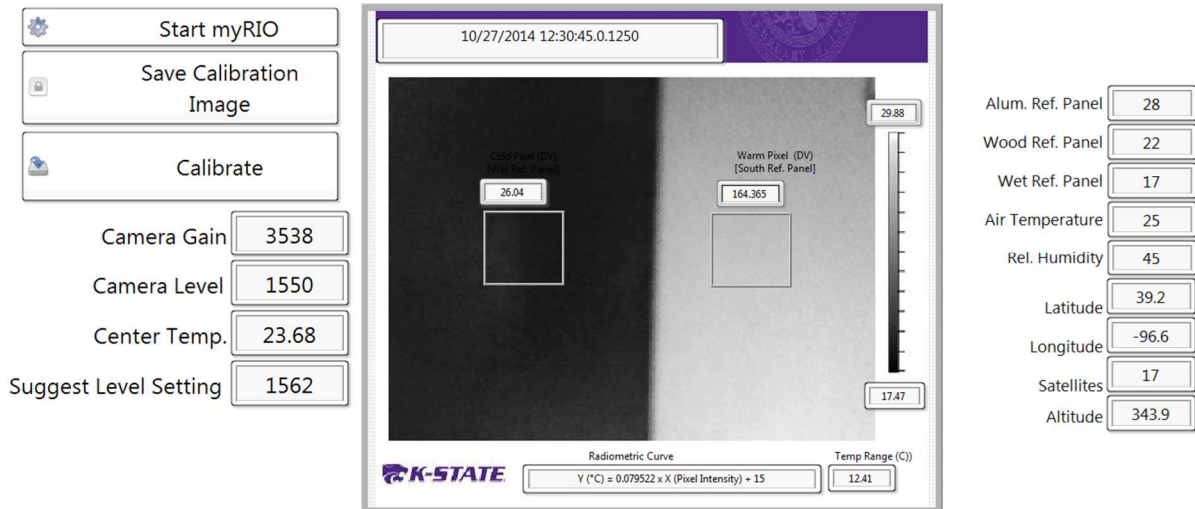


Figure B.12 OT Calibration VI front panel

Appendix C - Software CD

1. Complete LabVIEW™ Projects
 - a. VIs
 - i. TIR Camera Evaluation
 - ii. TIR Field Calibration
 - iii. Automated Greenhouse Monitoring System
 - iv. Auto Analyze Greenhouse Monitoring Data for Individual Crop Water Stress
 - v. AVI Segmentation to Filtered Images
 - b. Complete Sub-VIs
 - i. Thermistor Sensor
 - ii. Air Temperature/Relative Humidity Transmitter Sensor
 - iii. Upload and Download to USB
 - iv. GPS Read
 - v. Tamarisk® 320 Lens Distortion Correction
 - vi. Tamarisk® 640 Lens Distortion Correction
 - vii. FLIR® Tau 2 Lens Distortion Correction
 - viii. Save to CSV File
 - ix. Upload from CSV File
 - c. Remote Target VIs
 - i. MyRIO TIR Field Calibration and Flight Reference Data
 - ii. MyRIO TIR Cabinet Monitoring
 - iii. SBRIO Greenhouse Monitoring
2. Complete Agisoft™ Professional Image Bundles